MODELING LANDSLIDE-GENERATED TSUNAMIS WITH LONG-WAVE EQUATIONS

A Dissertation

Presented to the Faculty of the Graduate School

of Cornell University

in Partial Fulfillment of the Requirements for the Degree of

Doctor of Philosophy

by

Hong-Yueh Lo

May 2018

© 2018 Hong-Yueh Lo
ALL RIGHTS RESERVED

MODELING LANDSLIDE-GENERATED TSUNAMIS WITH LONG-WAVE EQUATIONS

Hong-Yueh Lo, Ph.D.

Cornell University 2018

Landslides are recognized as a generation mechanism of tsunamis. While earthquake-generated tsunamis are catastrophes on a more global scale, landslide-generated tsunamis tend to cause extreme local damage. Acknowledging the great uncertainty in the motion and the properties of real tsunamigenic landslides, and the challenges in assuming a complex multiphysics landslide model given the uncertainty, we focus on understanding the fundamental mechanics of the wave generation process. The main objectives of this study are to determine the most computationally efficient wave model that can be used to simulate the wave generation process due to a submarine landslide, and to construct a closed-form wave generation model that requires no computation.

New analytical solutions were derived for landslide-generated tsunamis in idealized scenarios. Analytical solutions not only provide the scaling relations between a submarine landslide and the resulting tsunami, but also reveal that the volume of a landslide, as opposed to its exact shape, has the greatest impact on the leading tsunami wave generated by the landslide. Therefore, in modeling, it is more important to match the landslide volume than to match the exact landslide shape.

Numerical solvers based on long-wave equations were constructed to complement the analytical solutions. By comparing the numerical results based on different long-wave equations, nonlinear effects and frequency dispersion effects were examined separately. Using the knowledge gained from both analytical solutions

and numerical simulations, we proposed criteria to determine whether nonlinearity is important and whether frequency dispersion is important in a landslide tsunami problem, and therefore the appropriate wave generation model to use.

Lastly, combining the findings of this study, we constructed a closed-form landslide tsunami generation model. As a function of relevant input parameters, the model outputs a tsunami wave profile due to a submarine landslide. In contrast to all existing closed-form landslide tsunami generation models, the new model is based on the newly derived analytical solutions, and provides information on not only the maximum wave height, but also the complete free surface profile, the flow velocity, and the duration of the wave generation stage. The new model was shown to be an improvement over a commonly used empirical model.

BIOGRAPHICAL SKETCH

Hong-Yueh Lo grew up in Taipei, Taiwan, and moved to the U.S. for higher education at the age of eighteen. He attended the engineering program at Green River Community College in Auburn, WA for two years before transferring to Cornell University in Ithaca, NY to study civil engineering. The junior-level introductory course to fluid mechanics taught by Professor Todd Cowen made Lo discover his passion for the subject of fluid mechanics. He then performed research as an undergraduate student under the supervision of Dr. Yong Sung Park and Professor Philip Liu. The research on the runup of solitary waves eventually became Lo's master's thesis. Continuing his love for fluid mechanics and Upstate New York, Lo stayed at Cornell University to study landslide-generated tsunamis for a Ph.D. degree. Aligned with his interests in fluid mechanics, Lo's hobbies include kayaking, skiing, windsurfing, and beer brewing.

ACKNOWLEDGEMENTS

I am grateful for the guidance and support I received from my committee chair, Professor Philip Liu, and my committee members, Professor Rowena Lohman and Professor Jim Jenkins. I thank Dr. Yong Sung Park and Professor Todd Cowen for their long-lasting positive impacts on me as I was just beginning my academic journey as an undergraduate. Professor Patrick Lynett and Professor Costas Synolakis at the University of Southern California were generous for taking me in as a visiting student during my last year and giving me valuable feedback on my work. Without all the amazing kayakers and outdoorsy people I've met over the years, I would not have been able to overcome the challenges in graduate school while remaining a healthy and happy person. Lastly, I am forever grateful for the love and emotional support that my family has always shown me.

TABLE OF CONTENTS

LIST OF TABLES

LIST OF FIGURES

CHAPTER 1

INTRODUCTION

Tsunamis are most commonly generated by a sudden vertical displacement of the seafloor due to an earthquake and are capable of causing large-scale damage. Notable recent events, to name just a few, include the 2011 Japan Tohoku earthquake and tsunami, which resulted in more than $15,000$ casualties (e.g., Mori et al., 2011), the 2009 Samoa earthquake and tsunami, which resulted in more than 180 casualties (e.g., Okal et al., 2010), and the 2004 Indian Ocean earthquake and tsunami, which resulted in more than $150,000$ casualties (e.g., Liu et al., 2005a).

The displacement of water due to a landslide is also recognized as a generation mechanism of tsunamis. For example, the 1998 Papua New Guinea (PNG) tsunami is commonly believed to have been caused by a submarine landslide, which resulted in over $2,000$ casualties and affected at least 25 km of coastline (e.g., Tappin, 1999; Synolakis et al., 2002; Lynett et al., 2003). However, landslide-generated tsunamis tend to be localized events. An extreme case is the 1958 Lituya Bay mega-tsunami, where a subaerial landslide generated water waves that produced a local runup height of 524 m (see Fritz et al., 2009). Some other examples include the 1934 Norway Tafjord tsunami, which was generated by a subaerial rockslide and resulted in more than 40 casualties (e.g., Harbitz et al., 1993), and the 1994 Alaska Skagway tsunami, which was generated by a submarine landslide and resulted in more than 15 million worth of damage but no casualties (see Kulikov et al., 1996). More recently, Ward and Day (2001) pointed out the possibility of a flank collapse on the volcanic island of La Palma, which might result in a quick release of $150 - 500$ km^3 of rock into the sea and cause a tsunami of at least 3 m high along the coasts of the Americas. Although these extreme initial estimates have been found

to be unlikely in later studies (see Løvholt et al., 2008, for a review), the risk is small but real. The generation mechanism of landslide-generated tsunamis is much more complex than that of earthquake-generated tsunamis. While the generation mechanism of earthquake-generated tsunamis is considered well-understood, that of landslide-generated tsunamis requires further study.

1.1 Literature review

Analytical studies have been performed to study landslide-generated tsunamis in idealized scenarios. Based on the Linear Shallow Water wave Equations (LSWE) in one horizontal dimension (1DH), Tinti et al. (2001) derived a closed-form analytical solution for the free surface elevation perturbed by a solid landslide moving at a constant speed in constant water depth. For water waves forced by a prescribed landslide traveling down a constant slope, Tuck and Hwang (1972) derived a general integral-form solution, consisting of three integrals. By specifying a deforming Gaussian-like landslide accelerating at the same rate as local wave celerity (wave celerity increases as water depth increases), Liu et al. (2003) simplified the integral-form solution down to one integral. Didenkulova et al. (2010, 2011) also found simplified solutions for water waves generated by a deforming submarine landslide on a convex slope, and examined resonance more closely. Extending the LSWE solutions from 1DH to 2DH, Sammarco and Renzi (2008) and Renzi (2010) derived the general integral-form landslide-generated wave solution (consisting of three integrals and a series) on a plane beach, and examined the large-time asymptotic behavior of the generated waves. The same solution process was later used to study landslide-generated waves around a conical island (Renzi and Sammarco, 2010) and the effects of landslide shape in LSWE (Renzi and Sammarco, 2012). Seo and Liu (2013) extended the solution process to allow for more arbitrary landslide shapes

and placed a stronger emphasis on the numerical integration methods. Analytical solutions based on the Linear and Fully Dispersive (LFD) wave equations are possible. For both 1DH and 2DH, Mei (1989) derived the general transformed solution for waves generated by a seafloor displacement as well as the asymptotic far-field leading wave solutions for specific bottom displacement functions.

Various laboratory and numerical studies have been performed on water waves forced by a short block sliding down an incline. One of the pioneering studies is Heinrich (1992), in which a solid block, shaped like an isosceles right triangle, sliding down a 45° incline, was investigated both experimentally and numerically with the two-dimensional (2D) Navier-Stokes equations. Assier Rzadkiewicz et al. (1997) and Watts (1997, 2000) conducted further studies with a similar landslide configuration, in which both solid and deformable landslides were considered. Liu et al. (2005b) then extended the solid-block landslide setup to 3D, and conducted large-scale laboratory experiments as well as numerical experiments based on the Large Eddy Simulation (LES) approach. Additional three-dimensional laboratory experiments include Panizzo et al. (2005), Enet and Grilli (2007), and Di Risio et al. (2009). To study the potential rockslide in Åkerneset, Norway, Sælevik et al. (2009) and Lindstrøm et al. (2014) conducted laboratory experiments in both 2D and 3D. On the other hand, several studies focused exclusively on the laboratory investigation of granular landslides (e.g. Fritz et al. 2004; Heller and Hager 2010; Mohammed and Fritz 2012). In the above examples, either the incline was steep or the landslide was short compared to water depth. Therefore, flow variation in the vertical direction was significant. Furthermore, intense wave breaking often occurs in cases where the landslide is initially subaerial. As a result, solving the full Navier-Stokes equations or the Euler equations is usually necessary to produce comparable numerical results in these configurations.

Long-wave equations, in which the wavelength is assumed to be much larger than the water depth, are often employed to study earthquake-generated tsunamis. For long waves, the flow velocity varies weakly in the vertical direction. Therefore, a velocity profile can be assumed and depth-averaged to eliminate the vertical dimension. As a result, a full 3D problem can be simplified to 2DH, and a 2D problem can be simplified to 1DH. Due to the significant reduction in the computation time, faster-than-real-time tsunami simulations on a global scale are possible, and sensitivity analysis based on multiple numerical simulations can be more easily performed. Long-wave equations can also be employed to study landslide-generated tsunamis. Jiang and LeBlond (1992) first considered long waves generated by a viscous landslide, in which the Nonlinear Shallow Water wave Equations (NSWE) were used to model the water waves, and the landslide was modeled as a Newtonian fluid with an assumed parabolic velocity profile and hydrostatic pressure distribution. The study was then extended to 2DH in Jiang and LeBlond (1994). A Bingham-plastic landslide model was also investigated in Jiang and LeBlond (1993). By comparing numerical results based on different equations, Lynett and Liu (2002) further examined the importance of frequency dispersion for water waves generated by a submarine solid landslide. More recently, Dutykh and Kalisch (2013) employed both NSWE and the Weakly Nonlinear and Weakly Dispersive wave model (WNWD, or commonly referred to as a Boussinesq-type model) to model 1DH water waves generated by a prescribed submarine landslide in a closed basin.

To the leading order, the characteristic wavelength of the generated waves is the same as the landslide length (the exact relation will be further investigated in this study). Therefore, the long-wave assumption effectively requires the landslide to be long in comparison with the water depth, which may be challenging to realize

in laboratory experiments. Relatively few laboratory experiments in which the long-wave assumption is reasonable exist – Grilli and Watts (2005) provided a small set of experimental data for submarine-landslide-generated waves on a 15° incline. Zhou and Teng (2010) conducted similar experiments, on three different slopes (5°, 10°, and 15°), to check the accuracy of their fourth-order accurate dispersive long-wave model. Sue et al. (2011) measured water waves, in both space and time, generated by a submarine solid landslide sliding down a 15° incline into constant water depth. Whittaker et al. (2015, 2017) provided water surface elevation measurements, in both time and space, caused by a solid landslide moving at a constant speed in a channel of constant water depth. The latter three of these experiments will be used as benchmarks to test the performance of our long-wave numerical model in this study.

1.2 Wave generation stage

Two stages can be defined in the landslide-generated tsunami problem – the wave generation stage and the wave-propagation stage. During the wave generation stage, the landslide is actively forcing water waves. After some time, the forced water waves eventually travel far enough ahead of the landslide to become free waves, which are no longer affected by the landslide behind them, and the wave propagation stage begins. The wave propagation stage is essentially the same as the earthquake-generated tsunami problem, in which a tsunami wave profile is specified as the initial conditions and the wave is allowed to propagate freely. Therefore, the wave propagation stage can be modeled with an existing tsunami propagation model, which generally cannot resolve a landslide. The wave generation stage – the focus of this study – is the new component in the landslide-generated tsunami

problem. The idea to model the two stages separately has been discussed and implemented in various studies, such as Watts et al. (1999); Synolakis et al. (2002); Lynett et al. (2003); Løvholt et al. (2008).

The wave generation stage is challenging to study, due to the deformation and motion of the landslide, the two-way coupling between the landslide and water, and the interfacial effects. More importantly, information on the landslide dynamics is nearly impossible to acquire in real landslide-generated tsunami events – we will likely never be able to witness or measure a tsunamigenic submarine landslide while it is in motion. While complex landslide models that capture a wide array of the relevant physics can be assumed and validated with elaborately set up laboratory experiments, their geophysical relevance is difficult to establish. At best, findings based on one specific landslide model cannot be easily generalized and applied to cases where a different landslide model is used. At worst, modelers exploit their choice for the landslide model to obtain desirable numerical results. It is therefore imperative to construct a more rigorous framework based on analytical knowledge, under which the wave generation stage can be examined systematically and generalizable findings can be obtained.

Two approaches are often adopted to model the wave generation stage – by using either a numerical simulation or an empirical/semi-empirical model. In some numerical studies (e.g., Watts et al., 2003; Løvholt et al., 2008; Abadie et al., 2012), a separate landslide wave generation simulation is first conducted near the landslide source. The wave profile from the generation model is then transferred to a separate tsunami propagation model as the initial conditions. Although the initial wave profile based on this approach may be more accurate (given the assumed landslide properties in the landslide model), a separate numerical simulation is needed and

the computation time may be significant if a complex landslide wave generation model is used. In addition, the assumptions made in the landslide generation model may not be valid in reality. Alternatively, an empirical or a semi-empirical wave generation model can be used to directly specify the initial wave profile in a tsunami propagation model (e.g., Synolakis et al., 2002; Lynett et al., 2003; Watts et al., 2005). Such a model requires minimal computational effort, since it outputs the landslide tsunami profile as a function of relevant parameters. Although the initial wave profile based on this approach may be less accurate, it is computationally efficient and the effects due to each parameter can be more easily examined.

1.3 Objectives of this study

In this study, we seek to study the wave generation stage with long-wave equations. Similarly to the earthquake tsunami problem, employing long-wave equations enables faster-than-real-time simulations and makes sensitivity analysis based on multiple numerical simulations more easily achievable. A landslide model that involves highly simple and tractable assumptions and in which the landslide speed and acceleration are left as input parameters, shall be adopted. Analytical solutions, which reveal the scaling relations between the landslide parameters and the generated water waves, are derived for idealized scenarios. As a result of using a simple landslide model and considering idealized scenarios, the landslide tsunami problem can be parameterized so that three or four input parameters define each scenario. Utilizing analytical knowledge, we determine the instant when the wave generation stage ends and when the wave-propagation stage begins. By carefully deriving each set of long-wave equations, each with a different level of theoretical accuracy, we are able to examine nonlinear effects and frequency dispersion

effects separately via numerical simulations. Based on a combination of analytical knowledge and numerical simulations, we propose criteria, as functions of the input parameters, that predict whether nonlinearity or frequency dispersion is important in the wave generation stage of a landslide-generated tsunami problem. As a result, the simplest acceptable (given an error tolerance) wave model, and thus the most computationally efficient model, can be determined. Then, utilizing both the analytical and the numerical findings of this study, we construct a closed-form semi-analytical landslide tsunami generation model, which provides a quick, leading-order-accurate landslide-generated tsunami wave profile at the end of the wave generation stage. The wave profile can then be specified as the initial conditions in a conventional tsunami propagation model, without having to model the landslide wave generation stage explicitly.

This thesis is organized as follows: in Chapter 2, we present several sets of linear wave equations for the landslide-generated tsunami problem, and show their analytical solutions relevant to this study. In Chapter 3, we first present a numerical solver for the two linear long-wave equations described in Chapter 2. Then, we present three sets of nonlinear long-wave equations for the landslide-generated tsunami problem, and the numerical solver used to solve the nonlinear equations. In Chapter 4, we consider four idealized scenarios, in which the landslide tsunami problem can be parameterized by three or four input parameters. As functions of the input parameters, we determine the instant when the wave generation stage ends, and propose expressions that estimate the importance of nonlinearity and the importance of frequency dispersion during the wave generation stage. Numerical simulations are then used to compute the empirical thresholds for when nonlinearity or frequency dispersion become significant, and therefore the appropriate long-wave model to use. In Chapter 5, we extend the above work for a landslide

moving at a constant speed to a landslide that accelerates. Analytical investigations are first attempted to gain insights on the process. Numerical simulations are then performed to obtain empirical expressions that quantify the wave lengthening effects on the leading tsunami wave due to landslide acceleration. In Chapter 6, we demonstrate how our criteria for determining model validity can be applied to laboratory experiments as well as the PNG tsunami. Inspired by the PNG event, in Chapter 7 we present a closed-form semi-analytical landslide tsunami generation model, which provides as a function of the relevant input parameters a complete wave profile, including both the free surface elevation and the flow velocity, for the leading wave generated by a submarine landslide. At the end of each chapter, a summary section is included, which summarizes the most important and practical findings of the chapter. The reader should be able to grasp the key ideas of this study after reading each summary section.

CHAPTER 2

ANALYTICAL SOLUTIONS

In this chapter, we review existing analytical solutions and derive new solutions for landslide-generated water waves. Solutions for both nondispersive models and dispersive models, in both 1DH and 2DH, and for waves both in a channel of constant depth and on a slope, are available. 1DH solutions shall be presented first before 2DH solutions. The models considered include: the Linear and Fully Dispersive wave model (LFD), the Linear and Weakly Dispersive wave model (LWD), and the Linear Shallow Water wave Equations (LSWE). In each section below, we shall first list the governing equations, show the normalization factors, and present all results in nondimensional form. Although the 2DH solutions can be simplified into the corresponding 1DH solutions by using a 1DH configuration, we choose to present the two sets of solutions separately, since the solution process in 1DH is more straightforward and paves the way for the more complicated solution process in 2DH. In addition, while the solutions presented here are for landslide-generated waves, the same solution approach can be applied to obtain analytical solutions for storm-generated waves and ship-generated waves, which are discussed in Appendix A.

Because the Fourier transform and the Laplace transform are frequently used in the solution process, we review the two transformations here. While the definition of the Laplace transform is universal, that of the Fourier transform varies. In this study, the Fourier transform of a function $f(x)$ is defined as

$$\begin{aligned} \mathcal{F}[f(x)](k) = \overline{f}(k) &= \frac{1}{\sqrt{2\pi}} \int_{-\infty}^{\infty} f(x) e^{-ikx} dx \\ \mathcal{F}^{-1}[\overline{f}(k)](x) = f(x) &= \frac{1}{\sqrt{2\pi}} \int_{-\infty}^{\infty} \overline{f}(k) e^{ikx} dk \end{aligned} , \tag{2.1}$$

in which the overline denotes Fourier transformed variables in the x direction. A

wide tilde will be used to denote that in the y direction. Fourier transforms are particularly useful in simplifying spatial derivatives, since

$$\overline{f_x} = ik\overline{f}, \quad \widetilde{f_y} = il\widetilde{f}, \tag{2.2}$$

where k is the wavenumber in the x-space and l is the wavenumber in the y-space.

The Laplace transform of a function $f(t)$ is defined as

$$\begin{aligned} \mathcal{L}[f(t)](s) &= \dddot{f}(s) = \int_0^\infty f(t)e^{-st}dt \\ \mathcal{L}^{-1}[\dddot{f}(s)](t) &= f(t) = \frac{1}{2\pi i}\lim_{T\to\infty}\int_{\gamma-iT}^{\gamma+iT} \dddot{f}(s)e^{st}ds \end{aligned}, \tag{2.3}$$

in which the triple dots denote Laplace transformed functions, and γ is a vertical contour in the complex plane chosen so that all singularities of $\dddot{f}(s)$ are to the left of it. Laplace transform, valid for $t \geq 0$, simplifies the computation of temporal derivatives as

$$\dddot{f_t} = s\dddot{f} - f(t=0). \tag{2.4}$$

2.1 1DH linear and fully dispersive model in constant depth

The 1DH landslide wave problem in constant depth is sketched in dimensional form in figure 2.1. The landslide has a characteristic length L, characteristic height A, and travels at a constant speed V in constant water depth d. $\eta'(x',t')$ is the dimensional water surface elevation from the still water level and $B'(x',t')$ denotes the bottom boundary deformation due to a landslide. As shown in Mei (1989), the solution to this type of problem, based on LFD, which is the potential flow theory subject to linearized boundary conditions, can be obtained by the use of Fourier

and Laplace transforms. The dimensionless governing equation and the boundary conditions in constant water depth read

$$\begin{aligned} &\mu^2\phi_{xx} + \phi_{zz} = 0, && -1 < z < 0 \\ &\phi_z = \mu^2 B_t, && z = -1 \\ &\phi_z = \mu^2 \eta_t, && z = 0 \\ &\phi_t + \eta = 0, && z = 0 \end{aligned} \quad , \tag{2.5}$$

where $\phi = \phi(x, z, t)$ is the normalized velocity potential. The characteristic landslide height A is assumed to be the same as the characteristic wave amplitude. To linearize the problem, A is required to be small compared to the water depth d so that $O(A/d) = O(\epsilon) \ll 1$. On the other hand, $\mu = d/L$ controls how strong frequency dispersion is in the problem. The variables are normalized as $x = x'/L$, $z = z'/d$, $t = t'\sqrt{gd}/L$ (g is the gravitational acceleration), $\eta(x,t) = \eta'(x',t')/A$, $B(x,t) = B'(x',t')/A$, and $\phi(x,z,t) = \phi'(x',z',t')/(\epsilon L\sqrt{gd})$. The normalized landslide speed is defined as the Froude number: $Fr = V/\sqrt{gd}$. After Laplace-Fourier transforming (2.5), combining the equations, and imposing the initial conditions

$$\eta(x,0) = 0 \quad \text{and} \quad \phi(x,0,0) = \text{constant}, \tag{2.6}$$

where the second condition corresponds to zero initial horizontal velocity on the free surface, the transformed solution of $\eta(x,t)$ can be found as

$$\overline{\overline{\eta}}\,(k,s) = \frac{\mu^2}{\cosh\mu k}\,\frac{s^2\overline{\overline{B}} - s\overline{B}(k,0)}{\mu^2 s^2 + \mu k \tanh\mu k}, \tag{2.7}$$

which is the solution obtained in Mei (1989) for water waves forced by a general seafloor displacement $B(x,t)$.

For a translating landslide $B(x,t) = B(x - Fr\cdot t) = B(\xi)$, its Fourier transform

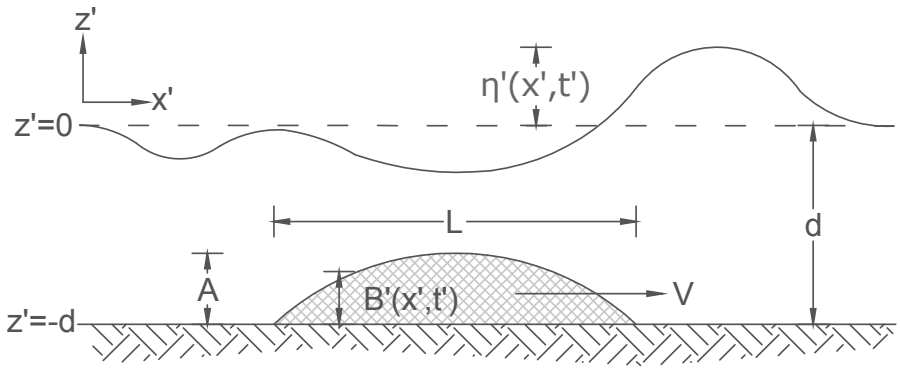

Figure 2.1: Definition sketch in dimensional form (not to scale) of the 1DH landslide wave problem in constant depth.

can be written as

$$\begin{aligned}\overline{B}(k,t) &= \frac{1}{\sqrt{2\pi}}\int_{-\infty}^{\infty} B(x-Fr\cdot t)e^{-ikx}dx = \frac{1}{\sqrt{2\pi}}\int_{-\infty}^{\infty} B(\xi)e^{-ikFr\cdot t}e^{-ik\xi}d\xi \\ &= \frac{1}{\sqrt{2\pi}}e^{-ikFr\cdot t}\int_{-\infty}^{\infty} B(x)e^{-ikx}dx = \overline{B(x,0)}e^{-ikFr\cdot t}\end{aligned} \quad . \tag{2.8}$$

If such a landslide forcing function is used, a closed-form inverse Laplace transform is available and the transformed solution (2.7) can be written as

$$\begin{aligned}\eta(x,t) &= \eta_{Fr}(x,t)+\eta_{+}(x,t)+\eta_{-}(x,t) \\ \eta_{Fr}(x,t) &= -\frac{1}{\sqrt{2\pi}}\int_{-\infty}^{\infty}\frac{1}{\cosh\mu k}\frac{Fr^2}{D^2-Fr^2}\overline{B(x,0)}e^{-ikFr\cdot t}e^{ikx}dk \\ \eta_{+}(x,t) &= \frac{1}{\sqrt{2\pi}}\int_{-\infty}^{\infty}\frac{1}{\cosh\mu k}\frac{Fr}{2(D-Fr)}\overline{B(x,0)}e^{-ikDt}e^{ikx}dk \\ \eta_{-}(x,t) &= -\frac{1}{\sqrt{2\pi}}\int_{-\infty}^{\infty}\frac{1}{\cosh\mu k}\frac{Fr}{2(D+Fr)}\overline{B(x,0)}e^{ikDt}e^{ikx}dk\end{aligned} \quad , \tag{2.9}$$

where

$$D=\sqrt{\frac{\tanh\mu k}{\mu k}} \tag{2.10}$$

is the normalized wave speed in LFD and is plotted in figure 2.2 as a function of μk. We note that $D(\mu k)$ has a maximum of one at $\mu k = 0$ (which implies that the longest wave corresponding to $k = 0$ travels at the fastest speed of one), and decays to zero as $|\mu k|$ increases (which implies that shorter waves, which have a larger wavenumber $|k|$, travel slower). In (2.9), a three-wave structure is evident:

$\eta_{Fr}(x,t) = \eta_{Fr}(x - Fr \cdot t)$ is a trapped wave that moves with the landslide, and η_+ and η_- are free waves that travel at the wave speed D.

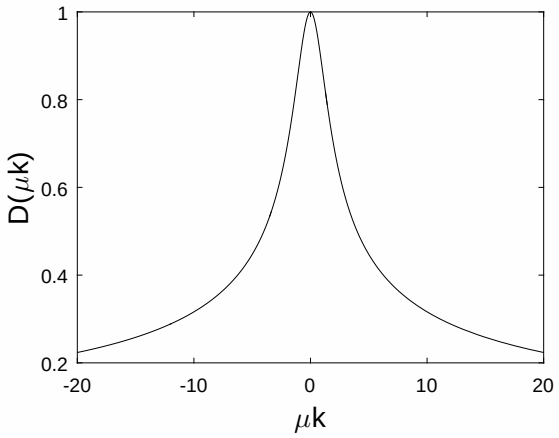

Figure 2.2: Frequency dispersive wave speed $D(\mu k)$, (2.10), plotted as a function of μk.

Since the solution for $\phi(x,z,t)$ is available and the horizontal and vertical velocities are given by $u(x,z,t) = \phi_x(x,z,t)$ and $w(x,z,t) = \phi_z(x,z,t)$, respectively, we can express the velocity solutions as

$$\begin{aligned}
u(x,z,t) &= u_{Fr}(x,z,t) + u_+(x,z,t) + u_-(x,z,t) \\
u_{Fr} &= \frac{-1}{\sqrt{2\pi}} \int_{-\infty}^{\infty} \frac{\overline{B(x,0)}}{\cosh \mu k} \frac{Fr^2}{D^2 - Fr^2} \Big(\frac{1}{Fr} \cosh(\mu k z) + \mu k Fr \sinh(\mu k z) \Big) e^{-ikFr \cdot t} e^{ikx} dk \\
u_+ &= \frac{1}{\sqrt{2\pi}} \int_{-\infty}^{\infty} \frac{\overline{B(x,0)}}{\cosh \mu k} \frac{Fr}{2(D - Fr)} \Big(\frac{1}{D} \cosh(\mu k z) + \mu k D \sinh(\mu k z) \Big) e^{-ikDt} e^{ikx} dk \\
u_- &= \frac{1}{\sqrt{2\pi}} \int_{-\infty}^{\infty} \frac{\overline{B(x,0)}}{\cosh \mu k} \frac{Fr}{2(D + Fr)} \Big(\frac{1}{D} \cosh(\mu k z) + \mu k D \sinh(\mu k z) \Big) e^{ikDt} e^{ikx} dk
\end{aligned} , \tag{2.11}$$

and

$$\begin{aligned}
w(x,z,t) &= w_{Fr}(x,z,t) + w_+(x,z,t) + w_-(x,z,t) \\
w_{Fr} &= \frac{i\mu}{\sqrt{2\pi}} \int_{-\infty}^{\infty} \frac{\overline{B(x,0)}}{\cosh \mu k} \frac{Fr^2}{D^2 - Fr^2} \Big(\frac{1}{Fr} \sinh(\mu k z) + \mu k Fr \cosh(\mu k z) \Big) e^{-ikFr \cdot t} e^{ikx} dk \\
w_+ &= \frac{-i\mu}{\sqrt{2\pi}} \int_{-\infty}^{\infty} \frac{\overline{B(x,0)}}{\cosh \mu k} \frac{Fr}{2(D - Fr)} \Big(\frac{1}{D} \sinh(\mu k z) + \mu k D \cosh(\mu k z) \Big) e^{-ikDt} e^{ikx} dk \\
w_- &= \frac{-i\mu}{\sqrt{2\pi}} \int_{-\infty}^{\infty} \frac{\overline{B(x,0)}}{\cosh \mu k} \frac{Fr}{2(D + Fr)} \Big(\frac{1}{D} \sinh(\mu k z) + \mu k D \cosh(\mu k z) \Big) e^{ikDt} e^{ikx} dk
\end{aligned} . \tag{2.12}$$

We recall that the initial conditions $\eta(x,0) = 0$ and $\phi(x,0,0) =$ constant were imposed in solving for η and ϕ. Due to allowance of flow variation in the vertical (z) direction, the initial flow velocity cannot be everywhere zero in LFD for a landslide moving at a constant speed.

2.1.1 Far-field leading wave solution

For $Fr \neq 1$ and given sufficient propagation time, the three waves in the solution (2.9) – η_{Fr}, η_+, and η_- – eventually separate from each other. η_+ and η_- are the free waves that travel in opposite directions and their shapes evolve in time due to frequency dispersion, whereas η_{Fr} is the trapped wave that moves with the landslide and has a permanent shape, as can be seen by the $e^{ik(x-Fr\cdot t)}$ term in the solution (2.9). For $0 < Fr < 1$, η_+ and η_- eventually overtake η_{Fr} to become the leading waves, and the method of stationary phase (for more details, see Mei, 1989; Bender and Orszag, 1999) can be used on frequency-dispersive free-wave solutions like η_+ and η_- to obtain closed-form asymptotic far-field leading wave solutions valid for large t and near $x = t$. Resonance occurs for $Fr = 1$ and will be discussed in the next section.

Since the approximation process to obtain the far-field leading wave solution (accurate for large t and near $x = t$) is fairly standard and has been described in Mei (1989), here we only outline the derivation for the right-going wave, η_+ in (2.9). In the expression for η_+, the exponential terms in the integral can be combined into $e^{i(kx-kDt)} = e^{if(k)}$, where $f(k) = kx - kDt$. The stationary phase method suggests that the largest non-zero contribution to the integral comes from the vicinity $k = k_0$ where $f'(k_0) = 0$. Taking the derivative and assuming $x = t$ then give $k_0 = 0$. According to (2.10), the fastest wave travels at speed 1. Hence,

$x = t$ corresponds to the leading wave and the leading wave solution is most accurate when $x - t \simeq 0$. The assumption $x = t$ is therefore consistent with our goal to obtain the leading wave solution.

For the leading wave, the integral for η_+ is largely determined by k near $k \simeq k_0 = 0$. The integral can therefore be approximated by expansions about $k = 0$, with the approximation being more accurate for larger t due to faster oscillation of the exponential term. Physically, this can be interpreted as the leading wave having sufficiently separated from the trailing waves. The Taylor series expansion for $f(k) = kx - kDt$ about $k = 0$ is

$$kx - kD(k)t = kx - k\sqrt{\frac{\tanh \mu k}{\mu k}}t \simeq kx - kt + \frac{1}{6}k^3\mu^2 t + O(k^5). \tag{2.13}$$

The far-field leading wave solution for η_+, η_+^*, can then be expressed as

$$\begin{aligned}\eta_+^*(x,t) = \frac{1}{\sqrt{2\pi}}\frac{Fr}{2(1-Fr)}\Big(&\overline{B(x,0)}(k=0) + k\overline{B(x,0)}'(k=0) \\ &+\frac{k^2}{2}\overline{B(x,0)}''(k=0) + \cdots\Big)\int_{-\infty}^{\infty} e^{i(kx-kt+\frac{1}{6}k^3\mu^2 t)}dk\end{aligned}. \tag{2.14}$$

With the substitution $k = [2/(\mu^2 t)]^{1/3}q$ so that q is the dummy variable, the above equation can be written as

$$\begin{aligned}\eta_+^*(x,t) = &\frac{1}{\sqrt{2\pi}}\frac{Fr}{2(1-Fr)}(\frac{2}{\mu^2 t})^{\frac{1}{3}}\overline{B(x,0)}(k=0)\int_{-\infty}^{\infty}\cos\Big((\frac{2}{\mu^2 t})^{\frac{1}{3}}(x-t)q + \frac{1}{3}q^3\Big)dq \\ &+\frac{1}{\sqrt{2\pi}}\frac{Fr}{2(1-Fr)}(\frac{2}{\mu^2 t})^{\frac{2}{3}}\overline{B(x,0)}'(k=0)\int_{-\infty}^{\infty} q\cos\Big((\frac{2}{\mu^2 t})^{\frac{1}{3}}(x-t)q + \frac{1}{3}q^3\Big)dq \\ &+\frac{1}{\sqrt{2\pi}}\frac{Fr}{2(1-Fr)}(\frac{2}{\mu^2 t})\frac{\overline{B(x,0)}''(k=0)}{2}\int_{-\infty}^{\infty} q^2\cos\Big((\frac{2}{\mu^2 t})^{\frac{1}{3}}(x-t)q + \frac{1}{3}q^3\Big)dq \\ &+\cdots\end{aligned}. \tag{2.15}$$

Since the Airy function is defined as

$$Ai(\xi) = \frac{1}{2\pi}\int_{-\infty}^{\infty}\cos(\xi q + \frac{q^3}{3})dq, \tag{2.16}$$

we can express the leading wave solution using the Airy function. We remark that the Airy function is well tabulated and has a maximum amplitude of about 0.536.

Keeping the first three (leading-order, second-order, and third-order) terms in the approximation, after some algebraic rearrangement we obtain the far-field leading wave solution $\eta_+^*(x,t)$ for the right-going wave:

$$\begin{aligned}\eta_+^*(x,t) = \; & S\frac{Fr}{2(1-Fr)}(\frac{2}{\mu^2 t})^{\frac{1}{3}} Ai\Big[(\frac{2}{\mu^2 t})^{\frac{1}{3}}(x-t)\Big] \\ & -M_1\frac{Fr}{2(1-Fr)}(\frac{2}{\mu^2 t})^{\frac{2}{3}} Ai'\Big[(\frac{2}{\mu^2 t})^{\frac{1}{3}}(x-t)\Big] \\ & +\frac{M_2}{2}\frac{Fr}{2(1-Fr)}(\frac{2}{\mu^2 t}) Ai''\Big[(\frac{2}{\mu^2 t})^{\frac{1}{3}}(x-t)\Big] + \cdots\end{aligned} \quad , \tag{2.17}$$

where Ai is the Airy function, S is the area enclosed by the landslide, M_1 is the first moment of the landslide forcing function at $t=0$ (i.e., $M_1 = \int_{-\infty}^{\infty} xB(x)dx$), and M_2 the second moment (i.e., $M_2 = \int_{-\infty}^{\infty} x^2 B(x)dx$). For a physical landslide, $S > 0$ and the first moment can be written as $M_1 = Sx_c$, where x_c is the initial center of mass of the landslide forcing function at $t=0$. Hence, the first two terms of the far-field leading wave solution (2.17) depend only on the area enclosed by the landslide, and the effect of the exact landslide shape first appears in the third-order term, in the form of the second moment M_2. We note that since (2.17) is accurate only near $x=t$, it is preferable to define the coordinate system such that $x_c = 0$ (i.e., the location of the landslide's initial center of mass is centered at $x=0$) to ensure the leading wave indeed travels along $x \simeq t$. If $x_c \neq 0$ is chosen, the asymptotic solution (2.17) still holds, but would require a longer time t for the asymptotic solution to become accurate.

A similar procedure can be performed on the left-going wave η_- to obtain the far-field leading wave solution $\eta_-^*(x,t)$:

$$\begin{aligned}\eta_-^*(x,t) = \; & -S\frac{Fr}{2(1+Fr)}(\frac{2}{\mu^2 t})^{\frac{1}{3}} Ai\Big[-(\frac{2}{\mu^2 t})^{\frac{1}{3}}(x+t)\Big] \\ & +M_1\frac{Fr}{2(1+Fr)}(\frac{2}{\mu^2 t})^{\frac{2}{3}} Ai'\Big[-(\frac{2}{\mu^2 t})^{\frac{1}{3}}(x+t)\Big] \\ & -\frac{M_2}{2}\frac{Fr}{2(1+Fr)}(\frac{2}{\mu^2 t}) Ai''\Big[-(\frac{2}{\mu^2 t})^{\frac{1}{3}}(x+t)\Big] + \cdots\end{aligned} \quad , \tag{2.18}$$

which is accurate for large t and near $x = -t$. Note that (2.18) and (2.17) are similar, except the sign difference and that the amplitude of (2.18) is much smaller in the vicinity of $Fr \sim 1$ – i.e., resonance does not occur for the left-going wave. In addition, we remark that the far-field leading wave solutions due to a translating landslide are similar to those due to an impulsive seafloor displacement derived in Mei (1989), the main difference being the additional Fr (landslide speed) effects on the wave amplitudes.

While the far-field leading wave solution becomes a better and better approximation near $x = t$ as $t \to \infty$, the accuracy of all solutions is limited by the accuracy of the governing equation, i.e., the truncation error $O(\epsilon)$ of LFD. In reality, as $t \to \infty$, the nonlinearity in an initially linear problem eventually grows enough so that $O(\epsilon)$ becomes significant, and the linear far-field solution breaks down when $t \gg O(1/\epsilon)$.

2.1.2 Landslide shape effect on the far-field leading wave

The far-field leading wave solutions (2.17) and (2.18) indicate that the area S enclosed by the landslide has the most important effect on the leading wave, and that the exact landslide shape first becomes relevant in the third-order term, which decays faster at the rate t^{-1} than the leading-order terms. As t becomes large, eventually the leading wave is affected by only the leading-order terms that depend on S. This analytical finding therefore supports the belief that it is more important to match the landslide area in 1DH (or volume in 2DH, which will be shown in the 2DH sections) in modeling than the exact landslide shape.

To check the performance of the far-field leading wave solutions, we use (2.17)

as an example and consider seven different landslide shapes that have the same characteristic height and area enclosed, initially centered at the origin so that $x_c = 0 = M_1$: a Gaussian curve (B_1), a parabolic cap (B_2), a quartic cap (B_3), a rectangle (B_4), and three different triangles (B_5, B_6, and B_7). The seven different landslide shapes are compared in figure 2.3, and the mathematical details on the shape definitions and their Fourier transforms are provided below.

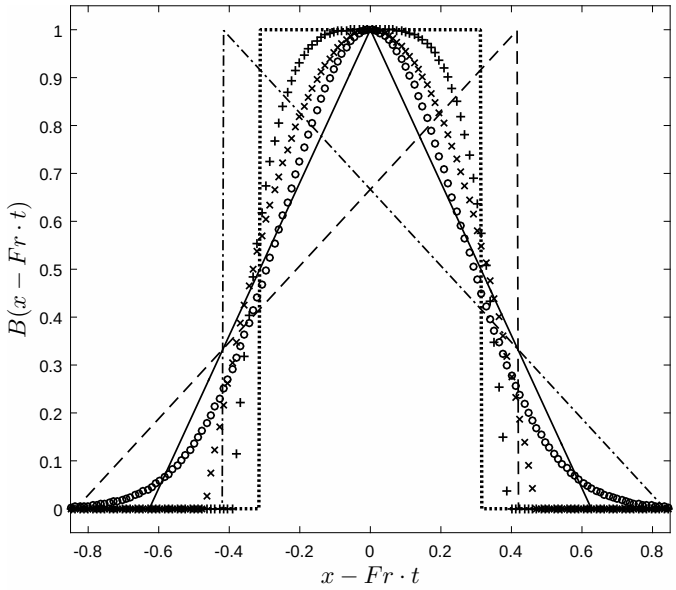

Figure 2.3: Comparison of the seven different landslide shapes that all have the same height, enclosed area, and center of mass $x_c = 0$. Circle: Gaussian curve (B_1); cross: parabolic cap (B_2); plus: quartic cap (B_3); dotted line: rectangle (B_4); solid line: triangle (B_5); dashed line: triangle (B_6); dash-dot line: triangle (B_7).

The (dimensionless) Gaussian-shaped landslide is defined so that the characteristic length is four standard deviations (thus $\sim 95\%$ of the area is contained in one characteristic length):

$$B_1(x - Fr \cdot t) = e^{-8(x - Fr \cdot t)^2}. \tag{2.19}$$

The area enclosed is $S_B = \sqrt{\pi/2}/2$, and the Fourier transform is

$$\overline{B_1} = \frac{1}{4} e^{-\frac{1}{32}k^2} e^{-ikFr \cdot t}. \tag{2.20}$$

The landslide shape can also be a parabolic cap of the same height and enclosed area:

$$B_2(x-Fr\cdot t)=\Big[H(x-Fr\cdot t+\frac{3}{8}\sqrt{\frac{\pi}{2}})-H(x-Fr\cdot t-\frac{3}{8}\sqrt{\frac{\pi}{2}})\Big]\Big[1-\frac{128}{9\pi}(x-Fr\cdot t)^2\Big], \tag{2.21}$$

where $H(x)$ is the Heaviside step function. Different from the Gaussian curve, the parabolic cap has a finite length of $3\sqrt{\pi/2}/4$. A closed-form Fourier transform is available for this landslide forcing function:

$$\overline{B_2}=\Big[-\frac{16}{3\pi k^2}(e^{-i\frac{3}{8}\sqrt{\frac{\pi}{2}}k}+e^{i\frac{3}{8}\sqrt{\frac{\pi}{2}}k})+i\frac{128\sqrt{2}}{9\pi^{\frac{3}{2}}k^3}(e^{-i\frac{3}{8}\sqrt{\frac{\pi}{2}}k}-e^{i\frac{3}{8}\sqrt{\frac{\pi}{2}}k})\Big]e^{-ikFr\cdot t}. \tag{2.22}$$

Similarly, a quartic cap can be used:

$$B_3(x-Fr\cdot t)=\Big[H(x-Fr\cdot t+\frac{5}{16}\sqrt{\frac{\pi}{2}})-H(x-Fr\cdot t-\frac{5}{16}\sqrt{\frac{\pi}{2}})\Big]\Big[1-(\frac{512}{25\pi})^2(x-Fr\cdot t)^4\Big], \tag{2.23}$$

which has a finite length $5\sqrt{\pi/2}/8$ and whose Fourier transform is

$$\begin{aligned}\overline{B_3}=\Big[&\frac{64}{125\pi^2k^4}(3072-25\pi k^2)(e^{-i\frac{5}{16}\sqrt{\frac{\pi}{2}}k}+e^{i\frac{5}{16}\sqrt{\frac{\pi}{2}}k})\\&-i\frac{1024\sqrt{2}}{625\pi^{\frac{5}{2}}k^5}(3072-75\pi k^2)(e^{-i\frac{5}{16}\sqrt{\frac{\pi}{2}}k}-e^{i\frac{5}{16}\sqrt{\frac{\pi}{2}}k})\Big]e^{-ikFr\cdot t}.\end{aligned} \tag{2.24}$$

Simple geometry such as a rectangle is also considered:

$$B_4(x-Fr\cdot t)=H(x-Fr\cdot t+\frac{\sqrt{2\pi}}{8})-H(x-Fr\cdot t-\frac{\sqrt{2\pi}}{8}), \tag{2.25}$$

which has a finite length $\sqrt{2\pi}/4$ and Fourier transform

$$\overline{B_4}=i\frac{1}{\sqrt{2\pi}k}(e^{-i\frac{\sqrt{2\pi}}{8}k}-e^{i\frac{\sqrt{2\pi}}{8}k})e^{-ikFr\cdot t}. \tag{2.26}$$

For an isosceles triangle,

$$\begin{aligned}B_5(x-Fr\cdot t)=&\Big[1+\frac{4}{\sqrt{2\pi}}(x-Fr\cdot t)\Big]\Big[H(x-Fr\cdot t+\frac{\sqrt{2\pi}}{4})-H(x-Fr\cdot t)\Big]\\&+\Big[1-\frac{4}{\sqrt{2\pi}}(x-Fr\cdot t)\Big]\Big[H(x-Fr\cdot t)-H(x-Fr\cdot t-\frac{\sqrt{2\pi}}{4})\Big],\end{aligned} \tag{2.27}$$

which has a finite length $\sqrt{2\pi}/2$ and Fourier transform

$$\overline{B_5} = \frac{2}{\pi k^2}(2 - e^{-i\frac{\sqrt{2\pi}}{4}k} - e^{i\frac{\sqrt{2\pi}}{4}k})e^{-ikFr\cdot t}. \tag{2.28}$$

The shape B_6 is a right triangle with a positive slope,

$$B_6(x - Fr\cdot t) = \Big[\frac{2}{3} + \frac{2}{\sqrt{2\pi}}(x - Fr\cdot t)\Big]\Big[H(x - Fr\cdot t + \frac{\sqrt{2\pi}}{3}) - H(x - Fr\cdot t - \frac{\sqrt{2\pi}}{6})\Big] \tag{2.29}$$

whose Fourier transform is

$$\overline{B_6} = \Big[\frac{1}{\pi k^2}(e^{-i\frac{\sqrt{2\pi}}{6}k} - e^{i\frac{\sqrt{2\pi}}{3}k}) + i\frac{1}{\sqrt{2\pi}k}e^{-i\frac{\sqrt{2\pi}}{6}k}\Big]e^{-ikFr\cdot t}. \tag{2.30}$$

The shape B_7 is a right triangle with a negative slope,

$$B_7(x - Fr\cdot t) = \Big[\frac{2}{3} - \frac{2}{\sqrt{2\pi}}(x - Fr\cdot t)\Big]\Big[H(x - Fr\cdot t + \frac{\sqrt{2\pi}}{6}) - H(x - Fr\cdot t - \frac{\sqrt{2\pi}}{3})\Big] \tag{2.31}$$

whose Fourier transform is

$$\overline{B_7} = \Big[\frac{1}{\pi k^2}(-e^{-i\frac{\sqrt{2\pi}}{3}k} + e^{i\frac{\sqrt{2\pi}}{6}k}) + i\frac{1}{\sqrt{2\pi}k}e^{i\frac{\sqrt{2\pi}}{6}k}\Big]e^{-ikFr\cdot t}. \tag{2.32}$$

Since these landslides all have the same height, enclosed area, and center of mass $x_c = 0$, we expect the exact analytical solutions to all eventually converge to the same asymptotic leading-wave solution (near $x = t$) as t increases. For $\mu = 0.25$ and $Fr = 0.5$, in figure 2.4 we compare the far-field leading wave solution (2.17), with only the first-order term (note that the second-order term is zero since $x_c = 0$), with the numerically integrated complete solution (2.9) for the seven different landslide shapes at three different times $t = 2, 5, 10$. We see that although the initial wave fields due to different landslide shapes can be very different, as time increases the leading waves indeed all converge to the same leading-order asymptotic solution, which depends on the area enclosed by the landslide.

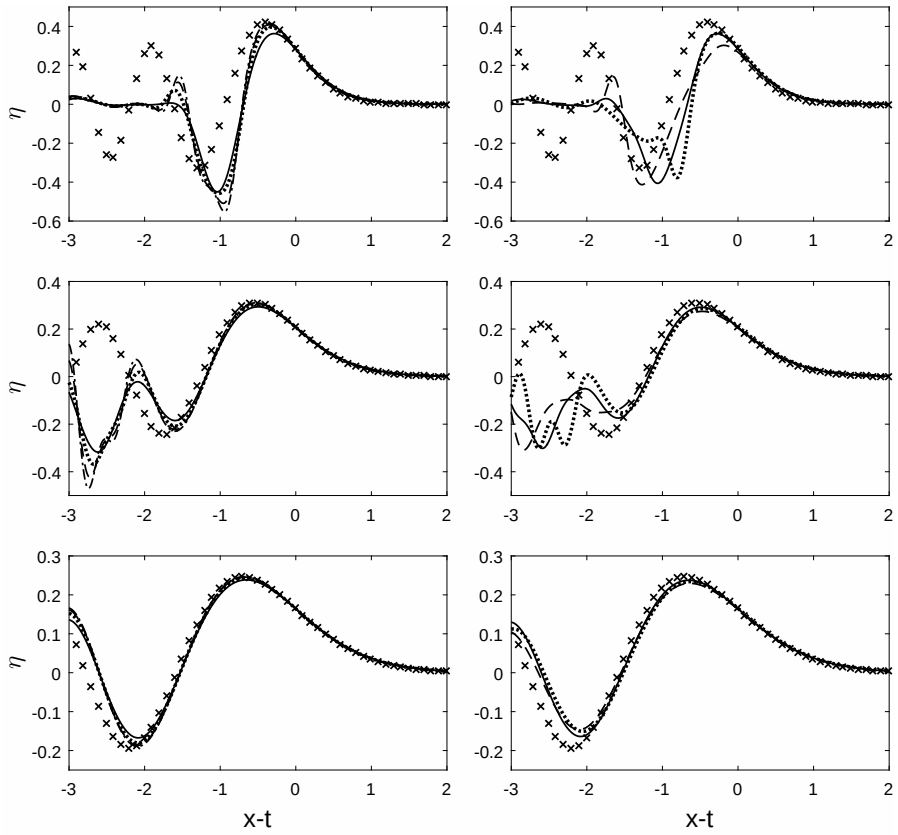

Figure 2.4: Comparison of water waves generated by landslides of different shapes whose initial centers of mass $x_c = 0$, for $\mu = 0.25$ and $Fr = 0.5$. Top row: $t = 2$; middle row: $t = 5$; bottom row: $t = 10$. In the left column, solid line: Gaussian curve (B_1); dotted line: parabolic cap (B_2); dashed line: quartic cap (B_3); dash-dot line: rectangle (B_4); cross: (2.17) with only the leading-order term. In the right column, solid line: triangle (B_5); dotted line: triangle (B_6); dashed line: triangle B_7; cross: asymptotic solution (2.17) with only the leading-order term.

2.1.3 Resonance solution

In the complete 1DH LFD solutions (2.9), discontinuities exist for $0 < D(\mu k) = Fr \leq 1$ (we recall that as plotted in figure 2.2, $D(\mu k)$ has a maximum of one at $\mu k = 0$), when resonance appears to occur. Here, we examine how the solution behaves near the discontinuities. First, we shall show that only the $Fr = 1$ resonance mode is significant, in which the right-going wave may grow indefinitely in time.

In (2.9), discontinuities exist in the expressions for η_{Fr} and η_+ when $k = k^*$ so

that $D(\mu k^*) = Fr$:

$$\begin{aligned}
\eta_{Fr}(x,t) &= -\frac{1}{\sqrt{2\pi}}\int_{-\infty}^{\infty}\frac{1}{\cosh\mu k}\frac{Fr^2}{D^2-Fr^2}\overline{B(x,0)}(k)e^{-ikFr\cdot t}e^{ikx}dk \\
\eta_{+}(x,t) &= \frac{1}{\sqrt{2\pi}}\int_{-\infty}^{\infty}\frac{1}{\cosh\mu k}\frac{Fr}{2(D-Fr)}\overline{B(x,0)}(k)e^{-ikDt}e^{ikx}dk \quad . \\
D &= \sqrt{\frac{\tanh\mu k}{\mu k}}
\end{aligned} \tag{2.33}$$

We recall that D is a smooth function with a peak of one at $k = 0$ (plotted in figure 2.2 as a function of μk). Here we show only the analysis for the discontinuity in η_+. A similar analysis can be repeated for η_{Fr}.

To isolate the discontinuity at $k = k^*$, we write

$$\begin{aligned}
\eta_+(x,t) = \lim_{\delta\to 0}\Bigg\{ &\frac{1}{\sqrt{2\pi}}\int_{-\infty}^{k^*-\delta}\frac{1}{\cosh\mu k}\frac{Fr}{2(D-Fr)}\overline{B(x,0)}(k)e^{-ikDt}e^{ikx}dk \\
&+\frac{1}{\sqrt{2\pi}}\int_{k^*-\delta}^{k^*+\delta}\frac{1}{\cosh\mu k}\frac{Fr}{2(D-Fr)}\overline{B(x,0)}(k)e^{-ikDt}e^{ikx}dk \quad . \\
&+\frac{1}{\sqrt{2\pi}}\int_{k^*+\delta}^{\infty}\frac{1}{\cosh\mu k}\frac{Fr}{2(D-Fr)}\overline{B(x,0)}(k)e^{-ikDt}e^{ikx}dk\Bigg\}
\end{aligned} \tag{2.34}$$

We therefore only need to focus on the term

$$I(x,t) = \lim_{\delta\to 0}\left\{\frac{1}{\sqrt{2\pi}}\int_{k^*-\delta}^{k^*+\delta}\frac{1}{\cosh\mu k}\frac{Fr}{2(D-Fr)}\overline{B(x,0)}(k)e^{-ikDt}e^{ikx}dk\right\}. \tag{2.35}$$

Taylor series expansion of D (hereafter treated as a function of k for simpler notation, as μ is a known constant in a given problem) about $k = k^*$ gives

$$D(k) = \sqrt{\frac{\tanh\mu k}{\mu k}} \simeq D(k^*) + D'(k^*)(k-k^*) + \frac{1}{2}D''(k^*)(k-k^*)^2 + \cdots . \tag{2.36}$$

For the case $0 < D(k^*) = Fr < 1$, $k^* \neq 0$ and $D'(k^*) \neq 0$. Hence, only the first two terms in (2.36) are needed for the leading-order behavior of $D(k)$ near $k = k^*$. With the additional assumption that the limit of $\overline{B(x,0)}(k)$ as $k \to k^*$

exists, (2.35) can be written as

$$\begin{aligned} I(x,t) = \lim_{\delta\to 0}\left\{ \frac{1}{\sqrt{2\pi}} \int_{k^*-\delta}^{k^*+\delta} \frac{Fr}{2\big[D'(k^*)(k-k^*)\big]} \frac{\overline{B(x,0)}(k\to k^*)}{\cosh \mu k^*} e^{-ik^* Fr\cdot t} e^{ik^* x} dk \right\} \\ = \frac{Fr\overline{B(x,0)}(k\to k^*)e^{-ik^* Fr\cdot t}e^{ik^* x}}{2\sqrt{2\pi}\cosh(\mu k^*)D'(k^*)} \lim_{\delta\to 0}\int_{k^*-\delta}^{k^*+\delta} \frac{1}{k-k^*} dk \ . \\ = \frac{Fr\overline{B(x,0)}(k\to k^*)e^{-ik^* Fr\cdot t}e^{ik^* x}}{2\sqrt{2\pi}\cosh(\mu k^*)D'(k^*)} \lim_{\delta\to 0}\int_{-\delta}^{\delta} \frac{1}{u} du \Bigg\} = 0 \end{aligned} \tag{2.37}$$

We see that for the case $0 < D(k^*) = Fr < 1$, the discontinuity at $k = k^*$ is integrable based on the Cauchy principal value. On the other hand, for the case $D(k^*) = Fr = 1$ (which means $k^* = 0$), since $D'(0) = 0$, the third term in the expansion (2.36) is needed and (2.35) becomes

$$\begin{aligned} I(x,t) = \lim_{\delta\to 0}\left\{ \frac{1}{\sqrt{2\pi}} \int_{k^*-\delta}^{k^*+\delta} \frac{Fr}{2\big[\frac{1}{2}D''(k^*)(k-k^*)^2\big]} \frac{\overline{B(x,0)}(k\to k^*)}{\cosh \mu k^*} e^{-ik^* Fr\cdot t} e^{ik^* x} dk \right\} \\ = \frac{Fr\overline{B(x,0)}(k\to k^*)e^{-ik^* Fr\cdot t}e^{ik^* x}}{\sqrt{2\pi}\cosh(\mu k^*)D''(k^*)} \lim_{\delta\to 0}\int_{k^*-\delta}^{k^*+\delta} \frac{1}{(k-k^*)^2} dk \ . \\ = \frac{Fr\overline{B(x,0)}(k\to k^*)e^{-ik^* Fr\cdot t}e^{ik^* x}}{\sqrt{2\pi}\cosh(\mu k^*)D''(k^*)} \lim_{\delta\to 0}\int_{-\delta}^{\delta} \frac{1}{u^2} du \end{aligned} \tag{2.38}$$

Since the limit does not exist, the discontinuity at $k = k^*$ is not integrable for the case $D(k^*) = Fr = 1$.

A similar analysis can be performed for η_{Fr} to obtain similar results. Hence, in the case $0 < D(k^*) = Fr < 1$, η_+ and η_{Fr} are both finite and do not grow indefinitely, whereas in the case $D(k^*) = Fr = 1$, both η_+ and η_{Fr} are infinite – the two terms become inseparable and together form the right-going wave, which may grow indefinitely in time. We therefore conclude that only the $Fr = 1$ resonance is significant.

Next, we focus on the case where $Fr = 1$. In the complete LFD solution (2.9), η_{Fr} is the steady state component, which is of a permanent form and moves at the same speed as the landslide, as indicated by the $e^{ik(x-Fr\cdot t)}$ term. η_+ and η_-

are the transient components that evolve in time due to frequency dispersion, as indicated by the $e^{ik(x-Dt)}$ and $e^{ik(x+Dt)}$ terms. When resonance occurs ($Fr = 1$), η_{Fr} and η_+ become inseparable and together form the leading wave. Since η_{Fr} is of a permanent form, the growth rate of the leading wave is solely determined by that of η_+. For $Fr = 1$, the leading-order far-field leading wave approximation (valid for large t and near $x = t$) for η_+ can be found by using the method of stationary phase to be

$$\begin{aligned}\eta_+^*(x,t) &= \frac{1}{2\pi} S \int_{-\infty}^{\infty} \frac{-3}{\mu^2 k^2} e^{i(kx - kt + \frac{1}{6}k^3\mu^2 t)} dk + \cdots \\ &= \frac{-3}{2\pi\mu^2} (\frac{\mu^2 t}{2})^{\frac{1}{3}} S \int_{-\infty}^{\infty} \frac{1}{q^2} e^{i\left[(\frac{2}{\mu^2 t})^{\frac{1}{3}}(x-t)q + \frac{1}{3}q^3\right]} dq + \cdots\end{aligned}, \tag{2.39}$$

where the substitution $k = (2/\mu^2 t)^{1/3} q$ is used to rewrite the k-integral and S is again the area enclosed by the landslide. We note that the q-integral is solely a function of $(2/\mu^2 t)^{1/3}(x - t)$, defined similarly to the Airy function but with the addition of $1/q^2$ in the integrand. Since the shape of the far-field leading wave is determined by the q-integral, we see that the resonance far-field leading wave solution grows in time at the rate $t^{1/3}$, instead of decaying at the rate $t^{-1/3}$, which is the case for $0 < Fr < 1$.

Although the far-field leading wave approximation for η_+, (2.39), can be obtained and the growth rate examined, we note that the improper integral in (2.39) is infinite due to the factor $1/q^2$. In fact, the far-field leading wave solution consists of both (2.39) and η_{Fr}, which is of a permanent form and also has an infinite magnitude for $Fr = 1$. Taylor series expansions about the discontinuities can be used to show that the two infinite magnitudes cancel out and the results end up finite. The complete far-field leading wave solution (valid for large t and near $x = t$) is therefore

$$\eta_{\text{lead}}(x,t) = \eta_{Fr}(x,t) + \eta_+^*(x,t), \quad Fr = 1. \tag{2.40}$$

(2.40) and the complete solution (2.9) are compared in figure 2.5, for a Gaussian landslide forcing function moving at a constant speed $Fr = 1$: $B(x,t) = e^{-8(x-t)^2}$ with $\mu = 0.3$. We see that the far-field leading wave solution (2.40) indeed becomes more accurate near $x = t$ as t increases. Nonetheless, we remark that for the resonance case the most important information gained from the far-field leading wave solution is the growth rate $t^{1/3}$ as indicated by (2.39). The asymptotic wave profile (2.40) is of little practical value since a numerical integration is still needed for plotting – computing the asymptotic solution (2.40) presents few benefits over computing the complete solution (2.9).

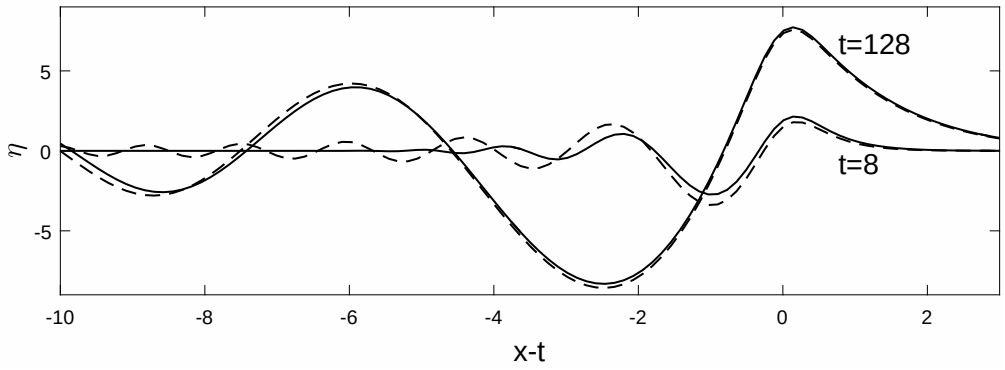

Figure 2.5: Wave profiles due to a Gaussian landslide forcing function with $Fr = 1$ and $\mu = 0.3$ at $t = 8$ and $t = 128$. Solid line: complete LFD solution (2.9); dashed line: far-field leading wave solution (2.40).

To test the asymptotic growth rate $t^{1/3}$, we numerically compute the full LFD solution (2.9) for a Gaussian landslide forcing function moving at a constant speed $Fr = 1$ with $\mu = 0.3$. The actual growth rate of the leading wave, obtained by determining the maximum height in space of the wave crest near $x = t$ in the full LFD solution (2.9), is then compared with the asymptotic rate of $t^{1/3}$ in figure 2.6. We see that the leading wave amplitude growth rate indeed approaches $t^{1/3}$ as t increases.

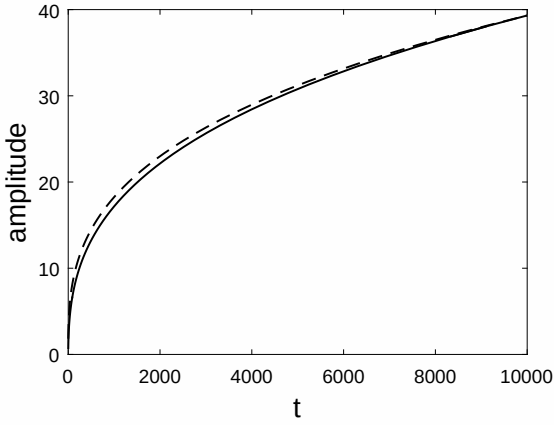

Figure 2.6: Amplitude of the leading wave as a function of t, for a Gaussian landslide forcing function with $Fr = 1$ and $\mu = 0.3$. Solid line: the complete LFD solution (2.9); dashed line: the asymptotic growth rate $t^{1/3}$.

2.2 1DH linear shallow water wave model in constant depth

The dimensionless mass and momentum equations of 1DH LSWE in constant water depth are

$$\eta_t + u_x = B_t \tag{2.41}$$

and

$$u_t = -\eta_x, , \tag{2.42}$$

where $u(x,t)$ is the horizontal velocity, normalized by $\epsilon\sqrt{gd}$. (2.41) and (2.42) can be combined to solve for either η or u first with Fourier and Laplace transforms. Solving for η only, Tinti et al. (2001) have shown that the dimensionless analytical solution for waves generated by a solid landslide moving at a constant speed is

simply

$$\begin{aligned}
\eta(x,t) &= \eta_{Fr}(x,t) + \eta_{+}(x,t) + \eta_{-}(x,t) \\
\eta_{Fr}(x,t) &= -\frac{Fr^2}{1-Fr^2} B(x - Fr \cdot t) \\
\eta_{+}(x,t) &= \frac{Fr}{2(1-Fr)} B(x-t) \\
\eta_{-}(x,t) &= -\frac{Fr}{2(1+Fr)} B(x+t)
\end{aligned} \quad . \tag{2.43}$$

Adding to the solution (2.43), we remark that the velocity solution can be recovered from the momentum equation (2.42) as

$$\begin{aligned}
u(x,t) &= u(x,0) + u_{Fr}(x,t) + u_{+}(x,t) + u_{-}(x,t) \\
u_{Fr}(x,t) &= -\frac{Fr}{1-Fr^2} B(x - Fr \cdot t) \\
u_{+}(x,t) &= \frac{Fr}{2(1-Fr)} B(x-t) \\
u_{-}(x,t) &= \frac{Fr}{2(1+Fr)} B(x+t)
\end{aligned} \quad . \tag{2.44}$$

While LSWE can be solved directly to obtain the above solutions, the same solutions can also be recovered from the LFD solutions in the shallow water limit, i.e. $\mu \to 0$.

In solving (2.41) and (2.42) for η, the imposed initial conditions are $\eta(x,0) = 0$ and $\eta_t(x,0) = B_t(x,0)$; the second condition results from setting $u_x(x,0) = 0$ in (2.41). Thus, the solution for η, (2.43), is valid for any initial flow setup with the initial conditions $\eta(x,0) = 0$ and $u(x,0) =$ constant. The precise initial velocity $u(x,0)$ can be specified only when the solution for u is considered; for initially quiescent water, one requires $u(x,0) = 0$ in (2.44).

The solution (2.43) reflects the three-wave structure of waves generated by a moving landslide – the two free waves η_+ and η_- that travel at wave celerity in opposite directions, and a trapped wave η_{Fr} that follows the landslide. In addition to the sign difference, the magnitude of the right-going wave, η_+, is always larger than that of the left-going wave, η_-, and the difference is especially significant

for $Fr \sim 1$, when resonance occurs. Tinti and Bortolucci (2000) showed that the resonance solution ($Fr = 1$) for 1DH LSWE can be obtained by the method of characteristics:

$$\eta(x,t) = \frac{t}{2}B_t(x-t) + \frac{1}{4}B(x-t) - \frac{1}{4}B(x+t). \tag{2.45}$$

In the resonance case, the right-going wave grows linearly in time and its form also depends on the first temporal derivative of the landslide forcing function.

2.3 1DH linear and weakly dispersive model in constant depth

LWD can be obtained by linearizing WNWD (Nwogu, 1993) or the Fully Nonlinear and Weakly Dispersive wave model (FNWD, see Wei et al., 1995; Lynett and Liu, 2002). Alternatively, it can be obtained as an approximated version of LFD based on the weakly dispersive assumption (e.g., Lynett and Liu, 2002, who demonstrated how to obtain weakly dispersive models from a fully dispersive model). LWD is accurate when both $O(\epsilon) \ll 1$ and $O(\mu^4) \ll 1$. In weakly dispersive models, the governing equations are often solved at a representative depth z_α, which is chosen to improve the characteristics of frequency dispersion; the horizontal velocity at depth $z = z_\alpha$ is written as $u(x, z_\alpha, t) = u_\alpha(x,t)$. For LWD in constant depth, $z_\alpha = \alpha$, since the normalized water depth is 1, and here we use $\alpha = -0.531$ as recommended by Nwogu (1993). The dimensionless continuity equation reads

$$\eta_t + u_{\alpha x} + \alpha_{11}u_{\alpha xxx} = B_t + \alpha_{12}B_{txx}, \tag{2.46}$$

and the momentum equation reads

$$u_{\alpha t} + \alpha_{21}u_{\alpha xxt} + \eta_x = \alpha_{22}B_{txt}, \tag{2.47}$$

where α_{11}, α_{12}, α_{21}, and α_{22} are constants of order $O(\mu^2)$:

$$\alpha_{11} = \mu^2(\frac{1}{2}\alpha^2 + \alpha + \frac{1}{3}), \quad \alpha_{12} = \mu^2(\alpha + \frac{1}{2}), \quad \alpha_{21} = \mu^2(\frac{1}{2}\alpha^2 + \alpha), \quad \alpha_{22} = \mu^2\alpha, \quad \alpha = -0.531 \tag{2.48}$$

Solving for u_α first is more convenient in this case, and (2.46) and (2.47) can be combined to yield

$$u_{\alpha xx} - u_{\alpha tt} + \alpha_{11}u_{\alpha xxxx} - \alpha_{21}u_{\alpha xxtt} = B_{tx} + \alpha_{12}B_{txxx} - \alpha_{22}B_{ttxt}. \tag{2.49}$$

LWD can be solved in a manner similar to those for LSWE and LFD. Here we only outline the solution process. When u_α is solved for first, the imposed initial conditions are

$$u_\alpha(x,0) = \mu^2 z_\alpha B_{tx} \quad \text{and} \quad u_{\alpha t}(x,0) + \alpha_{21}u_{\alpha xxt}(x,0) = \alpha_{22}B_{xtt}(x,0). \tag{2.50}$$

The first condition results from setting $u(x,0,0) = 0$ (initial horizontal velocity on the free surface is zero) and recovering $u_\alpha(x,0)$ from the velocity profile assumed in LWD. The second condition results from setting $\eta_x(x,0) = 0$ in (2.47); thus, $\eta(x,0) =$ constant. If the derivatives of u_α and B are all continuous, the order of differentiation does not matter. By Laplace-Fourier transforming (2.49) and applying the above initial conditions, (2.49) becomes

$$-k^2\dddot{\overline{u_\alpha}} - s^2\dddot{\overline{u_\alpha}} + \alpha_{11}k^4\dddot{\overline{u_\alpha}} + \alpha_{21}s^2k^2\dddot{\overline{u_\alpha}} = ik(1 - \alpha_{12}k^2 - \alpha_{22}s^2)\Big[s\dddot{\overline{B}} - \overline{B}(k,0)\Big], \tag{2.51}$$

from which $\dddot{\overline{u_\alpha}}$ can be solved for as

$$\dddot{\overline{u_\alpha}}(k,s) = \frac{ik(1 - \alpha_{12}k^2 - \alpha_{22}s^2)\Big[s\dddot{\overline{B}} - \overline{B}(k,0)\Big]}{(\alpha_{11}k^2 - 1)k^2 + (\alpha_{21}k^2 - 1)s^2}. \tag{2.52}$$

$\dddot{\overline{\eta}}$ can then be recovered from the transformed (2.46) or (2.47). If (2.46) is used, we obtain

$$\dddot{\overline{\eta}}(k,s) = \frac{s\dddot{\overline{B}} - \overline{B}(k,0)}{s}\left[(1 - \alpha_{12}k^2) - \frac{k^2\frac{1-\alpha_{11}k^2}{1-\alpha_{21}k^2}(1 - \alpha_{12}k^2 - \alpha_{22}s^2)}{s^2 + k^2\frac{1-\alpha_{11}k^2}{1-\alpha_{21}k^2}}\right] + \frac{\overline{\eta(x,0)}}{s}. \tag{2.53}$$

Since u_α is solved for first in this case, the precise initial condition for the free surface, $\eta(x,0)$, can be specified only when the solution for η is considered. Here we require $\eta(x,0)=0$.

For a translating landslide moving at a constant speed Fr so that $B(x,t) = B(x - Fr\cdot t)$, a closed-form inverse Laplace transform of (2.53) is available, and we find $\eta(x,t)$ to be

$$\begin{aligned}
&\eta(x,t) = \eta_{Fr}(x,t) + \eta_+(x,t) + \eta_-(x,t)\\
&\eta_{Fr}(x,t) = -\frac{1}{\sqrt{2\pi}}\int_{-\infty}^{\infty}(1-\alpha_{12}k^2+\alpha_{22}k^2D^2)\frac{Fr^2}{D^2-Fr^2}\overline{B(x,0)}e^{-ikFr\cdot t}e^{ikx}dk\\
&\eta_+(x,t) = \frac{1}{\sqrt{2\pi}}\int_{-\infty}^{\infty}(1-\alpha_{12}k^2+\alpha_{22}k^2D^2)\frac{Fr}{2(D-Fr)}\overline{B(x,0)}e^{-ikDt}e^{ikx}dk\\
&\eta_-(x,t) = -\frac{1}{\sqrt{2\pi}}\int_{-\infty}^{\infty}(1-\alpha_{12}k^2+\alpha_{22}k^2D^2)\frac{Fr}{2(D+Fr)}\overline{B(x,0)}e^{ikDt}e^{ikx}dk
\end{aligned}, \tag{2.54}$$

where

$$D = \sqrt{\frac{1-\alpha_{11}k^2}{1-\alpha_{21}k^2}} \tag{2.55}$$

is the normalized wave speed of LWD. We again see the three-wave structure and frequency dispersion effects.

Since LWD is essentially an expanded (approximated) version of LFD, we shall verify that the expressions (2.55) and (2.54) can be recovered from their LFD counterparts. We observe that the two differences are the definition of D and the scaling function of the magnitude of each wave number component (i.e., $1/\cosh\mu k$ in LFD and $1-\alpha_{12}k^2+\alpha_{22}k^2D^2$ in LWD). Upon writing out D^2 fully in LWD (2.55) in terms of α with the relations given in (2.48), we obtain

$$D^2 = \frac{1-(\frac{1}{2}\alpha^2+\alpha+\frac{1}{3})\mu^2k^2}{1-(\frac{1}{2}\alpha^2+\alpha)\mu^2k^2}, \tag{2.56}$$

which is exactly the same as the linear dispersion relation in Nwogu (1993)'s Boussinesq equations formulation (we note that our α is the z_α used in Nwogu, 1993).

By specifying α, (2.56) can be tuned to agree with the $O(\mu^4)$-accurate Padé approximation of the true linear dispersion relation (2.10) based on LFD:

$$\frac{\tanh \mu k}{\mu k} \simeq \frac{1 + \frac{1}{15}\mu^2 k^2}{1 + \frac{2}{5}\mu^2 k^2} + O(\mu^6). \tag{2.57}$$

Nwogu (1993) showed that using $\alpha = -0.531$ in (2.56) approximates the true linear dispersion relation (2.57) very well up to $O(\mu^4)$ accurate, even though strictly speaking weakly dispersive models are only $O(\mu^2)$ accurate.

Next, we look at the scaling functions $1/\cosh \mu k$ in LFD and $1 - \alpha_{12} k^2 + \alpha_{22} k^2 D^2$ in LWD. Taylor series expansion gives

$$\frac{1}{\cosh \mu k} \simeq 1 - \frac{1}{2}\mu^2 k^2 + \frac{5}{24}\mu^4 k^4 + O(\mu^6), \tag{2.58}$$

and (written in terms of α)

$$1 - \alpha_{12} k^2 + \alpha_{22} k^2 D^2 \simeq 1 - \frac{1}{2}\mu^2 k^2 - \frac{1}{3}\alpha \mu^4 k^4 + O(\mu^6). \tag{2.59}$$

We see that the two agree exactly up to $O(\mu^2)$, and α again can be tuned to improve the match of the $O(\mu^4)$ terms. We note that the choice $\alpha = -0.531$ was made to improve the linear dispersion relation; here $5/24 \simeq 0.208$ and $-\alpha/3 \simeq 0.177$.

The same asymptotic approximation method used to obtain the far-field leading wave solutions for LFD can be applied again to obtain that for LWD, and the results will be exactly the same, since the leading wave solution depends on only the leading-order $O(\mu^2)$ frequency dispersion effects which are included in LWD. The leading wave in the resonance case ($Fr = 1$) therefore also grows at the rate $t^{1/3}$.

For the velocity solutions, a closed-form inverse Laplace transform of (2.52) is

available, and we can express u_α, the horizontal velocity at depth z_α, as

$$\begin{aligned}
u_\alpha(x,t) &= u_{\alpha_{Fr}}(x,t) + u_{\alpha_+}(x,t) + u_{\alpha_-}(x,t) \\
u_{\alpha_{Fr}}(x,t) &= -\frac{1}{\sqrt{2\pi}}\int_{-\infty}^{\infty} \frac{\overline{B(x,0)}}{1-\alpha_{21}k^2}\frac{Fr^2}{D^2-Fr^2}\frac{1-\alpha_{12}k^2+\alpha_{22}k^2Fr^2}{Fr}e^{-ikFr\cdot t}e^{ikx}dk \\
u_{\alpha_+}(x,t) &= \frac{1}{\sqrt{2\pi}}\int_{-\infty}^{\infty} \frac{\overline{B(x,0)}}{1-\alpha_{21}k^2}\frac{Fr}{2(D-Fr)}\frac{1-\alpha_{12}k^2+\alpha_{22}k^2D^2}{D}e^{-ikDt}e^{ikx}dk \\
u_{\alpha_-}(x,t) &= \frac{1}{\sqrt{2\pi}}\int_{-\infty}^{\infty} \frac{\overline{B(x,0)}}{1-\alpha_{21}k^2}\frac{Fr}{2(D+Fr)}\frac{1-\alpha_{12}k^2+\alpha_{22}k^2D^2}{D}e^{ikDt}e^{ikx}dk
\end{aligned} \tag{2.60}$$

The full horizontal and vertical velocities (u and w respectively) in LWD can be expressed as

$$\begin{aligned}
u(x,z,t) &= u_\alpha(x,t) - \mu^2\Big(\frac{1}{2}(z^2-\alpha^2)u_{\alpha xx} + (z-\alpha)(u_{\alpha xx} - B_{tx})\Big) + O(\mu^4) \\
w(x,z,t) &= -\mu^2\Big(zu_x(x,0,t) + u_x(x,0,t) - B_t\Big) + O(\mu^4)
\end{aligned} \tag{2.61}$$

We note that the expressions in (2.61) are not unique, since alternate $O(\mu^2)$ terms may be used. For more details on recovering the velocity field from u_α in weakly dispersive models, see, for example Lynett and Liu (2002).

2.4 Comparison of the 1DH analytical solutions in constant depth

The analytical solutions based on different wave models (LSWE, LWD, and LFD) are compared (integral-form solutions are numerically integrated when necessary) in this section for three selected cases, $\mu = 0.05$, $\mu = 0.2$, and $\mu = 0.4$. We recall that μ is water depth divided by landslide length and controls how strong frequency dispersion is in a problem. Since LSWE has a theoretical truncation error of $O(\mu^2)$, LWD has a theoretical truncation error of $O(\mu^4)$, and LFD has no restriction on μ, we expect the three models to yield essentially identical results for

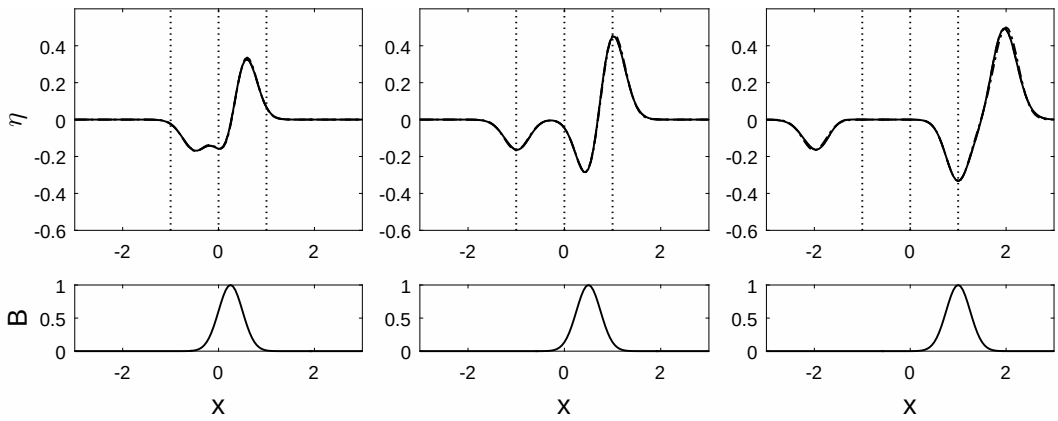

Figure 2.7: The free surface elevation $\eta(x,t)$ at different times and locations, due to a very long Gaussian-shaped landslide with $\mu = 0.05$ moving at speed $Fr = 0.5$. Left panels: $t = 0.5$; middle panels: $t = 1.0$; right panels: $t = 2.0$. Solid line: LFD solution (2.9); dashed line: LWD solution (2.54); dash-dot line: LSWE solution (2.43); dotted line: locations at which the velocity solutions are shown.

a very long landslide with small μ (e.g. $\mu = 0.05$). As the landslide length shortens (e.g. $\mu = 0.2$ and $\mu = 0.4$), LSWE and LWD become less and less accurate.

For a 1DH Gaussian-shaped landslide with $\mu = 0.05$ moving at speed $Fr = 0.5$ in constant water depth, we compare the solutions for η in figure 2.7. Since the landslide is sufficiently long compared to the water depth, the three solutions are nearly identical. The velocity solutions are compared in figure 2.8 and figure 2.9. We note that although the characteristics of the velocity solutions in LSWE are fundamentally different from those in LWD or LFD, i.e. no vertical variation of the horizontal velocity and no vertical velocity, the difference is small in magnitude, which is expected since LSWE has a theoretical truncation error of $O(\mu^2)$ and in this case $\mu = 0.05$ is negligibly small.

We found $\mu = 0.2$ to be an intermediate landslide length for which LSWE is inaccurate but LWD remains accurate. For a Gaussian-shaped landslide with $\mu = 0.2$ moving at speed $Fr = 0.5$, the free surface elevation solutions are compared in figure 2.10 and the velocity solutions are compared in figure 2.11 and figure 2.12.

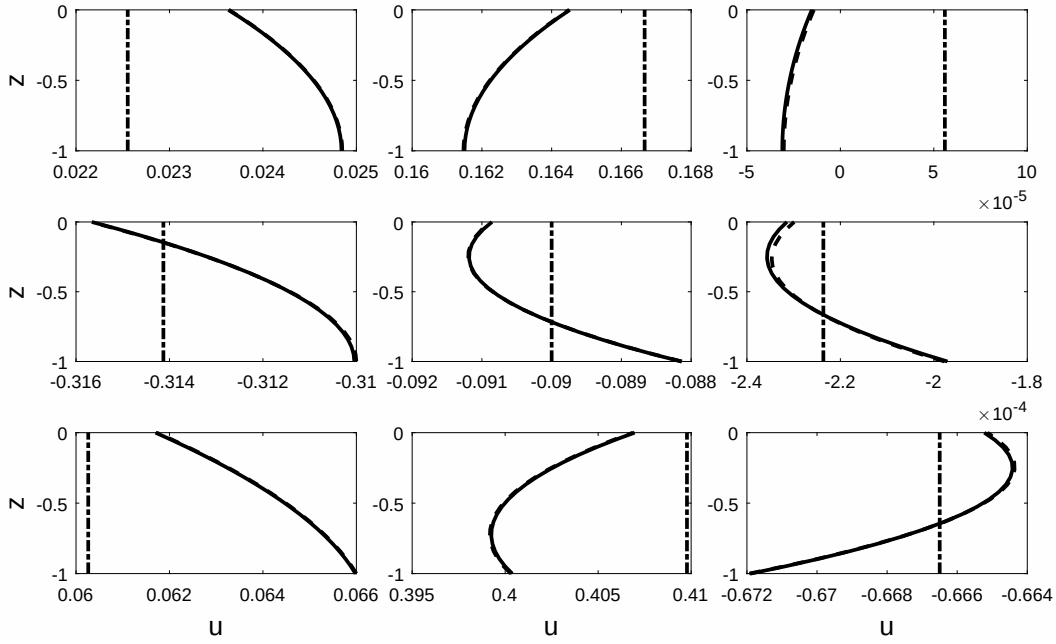

Figure 2.8: The vertical distribution of the horizontal velocity $u(x, z, t)$ at different times and locations, due to a very long Gaussian-shaped landslide with $\mu = 0.05$ moving at speed $Fr = 0.5$. Note that the scale of the horizontal axis varies greatly from panel to panel. Left column: $t = 0.5$; middle column: $t = 1.0$; right column: $t = 2.0$. Top row: $x = -1$; middle row: $x = 0$; bottom row: $x = 1$. Solid line: LFD solution (2.11); dashed line: LWD solution recovered from (2.61); dash-dot line: LSWE solution (2.44).

While LSWE is clearly inaccurate for this problem setup, the LWD solutions overall agree well with the LFD solutions.

As the landslide length shortens further, LWD eventually becomes invalid. For a Gaussian-shaped landslide with $\mu = 0.4$, the solutions are compared in figures 2.13-2.15. Significant differences now show between the LWD solutions and the LFD solutions, suggesting that LWD is no longer an accurate wave model to describe this landslide wave problem.

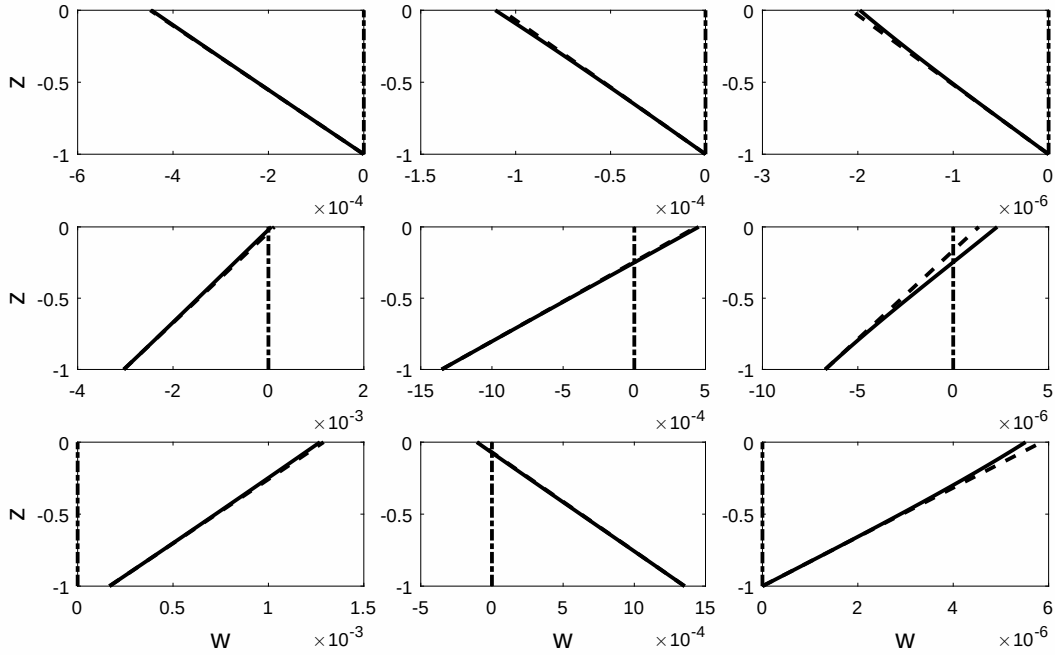

Figure 2.9: The vertical distribution of the vertical velocity $w(x, z, t)$ at different times and locations, due to a very long Gaussian-shaped landslide with $\mu = 0.05$ moving at speed $Fr = 0.5$. Note that the scale of the horizontal axis varies greatly from panel to panel. Left column: $t = 0.5$; middle column: $t = 1.0$; right column: $t = 2.0$. Top row: $x = -1$; middle row: $x = 0$; bottom row: $x = 1$. Solid line: LFD solution (2.12); dashed line: LWD solution recovered from (2.61); dash-dot line: LSWE solution (zero vertical velocity).

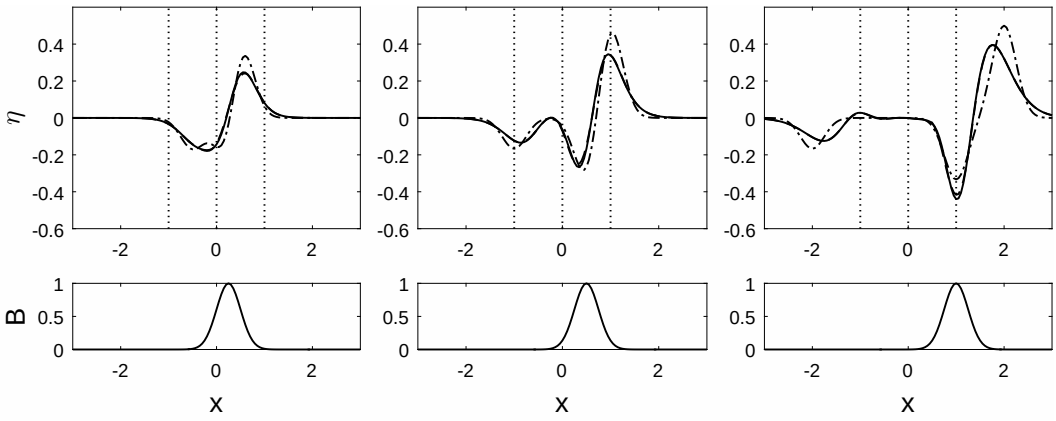

Figure 2.10: The free surface elevation $\eta(x, t)$ at different times and locations, due to a moderately long Gaussian-shaped landslide with $\mu = 0.2$ moving at speed $Fr = 0.5$. Left panels: $t = 0.5$; middle panels: $t = 1.0$; right panels: $t = 2.0$. Solid line: LFD solution (2.9); dashed line: LWD solution (2.54); dash-dot line: LSWE solution (2.43); dotted line: locations at which the velocity solutions are shown.

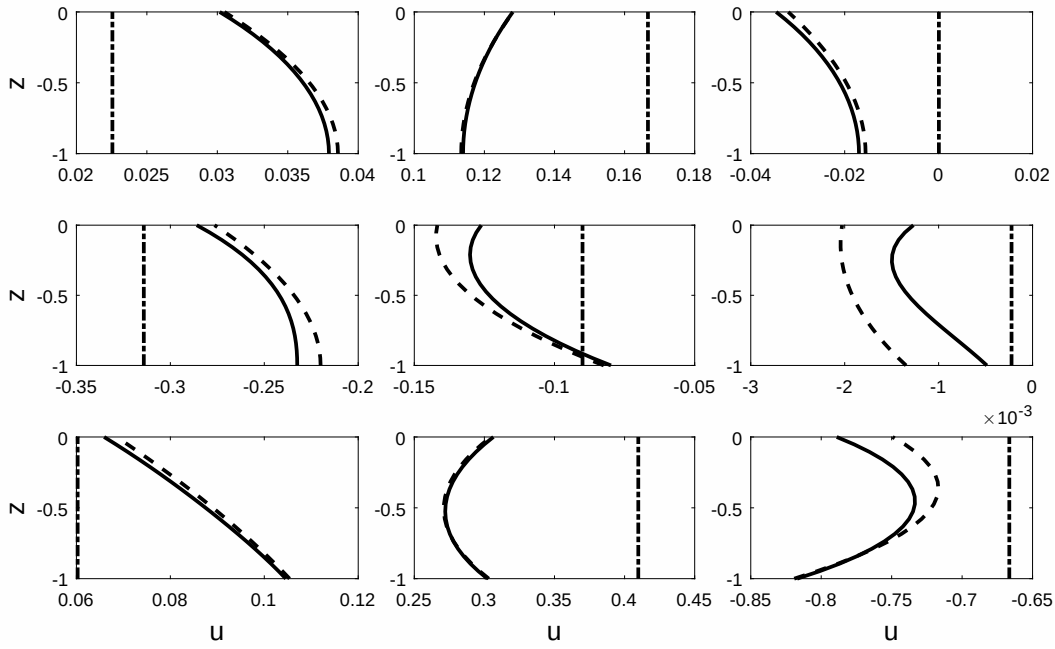

Figure 2.11: The vertical distribution of the horizontal velocity $u(x, z, t)$ at different times and locations, due to a moderately long Gaussian-shaped landslide with $\mu = 0.2$ moving at speed $Fr = 0.5$. Note that the scale of the horizontal axis varies greatly from panel to panel. Left column: $t = 0.5$; middle column: $t = 1.0$; right column: $t = 2.0$. Top row: $x = -1$; middle row: $x = 0$; bottom row: $x = 1$. Solid line: LFD solution (2.11); dashed line: LWD solution recovered from (2.61); dash-dot line: LSWE solution (2.44).

2.5 1DH linear shallow water wave equations on a slope

The dimensionless 1DH LSWE on a slope read

$$\eta_t + (uh)_x = B_t \tag{2.62}$$

and

$$u_t = -\eta_x, \tag{2.63}$$

where (η,B) are normalized by the landslide thickness A, x is normalized by the landslide length L, $h = x$, normalized by $L\tan\theta$, is the still water depth on a constant slope of angle θ, u is normalized by $A\sqrt{gL\tan\theta}/L\tan\theta$, and t is normalized by $\sqrt{L/g\tan\theta}$. The landslide forcing function B is described in the water

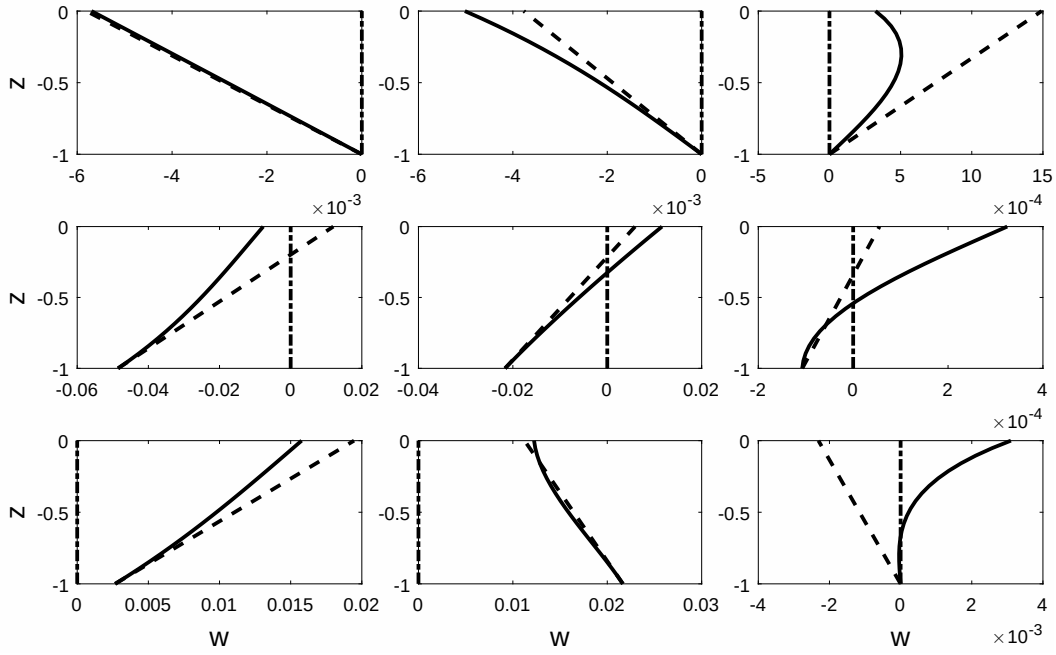

Figure 2.12: The vertical distribution of the vertical velocity $w(x, z, t)$ at different times and locations, due to a moderately long Gaussian-shaped landslide with $\mu = 0.2$ moving at speed $Fr = 0.5$. Note that the scale of the horizontal axis varies greatly from panel to panel. Left column: $t = 0.5$; middle column: $t = 1.0$; right column: $t = 2.0$. Top row: $x = -1$; middle row: $x = 0$; bottom row: $x = 1$. Solid line: LFD solution (2.12); dashed line: LWD solution recovered from (2.61); dash-dot line: LSWE solution (zero vertical velocity).

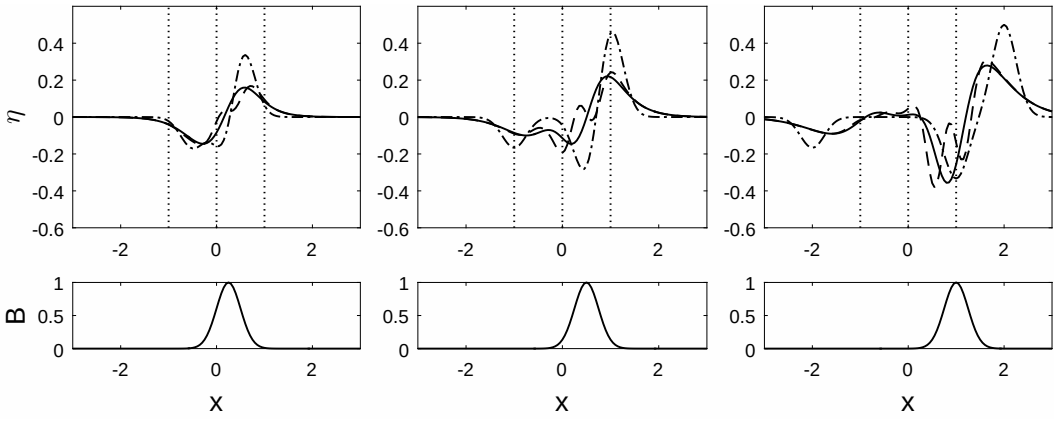

Figure 2.13: The free surface elevation $\eta(x, t)$ at different times and locations, due to a Gaussian-shaped landslide with $\mu = 0.4$ moving at speed $Fr = 0.5$. Left panels: $t = 0.5$; middle panels: $t = 1.0$; right panels: $t = 2.0$. Solid line: LFD solution (2.9); dashed line: LWD solution (2.54); dash-dot line: LSWE solution (2.43); dotted line: locations at which the velocity solutions are shown.

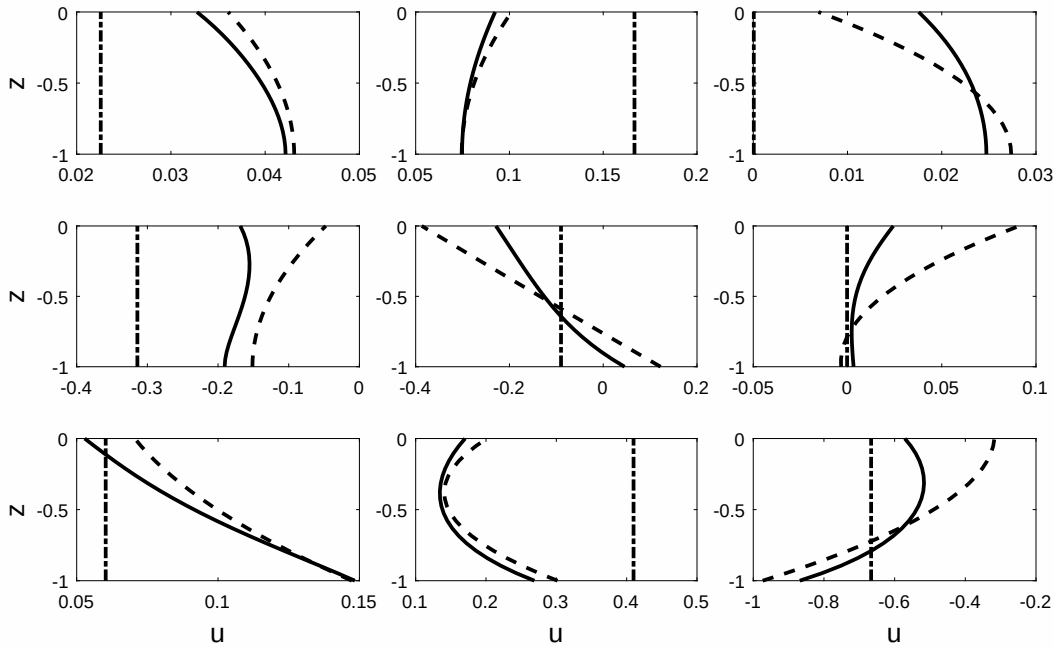

Figure 2.14: The vertical distribution of the horizontal velocity $u(x, z, t)$ at different times and locations, due to a Gaussian-shaped landslide with $\mu = 0.05$ moving at speed $Fr = 0.5$. Note that the scale of the horizontal axis varies greatly from panel to panel. Left column: $t = 0.5$; middle column: $t = 1.0$; right column: $t = 2.0$. Top row: $x = -1$; middle row: $x = 0$; bottom row: $x = 1$. Solid line: LFD solution (2.11); dashed line: LWD solution recovered from (2.61); dash-dot line: LSWE solution (2.44).

coordinate system (vertical-horizontal). The shoreline is located at $x = 0$ and the physical domain of interest is $x > 0$.

Again, either η or u can be solved for first. To solve for η first, (2.62) and (2.63) can be combined into

$$x\eta_{xx} + \eta_x - \eta_{tt} = -B_{tt}. \tag{2.64}$$

Tuck and Hwang (1972) first solved this equation using the Laplace and Hankel transforms to obtain the integral-form solution for η. Here, we impose the initial conditions

$$\eta(x, 0) = 0 \quad \text{and} \quad \eta_t(x, 0) = B_t(x, 0), \tag{2.65}$$

the latter resulting from setting $[u(x, 0)h]_x = 0$ in (2.62) – on a constant slope with

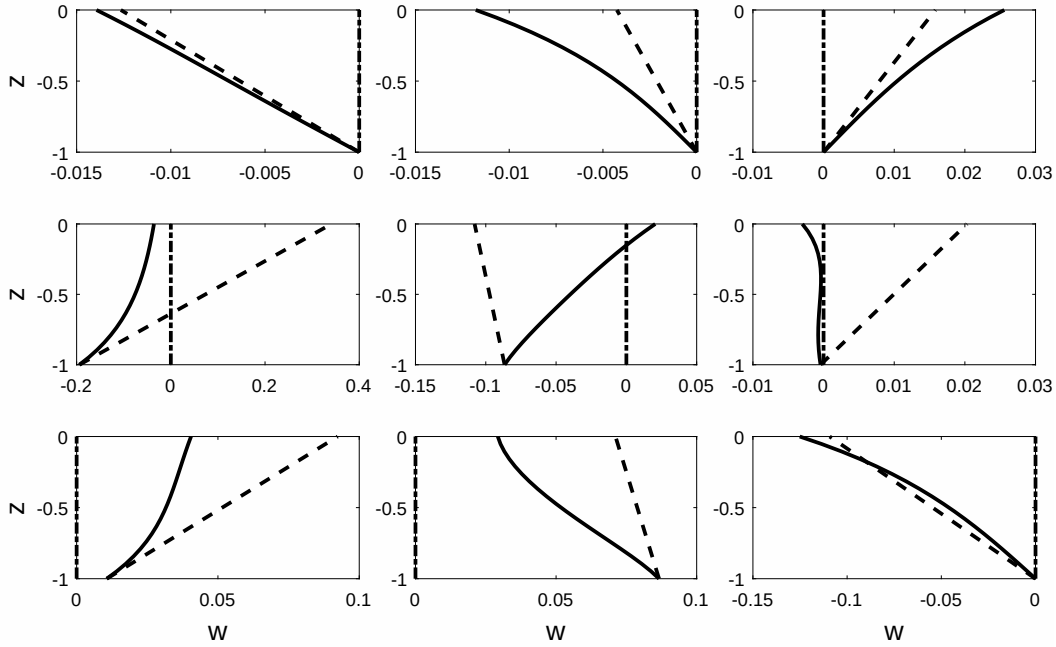

Figure 2.15: The vertical distribution of the vertical velocity $w(x, z, t)$ at different times and locations, due to a Gaussian-shaped landslide with $\mu = 0.4$ moving at speed $Fr = 0.5$. Note that the scale of the horizontal axis varies greatly from panel to panel. Left column: $t = 0.5$; middle column: $t = 1.0$; right column: $t = 2.0$. Top row: $x = -1$; middle row: $x = 0$; bottom row: $x = 1$. Solid line: LFD solution (2.12); dashed line: LWD solution recovered from (2.61); dash-dot line: LSWE solution (zero vertical velocity).

$h = x$, this corresponds to $u(x, 0) = \text{constant}/x$ – and rederive the integral-form solution (valid for $x > 0, t > 0$) as

$$\eta(x,t) = 2\int_0^\infty J_0(2\sqrt{\lambda x})\int_0^t \cos\left(\sqrt{\lambda}(t-\tau)\right)\int_0^\infty sB_\tau(s^2,\tau)J_0(2\sqrt{\lambda}s)dsd\tau d\lambda, \tag{2.66}$$

where J_0 is the Bessel function of the first kind with order 0. The solution for u can then be recovered from (2.63) as

$$\begin{aligned} &u(x,t) = u(x,0) \\ &+\frac{2}{\sqrt{x}}\int_0^\infty \sqrt{\lambda}J_1(2\sqrt{\lambda x})\int_0^t\int_0^\psi \cos\left(\sqrt{\lambda}(t-\tau)\right)\int_0^\infty sB_\tau(s^2,\tau)J_0(2\sqrt{\lambda}s)dsd\tau d\psi d\lambda \end{aligned}. \tag{2.67}$$

The precise initial condition for the horizontal velocity, $u(x, 0)$, can be specified only when the solution for u is considered; here we require $u(x, 0) = 0$ for initially

quiescent water.

While the solution for η, (2.66), is in a slightly different form from that presented in Tuck and Hwang (1972), we have verified that the two solutions are indeed the same. Our next task is to seek special landslide forcing functions $B(x,t)$ that have closed-form integrals in (2.66). Liu et al. (2003) showed that using a deforming Gaussian-like landslide moving at the same speed as wave celerity reduces the number of integrals to one.

We consider a ramp-like landslide forcing function:

$$B(x,t) = R(\beta t - \sqrt{x}), \tag{2.68}$$

where β is a constant to be chosen and R is the ramp function defined as

$$R(\xi) = \begin{cases} \xi, \xi \geq 0 \\ 0, \xi < 0 \end{cases}. \tag{2.69}$$

Thus, the temporal derivative of B is

$$B_t(x,t) = \beta H(\beta t - \sqrt{x}), \tag{2.70}$$

where H denotes the Heaviside step function. A closed-form Hankel transform is available for the step function (Poularikas, 2000) and (2.66) can be written as

$$\begin{aligned} \eta(x,t) = \beta^2 \int_0^\infty \frac{J_0(2\sqrt{\lambda}\sqrt{x})}{\sqrt{\lambda}} \Bigg[\cos(\sqrt{\lambda}t) \int_0^t \tau \cos(\sqrt{\lambda}\tau) J_1(2\beta\sqrt{\lambda}\tau) d\tau \\ + \sin(\sqrt{\lambda}t) \int_0^t \tau \sin(\sqrt{\lambda}\tau) J_1(2\beta\sqrt{\lambda}\tau) d\tau \Bigg] d\lambda. \end{aligned} \tag{2.71}$$

Furthermore, if we choose $\beta = 1/2$, the τ-integrals can be evaluated (Rosenheinrich, 2015) and the equation becomes

$$\eta(x,t) = \frac{t^2}{12} \int_0^\infty \frac{J_0(2\sqrt{\lambda}\sqrt{x}) J_1(\sqrt{\lambda}t)}{\sqrt{\lambda}} d\lambda = \frac{t^2}{12} \int_0^\infty J_0(\sqrt{x}\omega) J_1(\frac{t}{2}\omega) d\omega. \tag{2.72}$$

This last integral can also be evaluated (Gradshteyn and Ryzhik, 2007) and we have simply

$$\eta(x,t) = \frac{t}{6} H\left[-(\sqrt{x} - \frac{t}{2})\right], \tag{2.73}$$

which is a jump from $t/6$ to 0 traveling along $x = t^2/4$, where the front of the landslide is. Similar to the landslide used in Liu et al. (2003), the landslide accelerates so that it always travels at the local wave speed. The solution for u can be recovered from (2.63), with the initial condition $u(x,0) = 0$, as

$$u(x,t) = \frac{1}{3} H\left[-(\sqrt{x} - \frac{t}{2})\right], \tag{2.74}$$

which is a step function whose amplitude does not change. The analytical solution (2.73) serves as a challenging benchmark for numerical models, since it consists of a shock and a "shoreline" ($x \to 0$) in linear theory. We shall use it as a tool to verify our numerical solver in Chapter 3.

2.6 2DH linear and fully dispersive model in constant depth

The 2DH configuration, as sketched in figure 2.16, is similar to the 1DH one, except for the addition of the new transverse dimension, y. Dimensionlessly, 2DH LFD and the linearized boundary conditions read

$$\begin{aligned} \mu^2\phi_{xx} + \mu^2\phi_{yy} + \phi_{zz} = 0, &\quad -1 < z < 0 \\ \phi_z = \mu^2 B_t, &\quad z = -1 \\ \phi_z = \mu^2 \eta_t, &\quad z = 0 \\ \phi_t + \eta = 0, &\quad z = 0 \end{aligned} \quad , \tag{2.75}$$

where $\phi(x,y,z,t)$ is the velocity potential, $B(x,y,t)$ is the bottom boundary deformation due to a moving landslide, and η is the water surface elevation. Using

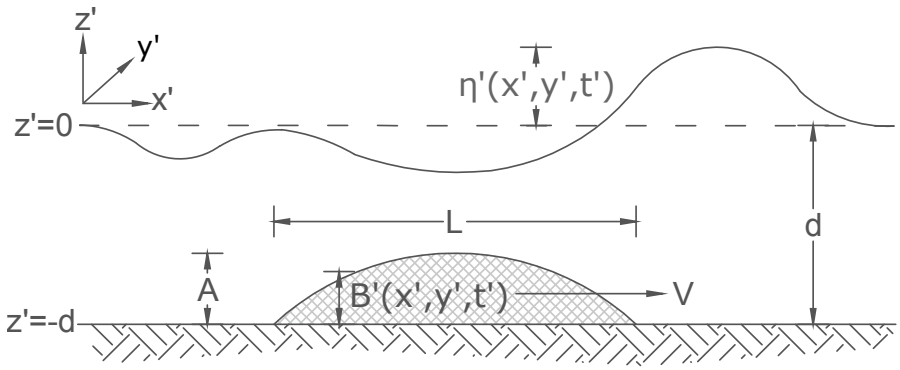

Figure 2.16: Definition sketch in dimensional form (not to scale) of the 2DH landslide wave problem in constant depth.

primes to denote dimensional variables, we have defined the dimensionless variables as $x = x'/L$, $x = y'/L$, $z = z'/d$, $t = t'\sqrt{gd}/L$, $\eta(x,y,t) = \eta'(x',y',t')/A$, $B(x,y,t) = B'(x',y',t')/A$, and $\phi(x,y,z,t) = \phi'(x',y',z',t')/(\epsilon L\sqrt{gd})$, where L is the characteristic wavelength (which is assumed to be the length of the landslide), A is the characteristic wave amplitude (which is assumed to be the height of the landslide), d is the constant water depth, g is the gravitational acceleration, $\epsilon = A/d$, and $\mu = d/L$. For consistency of the coordinate system and without loss of generality, we shall define the landslide forcing function B so that its center of mass is located at the origin $(x,y) = (0,0)$ at $t = 0$. The landslide starts moving at a constant speed $Fr = V/\sqrt{gd}$ in the x direction for $t > 0$.

For landslide-generated waves, we impose the initial conditions

$$\eta(x,y,0) = 0, \quad \phi(x,y,0,0) = \text{constant} \tag{2.76}$$

in (2.75). Whereas $\eta(x,y,0) = 0$ means an initially flat water surface, $\phi(x,y,0,0) = \text{constant}$ means zero initial horizontal velocities on the still water surface, $z = 0$. $B(x,y,0)$ is known since B, the landslide forcing function, is prescribed.

Just like 1DH LFD, 2DH LFD given in (2.75) can be solved by applying the

Laplace and Fourier transforms (two Fourier transforms are needed in 2DH – one in the x direction and the other in the y direction). After transforming (2.75), we have

$$\begin{aligned} -\mu^2(k^2+l^2)\overset{\tilde{\cdot}\tilde{\cdot}\tilde{\cdot}}{\overline{\phi}} + \overset{\tilde{\cdot}\tilde{\cdot}\tilde{\cdot}}{\overline{\phi}}_{zz} &= 0, && -1 < z < 0 \\ \overset{\tilde{\cdot}\tilde{\cdot}\tilde{\cdot}}{\overline{\phi}}_z &= \mu^2 s\overset{\tilde{\cdot}\tilde{\cdot}\tilde{\cdot}}{\overline{B}} - \mu^2\widetilde{\overline{B(x,y,t=0)}}, && z=-1 \\ \overset{\tilde{\cdot}\tilde{\cdot}\tilde{\cdot}}{\overline{\phi}}_z &= \mu^2 s\overset{\tilde{\cdot}\tilde{\cdot}\tilde{\cdot}}{\overline{\eta}} - \mu^2\widetilde{\overline{\eta(x,y,t=0)}}, && z=0 \\ s\overset{\tilde{\cdot}\tilde{\cdot}\tilde{\cdot}}{\overline{\phi}} - \widetilde{\overline{\phi(x,y,z=0,t=0)}} + \overset{\tilde{\cdot}\tilde{\cdot}\tilde{\cdot}}{\overline{\eta}} &= 0, && z=0 \end{aligned} \quad . \tag{2.77}$$

Combining the boundary conditions at $z = 0$ we obtain

$$\overset{\tilde{\cdot}\tilde{\cdot}\tilde{\cdot}}{\overline{\phi}}_z + \mu^2 s^2\overset{\tilde{\cdot}\tilde{\cdot}\tilde{\cdot}}{\overline{\phi}} = \mu^2 s\widetilde{\overline{\phi(x,y,0,0)}} - \mu^2\widetilde{\overline{\eta(x,y,0)}}, \quad z=0. \tag{2.78}$$

$\overset{\tilde{\cdot}\tilde{\cdot}\tilde{\cdot}}{\overline{\phi}}$ can be solved for from (2.77) and (2.78):

$$\begin{aligned} \overset{\tilde{\cdot}\tilde{\cdot}\tilde{\cdot}}{\overline{\phi}} = \frac{1}{\cosh\mu q}\frac{1}{s^2+q^2D^2}\Bigg(&\Big(s\widetilde{\overline{\phi(x,y,0,0)}} - \widetilde{\overline{\eta(x,y,0)}}\Big)\cosh\Big(\mu q(z+1)\Big) \\ &-\Big(s\overset{\tilde{\cdot}\tilde{\cdot}\tilde{\cdot}}{\overline{B}} - \widetilde{\overline{B(x,y,0)}}\Big)\cosh(\mu q z) + \frac{\mu s^2}{q}\Big(s\overset{\tilde{\cdot}\tilde{\cdot}\tilde{\cdot}}{\overline{B}} - \widetilde{\overline{B(x,y,0)}}\Big)\sinh(\mu q z)\Bigg) \end{aligned}, \tag{2.79}$$

where

$$q = \sqrt{k^2+l^2} \tag{2.80}$$

is used to simplify the expressions, and

$$D = \sqrt{\frac{\tanh(\mu q)}{\mu q}} \tag{2.81}$$

is the normalized wave celerity of linear dispersive waves in 2DH constant depth. $D(\mu q)$ is plotted in figure 2.17 – it has a maximum of one at $\mu q = 0$, and decays to zero as μq increases (we note that $q \geq 0$). $\overset{\tilde{\cdot}\tilde{\cdot}\tilde{\cdot}}{\overline{\eta}}$ can then be recovered from the last equation in (2.77) as

$$\overset{\tilde{\cdot}\tilde{\cdot}\tilde{\cdot}}{\overline{\eta}} = -s\widetilde{\overline{\phi(x,y,0,t)}} + \widetilde{\overline{\phi(x,y,0,0)}}. \tag{2.82}$$

The velocity components in the x, y, and z directions – $u(x,y,z,t)$, $v(x,y,z,t)$, and $w(x,y,z,t)$, respectively – can be calculated as

$$u = \phi_x, \quad v = \phi_y, \quad w = \phi_z. \tag{2.83}$$

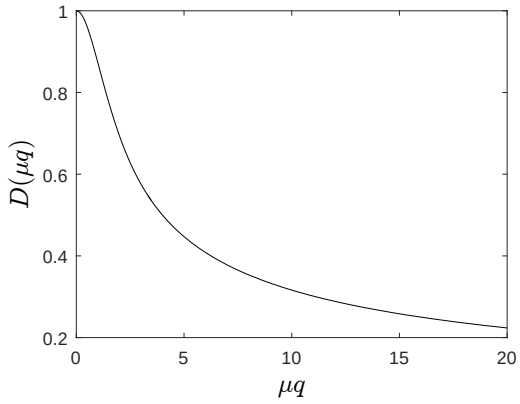

Figure 2.17: Frequency dispersive wave speed $D(\mu q)$ (2.81) plotted as a function of μq.

For a landslide translating at a constant speed Fr in the x direction, the landslide forcing function $B(x, y, t)$ can be written as

$$B(x, y, t) = B(x - Fr \cdot t, y). \tag{2.84}$$

Fourier transforming a translating landslide, $B(x, y, t) = B(x - Fr \cdot t, y)$, results in

$$\widetilde{\overline{B}}(k, l, t) = \widetilde{\overline{B(x, y, 0)}} e^{-ik \cdot Fr \cdot t} = \widetilde{\overline{B_0(x, y)}} e^{-ik \cdot Fr \cdot t}, \tag{2.85}$$

where for convenience we define $B_0(x, y) = B(x, y, 0)$ as the landslide shape function that excludes the translation. Using (2.85) we then obtain

$$\dddot{\overline{B}} = \widetilde{\overline{B_0}}(k, l) \frac{1}{s + ik \cdot Fr}. \tag{2.86}$$

After specifying the landslide forcing function as (2.86) and imposing the initial conditions (2.76), the expression for the transformed free surface (2.82) becomes

$$\dddot{\overline{\eta}}(k, l, s) = \frac{-ik \cdot Fr \cdot \widetilde{\overline{B_0}}}{\cosh(\mu q)} \frac{s}{s + ik \cdot Fr} \frac{1}{s^2 + q^2 D^2}, \tag{2.87}$$

for which a closed-form inverse Laplace transform is available:

$$\widetilde{\overline{\eta}}(k, l, t) = \frac{\widetilde{\overline{B_0}}}{\cosh(\mu q)} \Big(- \frac{Fr^2 \frac{k^2}{q^2}}{D^2 - Fr^2 \frac{k^2}{q^2}} e^{-ik \cdot Fr \cdot t} + \frac{Fr \frac{k}{q}}{2(D - Fr \frac{k}{q})} e^{-iqDt} - \frac{Fr \frac{k}{q}}{2(D + Fr \frac{k}{q})} e^{iqDt} \Big). \tag{2.88}$$

Recognizing the three-wave structure and writing out the definition of the inverse Fourier transform, we then have the analytical solution in integral form as

$$\begin{aligned}
&\eta(x,y,t) = \eta_{Fr}(x,y,t) + \eta_{+}(x,y,t) \\
&\eta_{Fr}(x,y,t) = -\frac{1}{2\pi}\int_{-\infty}^{\infty}\int_{-\infty}^{\infty}\frac{\widetilde{\overline{B_0}}(k,l)}{\cosh(\mu q)}\frac{Fr^2\frac{k^2}{q^2}}{D^2 - Fr^2\frac{k^2}{q^2}}e^{-ik\cdot Fr\cdot t}e^{ikx}e^{ily}dkdl \\
&\eta_{+}(x,y,t) = \frac{1}{2\pi}\int_{-\infty}^{\infty}\int_{-\infty}^{\infty}\frac{\widetilde{\overline{B_0}}(k,l)}{\cosh(\mu q)}\Big(\frac{Fr\frac{k}{q}}{2(D - Fr\frac{k}{q})}e^{-iqDt} - \frac{Fr\frac{k}{q}}{2(D + Fr\frac{k}{q})}e^{iqDt}\Big) \\
&\qquad\qquad e^{ikx}e^{ily}dkdl
\end{aligned} \tag{2.89}$$

Introducing a moving coordinate that follows the landslide, $\xi = x - Fr\cdot t$, we write $\eta_{Fr}(x,y,t)$ as $\eta_{Fr}(\xi,y)$. Thus, η_{Fr} is a trapped wave of permanent shape moving with the landslide. In other words, $\eta_{Fr}(x,y,t)$ is the so-called steady-state solution.

In 2DH, it is often convenient to express the solutions in polar coordinates. By using the substitutions $x = r\cos\theta$, $y = r\sin\theta$, $k = q\cos\psi$, and $l = q\sin\psi$, we write the integral-form solutions as

$$\eta_{Fr}(r,\theta,t) = -\frac{1}{2\pi}\int_0^{2\pi}\int_0^{\infty}\frac{q\widetilde{\overline{B_0}}(q,\psi)}{\cosh(\mu q)}\frac{Fr^2\cos^2\psi}{D^2 - Fr^2\cos^2\psi}e^{-iq\cdot Fr\cos\psi\cdot t}e^{iqr\cos(\psi-\theta)}dqd\psi \tag{2.90}$$

and

$$\begin{aligned}
\eta_{+}(r,\theta,t) = \frac{1}{2\pi}\int_0^{2\pi}\int_0^{\infty}\frac{q\widetilde{\overline{B_0}}(q,\psi)}{\cosh(\mu q)}\Big(&\frac{Fr\cos\psi}{2(D - Fr\cos\psi)}e^{-iqDt} \\
&-\frac{Fr\cos\psi}{2(D + Fr\cos\psi)}e^{iqDt}\Big)e^{iqr\cos(\psi-\theta)}dqd\psi
\end{aligned} \tag{2.91}$$

Here, η_{+} represents transient free waves that travel at a speed of D (as indicated by the e^{iqDt} and e^{-iqDt} terms), which is the linear dispersive wave speed for the wave component μq. Similarly, the integral-form solutions for the velocities can be

obtained from (2.79) and (2.83):

$$
\begin{aligned}
&u(r,\theta,z,t) = u_{_{Fr}}(r,\theta,z,t) + u_{+}(r,\theta,z,t)\\
&u_{_{Fr}} = \frac{-1}{2\pi}\int_0^{2\pi}\int_0^{\infty} \frac{q\widetilde{\overline{B_0}}(q,\psi)}{\cosh(\mu q)}\cos\psi\Big[\frac{1}{Fr\cos\psi}\cosh(\mu q z) + \mu q\cdot Fr\cos\psi\sinh(\mu q z)\Big]\\
&\qquad\qquad \frac{Fr^2\cos^2\psi}{D^2 - Fr^2\cos^2\psi} e^{-iq\cdot Fr\cos\psi\cdot t} e^{iqr\cos(\psi-\theta)} dq d\psi \ ,\\
&u_{+} = \frac{1}{2\pi}\int_0^{2\pi}\int_0^{\infty} \frac{q\widetilde{\overline{B_0}}(q,\psi)}{\cosh(\mu q)}\cos\psi\Big[\frac{1}{D}\cosh(\mu q z) + \mu q D\sinh(\mu q z)\Big]\\
&\qquad \Big(\frac{Fr\cos\psi}{2(D - Fr\cos\psi)} e^{-iqDt} + \frac{Fr\cos\psi}{2(D + Fr\cos\psi)} e^{iqDt}\Big) e^{iqr\cos(\psi-\theta)} dq d\psi
\end{aligned}
\tag{2.92}
$$

$$
\begin{aligned}
&v(r,\theta,z,t) = v_{_{Fr}}(r,\theta,z,t) + v_{+}(r,\theta,z,t)\\
&v_{_{Fr}} = \frac{-1}{2\pi}\int_0^{2\pi}\int_0^{\infty} \frac{q\widetilde{\overline{B_0}}(q,\psi)}{\cosh(\mu q)}\sin\psi\Big[\frac{1}{Fr\cos\psi}\cosh(\mu q z) + \mu q\cdot Fr\cos\psi\sinh(\mu q z)\Big]\\
&\qquad\qquad \frac{Fr^2\cos^2\psi}{D^2 - Fr^2\cos^2\psi} e^{-iq\cdot Fr\cos\psi\cdot t} e^{iqr\cos(\psi-\theta)} dq d\psi \ ,\\
&v_{+} = \frac{1}{2\pi}\int_0^{2\pi}\int_0^{\infty} \frac{q\widetilde{\overline{B_0}}(q,\psi)}{\cosh(\mu q)}\sin\psi\Big[\frac{1}{D}\cosh(\mu q z) + \mu q D\sinh(\mu q z)\Big]\\
&\qquad \Big(\frac{Fr\cos\psi}{2(D - Fr\cos\psi)} e^{-iqDt} + \frac{Fr\cos\psi}{2(D + Fr\cos\psi)} e^{iqDt}\Big) e^{iqr\cos(\psi-\theta)} dq d\psi
\end{aligned}
\tag{2.93}
$$

and

$$
\begin{aligned}
&w(r,\theta,z,t) = w_{_{Fr}}(r,\theta,z,t) + w_{+}(r,\theta,z,t)\\
&w_{_{Fr}} = \frac{i\mu}{2\pi}\int_0^{2\pi}\int_0^{\infty} \frac{q\widetilde{\overline{B_0}}(q,\psi)}{\cosh(\mu q)}\Big[\frac{1}{Fr\cos\psi}\sinh(\mu q z) + \mu q\cdot Fr\cos\psi\cosh(\mu q z)\Big]\\
&\qquad\qquad \frac{Fr^2\cos^2\psi}{D^2 - Fr^2\cos^2\psi} e^{-iq\cdot Fr\cos\psi\cdot t} e^{iqr\cos(\psi-\theta)} dq d\psi \ .\\
&w_{+} = \frac{-i\mu}{2\pi}\int_0^{2\pi}\int_0^{\infty} \frac{q\widetilde{\overline{B_0}}(q,\psi)}{\cosh(\mu q)}\Big[\frac{1}{D}\sinh(\mu q z) + \mu q D\cosh(\mu q z)\Big]\\
&\qquad \Big(\frac{Fr\cos\psi}{2(D - Fr\cos\psi)} e^{-iqDt} + \frac{Fr\cos\psi}{2(D + Fr\cos\psi)} e^{iqDt}\Big) e^{iqr\cos(\psi-\theta)} dq d\psi
\end{aligned}
\tag{2.94}
$$

The expressions for the velocities are highly similar to those for the free surface elevation, (2.90) and (2.91), with the addition of the terms in the square brackets and the $\cos\psi$ or $\sin\psi$, if any, in front of the brackets. Again, $u_{_{Fr}}$, $v_{_{Fr}}$, and $w_{_{Fr}}$ are direct responses to the landslide – they move with the landslide and do not change

shape.

We observe that discontinuities exist in the solutions when $D(\mu q) = \pm Fr \cos\psi$. Since $0 < D \leq 1$ and $-1 \leq \cos\psi \leq 1$, discontinuities occur for all Fr. We make the following observations for the three cases separately: $0 < Fr < 1$, $Fr = 1$, and $Fr > 1$. When $0 < Fr < 1$, the landslide moves slower than the fastest (and the longest) water wave, which propagates at a speed of one. However, the landslide moves at the same speed as the wave component that travels at the speed $D(\mu q) = \pm Fr \cos\psi$. In this case, the discontinuities in (2.90) and (2.91) can be shown using the same analysis discussed in the 1DH case to be integrable, resulting in zero contribution. Since the waves do not grow indefinitely in time, resonance does not occur for $0 < Fr < 1$. For $Fr = 1$, the landslide moves at the same speed as the fastest water wave, and resonance occurs in the $\theta = 0$ direction. For $Fr > 1$, discontinuities still exist as $D(\mu q) = \pm Fr \cos\psi$ is possible due to the $\cos\psi$ term (which is absent in the 1DH case). In this study, we consider only the case $0 < Fr < 1$. The other two cares are left for future studies.

Lastly, we note that if a 1DH landslide forcing function is used, i.e., $B(x, y, t) = B(x, t)$, the Fourier transformed function becomes $\widetilde{\overline{B}} = \overline{B}\delta(l)\sqrt{2\pi}$, where $\delta(l)$ is the Dirac delta function, and the 1DH solutions for landslide-generated waves can be recovered.

2.6.1 Integral-form solutions in the near field

While simplified solutions can be obtained in the far field (far away from the origin and the landslide; to be shown in the next section), solutions in the near field (near the origin or the landslide) cannot be simplified, and the integral-form solutions,

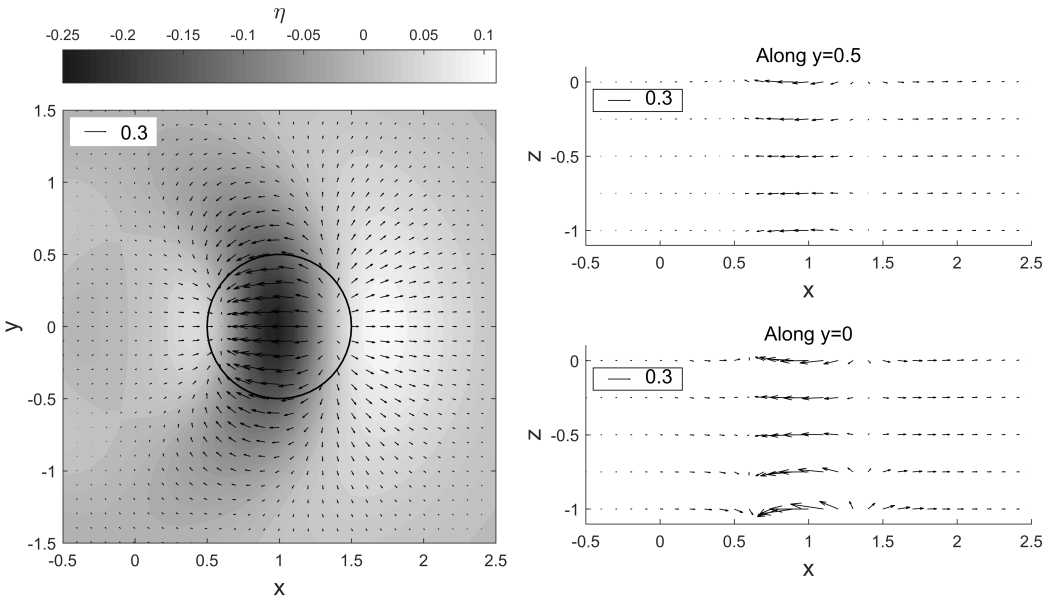

Figure 2.18: Free surface elevation and flow velocity based on the numerically evaluated complete integral-form LFD solutions, plotted near the landslide of shape $B_0(r) = e^{-8r^2}$, $Fr = 0.5$, $\mu = 0.3$, at $t = 2$. The horizontal velocity solutions on the still water surface, $z = 0$, are shown in the left panel. The landslide location is marked as a circle with a diameter of one characteristic landslide length.

i.e., (2.90)-(2.94), must be computed numerically. In this section, we will plot and discuss the solutions in the near field. We again use the Gaussian-shaped landslide with $Fr = 0.5$ and $\mu = 0.3$ as an example, and plot both the free surface solutions and the velocity solutions near the landslide at $t = 2$ in figure 2.18.

We see that the flow velocity appears to vary noticeably in depth near the landslide. Away from the landslide, the vertical distribution of the velocities becomes more and more uniform. A dipole structure can be observed in the vertical velocities near the landslide – a source along $z = -1$ seems to exist in front of the landslide, e.g., near $(x, y, z) = (1.3, 0, -1)$, and a sink seems to exist behind the landslide, e.g., near $(x, y, z) = (0.7, 0, -1)$. At these locations, the vertical velocity on the still water surface, $z = 0$, has an opposite sign to that at $z = -1$, and somewhere in mid-depth the vertical velocity is zero.

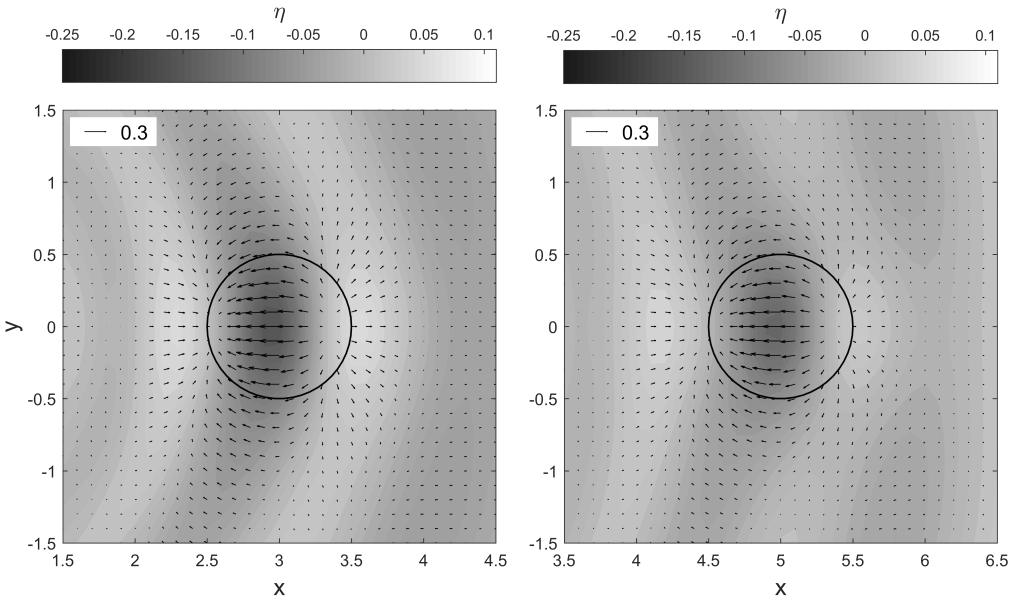

Figure 2.19: Free surface elevation and horizontal flow velocity on the still water surface, $z = 0$, based on the numerically evaluated complete integral-form LFD solutions, plotted near the landslide of shape $B_0(r) = e^{-8r^2}$, $Fr = 0.5$, $\mu = 0.3$. The landslide location is marked as a circle with a diameter of one characteristic landslide length. Left panel: $t = 6$; right panel: $t = 10$.

As t increases, we expect the steady-state trapped-wave solutions to separate from the transient free-wave solutions and dominate the near-field solutions. To see how the solutions near the landslide evolve in time, in figure 2.19 we plot the free surface elevation and the horizontal flow velocity on the still water surface, $z = 0$, at $t = 6, 10$. Although the velocity vectors at different instants differ slightly, the overall characteristics of the velocity field near the landslide, as well as those of the free surface elevation, remain highly identical, and appear to converge to the steady-state trapped-wave solutions as time increases, i.e., as the transient free-wave solutions become more and more separated from the steady-state trapped-wave solutions.

Since the steady-state trapped-wave solutions are direct responses to the landslide, they are highly dependent on the landslide shape. For instance, the dipole

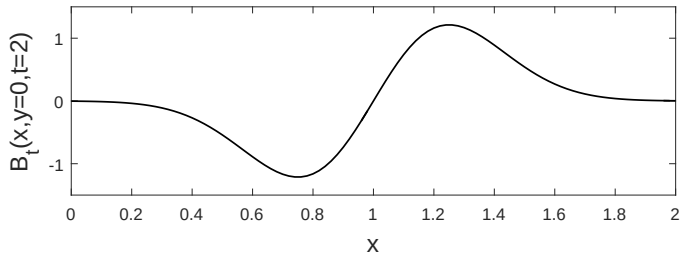

Figure 2.20: Plot of $B_t(x, y, t) = 16Fr(x - Fr \cdot t)e^{-8(x-Fr\cdot t)^2}e^{-8y^2}$ as a function of x, for $y = 0$, $t = 2$, and $Fr = 0.5$.

structure observed in figure 2.18 is a direct outcome of the choice of the landslide shape. We recall that the bottom boundary condition was specified in (2.75) as

$$\phi_z = w = \mu^2 B_t, \quad z = -1. \tag{2.95}$$

Therefore, the vertical velocity at $z = -1$ is always exactly $\mu^2 B_t$. The dipole structure observed in figure 2.18 simply reflects the characteristics of B_t – for the Gaussian-shaped landslide used in the example,

$$B(x, y, t) = e^{-8(x-Fr\cdot t)^2}e^{-8y^2}, \quad B_t(x, y, t) = 16Fr(x - Fr \cdot t)e^{-8(x-Fr\cdot t)^2}e^{-8y^2}. \tag{2.96}$$

In figure 2.20, B_t is plotted as a function of x, for $(y, t, Fr) = (0, 2, 0.5)$. The dipole structure can be clearly seen in the figure. Obviously, if a different landslide shape is used, B_t and thus the pattern of the vertical velocities may be very different. We note that although the steady-state trapped-wave components cannot be further simplified and always depend on the landslide shape, they do not evolve in time (other than the translation in the x direction). Therefore, they only need to be computed once in any given example.

The trapped wave that follows the landslide (which travels at a speed of Fr) is essentially the same as a uniform flow (which has a uniform speed of Fr) over a submerged bump, if the frame of reference is changed. In a 1DH open channel flow,

depending on the Froude number, the free surface on top of the bump (landslide) is a depression for a low $0 < Fr < 1$, a "hydraulic-jump-like" solution (since hydraulic jumps do not actually occur in linear theory) for a high $0 < Fr < 1$, or an elevation for a supercritical $Fr > 1$. We expect similar features to show in the 2DH problem. The vertical velocity of the flow on the still water surface, $z = 0$, responds to the rate of change of the surface elevation, due to the kinematic boundary condition on the free surface, specified in (2.75):

$$\phi_z = w = \mu^2 \eta_t, \quad z = 0. \tag{2.97}$$

Therefore, the reversal of the sign of the vertical velocities, seen in figure 2.18, is Froude number dependent, and is directly related to how the water surface responds to the landslide.

To illustrate how the free surface elevation and the velocity structure near the landslide change in 2DH with respect to Fr, in figure 2.21 we plot the numerically evaluated complete LFD solutions along $y = 0$ at $t = 10$, for the same Gaussian landslide example with $\mu = 0.3$. To exaggerate the features of the solutions, a fairly large $\epsilon = 0.3$ is used to scale the landslide and free surface elevation in the figure. It can be seen that, overall, the solutions behave expectedly as Fr changes, and that the vertical velocities at $z = 0$ indeed depend on how the free surface evolves. The reversal of the sign of the vertical velocities, observed for $Fr = 0.25, 0.5, 0.75$, does not occur for $Fr = 1.5$.

2.6.2 Far-field asymptotic solutions

In the far field (far away from the origin and the landslide), asymptotic solutions can be sought to reduce the complexity of the integral-form solutions and increase

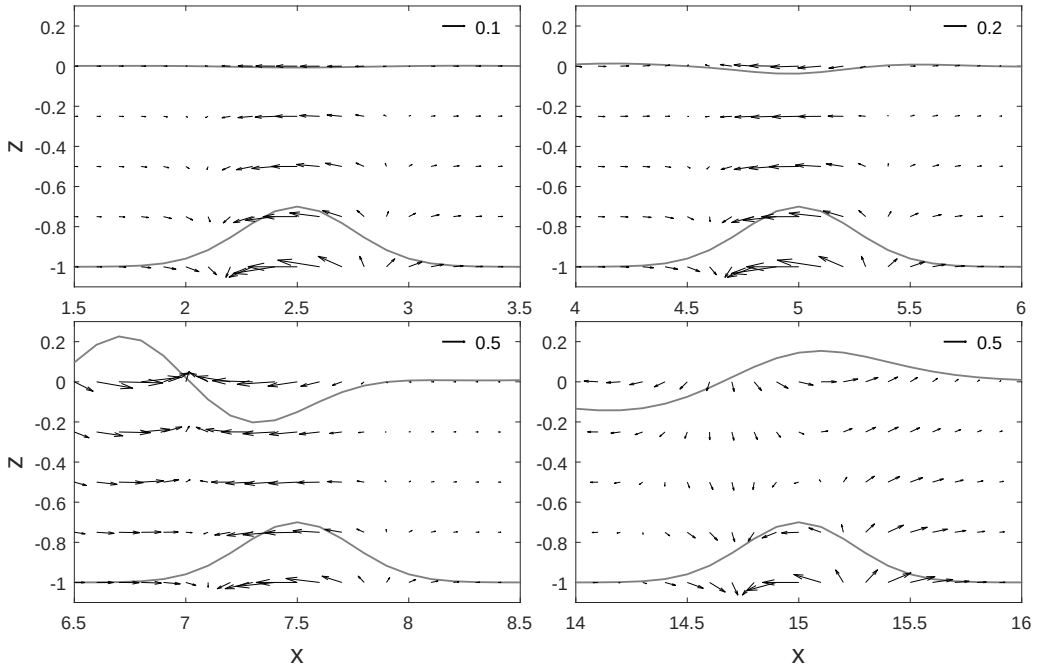

Figure 2.21: Free surface elevation and flow velocity based on the numerically evaluated 2DH integral-form LFD solutions, plotted along $y = 0$ and near the landslide at $t = 10$, for a Gaussian-shaped landslide with $B_0(r) = e^{-8r^2}$ and $\mu = 0.3$. To exaggerate the features of the solutions, a fairly large $\epsilon = 0.3$ is used to plot the landslide and the free surface elevation. Top left: $Fr = 0.25$; top right: $Fr = 0.5$; bottom left: $Fr = 0.75$; bottom right: $Fr = 1.5$.

their usability. For $0 < Fr < 1$, the free wave, η_+, eventually separates from the trapped wave η_{Fr} to become the leading wave. Hence, it is sufficient to consider only η_+ in the far-field solution. For large r, the stationary phase approximation can be applied to the ψ-integral in (2.91). The phase function $q\cos(\psi - \theta)$ has stationary points at $\psi_0 = n\pi + \theta$, where n is an integer. For easier application of the stationary phase approximation, we shift the integration limits for ψ to the left by some small distance so that $\psi_0 = \theta, \pi + \theta$ are the two stationary points contained in the interval (this is permissible as the integrand is periodic in ψ with a period of 2π). The main contributions to the integral then come from the vicinity

of $\psi = \theta$ and $\psi = \pi + \theta$, and the ψ-integrals can be approximated for large r as

$$\begin{aligned}
\eta_+ \;\simeq\; & -\frac{1}{\sqrt{2\pi}} r^{-\frac{1}{2}} \int_0^\infty \frac{\widetilde{\overline{B_0}}(q,\pi+\theta)}{\cosh(\mu q)} \frac{Fr\cos\theta}{2(D+Fr\cos\theta)} q^{\frac{1}{2}} e^{-i\left(q(r+Dt)-\frac{\pi}{4}\right)} dq \\
& + \frac{1}{\sqrt{2\pi}} r^{-\frac{1}{2}} \int_0^\infty \frac{\widetilde{\overline{B_0}}(q,\theta)}{\cosh(\mu q)} \frac{Fr\cos\theta}{2(D-Fr\cos\theta)} q^{\frac{1}{2}} e^{i\left(q(r-Dt)-\frac{\pi}{4}\right)} dq \\
& + \frac{1}{\sqrt{2\pi}} r^{-\frac{1}{2}} \int_0^\infty \frac{\widetilde{\overline{B_0}}(q,\pi+\theta)}{\cosh(\mu q)} \frac{Fr\cos\theta}{2(D-Fr\cos\theta)} q^{\frac{1}{2}} e^{-i\left(q(r-Dt)-\frac{\pi}{4}\right)} dq \\
& - \frac{1}{\sqrt{2\pi}} r^{-\frac{1}{2}} \int_0^\infty \frac{\widetilde{\overline{B_0}}(q,\theta)}{\cosh(\mu q)} \frac{Fr\cos\theta}{2(D+Fr\cos\theta)} q^{\frac{1}{2}} e^{i\left(q(r+Dt)-\frac{\pi}{4}\right)} dq
\end{aligned} \tag{2.98}$$

Since $t > 0$ is required in our problem and r has to be large for the above approximation to be valid, $(r + Dt)$ is always large as well. As a result, the two integrals with $(r + Dt)$ in the exponential functions in (2.98) vanish quickly due to fast-oscillating integrands. On the other hand, $(r - Dt)$ can remain small for large r as long as $Dt \simeq r$ (when the waves are given a sufficiently large time t to propagate the large distance r). As a result, the two integrals with $(r - Dt)$ in the exponential functions in (2.98) must be kept. For the leading-order solution, the two integrals involving $(r + Dt)$ can be ignored, and we define the far-field solution η_{far}, valid for large r, as

$$\begin{aligned}
\eta_{\text{far}} \;=\; & \frac{1}{\sqrt{2\pi}} r^{-\frac{1}{2}} \int_0^\infty \frac{\widetilde{\overline{B_0}}(q,\theta)}{\cosh(\mu q)} \frac{Fr\cos\theta}{2(D-Fr\cos\theta)} q^{\frac{1}{2}} e^{i\left(q(r-Dt)-\frac{\pi}{4}\right)} dq \\
& + \frac{1}{\sqrt{2\pi}} r^{-\frac{1}{2}} \int_0^\infty \frac{\widetilde{\overline{B_0}}(q,\pi+\theta)}{\cosh(\mu q)} \frac{Fr\cos\theta}{2(D-Fr\cos\theta)} q^{\frac{1}{2}} e^{-i\left(q(r-Dt)-\frac{\pi}{4}\right)} dq
\end{aligned} \tag{2.99}$$

which is an accurate approximation of the exact solution (2.91) for large r and $0 < Fr < 1$. For the purpose of verification, we have also directly computed the integrals involving $(r + Dt)$ and found them to be indeed negligibly small for large r. More details on the stationary phase approximation can be found in many classic textbooks, e.g., Mei (1989) and Bender and Orszag (1999).

Some interesting observations can be made here on the far-field solution (2.99). First, the 2DH far-field solution (2.99) decays in space as $r^{-1/2}$. In addition, the landslide speed Fr shows up as $Fr\cos\theta$, which is the effective landslide speed in a given direction, θ. Lastly, in the vicinity of $\theta = \pm\pi/2$, $\cos\theta \to 0$ and the amplitude of the far-field solution vanishes. Thus, landslide-generated waves have the smallest (if not negligible) amplitude near the y-axis, for a landslide traveling in the x direction from the origin.

A similar asymptotic approximation can be performed on the velocities solutions to obtain the far-field velocities solutions:

$$\begin{aligned} u_{\text{far}} &= \frac{1}{\sqrt{2\pi}} r^{-\frac{1}{2}} \int_0^\infty \frac{\widetilde{\overline{B_0}}(q,\theta)}{\cosh(\mu q)} \frac{Fr\cos\theta}{2(D - Fr\cos\theta)} q^{\frac{1}{2}} \\ &\quad \cos\theta\Big[\frac{1}{D}\cosh(\mu q z) + \mu q D \sinh(\mu q z)\Big] e^{i\left(q(r-Dt)-\frac{\pi}{4}\right)} dq \\ &\quad + \frac{1}{\sqrt{2\pi}} r^{-\frac{1}{2}} \int_0^\infty \frac{\widetilde{\overline{B_0}}(q,\pi+\theta)}{\cosh(\mu q)} \frac{Fr\cos\theta}{2(D - Fr\cos\theta)} q^{\frac{1}{2}} \\ &\quad \cos\theta\Big[\frac{1}{D}\cosh(\mu q z) + \mu q D \sinh(\mu q z)\Big] e^{-i\left(q(r-Dt)-\frac{\pi}{4}\right)} dq \end{aligned}, \tag{2.100}$$

$$\begin{aligned} v_{\text{far}} &= \frac{1}{\sqrt{2\pi}} r^{-\frac{1}{2}} \int_0^\infty \frac{\widetilde{\overline{B_0}}(q,\theta)}{\cosh(\mu q)} \frac{Fr\cos\theta}{2(D - Fr\cos\theta)} q^{\frac{1}{2}} \\ &\quad \sin\theta\Big[\frac{1}{D}\cosh(\mu q z) + \mu q D \sinh(\mu q z)\Big] e^{i\left(q(r-Dt)-\frac{\pi}{4}\right)} dq \\ &\quad + \frac{1}{\sqrt{2\pi}} r^{-\frac{1}{2}} \int_0^\infty \frac{\widetilde{\overline{B_0}}(q,\pi+\theta)}{\cosh(\mu q)} \frac{Fr\cos\theta}{2(D - Fr\cos\theta)} q^{\frac{1}{2}} \\ &\quad \sin\theta\Big[\frac{1}{D}\cosh(\mu q z) + \mu q D \sinh(\mu q z)\Big] e^{-i\left(q(r-Dt)-\frac{\pi}{4}\right)} dq \end{aligned}, \tag{2.101}$$

and

$$\begin{aligned} w_{\text{far}} &= -\frac{i\mu}{\sqrt{2\pi}} r^{-\frac{1}{2}} \int_0^\infty \frac{\widetilde{\overline{B_0}}(q,\theta)}{\cosh(\mu q)} \frac{Fr\cos\theta}{2(D - Fr\cos\theta)} q^{\frac{1}{2}} \\ &\quad \Big[\frac{1}{D}\sinh(\mu q z) + \mu q D \cosh(\mu q z)\Big] e^{i\left(q(r-Dt)-\frac{\pi}{4}\right)} dq \\ &\quad - \frac{i\mu}{\sqrt{2\pi}} r^{-\frac{1}{2}} \int_0^\infty \frac{\widetilde{\overline{B_0}}(q,\pi+\theta)}{\cosh(\mu q)} \frac{Fr\cos\theta}{2(D - Fr\cos\theta)} q^{\frac{1}{2}} \\ &\quad \Big[\frac{1}{D}\sinh(\mu q z) + \mu q D \cosh(\mu q z)\Big] e^{-i\left(q(r-Dt)-\frac{\pi}{4}\right)} dq \end{aligned}. \tag{2.102}$$

The horizontal velocities in the x and y directions can be converted to velocities in the r and θ directions (R and Θ, respectively) by

$$\begin{aligned} R(r,\theta,z,t) &= u(r,\theta,z,t)\cos\theta + v(r,\theta,z,t)\sin\theta \\ \Theta(r,\theta,z,t) &= -u(r,\theta,z,t)\sin\theta + v(r,\theta,z,t)\cos\theta \end{aligned} . \tag{2.103}$$

From (2.100) and (2.101), the far-field velocity solutions in the radial (r) and tangential (θ) directions then become

$$\begin{aligned} R_{\text{far}} \;=\; & \frac{1}{\sqrt{2\pi}} r^{-\frac{1}{2}} \int_0^\infty \frac{\widetilde{\overline{B_0}}(q,\theta)}{\cosh(\mu q)} \frac{Fr\cos\theta}{2(D - Fr\cos\theta)} q^{\frac{1}{2}} \\ & \Big[\frac{1}{D}\cosh(\mu q z) + \mu q D \sinh(\mu q z)\Big] e^{i\left(q(r-Dt)-\frac{\pi}{4}\right)} dq \\ & + \frac{1}{\sqrt{2\pi}} r^{-\frac{1}{2}} \int_0^\infty \frac{\widetilde{\overline{B_0}}(q,\pi+\theta)}{\cosh(\mu q)} \frac{Fr\cos\theta}{2(D - Fr\cos\theta)} q^{\frac{1}{2}} \\ & \Big[\frac{1}{D}\cosh(\mu q z) + \mu q D \sinh(\mu q z)\Big] e^{-i\left(q(r-Dt)-\frac{\pi}{4}\right)} dq \end{aligned} , \tag{2.104}$$

and

$$\Theta_{\text{far}} = 0. \tag{2.105}$$

The results suggest that in the far field, the water waves spread strictly radially, as the tangential velocity is zero.

2.6.3 Far-field leading wave solutions

The far-field solutions still consist of q-integrals that need to be numerically evaluated. The classic approach to obtain the "far-field leading wave solution", as done in the 1DH section and outlined in Mei (1989), can be used to further simplify the solutions. Take the far-field free surface solution, (2.99), for example, for large t and with the assumption that $r = t$, $q = 0$ is a stationary point in the q-integrals. Thus, the stationary phase approximation can be applied again. After applying the stationary phase approximation, expanding $q\big(r - D(\mu q)t\big)$ about $q = 0$, and

retaining the first two non-zero terms, the far-field leading wave solution (accurate for large r, t and near $r = t$) is found to be

$$\begin{aligned}\eta_{\text{lead}} &= \frac{2}{3}(\frac{2}{\mu^2 t})^{\frac{1}{2}}\frac{1}{\sqrt{2\pi}}r^{-\frac{1}{2}}\frac{Fr\cos\theta}{2(1-Fr\cos\theta)}\widetilde{\overline{B_0}}(0,\theta) \\ &\quad \left[e^{-i\frac{\pi}{4}}\int_0^\infty e^{i\left((\frac{2}{\mu^2 t})^{\frac{1}{3}}(r-t)p^{\frac{2}{3}}+\frac{1}{3}p^2\right)}dp + e^{i\frac{\pi}{4}}\int_0^\infty e^{-i\left((\frac{2}{\mu^2 t})^{\frac{1}{3}}(r-t)p^{\frac{2}{3}}+\frac{1}{3}p^2\right)}dp\right],\end{aligned} \tag{2.106}$$

where the substitution $p = (\mu^2 t/2)^{1/2} q^{3/2}$ is used.

Since $q = \sqrt{k^2 + l^2} = 0$ implies $(k, l) = 0$, $\widetilde{\overline{B_0}}(q = 0, \theta)$ is the same as $\widetilde{\overline{B_0}}(k = 0, l = 0)$ and is independent of θ. Writing out the expression fully for $\widetilde{\overline{B_0}}(k = 0, l = 0)$:

$$\begin{aligned}\widetilde{\overline{B_0}}(k=0,l=0) &= \frac{1}{2\pi}\int_{-\infty}^{\infty}\int_{-\infty}^{\infty}B_0(x,y)e^{-i\cdot 0\cdot x}e^{-i\cdot 0\cdot y}dxdy \\ &= \frac{1}{2\pi}\int_{-\infty}^{\infty}\int_{-\infty}^{\infty}B_0(x,y)dxdy\end{aligned}, \tag{2.107}$$

we see that $\widetilde{\overline{B_0}}(k = 0, l = 0)$ is related to the landslide volume V_B by

$$\widetilde{\overline{B_0}}(k=0,l=0) = \frac{V_B}{2\pi}. \tag{2.108}$$

In addition, we note that the p-integrals in (2.106) are functions of $s = (2/\mu^2 t)^{1/3}(r - t)$. Since s is always real in our physical problem, the terms in the square brackets can be simplified. We therefore write the far-field leading wave solution as

$$\eta_{\text{lead}}(r,\theta,t) = \frac{2V_B}{3\sqrt{\pi}}\frac{Fr\cos\theta}{2(1-Fr\cos\theta)}r^{-\frac{1}{2}}(\frac{2}{\mu^2 t})^{\frac{1}{2}}\Omega_1\Big((\frac{2}{\mu^2 t})^{\frac{1}{3}}(r-t)\Big), \tag{2.109}$$

where the function $\Omega_1(s)$ is defined as

$$\Omega_1(s) = \frac{\int_0^\infty \cos\left(sp^{\frac{2}{3}}+\frac{1}{3}p^2\right)dp + \int_0^\infty \sin\left(sp^{\frac{2}{3}}+\frac{1}{3}p^2\right)dp}{2\pi}, \tag{2.110}$$

which accounts for the exact shape of the far-field leading wave solution (2.109). We remark that the role of $\Omega_1(s)$ in the 2DH landslide-generated wave problem is

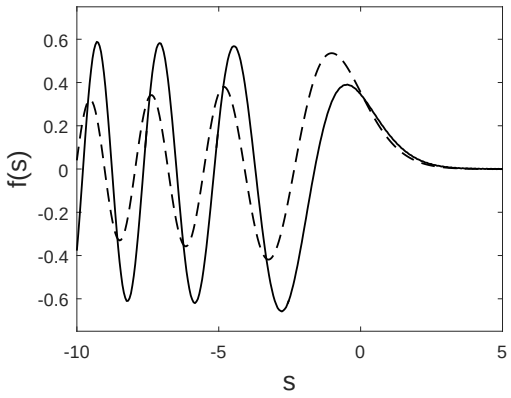

Figure 2.22: Plot of $\Omega_1(s)$ and $Ai(s)$. Solid line: $f(s) = \Omega_1(s)$; dashed line: $f(s) = Ai(s)$.

similar to that of the function $T(p)$ presented in Mei (1989) and Kajiura (1963) for a specific forcing function in the 2DH earthquake-generated wave problem.

In the 1DH LFD far-field leading wave free surface solution, (2.17), the function that accounts for the exact wave shape is the Airy function, defined as

$$Ai(s) = \frac{\int_0^\infty \cos(sp + \frac{1}{3}p^3)dp}{\pi}. \tag{2.111}$$

While the integral representation of the Airy function is well-known, the p-integrals in $\Omega_1(s)$ are not of a common form, and will need to be examined more closely. The two functions are compared in figure 2.22. A main difference between $\Omega_1(s)$ and $Ai(s)$ is that while the leading wave in $Ai(s)$ has the largest amplitude, the trailing waves in $\Omega_1(s)$ each have a larger amplitude than the leading wave. We remark that this analytical finding is in agreement with the observation made by Okal and Synolakis (2016) that the first wave of a tsunami is not always the largest. The leading wave in $\Omega_1(s)$ has a maximum of 0.390 at $s \simeq -0.467$, and the first trailing wave has a maximum of 0.568 at $s \simeq -4.47$. On the other hand, the leading wave in $Ai(s)$ has a maximum of 0.536 at $s \simeq -1.02$, and the first trailing wave has a maximum of 0.380 at $s \simeq -4.83$.

As is the case in 1DH, to the leading order, the far-field leading wave generated by a landslide in 2DH depends only on the landslide volume (or area in 1DH) and not its exact shape, provided that the shape variation does not change the characteristic landslide scales used to normalize the solution. Wave spreading in two horizontal dimensions is accounted for by the addition of $r^{-1/2}$ and $\cos\theta$ in the solution. In addition, the far-field leading wave in 2DH decays as $t^{-1/2}$, whereas that in 1DH decays as $t^{-1/3}$. Due to the term $Fr\cos\theta/2(1 - Fr\cos\theta)$, landslide-generated waves always vanish near $\theta = \pm\pi/2$, i.e., near the y-axis for a landslide moving in the x direction from the origin. While the far-field leading wave solution (2.109) appears simple and universal, the downside is that the trailing waves (where the assumption $r \simeq t$ is not valid) are not captured at all. Thus, little insight on the rest of the wave field can be gained without numerically evaluating the more representative integral-form solutions (2.89), (2.91), or (2.99).

To graphically examine how quickly the full solution converges to the far-field leading wave solution (2.109), we compare the complete analytical solution (2.89), evaluated numerically, with the far-field leading wave solution (2.109). For a Gaussian-shaped landslide with $Fr = 0.5$ and $\mu = 0.3$, the complete wave fields at $t = 2, 6, 10$ are shown in figure 2.23. Even though the far-field leading wave solutions is theoretically accurate only for large r, t and near $r = t$, and has a discontinuity at the origin (resulting in very large amplitudes near the origin), they are nevertheless plotted over the whole domain in figure 2.23. Qualitatively, in figure 2.23, the far-field leading wave solutions appear to capture the key characteristics of the wave field satisfactorily. Taking a closer look, we plot the wave profiles along the line $x = y$ in figure 2.24. The discrepancy can now be seen clearly: while the leading wave near $r = t$ quickly converges to the far-field leading wave solution, the trailing waves do not. Hence, consistent with the asymptotic approximations

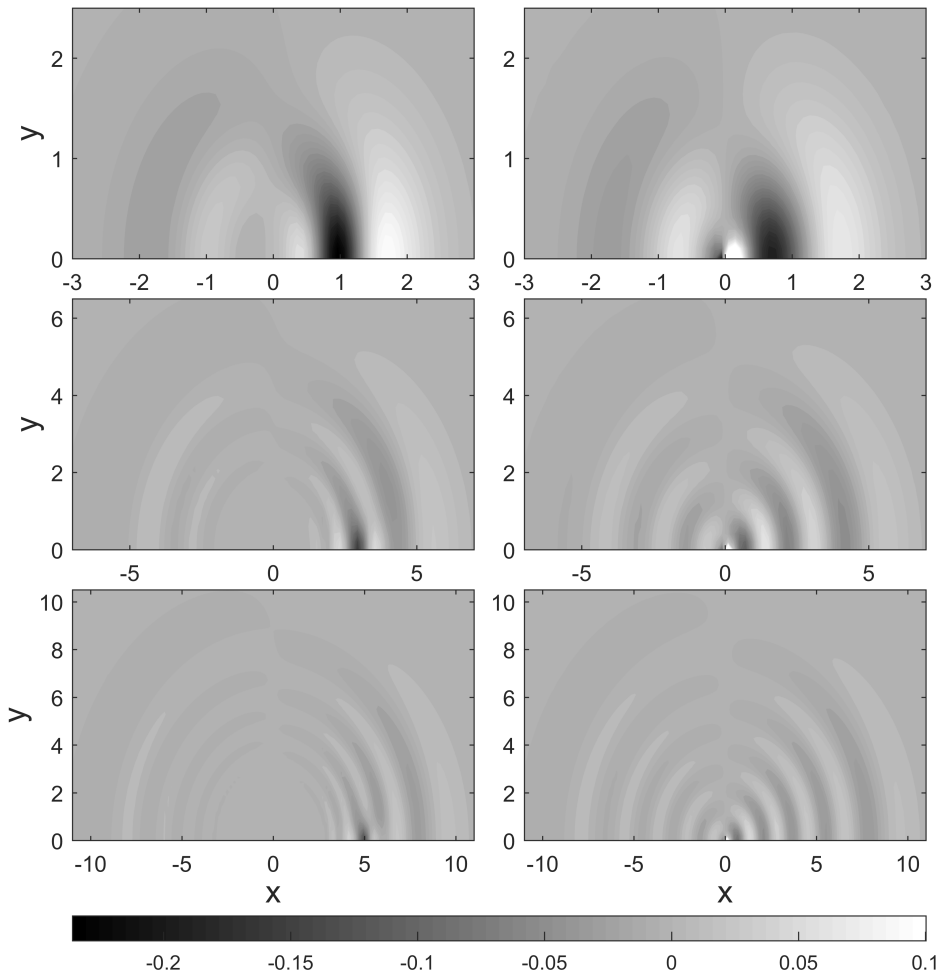

Figure 2.23: Free surface elevation predicted by LFD due to a landslide of shape $B_0(r) = e^{-8r^2}$, $Fr = 0.5$, $\mu = 0.3$. The wave field is symmetric about the x-axis. Top row: $t = 2$, and the landslide is centered at $(1, 0)$; middle row: $t = 6$, and the landslide is centered at $(3, 0)$; bottom row: $t = 10$, and the landslide is centered at $(5, 0)$. Left column: complete analytical solution (2.89); right column: far-field leading wave solution (2.109) which is valid only for large r, t and near $r = t$, and approaches infinity near the origin.

made in the solution process, the closed-form far-field leading wave solution (2.109) is valid only near the leading wave $r = t$ for large r, t; in this example, $r \simeq t = 6$ appears to be sufficiently large.

Likewise, the velocity solutions for the far-field leading wave can also be derived

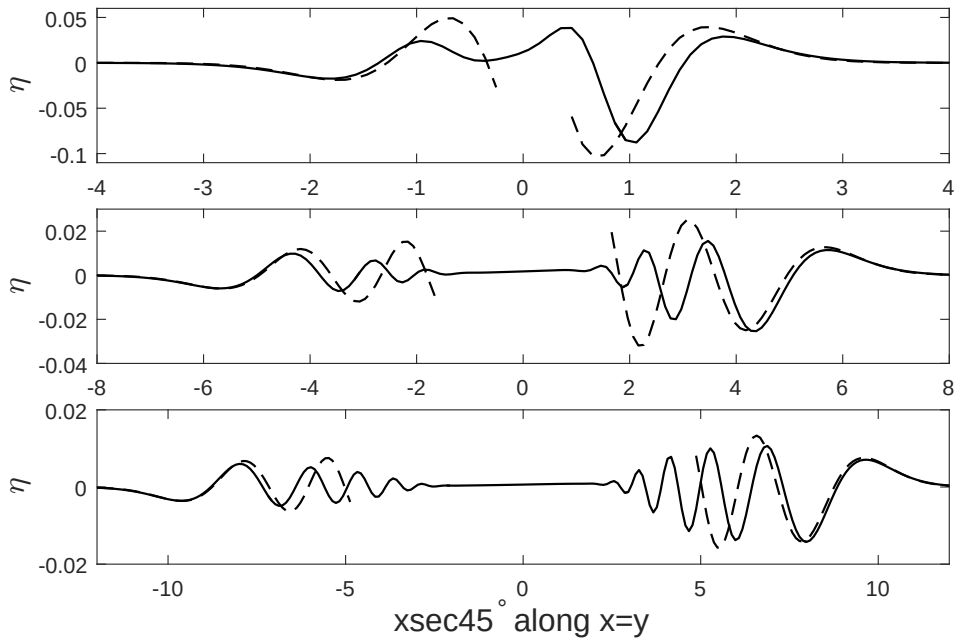

Figure 2.24: Wave profiles along $x = y$ predicted by LFD due to a landslide of shape $B_0(r) = e^{-8r^2}$, $Fr = 0.5$, $\mu = 0.3$. Top panel: $t = 2$; middle panel: $t = 6$; bottom panel: $t = 10$. Solid line: complete analytical solution (2.89); dashed line: far-field leading wave solution (2.109) plotted only near the leading wave.

from the far-field solutions, (2.100)-(2.102), and the results are

$$u_{\text{lead}}(r,\theta,t) = \eta_{\text{lead}}(r,\theta,t)\cos\theta,\ \ v_{\text{lead}}(r,\theta,t) = \eta_{\text{lead}}(r,\theta,t)\sin\theta,\ \ w_{\text{lead}}(r,\theta,t) = 0, \tag{2.112}$$

where the expression for η_{lead} has been given in (2.109). Since the longest wave corresponding to $q = 0$ travels the fastest to become the leading wave, the far-field leading waves are long waves. Consistent with the characteristics of long waves, the far-field leading wave solutions (2.112) show no depth variation in the horizontal velocities (i.e., u_{lead} and v_{lead} do not depend on z), and no vertical velocity ($w_{\text{lead}} = 0$), which result from taking the limit as $q \to 0$ in the far-field leading wave approximation.

When the horizontal velocities are expressed in the radial (r) and tangential

(θ) directions, related by

$$\begin{aligned} R_{\text{lead}}(r,\theta,z,t) &= u_{\text{lead}}(r,\theta,z,t)\cos\theta + v_{\text{lead}}(r,\theta,z,t)\sin\theta \\ \Theta_{\text{lead}}(r,\theta,z,t) &= -u_{\text{lead}}(r,\theta,z,t)\sin\theta + v_{\text{lead}}(r,\theta,z,t)\cos\theta \end{aligned}, \tag{2.113}$$

the far-field leading wave velocity solutions become even more concise:

$$R_{\text{lead}}(r,\theta,t) = \eta_{\text{lead}}(r,\theta,t), \quad \Theta_{\text{lead}}(r,\theta,t) = 0, \quad w_{\text{lead}}(r,\theta,t) = 0. \tag{2.114}$$

To see how well the far-field leading wave velocity solutions (2.114) compare with the complete integral-form solutions (2.92)-(2.94), the solutions are compared in figure 2.25 for the same Gaussian landslide example. It can be seen that, qualitatively, the far-field leading wave solutions indeed agree with the complete solutions, in the far field (large r) and near the leading wave (near $r = t$). We have shown that in the far field (large r), the horizontal velocity in the tangential (θ) direction is zero – this finding can be observed in the complete velocity solutions plotted in figure 2.25.

2.7 2DH linear shallow water wave equations in constant depth

In dispersive wave theory, closed-form analytical expressions are available only for the far-field leading wave, i.e., for large r, t and near $r = t$. In the shallow water limit, $\mu \to 0$, the LFD solutions reduce to the LSWE solutions, and closed-form analytical expressions can be found for the entire far field, i.e., for large r. The shallow water solutions are useful as they are always simpler than the dispersive solutions, and can be seen as the most basic wave solutions. However, due to the lack of frequency dispersion, the shallow water solutions always depend on the

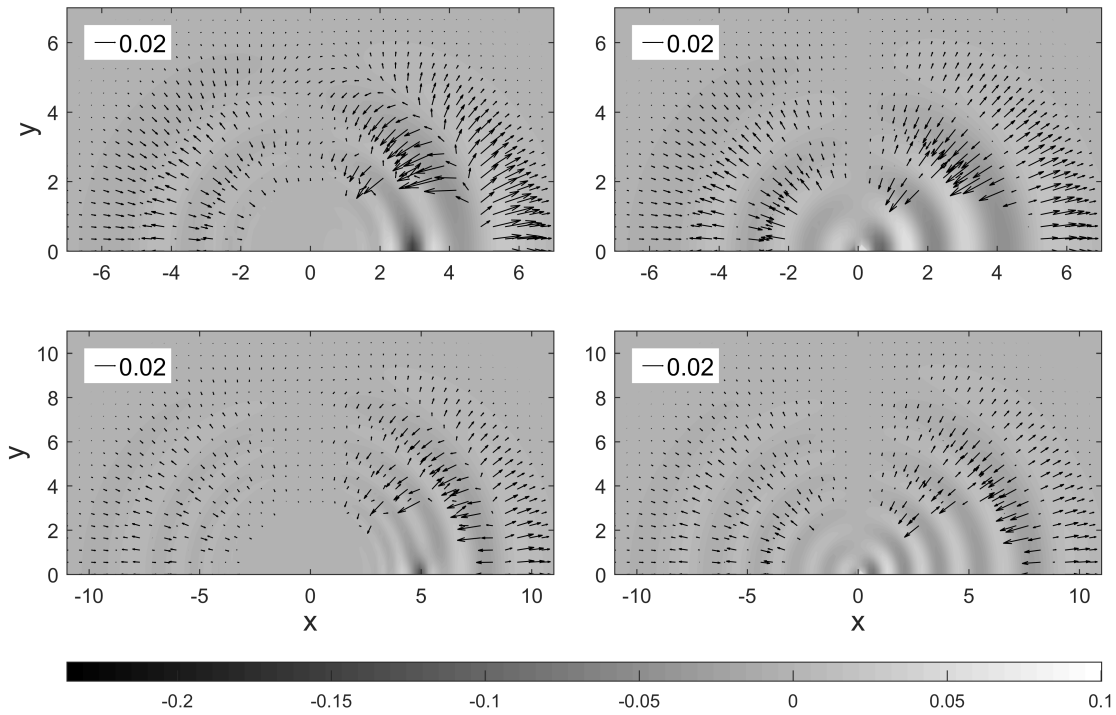

Figure 2.25: Horizontal flow velocity predicted by LFD due to a landslide of shape $B_0(r) = e^{-8r^2}$, $Fr = 0.5$, $\mu = 0.3$. The free surface elevation from figure 2.23 is shown in the background. The solutions are symmetric about the x-axis. Velocities are not shown near the landslide or the origin, where the far-field leading wave solutions are not valid. Top row: $t = 6$; bottom row: $t = 10$. Left column: complete analytical solutions (2.92) and (2.93) on the still water surface, $z = 0$; right column: far-field leading wave solutions (2.112).

exact landslide shape, and the far-field leading wave solution (2.109) based on dispersive theory, can never be reached. For the landslide-generated wave problem, the shallow water solution can be found by taking the limit as $\mu \to 0$ (which corresponds to a infinitely long landslide length in finite water depth) in the dispersive solution (2.99), or solving LSWE directly.

Taking the limit of (2.99) as $\mu \to 0$, we obtain

$$\begin{aligned}\eta_{\text{far}} \quad = \quad & \frac{1}{\sqrt{2\pi}} r^{-\frac{1}{2}} \frac{Fr\cos\theta}{2(1-Fr\cos\theta)} \int_0^\infty \widetilde{\overline{B_0}}(q,\theta) q^{\frac{1}{2}} e^{\,i\left(q(r-t)-\frac{\pi}{4}\right)} dq \\ & + \frac{1}{\sqrt{2\pi}} r^{-\frac{1}{2}} \frac{Fr\cos\theta}{2(1-Fr\cos\theta)} \int_0^\infty \widetilde{\overline{B_0}}(q,\pi+\theta) q^{\frac{1}{2}} e^{\,-i\left(q(r-t)-\frac{\pi}{4}\right)} dq \end{aligned} \quad . \tag{2.115}$$

The integrands are simpler in this case and closed-form expressions are available for specific landslide shape functions B_0.

The LSWE solutions can also be derived directly from the governing equations, LSWE. Here we quickly describe the solution steps. Dimensionally, the 2DH LSWE admitting a landslide forcing function $B'(x', y', t')$ reads

$$\begin{aligned} &\eta'_{t'} + (u'h')_{x'} + (v'h')_{y'} = B'_{t'} \\ &u'_{t'} = -g\eta'_{x'}, \quad v'_{t'} = -g\eta'_{y'} \end{aligned}, \tag{2.116}$$

where u' is the flow velocity in the x' direction, v' is that in the y' direction, h' is the still water depth, and g is the gravitational acceleration. In constant water depth, the normalized water depth is one. With the normalization $(x, y) = (x', y')/L$, $(\eta, B) = (\eta', B')/A$, $t = t'/\sqrt{L/(gd)}$, and $(u, v) = (u', v')/\epsilon\sqrt{gd}$, where A is the characteristic wave amplitude, L is the characteristic wavelength, d is the constant water depth, and $\epsilon = A/d$, the dimensionless LSWE in constant water depth reads

$$\begin{aligned} &\eta_t + u_x + v_y = B_t \\ &u_t = -\eta_x, \quad v_t = -\eta_y \end{aligned}. \tag{2.117}$$

The three equations can be combined into one:

$$\eta_{tt} - \eta_{xx} - \eta_{yy} = B_{tt}. \tag{2.118}$$

After applying the Laplace transform (in t) and the double Fourier transform (in x and y) and imposing the initial conditions $\eta(x, y, 0) = 0$ and $u_x(x, y, 0) + v_y(x, y, 0) = 0$, we obtain the transformed solution

$$\dddot{\tilde{\eta}} = \frac{s^2\dddot{\tilde{B}} - s\widetilde{B(x, y, 0)}}{s^2 + k^2 + l^2}. \tag{2.119}$$

From this point forth the solution approach is exactly the same as that for LFD, and closed-form inverse Laplace transform of $\dddot{\tilde{\eta}}$ is available for landslide-generated

waves. The solutions based on LSWE can be shown to be exactly the same as those based on LFD in the shallow water limit $\mu \to 0$.

The velocity solutions can be recovered from the dimensionless momentum equations in (2.117), or by taking the limit $\mu \to 0$ of the LFD velocity solutions. The exact initial velocities, $u(x, y, 0)$ and $v(x, y, 0)$, can be further specified only when the velocity solutions are recovered, from the momentum equations in (2.117), as

$$u(x, y, t) = u(x, y, 0) - \int_0^t \eta_x dt, \quad v(x, y, t) = v(x, y, 0) - \int_0^t \eta_y dt. \tag{2.120}$$

For initially quiescent water, we require $u(x, y, 0) = v(x, y, 0) = 0$.

2.7.1 Radially symmetric landslide

Here we consider a radially symmetric landslide shape function where $B_0(x, y) = B_0(r)$. $\widetilde{\overline{B_0}}$ can then be simplified to

$$\begin{aligned}
\widetilde{\overline{B_0}} &= \frac{1}{2\pi} \int_{-\infty}^{\infty} \int_{-\infty}^{\infty} B_0(x, y) e^{-ikx} e^{-ily} dx dy = \frac{1}{2\pi} \int_0^{\infty} \int_0^{2\pi} B_0(r) e^{-iqr\cos(\theta-\psi)} r d\theta dr \\
&= \frac{1}{2\pi} \int_0^{\infty} B_0(r) r \int_0^{2\pi} e^{-iqr\cos(\theta-\psi)} d\theta dr = \frac{1}{2\pi} \int_0^{\infty} B_0(r) r \int_0^{2\pi} e^{-iqr\cos\alpha} d\alpha dr \\
&= \int_0^{\infty} B_0(r) r J_0(qr) dr = \mathcal{H}_0\{B_0(r)\},
\end{aligned} \tag{2.121}$$

where $J_n(s)$ is the order-n Bessel function of the first kind and $\mathcal{H}_n\{f\}$ denotes the order-n Hankel transform of the function f. The expression for the Bessel's integral $J_0(qr) = \int_0^{2\pi} e^{-iqr\cos\alpha} d\alpha/2\pi$ is used in the above equation.

For a real-valued landslide shape function B_0, $\mathcal{H}_0(B_0)$ is also real. The far-field

solution (2.115) can then be simplified for a radially symmetric landslide as

$$\eta_{\text{far}} = \frac{1}{\sqrt{\pi}} \frac{Fr\cos\theta}{2(1-Fr\cos\theta)} r^{-\frac{1}{2}} \int_0^\infty \mathcal{H}_0\{B_0\} q^{\frac{1}{2}} \left(\cos\Big(q(r-t)\Big) + \sin\Big(q(r-t)\Big) \right) dq. \tag{2.122}$$

The q-integral in the equation above can be evaluated in closed-form for a Gaussian landslide shape. To illustrate this, we have chosen a Gaussian curve whose characteristic length is four times its standard deviation:

$$B_0(r) = e^{-8r^2}, \quad \widetilde{B_0} = \mathcal{H}_0(B_0) = \frac{1}{16} e^{-\frac{q^2}{32}}. \tag{2.123}$$

The far-field solution (2.122) then becomes

$$\eta_{\text{far}}(r,\theta,t) = \sqrt{\pi} \frac{Fr\cos\theta}{2(1-Fr\cos\theta)} r^{-\frac{1}{2}} \Omega_2(r-t). \tag{2.124}$$

The function $\Omega_2(r-t) = \Omega_2(s)$ is a function of one variable only, and is the only term that accounts for the exact wave shape in (2.124):

$$\Omega_2(s) = |s|^{\frac{3}{2}} e^{-4s^2} \left[I_{\frac{5}{4}}\big(4s^2\big) - I_{\frac{1}{4}}\big(4s^2\big) + \frac{1}{8s^2} I_{\frac{1}{4}}\big(4s^2\big) + \text{sgn}(s)\Big(I_{-\frac{1}{4}}\big(4s^2\big) - I_{\frac{3}{4}}\big(4s^2\big) \Big) \right], \tag{2.125}$$

where $I_n(s)$ is the modified Bessel function of the first kind of order n, and $\text{sgn}(s)$ returns the sign (± 1) of s. $\Omega_2(s)$ is plotted in figure 2.26. We see that $\Omega_2(s)$ has a maximum of 0.213 at $s \simeq 0.138$, and a minimum of -0.0979 at $s \simeq -0.437$.

To see how quickly the full solution converges to the far-field solution, we compare the far-field solution with the numerical solution, obtained by numerically solving LSWE. The numerical solver will be discussed in detail in Chapter 3. For a Gaussian-shaped landslide with $Fr = 0.5$, the wave fields are compared in figure 2.27 at $t = 2, 6, 10$. Since LSWE is not frequency dispersive, the two-wave structure consisting of the transient free wave, η_+, and the trapped wave, η_{Fr}, which follows the landslide, is clearly visible in the figure. A closer comparison along the line

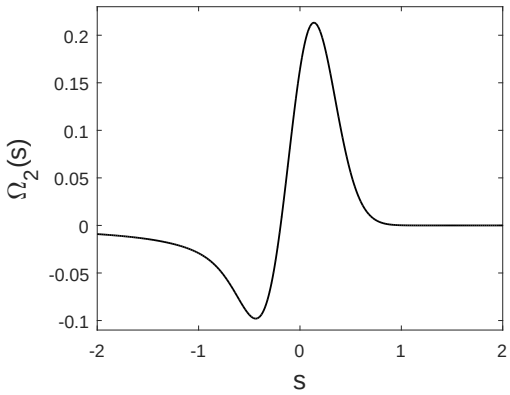

Figure 2.26: Plot of $\Omega_2(s)$ in (2.124).

$x = y$ is shown in figure 2.28. It can be seen that the far-field solution quickly becomes accurate for $r \gtrsim 6$.

The far-field velocity solutions, valid for large r, can be found by taking the limit of (2.100) and (2.101) as $\mu \to 0$, to be

$$u_{\text{far}}(r,\theta,t) = \eta_{\text{far}}(r,\theta,t)\cos\theta, \quad v_{\text{far}}(r,\theta,t) = \eta_{\text{far}}(r,\theta,t)\sin\theta. \tag{2.126}$$

Or, expressed in the radial and tangential directions:

$$R_{\text{far}}(r,\theta,t) = \eta_{\text{far}}(r,\theta,t), \quad \Theta_{\text{far}}(r,\theta,t) = 0. \tag{2.127}$$

2.7.2 Antisymmetric landslide

Here we consider an antisymmetric landslide shape function, $B_0(r,\theta) = b_0(r)\cos\theta$. The transformation then becomes

$$\begin{aligned}\widetilde{B_0} &= \frac{1}{2\pi}\int_0^\infty b_0(r) r \int_0^{2\pi} \cos\theta e^{-iqr\cos(\theta-\psi)} d\theta dr \\ &= \frac{1}{2\pi}\int_0^\infty b_0(r) r \int_0^{2\pi} \cos(\alpha+\psi) e^{-iqr\cos\alpha} d\alpha dr \\ &= -i\cos\psi \int_0^\infty b_0(r) r J_1(qr) dr = -i\cos\psi \mathcal{H}_1\{b_0\},\end{aligned} \tag{2.128}$$

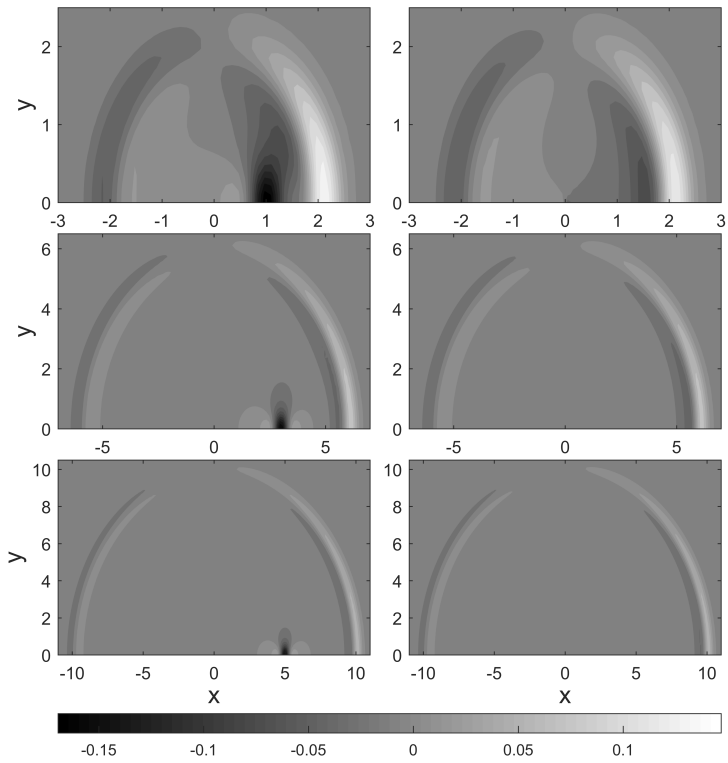

Figure 2.27: Free surface elevation predicted by LSWE due to a landslide of shape $B_0(r) = e^{-8r^2}$, $Fr = 0.5$. The wave field is symmetric about the x-axis. Top row: $t = 2$; middle row: $t = 6$; bottom row: $t = 10$. Left column: direct numerical solution; right column: far-field solution (2.124), which is valid for large r and has a discontinuity at the origin.

where trigonometric identity and Bessel's integral are used to obtain the expression. For a real-valued landslide shape function $B_0 = b_0 \cos\theta$, $\mathcal{H}_1(b_0)$ is also real. The far-field solution (2.115) can then be simplified to be

$$\eta_{\text{far}} = \frac{1}{\sqrt{\pi}} \frac{Fr\cos\theta}{2(1 - Fr\cos\theta)} r^{-\frac{1}{2}} \cos\theta \int_0^\infty \mathcal{H}_1\{b_0\} q^{\frac{1}{2}} \left(\sin\Big(q(r-t)\Big) - \cos\Big(q(r-t)\Big) \right) dq \,. \tag{2.129}$$

A similar procedure can be performed for $B_0(r, \theta) = b_0(r) \sin\theta$, in which case the $\cos\theta$ in (2.129) is replaced with $\sin\theta$.

No closed-form order-one Hankel transform is available for $b_0(r) = e^{-8r^2}$, which in the landslide-generated wave context would correspond to a severely warped

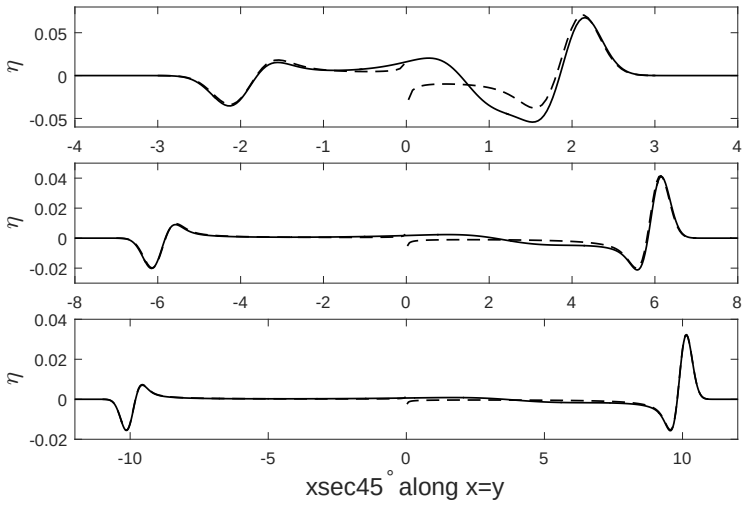

Figure 2.28: Wave profile along $x = y$ predicted by LSWE due to a landslide of shape $B_0(r) = e^{-8r^2}$, $Fr = 0.5$. Top panel: $t = 2$; middle panel: $t = 6$; bottom panel: $t = 10$. Solid line: direct numerical solution; dashed line: far-field solution (2.124), which is valid for large r and has a discontinuity at the origin.

landslide with a discontinuity at $r = 0$ due to the multiplication with $\cos\theta$ or $\sin\theta$. A closed-form order-one Hankel transform is available for $b_0(r) = 4\sqrt{e}re^{-8r^2}$, however, where $4\sqrt{e}$ is introduced to ensure that the maximum of the landslide function is 1:

$$b_0(r) = 4\sqrt{e}re^{-8r^2}, \quad \mathcal{H}_1\{b_0\} = \mathcal{H}_1\{4\sqrt{e}re^{-8r^2}\} = \frac{\sqrt{e}}{64}qe^{-\frac{q^2}{32}}, \tag{2.130}$$

and the resulting q-integral in (2.129) can be evaluated.

For $B_0(r,\theta) = 4\sqrt{e}re^{-8r^2}\cos\theta$, the far-field solution is

$$\eta_{\text{far}}(r,\theta,t) = \sqrt{\pi}\frac{Fr\cos\theta}{2(1-Fr\cos\theta)}r^{-\frac{1}{2}}\cos\theta\Omega_3(r-t). \tag{2.131}$$

Just like $\Omega_2(s)$, $\Omega_3(r-t) = \Omega_3(s)$ is a function of one variable only, and accounts for the exact wave shape:

$$\begin{aligned}\Omega_3(s) = 4\sqrt{e}|s|^{\frac{5}{2}}e^{-4s^2}\Bigg[&I_{-\frac{1}{4}}\big(4s^2\big) - \frac{1}{16s^2}I_{-\frac{1}{4}}\big(4s^2\big) - I_{\frac{3}{4}}\big(4s^2\big)\\ &+\operatorname{sgn}(s)\Big(I_{\frac{5}{4}}\big(4s^2\big) - I_{\frac{1}{4}}\big(4s^2\big) + \frac{3}{16s^2}I_{\frac{1}{4}}\big(4s^2\big)\Big)\Bigg].\end{aligned} \tag{2.132}$$

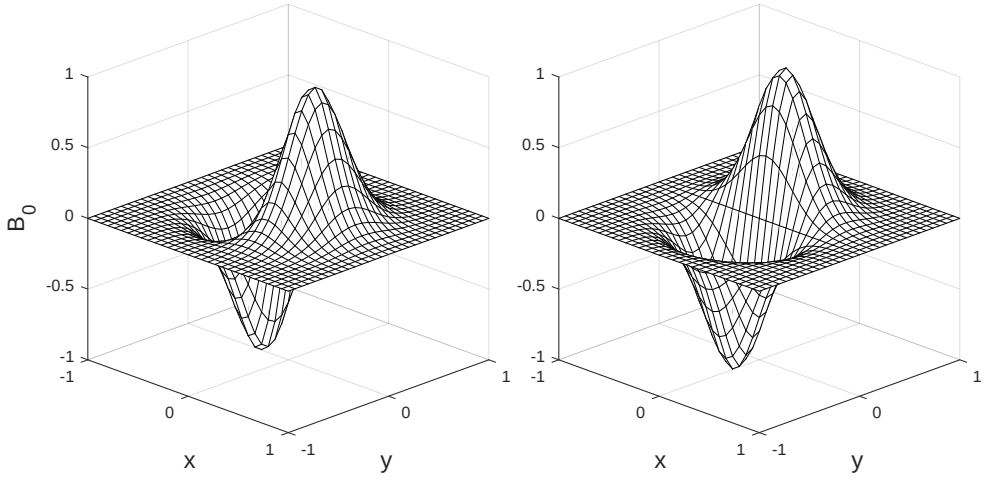

Figure 2.29: Left: $B_0(r,\theta) = 4\sqrt{e}re^{-8r^2}\cos\theta$; right: $B_0(r,\theta) = 4\sqrt{e}re^{-8r^2}\sin\theta$.

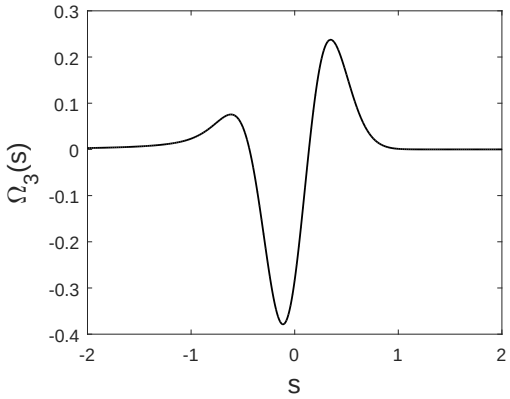

Figure 2.30: Plot of $\Omega_3(s)$ in (2.131) and (2.133).

For $B_0(r,\theta) = 4\sqrt{e}re^{-8r^2}\sin\theta$, the far-field solution is

$$\eta_{\text{far}}(r,\theta,t) = \sqrt{\pi}\frac{Fr\cos\theta}{2(1-Fr\cos\theta)}r^{-\frac{1}{2}}\sin\theta\Omega_3(r-t). \tag{2.133}$$

The two landslide shapes are shown in figure 2.29.

To gain further insight on the wave shape, we need to examine the function $\Omega_3(s)$, which is plotted in figure 2.30. We see that it has a maximum of 0.237 at $s \simeq 0.347$, a minimum of -0.379 at $s \simeq -0.113$, and a local maximum of 0.0756 at $s \simeq -0.615$.

The expressions for the far-field velocities are the same as (2.126) and (2.127), where the corresponding η_{far}, (2.131) or (2.133), should be used.

2.7.3 Landslide aspect ratio

For a specified landslide shape, the shallow water solution can be employed to study the effects of landslide aspect ratio in closed form. Here we consider a double-Gaussian landslide shape

$$B_0(x,y) = e^{-8(\frac{x}{\sqrt{\sigma}})^2} e^{-8(y\sqrt{\sigma})^2} \tag{2.134}$$

defined such that the landslide always has the same enclosed volume as the radially symmetric Gaussian landslide shape $B_0(r) = e^{-8r^2}$ (the special case when $\sigma = 1$). σ is the landslide x-to-y aspect ratio, defined as the ratio of the characteristic landslide length in the x direction to that in the y direction. $\sigma > 1$ means a landslide longer in the x direction and shorter in the y direction, and vice versa for $0 < \sigma < 1$. Fourier transform is available for the double-Gaussian shape:

$$\widetilde{B_0}(k,l) = \frac{1}{16} e^{-\frac{\sigma k^2}{32}} e^{-\frac{l^2}{32\sigma}} = \frac{1}{16} e^{-\frac{1}{32}(\sigma k^2 + \frac{l^2}{\sigma})} = \frac{1}{16} e^{-\frac{1}{32} q^2 (\sigma \cos^2\psi + \frac{1}{\sigma}\sin^2\psi)} = \widetilde{B_0}(q,\psi). \tag{2.135}$$

Following the same solution process, we find the far-field solution (valid for large r) to be

$$\eta_{\text{far}} = \sqrt{\pi} \frac{Fr\cos\theta}{2(1 - Fr\cos\theta)} r^{-\frac{1}{2}} (\sigma\cos^2\theta + \frac{1}{\sigma}\sin^2\theta)^{-\frac{3}{4}} \Omega_2\Big(\frac{r-t}{(\sigma\cos^2\theta + \frac{1}{\sigma}\sin^2\theta)^{\frac{1}{2}}}\Big), \tag{2.136}$$

where the difference from the solution for the radially symmetric Gaussian landslide shape (2.124), effectively the special case when $\sigma = 1$, is the terms involving

$$\nu = \sigma\cos^2\theta + \frac{1}{\sigma}\sin^2\theta. \tag{2.137}$$

Again, the expressions for the far-field velocities, (2.126) and (2.127), still hold.

The landslide aspect ratio σ has two effects: the amplitude of the generated wave is amplified by $\nu^{-3/4}$, and the wavelength is lengthened by $\nu^{1/2}$. The effect on the wavelength is particularly significant as the generated waves now also have different wavelengths in different directions. For the radially symmetric case $\sigma = 1$, $\nu = 1$ always. To study the deviation from the radially symmetric case due to the effects of the landslide aspect ratio, it is of interest to know when ν becomes greater or less than one for $\sigma \neq 1$. Setting $\nu > 1$ for $\sigma \neq 1$, the critical angle can be found:

$$\theta_{crit} = \cos^{-1}\sqrt{\frac{1}{\sigma+1}}, \quad 0 < \theta_{crit} < \frac{\pi}{2}, \quad \text{for } \sigma > 0 \text{ and } \sigma \neq 1, \tag{2.138}$$

defined so that $\nu > 1$, i.e., the wave is lengthened and the amplitude is reduced compared to the radially symmetric case, in the range

$$\begin{cases} -\theta_{crit} < \theta < \theta_{crit}, \quad (\pi - \theta_{crit}) < \theta < (\pi + \theta_{crit}), & \text{for } \sigma > 1 \\ \theta_{crit} < \theta < (\pi - \theta_{crit}), \quad (\pi + \theta_{crit}) < \theta < (2\pi - \theta_{crit}), & \text{for } 0 < \sigma < 1 \end{cases}. \tag{2.139}$$

Therefore, in the range (2.139), the waves generated by a landslide of aspect ratio $\sigma \neq 1$ will have longer wavelengths and smaller amplitudes than those in the radially symmetric case ($\sigma = 1$), and vice versa outside the range. The critical angle (2.138) is plotted as a function of σ in figure 2.31.

In a fixed direction θ, it is possible for two different σ to achieve the same modification factor $\nu = (\sigma \cos^2\theta + \sin^2\theta/\sigma) > 0$. This equation can be solved to yield

$$\sigma = \frac{\nu \pm \sqrt{\nu^2 - 4\cos^2\theta \sin^2\theta}}{2\cos^2\theta}, \tag{2.140}$$

in which only real and positive σ is allowed in our physical problem. For example, to have a wave in the $\theta = \pi/4$ direction with $\nu = 2.125$ so that the wave is $2.125^{-3/4} \simeq 0.568$ times as high and $2.125^{1/2} \simeq 1.458$ times as long as that in

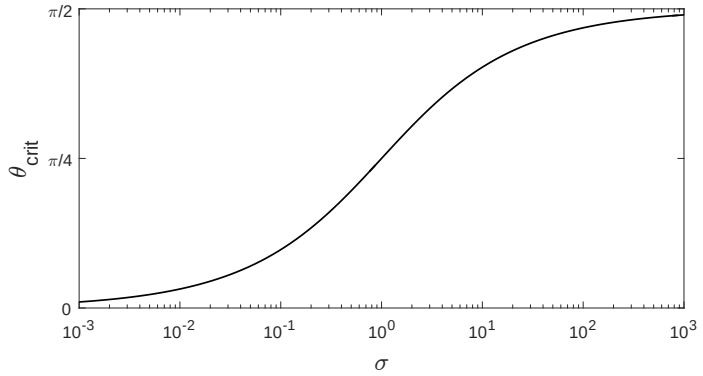

Figure 2.31: The critical angle θ_{crit} (2.138) plotted as a function of the landslide aspect ratio σ, $\sigma \neq 1$.

the radially symmetric case, a landslide of aspect ratio $\sigma = 4$ or $\sigma = 1/4$ can be used. This finding can be found to be also valid in the far-field solution of LFD, by substituting the double-Gaussian landslide shape (2.135) into the far-field solution (2.99).

2.8 2DH linear and weakly dispersive model in constant depth

2DH LWD solutions can also be derived. The dimensionless continuity equation reads

$$\eta_t + u_{\alpha x} + v_{\alpha y} + \alpha_{11}(u_{\alpha xxx} + u_{\alpha xyy} + v_{\alpha yyy} + v_{\alpha xxy}) = B_t + \alpha_{12}(B_{txx} + B_{tyy}), \quad (2.141)$$

and the momentum equations read

$$u_{\alpha t} + \alpha_{21}(u_{\alpha xxt} + v_{\alpha xyt}) + \eta_x = \alpha_{22} B_{xtt}, \quad v_{\alpha t} + \alpha_{21}(u_{\alpha xyt} + v_{\alpha yyt}) + \eta_y = \alpha_{22} B_{ytt}, \quad (2.142)$$

where α_{11}, α_{12}, α_{21}, and α_{22} are constants of order $O(\mu^2)$ (they are the same as in the 1DH case):

$$\alpha_{11}=\mu^2(\frac{1}{2}\alpha^2+\alpha+\frac{1}{3}),\quad \alpha_{12}=\mu^2(\alpha+\frac{1}{2}),\quad \alpha_{21}=\mu^2(\frac{1}{2}\alpha^2+\alpha),\quad \alpha_{22}=\mu^2\alpha,\quad \alpha=-0.531 \tag{2.143}$$

We recall that LWD has a formal accuracy of $O(\mu^2)$, and that the velocity solutions, $u_\alpha(x,y,t)$ and $v_\alpha(x,y,t)$, are solved for at a characteristic depth $z=z_\alpha=\alpha$. The velocity profiles can be recovered as

$$\begin{aligned} U(x,y,z,t)&=u_\alpha-\mu^2(\frac{1}{2}z^2+z-\frac{1}{2}\alpha^2-\alpha)(u_{\alpha xx}+v_{\alpha xy})+\mu^2(z-\alpha)B_{xt}+O(\mu^4)\\ V(x,y,z,t)&=v_\alpha-\mu^2(\frac{1}{2}z^2+z-\frac{1}{2}\alpha^2-\alpha)(u_{\alpha xy}+v_{\alpha yy})+\mu^2(z-\alpha)B_{yt}+O(\mu^4)\end{aligned} \tag{2.144}$$

The initial conditions to be imposed are

$$\eta(x,y,t=0)=0,\quad U(x,y,z=0,t=0)=0,\quad V(x,y,z=0,t=0)=0, \tag{2.145}$$

i.e., the free surface is initially quiescent, and the flow velocities on the free surface are zero initially. The velocity conditions translate to

$$\begin{aligned} U(x,y,0,0)&=u_\alpha(t=0)+\alpha_{21}\Big(u_{\alpha xx}(t=0)+v_{\alpha xy}(t=0)\Big)-\alpha_{22}B_{xt}+O(\mu^4)\\ V(x,y,0,0)&=v_\alpha(t=0)+\alpha_{21}\Big(u_{\alpha xy}(t=0)+v_{\alpha yy}(t=0)\Big)-\alpha_{22}B_{yt}+O(\mu^4)\end{aligned} \tag{2.146}$$

According to (2.144),

$$\begin{aligned} u_\alpha(x,y,0)&=U(x,y,0,0)+O(\mu^2)=0+O(\mu^2)\\ v_\alpha(x,y,0)&=V(x,y,0,0)+O(\mu^2)=0+O(\mu^2)\end{aligned} \tag{2.147}$$

i.e., to the leading order, $O(1)$, u_α and $U(x,y,0,0)$, as well as v_α and $V(x,y,0,0)$, are interchangeable. Therefore, without affecting the formal accuracy of LWD, which is accurate to $O(\mu^2)$, the terms multiplied by α_{21} in (2.146) can be replaced

with zero, since $U(x,y,z=0,t=0)$ and $V(x,y,z=0,t=0)$ and their spatial derivatives are zero. The initial conditions to be imposed then become

$$\eta(x,y,t=0)=0, \quad u_\alpha(x,y,0)=\alpha_{22}B_{xt}, \quad v_\alpha(x,y,0)=\alpha_{22}B_{yt}. \tag{2.148}$$

Applying double Fourier transforms in space and Laplace transform in time to (2.141) and (2.142), and imposing the initial conditions (2.148), the governing equations become

$$\begin{aligned}
&s\overset{\cdots}{\overline{\eta}}+ik(1-\alpha_{11}q^2)\overset{\cdots}{\widetilde{\overline{u_\alpha}}}+il(1-\alpha_{11}q^2)\overset{\cdots}{\overline{v_\alpha}}=(1-\alpha_{12}q^2)(s\overset{\cdots}{\widetilde{\overline{B}}}-\widetilde{\overline{B_0}})\\
&\overset{\cdots}{\widetilde{\overline{u_\alpha}}}(s-sk^2\alpha_{21})=ik\alpha_{22}(s^2\overset{\cdots}{\widetilde{\overline{B}}}-s\widetilde{\overline{B_0}})-ik\overset{\cdots}{\overline{\eta}}+skl\alpha_{21}\overset{\cdots}{\overline{v_\alpha}}+O(\mu^4) \quad ,\\
&\overset{\cdots}{\overline{v_\alpha}}(s-sl^2\alpha_{21})=il\alpha_{22}(s^2\overset{\cdots}{\widetilde{\overline{B}}}-s\widetilde{\overline{B_0}})-il\overset{\cdots}{\overline{\eta}}+skl\alpha_{21}\overset{\cdots}{\widetilde{\overline{u_\alpha}}}+O(\mu^4)
\end{aligned} \tag{2.149}$$

where $q^2=k^2+l^2$ is again used to simplify the notations. The latter two equations can be combined to express $\overset{\cdots}{\widetilde{\overline{u_\alpha}}}$ and $\overset{\cdots}{\overline{v_\alpha}}$ in terms of $\overset{\cdots}{\overline{\eta}}$:

$$\overset{\cdots}{\widetilde{\overline{u_\alpha}}}=\frac{1}{s}\frac{ik}{1-\alpha_{21}q^2}\Big(\alpha_{22}(s^2\overset{\cdots}{\widetilde{\overline{B}}}-s\widetilde{\overline{B_0}})-\overset{\cdots}{\overline{\eta}}\Big), \quad \overset{\cdots}{\overline{v_\alpha}}=\frac{1}{s}\frac{il}{1-\alpha_{21}q^2}\Big(\alpha_{22}(s^2\overset{\cdots}{\widetilde{\overline{B}}}-s\widetilde{\overline{B_0}})-\overset{\cdots}{\overline{\eta}}\Big). \tag{2.150}$$

Substituting the above expressions back into the first equation in (2.149), $\overset{\cdots}{\overline{\eta}}$ can be solved for as

$$\overset{\cdots}{\overline{\eta}}=\frac{1}{s^2+D^2q^2}(s^2\overset{\cdots}{\widetilde{\overline{B}}}-s\widetilde{\overline{B_0}})(1-\alpha_{12}q^2+\alpha_{22}D^2q^2), \tag{2.151}$$

where

$$D(q)=\sqrt{\frac{1-\alpha_{11}q^2}{1-\alpha_{21}q^2}} \tag{2.152}$$

is the normalized wave speed of LWD in 2DH.

For a landslide translating at a constant speed Fr in the x direction, the transformed free surface solution simplifies to

$$\overset{\cdots}{\overline{\eta}}=\frac{s}{s+ikFr}\frac{1}{s^2+D^2q^2}(-ikFr\widetilde{\overline{B_0}})(1-\alpha_{12}q^2+\alpha_{22}D^2q^2), \tag{2.153}$$

for which an inverse Laplace transform is available. After simplification and converting to polar coordinates, we obtain the 2HD LWD free surface solution:

$$\begin{aligned}\eta_{Fr}(r,\theta,t) &= -\frac{1}{2\pi}\int_0^{2\pi}\int_0^{\infty} q(1-\alpha_{12}q^2+\alpha_{22}D^2q^2)\widetilde{\overline{B_0}}\frac{Fr^2\cos^2\psi}{D^2-Fr^2\cos^2\psi} \\ &\qquad e^{-iqFr\cos\psi t}e^{iqr\cos(\psi-\theta)}dqd\psi \\ \eta_{+}(r,\theta,t) &= \frac{1}{2\pi}\int_0^{2\pi}\int_0^{\infty} q(1-\alpha_{12}q^2+\alpha_{22}D^2q^2)\widetilde{\overline{B_0}} \\ &\qquad \Big(\frac{Fr\cos\psi}{2(D-Fr\cos\psi)}e^{-iqDt}-\frac{Fr\cos\psi}{2(D+Fr\cos\psi)}e^{iqDt}\Big)e^{iqr\cos(\psi-\theta)}dqd\psi\end{aligned} \quad . \tag{2.154}$$

We remark that the expressions in (2.154) are highly similar to the LFD solutions, (2.90) and (2.91) – the only differences are the definition of D and the replacement of $1/\cosh(\mu q)$ with $1-\alpha_{12}q^2+\alpha_{22}D^2q^2$. The analysis shown in the 1DH LWD section can be repeated to confirm that the 2DH LWD solutions are indeed expansions (approximations) of the 2DH LFD solutions.

The velocity solutions can be recovered as

$$\begin{aligned}u_{\alpha Fr}(r,\theta,t) &= -\frac{1}{2\pi}\int_0^{2\pi}\int_0^{\infty}\frac{q\widetilde{\overline{B_0}}}{1-\alpha_{21}q^2}\cos\psi(\frac{1-\alpha_{12}q^2}{Fr\cos\psi}+\alpha_{22}q^2Fr\cos\psi) \\ &\qquad \frac{Fr^2\cos^2\psi}{D^2-Fr^2\cos^2\psi}e^{-iq\cdot Fr\cos\psi\cdot t}e^{iqr\cos(\psi-\theta)}dqd\psi \\ u_{\alpha+}(r,\theta,t) &= \frac{1}{2\pi}\int_0^{2\pi}\int_0^{\infty}\frac{q\widetilde{\overline{B_0}}}{1-\alpha_{21}q^2}\cos\psi(\frac{1-\alpha_{12}q^2}{D}+\alpha_{22}q^2D) \\ &\qquad \Big(\frac{Fr\cos\psi}{2(D-Fr\cos\psi)}e^{-iqDt}+\frac{Fr\cos\psi}{2(D+Fr\cos\psi)}e^{iqDt}\Big)e^{iqr\cos(\psi-\theta)}dqd\psi\end{aligned} \quad , \tag{2.155}$$

and

$$\begin{aligned}v_{\alpha Fr}(r,\theta,t) &= -\frac{1}{2\pi}\int_0^{2\pi}\int_0^{\infty}\frac{q\widetilde{\overline{B_0}}}{1-\alpha_{21}q^2}\sin\psi(\frac{1-\alpha_{12}q^2}{Fr\cos\psi}+\alpha_{22}q^2Fr\cos\psi) \\ &\qquad \frac{Fr^2\cos^2\psi}{D^2-Fr^2\cos^2\psi}e^{-iq\cdot Fr\cos\psi\cdot t}e^{iqr\cos(\psi-\theta)}dqd\psi \\ v_{\alpha+}(r,\theta,t) &= \frac{1}{2\pi}\int_0^{2\pi}\int_0^{\infty}\frac{q\widetilde{\overline{B_0}}}{1-\alpha_{21}q^2}\sin\psi(\frac{1-\alpha_{12}q^2}{D}+\alpha_{22}q^2D) \\ &\qquad \Big(\frac{Fr\cos\psi}{2(D-Fr\cos\psi)}e^{-iqDt}+\frac{Fr\cos\psi}{2(D+Fr\cos\psi)}e^{iqDt}\Big)e^{iqr\cos(\psi-\theta)}dqd\psi\end{aligned} \quad , . \tag{2.156}$$

The far-field and the far-field leading wave solutions can be sought from (2.154)-(2.156) using the same approaches discussed in the 2DH LFD section. While the far-field (large r and away from the landslide) solutions will be highly similar but different (the different definition of D and the replacement of $1/\cosh(\mu q)$ with $1-\alpha_{12}q^2+\alpha_{22}D^2q^2$), the far-field leading wave solutions will be exactly the same, since the far-field leading wave depends only on the leading-order frequency dispersion effects, which are captured in LWD. However, we note that the 2DH LWD far-field solutions are not particularly useful, since they still require the same amount of numerical computation as that required by the 2DH LFD solutions. On the other hand, the full LWD solutions are useful for verifying the accuracy of numerical solvers, as will be utilized in Chapter 3.

2.9 2DH linear shallow water wave equations on a slope

The dimensionless 2DH LSWE in variable water depth read

$$\eta_t+(uh)_x+(vh)_y=B_t \tag{2.157}$$

$$u_t=-\eta_x,\quad v_t=-\eta_y, \tag{2.158}$$

which are normalized in the same way as (2.62) and (2.63). On a plane beach of angle θ with the shoreline located at $x=0$ so that y is in the longshore direction, the physical domain of interest is $x>0$ and the normalized (by $L\tan\theta$) still water depth is $h(x,y)=x$. Combining the equations to solve for η first, we obtain

$$\eta_{tt}-x\eta_{xx}-\eta_x-x\eta_{yy}=B_{tt}. \tag{2.159}$$

We seek the analytical solution to (2.159). We note that, like in the 1DH case, the landslide forcing function $B(x,y,t)$ is described in the water coordinate system (vertical-horizontal).

The analytical solution to (2.159) for the landslide wave problem, valid for $x > 0, t > 0$, was first obtained in Sammarco and Renzi (2008) and Renzi (2010) with the initial conditions $\eta(x, y, 0) = 0$ and $\eta_t(x, y, 0) = 0$, for any landslide forcing function symmetric about the x-axis. However, we note that the initial condition $\eta_t(x, y, 0) = 0$ does not fulfill the quiescent water condition in LSWE, and would result in initial water velocities that depend on $B_t(x, y, 0)$ (which can be nonzero): by setting $\eta_t(x, y, 0) = 0$ in (2.157), we obtain $[u(x, y, 0)h]_x + [v(x, y, 0)h]_y = B_t(x, y, 0)$; under this condition, $u(x, y, 0) = 0 = v(x, y, 0)$ is not possible for $B_t(x, y, 0) \neq 0$.

Similarly to the 1DH cases previously discussed, when solving for η first, to allow for the quiescent water condition, the initial conditions that should be imposed are

$$\eta(x, y, 0) = 0 \quad \text{and} \quad \eta_t(x, y, 0) = B_t(x, y, 0), \tag{2.160}$$

the latter resulting from setting $[u(x, y, 0)h]_x + [v(x, y, 0)h]_y = 0$ in (2.157), which allows for the possibility that $u(x, y, 0) = 0 = v(x, y, 0)$. The precise initial velocities, $u(x, y, 0)$ and $v(x, y, 0)$, can be specified only when the solutions for $u(x, y, t)$ and $v(x, y, t)$ are considered. We note that the two different initial conditions used, i.e., $\eta_t(x, y, 0) = 0$ and $\eta_t(x, y, 0) = B_t(x, y, 0)$, become identical only when a landslide forcing function with $B_t(x, y, 0) = 0$ is chosen.

We rederive the analytical solution using the new initial conditions and obtain

$$\eta(x, y, t) = 2\sqrt{\frac{2}{\pi}} \sum_{n=0}^{\infty} \int_0^{\infty} L_n(2kx) k e^{-kx} \cos(ky) \int_0^{\infty} L_n(2ks) e^{-ks} \left[\overline{B}(s, k, t) - \cos(\sqrt{\lambda} t) \overline{B}(s, k, 0) - \sqrt{\lambda} \int_0^t \sin\left(\sqrt{\lambda}(t - \tau)\right) \overline{B}(s, k, \tau) d\tau \right] ds dk \,, \tag{2.161}$$

where $L_n(x)$ is the n-th order Laguerre polynomial, $\overline{B}$ is the Fourier-transformed

B with respect to y (B is assumed to be symmetric about the x-axis), and

$$\lambda = k(2n+1). \tag{2.162}$$

The velocity solutions based on the new solution for η, (2.161), can be recovered from the momentum equation (2.158) as

$$\begin{aligned}
&u(x,y,t) = u(x,y,0) \\
&+2\sqrt{\frac{2}{\pi}}\sum_{n=0}^{\infty}\int_0^{\infty} L_n(2kx)k^2e^{-kx}\cos(ky)\int_0^{\infty} L_n(2ks)e^{-ks}\Bigg[\int_0^t \overline{B}(s,k,\psi)d\psi \\
&-\frac{1}{\sqrt{\lambda}}\sin(\sqrt{\lambda}t)\overline{B}(s,k,0) - \sqrt{\lambda}\int_0^t\int_0^{\psi}\sin\Big(\sqrt{\lambda}(\psi-\tau)\Big)\overline{B}(s,k,\tau)d\tau d\psi\Bigg]dsdk \\
&+4\sqrt{\frac{2}{\pi}}\sum_{n=1}^{\infty}\int_0^{\infty} L_{n-1}^{(1)}(2kx)k^2e^{-kx}\cos(ky)\int_0^{\infty} L_n(2ks)e^{-ks}\Bigg[\int_0^t \overline{B}(s,k,\psi)d\psi \\
&-\frac{1}{\sqrt{\lambda}}\sin(\sqrt{\lambda}t)\overline{B}(s,k,0) - \sqrt{\lambda}\int_0^t\int_0^{\psi}\sin\Big(\sqrt{\lambda}(\psi-\tau)\Big)\overline{B}(s,k,\tau)d\tau d\psi\Bigg]dsdk
\end{aligned} \tag{2.163}$$

and

$$\begin{aligned}
&v(x,y,t) = v(x,y,0) \\
&+2\sqrt{\frac{2}{\pi}}\sum_{n=0}^{\infty}\int_0^{\infty} L_n(2kx)k^2e^{-kx}\sin(ky)\int_0^{\infty} L_n(2ks)e^{-ks}\Bigg[\int_0^t \overline{B}(s,k,\psi)d\psi \\
&-\frac{1}{\sqrt{\lambda}}\sin(\sqrt{\lambda}t)\overline{B}(s,k,0) - \sqrt{\lambda}\int_0^t\int_0^{\psi}\sin\Big(\sqrt{\lambda}(\psi-\tau)\Big)\overline{B}(s,k,\tau)d\tau d\psi\Bigg]dsdk
\end{aligned} \tag{2.164}$$

For initially quiescent water, we further require $u(x,y,0) = 0 = v(x,y,0)$, in addition to the initial conditions already imposed when solving for η, i.e. $\eta(x,y,0) = 0$ and $[u(x,y,0)h]_x + [v(x,y,0)h]_y = 0$.

The analytical solutions in all existing studies (e.g. Sammarco and Renzi, 2008; Renzi, 2010; Renzi and Sammarco, 2010, 2012; Seo and Liu, 2013) include an extra term in addition to (2.161) due to nonzero initial water velocities:

$$\begin{aligned}
&\eta_{\text{extra}}(x,y,t) = 2\sqrt{\frac{2}{\pi}}\sum_{n=0}^{\infty}\int_0^{\infty} L_n(2kx)ke^{-kx}\cos(ky)\int_0^{\infty} L_n(2ks)e^{-ks} \\
&\quad\Bigg[-\frac{\overline{B}_t(s,k,0)\sin(\sqrt{\lambda}t)}{\sqrt{\lambda}}\Bigg]dsdk
\end{aligned} \tag{2.165}$$

Therefore, we only need to examine the term (2.165) to evaluate how it affects previous findings. Clearly, the extra term vanishes if a landslide forcing function with $B_t(x, y, 0) = 0$ is used.

To examine the significance of η_{extra}, we follow the asymptotic analysis discussed in Sammarco and Renzi (2008), Renzi (2010), and Seo and Liu (2013), and find the large-t asymptotic approximation of η_{extra} for $y > 0$ to be

$$\eta_{\text{extra}}(x, y, t) \simeq 2 \sum_{n=0}^{\infty} L_n(2k_0 x) e^{-k_0 x} \left(\frac{1}{t|\omega_0''|}\right)^{\frac{1}{2}} C_n \sin(k_0 y - \omega_0 t + \frac{\pi}{4}), t \to \infty \quad (2.166)$$

where

$$k_0 = \frac{2n+1}{4}\left(\frac{t}{y}\right)^2, \quad \omega_0 = \sqrt{k_0(2n+1)}, \quad \omega_0'' = -\frac{\sqrt{k_0(2n+1)}}{4k_0^2}, \\ C_n = \frac{k_0}{\omega_0} \int_0^{\infty} L_n(2k_0 s) e^{-k_0 s} \overline{B_t}(s, k_0, 0) ds \quad . \quad (2.167)$$

(2.166) is the extra term included in the asymptotic solution in previous studies. It has the same form as a part of the asymptotic approximation of the true solution (2.161), the key difference being the C_n term. Similar terms exist in the asymptotic approximation of (2.161). These terms need to be numerically evaluated and may depend on time, but in general their amplitudes do not grow in time for the translating landslide forcing functions considered in both previous studies and the present study. Therefore, while the asymptotic decay rate $t^{-1/2}$ remains the same, the exact wave shape can be very different due to the difference in the initial conditions used.

In previous studies, translating landslides moving at a constant speed, for which $B_t(x, y, 0) \neq 0$, were used in plotting and further examining the solutions. Choosing as an example a double-Gaussian landslide forcing function moving at a constant speed 1 from $x = 0$, i.e., $B(x, y, t) = e^{-8(x-t)^2} e^{-8y^2}$, we solved the 2DH LSWE numerically with a fairly fine grid spacing of $\Delta x = \Delta y = 0.01$ (details on the numerical solver will be provided in Chapter 3), and compare the results with the

50-mode analytical solution (2.161) evaluated with numerical integration methods described by Seo and Liu (2013). The resulting free surface elevations at $t = 1, 2, 3$ are shown in figure 2.32. Although the numerical solution of LSWE can be problematic near the shoreline, it is robust and reliable away from the shoreline. Since the integral-form analytical solution requires further numerical evaluation and approximation in plotting, in this case the numerical solution is a better choice as the reference solution when the overall wave field (i.e., not the edge waves) is of concern, such as those shown in figure 2.32. While the numerically-evaluated analytical solutions generally agree well with the numerical solutions, some oscillations are clearly visible (e.g. along $y = 2$ at $t = 2$). On the other hand, we see that in this example the magnitude of η_{extra} is always significant when compared with the true solution, suggesting that its impact on the true solution is not negligible.

Upon closer inspection of the oscillations observed in the analytical solutions in figure 2.32, we found the cause to be a poor convergence rate of the analytical solution with respect to the number of modes considered in (2.161). To highlight this issue, we focus on the wave profile along $y = 2$ in figure 2.32, which appears to be highly problematic, and compare in figure 2.33 the numerical solution with analytical solutions computed using different numbers of modes. We see that in this case, convergence of the solution is not reached even with 50 modes considered. To further examine the convergence rate, in figure 2.34 we pick a point $(x, y, t) = (2.5, 2, 2)$ and plot $\eta(2.5, 2, 2)$ as a function of the number of modes considered. Based on figure 2.32, this point is situated ahead of the leading wave. We thus expect a very small value here – the numerical solution predicts $\eta(2.5, 2, 2) \simeq 0.008$, yet the analytical solution is still only slowing converging even with 300 modes considered. We remark that the numerical integration can be time-consuming, and it is often undesirable to consider more than ~ 20 modes. As a reference,

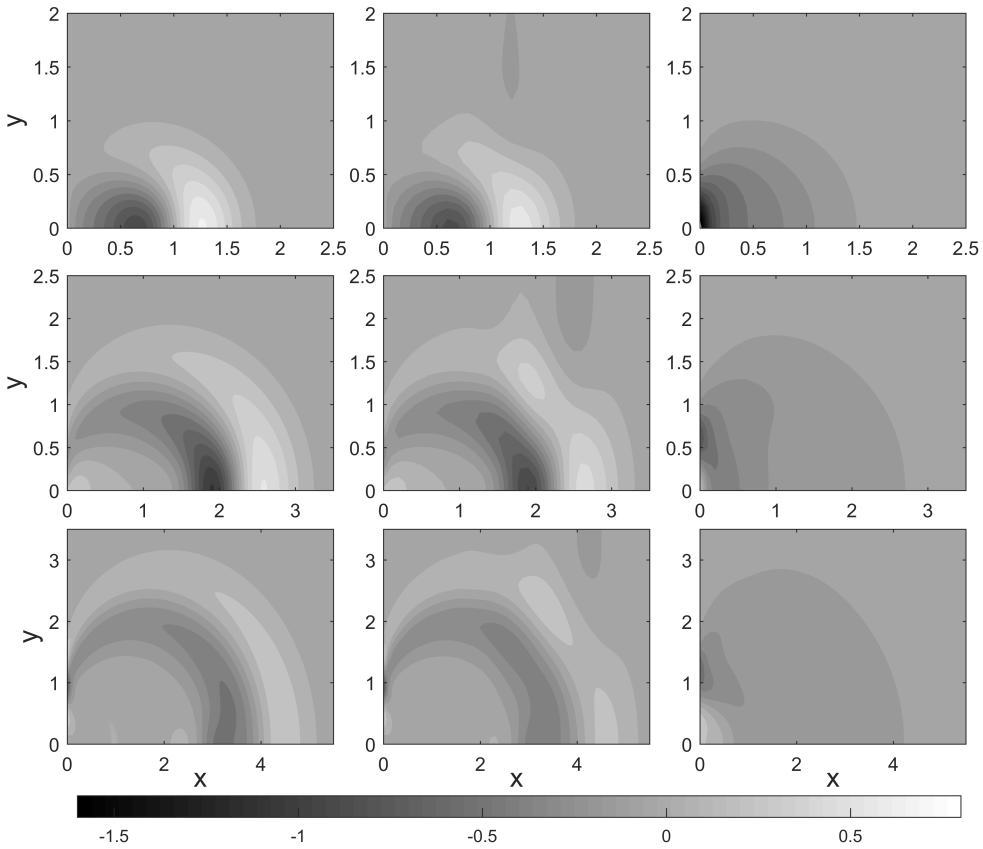

Figure 2.32: Wave fields generated by a double-Gaussian landslide forcing function moving at a constant speed 1 from $x = 0$. The solution is symmetric about the x-axis. Top row: $t = 1$; middle row: $t = 2$; bottom row: $t = 3$. Left column: numerical solution with $\Delta x = \Delta y = 0.01$; middle column: 50-mode analytical solution; right column: 50-mode η_{extra}.

Sammarco and Renzi (2008) and Renzi (2010) mostly considered only the first 6 modes, and Seo and Liu (2013) considered only the first 10 modes.

The analytical solution shines when the edge waves that propagate along $x = 0$ or the large-time/far-field solutions are of interest, for which accurate numerical solutions are difficult to obtain. As mentioned previously, the numerical shoreline boundary treatment in linear theory is problematic. In addition, the computational cost can be significant when the far-field or the large-time solution is sought, since numerical simulations have to resolve the entire domain starting from $t = 0$. Ana-

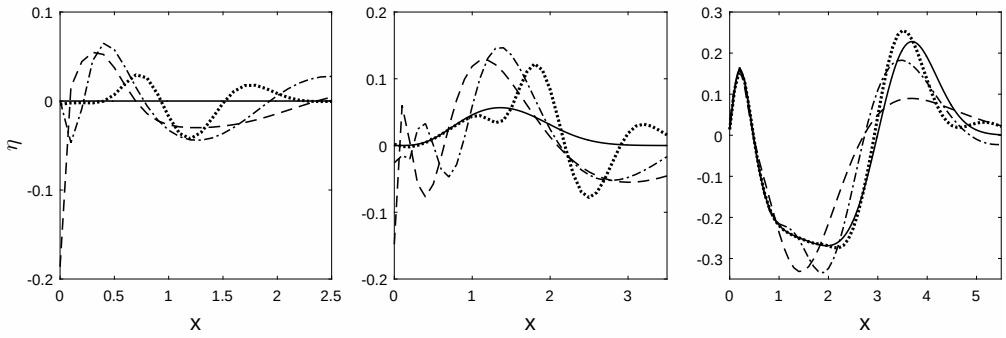

Figure 2.33: Analytical solutions of the free surface elevation along $y = 2$ due to a double-Gaussian landslide forcing function moving at a constant speed 1 from $x = 0$. Solid line: numerical solution with $\Delta x = \Delta y = 0.01$; dashed line: 6-mode analytical solution; dash-dot line: 10-mode analytical solution; dotted line: 50-mode analytical solution. Left panel: $t = 1$; middle panel: $t = 2$; right panel: $t = 3$.

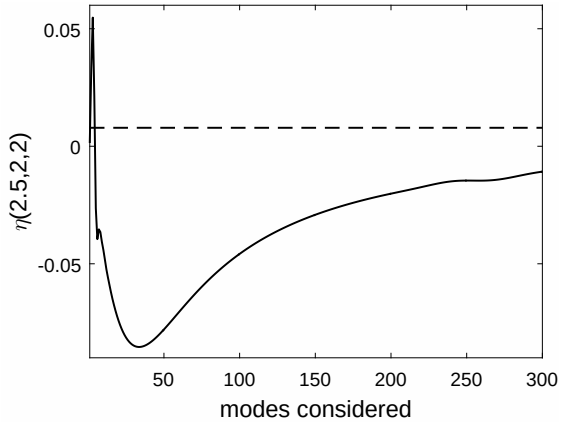

Figure 2.34: Plot examining the convergence rate of the analytical solution for $\eta(2.5, 2, 2)$. Solid line: analytical solution as a function of the number of modes considered; dashed line: numerical solution.

lytical solution is thus highly preferable in these situations. To examine the edge wave solutions more closely, in figure 2.35 we compare the analytical solutions with the numerical solution for the same double-Gaussian landslide forcing function case along $(x, y, t) = (0, y, 5)$. In this case, we find the 10-mode analytical solution to be nearly identical to the 15-mode solution, suggesting that consideration of the first 10 modes is sufficient in this case (while not shown here, 6 modes are still insufficient in this example). We therefore advise that a convergence test

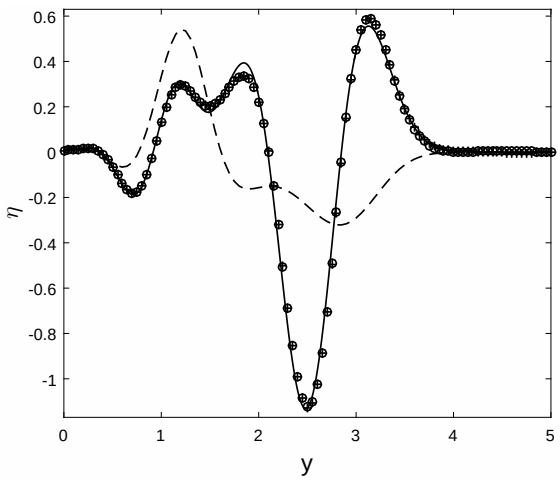

Figure 2.35: Edge waves ($x = 0$) at $t = 5$ due to a double-Gaussian landslide forcing function moving at a constant speed 1 from $x = 0$. Solid line: numerical solution with $\Delta x = \Delta y = 0.01$; plus: 10-mode analytical solution; circle: 15-mode analytical solution; dashed line: 15-mode η_{extra}.

be performed every time the analytical solution is used at a different location, to ensure that satisfactory convergence is reached within a reasonable number of modes considered. In figure 2.35, we also included η_{extra} and see that its amplitude is significant, again showing its permanent effect on the wave shape. On the other hand, even with the fine grid spacing $\Delta x = \Delta y = 0.01$, the numerical edge wave solutions still do not fully agree with the analytical solutions, which in this case have converged and should be regarded as the reference solution.

2.10 Summary

In this chapter, we reviewed existing analytical solutions and derived new solutions for landslide-generated waves. The analytical solutions not only serve as reliable benchmark tests for numerical models, but also provide unique insights unattainable via other means. Here, we summarize the most important new findings that will be utilized repeatedly later in this study.

First, based on the linear and fully dispersive wave model (LFD) in constant water depth, the far-field leading wave (valid for large r and near $r = t$) generated by a solid landslide moving at a constant speed Fr evolves into a fixed shape due to frequency dispersion, regardless of the exact landslide shape. To the leading order, the wave height of the leading wave is determined by the volume (or area in 1DH) enclosed by the landslide, rather than its exact shape. Therefore, in modeling, it is more important to match the landslide volume than the exact landslide shape.

In the shallow water limit, frequency dispersion effects are neglected, and closed-form far-field solutions (as opposed to the more limited far-field leading wave solutions) can be found for certain landslide shapes. For a Gaussian-shaped landslide with a x-to-y aspect ratio σ in 2DH constant water depth, the far-field solution (valid for large r) was found to be

$$\eta_{\text{far}}(r,\theta,t) = \sqrt{\pi}\frac{Fr\cos\theta}{2(1-Fr\cos\theta)} r^{-\frac{1}{2}}\nu^{-\frac{3}{4}}\Omega_2\Big(\frac{r-t}{\nu^{\frac{1}{2}}}\Big), \tag{2.168}$$

where

$$\nu = \sigma\cos^2\theta + \frac{1}{\sigma}\sin^2\theta \tag{2.169}$$

is the wave height and wavelength modification factor due to the landslide aspect ratio, and

$$\Omega_2(s) = |s|^{\frac{3}{2}}e^{-4s^2}\left[I_{\frac{5}{4}}\big(4s^2\big) - I_{\frac{1}{4}}\big(4s^2\big) + \frac{1}{8s^2}I_{\frac{1}{4}}\big(4s^2\big) + \text{sgn}(s)\Big(I_{-\frac{1}{4}}\big(4s^2\big) - I_{\frac{3}{4}}\big(4s^2\big)\Big)\right], \tag{2.170}$$

plotted in figure 2.26, controls the wave shape. The far-field solution (2.168) based on the Linear Shallow Water wave Equations (LSWE) is useful because it reveals the scaling relation between the landslide and the wave it generates and how the wave spreads.

CHAPTER 3

NUMERICAL MODELS

In this chapter, we will present the dimensional governing wave equations that are to be solved numerically. Unless otherwise noted, all mathematical expressions in this chapter are in dimensional form. The equations considered include: the Linear Shallow Water wave Equations (LSWE), the Linear and Weakly Dispersive wave model (LWD), the Nonlinear Shallow Water wave Equations (NSWE), the Weakly Nonlinear and Weakly Dispersive wave model (WNWD), and the Fully Nonlinear and Weakly Dispersive wave model (FNWD). The linear equations, LSWE and LWD, are solved with a finite-difference solver, and the nonlinear equations, NSWE, WNWD, and FNWD, are solved with a hybrid finite-volume/finite-difference shock-capturing solver. For each numerical solver, the governing equations are written in a way such that a hierarchy of model accuracy is clear and the same solver can be easily adjusted to solve the various governing equations. After the governing wave equations are presented, we will describe the numerical methods used and then show select benchmark tests to check the performance of the numerical solvers.

In long-wave equations, the characteristic wavelength (L) of the waves are assumed to be much larger than the characteristic water depth (d). Two dimensionless parameters are of importance in long-wave theory:

$$\mu^2 = (\frac{A}{L})^2, \quad \epsilon = \frac{A}{d}, \tag{3.1}$$

where A is the characteristic wave height. In (3.1), μ^2 indicates how shallow the water depth is compared to the wavelength. In all long-wave equations, $\mu^2 \ll 1$ is required; however, how much smaller than 1 depends on the formal accuracy of each set of long-wave equations. On the other hand, ϵ indicates how nonlinear the

waves are compared to water depth. Long-wave equations can be further linearized for $\epsilon \ll 1$.

Within the context of long-wave theory, a landslide is interpreted as a changing bathymetry – the still water depth (bathymetry) is allowed to vary in both space and time. Detailed derivation of the long-wave equations can be found in Wei et al. (1995) and Lynett and Liu (2002). Using asterisks to denote dimensionless variables, here we present the dimensionless mass and momentum equations adopted from Lynett and Liu (2002):

$$\frac{1}{\epsilon}H^*_{t^*} + \nabla \cdot \Big[H^*(\vec{u}^*_\alpha + \mu^2 \vec{u}^*_1)\Big] = O(\mu^4), \tag{3.2}$$

and

$$\begin{aligned}
&\vec{u}^*_{\alpha,t^*} + \epsilon(\vec{u}^*_\alpha \cdot \nabla)\vec{u}^*_\alpha + \nabla\eta^* + \mu^2\left\{ z^*_\alpha \nabla G^*_1 + \frac{1}{2}z^{*2}_\alpha \nabla G^*_2 \right\}_{t^*} \\
&+\epsilon\mu^2\left\{ G^*_1 \nabla G^*_1 - \nabla(\eta^* G^*_{1,t^*}) + \Big[\vec{u}^*_\alpha \cdot (\nabla z^*_\alpha)\Big](\nabla G^*_1 + z^*_\alpha \nabla G^*_2) \right. \\
&\qquad \left. +z^*_\alpha \nabla(\vec{u}^*_\alpha \cdot \nabla G^*_1) + \frac{1}{2}z^{*2}_\alpha \nabla(\vec{u}^*_\alpha \cdot \nabla G^*_2) \right\}, \\
&+\epsilon^2\mu^2\nabla\left\{ \eta^* G^*_1 G^*_2 - \eta^* \vec{u}^*_\alpha \cdot \nabla G^*_1 - \frac{1}{2}\eta^{*2} G^*_{2,t^*} \right\} \\
&+\epsilon^3\mu^2\nabla\left\{ \frac{1}{2}\eta^{*2}(G^{*2}_2 - \vec{u}^*_\alpha \cdot \nabla G^*_2) \right\} = O(\mu^4)
\end{aligned} \tag{3.3}$$

where

$$\begin{aligned}
\vec{u}^*_1 &= \left\{ z^*_\alpha + \frac{1}{2}(h^* - \epsilon\eta^*) \right\}\nabla G^*_1 + \left\{ \frac{1}{2}z^{*2}_\alpha - \frac{1}{6}\Big[(\epsilon\eta^*)^2 - \epsilon\eta^* h^* + h^{*2}\Big] \right\}\nabla G^*_2 \\
G^*_1 &= \nabla \cdot (h^* \vec{u}^*_\alpha) + \frac{1}{\epsilon}h^*_{t^*} \\
G^*_2 &= \nabla \cdot \vec{u}^*_\alpha
\end{aligned} \tag{3.4}$$

The spatial variables (x^*, y^*) are normalized by L, and the time variable t^* is normalized by $L/\sqrt{gd}$ (g is the gravitational acceleration), the free surface elevation η^* is normalized by the characteristic wave height A, the bathymetry (still water

depth) h^* is normalized by the characteristic water depth d, and the total water depth H^* can be written as $H^* = h^* + \epsilon\eta$. In landslide wave problems, the characteristic wave height A is assumed to be the same as the characteristic landslide thickness, and the characteristic wavelength L is assumed to be the same as the characteristic landslide length. In addition, it is convenient to isolate the landslide from the bathymetry, by writing

$$h^*(x^*, y^*, t^*) = h_0^*(x^*, y^*) - \epsilon B^*(x^*, y^*, t^*), \tag{3.5}$$

where $h_0^*(x^*, y^*)$ is the still water depth that does not change in time, and $B^*(x^*, y^*, t^*)$, normalized by A, is the landslide forcing function, which changes the bathymetry as the landslide travels. The landslide forcing function B^* has to be prescribed in a way consistent with the scaling assumption in (3.2) and (3.3). Namely, B^* and its derivatives, normalized by L in length, A in height, and $L/\sqrt{gd}$ in time, are required to remain of order one. Therefore, a landslide of a locally fast-varying shape (which has locally large derivatives of B^*), such as a semi-ellipse (the slope approaches infinity near the two ends), violates the scaling assumption and cannot be accurately resolved by long-wave models.

$\vec{u}_\alpha^* = (u_\alpha^*, v_\alpha^*)$, normalized by $\epsilon\sqrt{gd}$, is the leading-order flow velocity at a representative depth z_α^*. The representative depth, z_α^*, first proposed by Nwogu (1993), can be chosen to improve frequency dispersion and maximize the accuracy of the long-wave equations. For best overall performance, Kennedy et al. (2001) and Shi et al. (2012) recommended the form

$$z_\alpha^* = \alpha h^* + \epsilon(1+\alpha)\eta^*, \quad \alpha = -0.531. \tag{3.6}$$

The full velocity distribution can be recovered as

$$\vec{U}^*(x^*, y^*, z^*, t^*) = \vec{u}_\alpha^* - \mu^2 \left\{ \frac{1}{2}(z^{*2} - z_\alpha^{*2})\nabla(\nabla\cdot\vec{u}_\alpha^*) + (z^* - z_\alpha^*)\nabla\left[\nabla\cdot(h^*\vec{u}_\alpha^* + \frac{h_{t^*}^*}{\epsilon})\right] \right\}, \tag{3.7}$$

where the terms multiplied by μ^2 are the higher-order velocity correction. After depth-averaging, the higher-order velocity correction becomes $\vec{u}_1^* = (u_1^*, v_1^*)$, normalized by $\epsilon\sqrt{gd}$. We note that $\vec{u}_1^*$ is defined so that it is of $O(1)$. However, it shows up as $\mu^2\vec{u}_1^*$ in the equations.

We refer to (3.2) and (3.3) as FNWD, which is accurate up to $O(\mu^2)$, has a truncation error of $O(\mu^4)$, and invokes no assumption on the wave nonlinearity ϵ. FNWD is fully nonlinear and weakly dispersive. It is the most accurate, and therefore the most computationally expensive, long-wave model considered in this study. By making further assumptions on μ^2 and ϵ, simpler and therefore less accurate and less expensive long-wave models can be obtained: neglecting the $\epsilon\mu^2$, $\epsilon^2\mu^2$, and $\epsilon^3\mu^2$ terms in (3.2) and (3.3) results in WNWD, which is weakly nonlinear and weakly dispersive and has a truncation error of $O(\mu^4, \epsilon\mu^2)$; neglecting all terms involving μ^2 results in NSWE, which is nonlinear and nondispersive and has a truncation error of $O(\mu^2)$; neglecting all terms involving ϵ results in LWD, which is linear and weakly dispersive and has a truncation error of $O(\mu^4, \epsilon)$; neglecting all terms involving ϵ or μ^2 results in LSWE, which is linear and nondispersive, and has a truncation error of $O(\mu^2, \epsilon)$.

3.1 Linear long-wave equations solver

As discussed in Chapter 2, closed-form analytical solutions for landslide waves are sometimes available. When analytical solutions are not available (or when the integral-form solutions become too expensive to numerically integrate), we solve the linear equations numerically using the fourth-order central difference scheme in space and the third-order Strong Stability Preserving Runge-Kutta (SSP-RK; see Gottlieb et al. 2001) scheme in time. After rearranging the governing equations

into a form suitable for the numerical solver, the dimensional mass equation reads

$$\eta_t + \Big[h_0(u_\alpha + u_1)\Big]_x + \Big[h_0(v_\alpha + v_1)\Big]_y = B_t, \tag{3.8}$$

and the dimensional momentum equations read

$$(u_\alpha + u_2)_t = -g\eta_x, \quad (v_\alpha + v_2)_t = -g\eta_y, \tag{3.9}$$

where $h_0(x, y)$ is the still water depth that excludes the landslide, and u_α and v_α are the flow velocities at a representative depth z_α. For LSWE, $u_1 = u_2 = v_1 = v_2 = 0$. For LWD,

$$\begin{cases} u_1 = (z_\alpha + \frac{1}{2}h_0)G_{1,x} + (\frac{1}{2}z_\alpha^2 - \frac{1}{6}h_0^2)G_{2,x}, \quad u_2 = z_\alpha G_{1,x} + \frac{1}{2}z_\alpha^2 G_{2,x} \\ v_1 = (z_\alpha + \frac{1}{2}h_0)G_{1,y} + (\frac{1}{2}z_\alpha^2 - \frac{1}{6}h_0^2)G_{2,y}, \quad v_2 = z_\alpha G_{1,y} + \frac{1}{2}z_\alpha^2 G_{2,y} \\ z_\alpha = \alpha h_0, \quad \alpha = -0.531 \\ G_1 = (h_0 u_\alpha)_x + (h_0 v_\alpha)_y + h_t, \quad G_2 = u_{\alpha,x} + v_{\alpha,y} \end{cases}, \tag{3.10}$$

$h(x, y, t) = h_0(x, y) - B(x, y, t)$ is the still water depth that includes the landslide. While u_1 and v_1 are the depth-averaged higher-order velocity corrections, u_2 and v_2 do not have a physical meaning.

At each iteration in time based on the SSP-RK scheme, η, $\phi = (u_\alpha + u_2)$, and $\psi = (v_\alpha + v_2)$ are updated via equations (3.8) and (3.9). While $u_\alpha = \phi$ and $v_\alpha = \psi$ can be recovered directly in LSWE since $u_2 = v_2 = 0$, a matrix system needs to be solved for each velocity component in LWD, since u_2 and v_2 depend on u_α and v_α. Here we briefly explain the process: writing u_2 out fully, we have

$$u_2 = z_\alpha(h_0 u_\alpha)_{xx} + z_\alpha(h_0 v_\alpha)_{yx} + z_\alpha h_{tx} + \frac{1}{2}z_\alpha^2 u_{\alpha xx} + \frac{1}{2}z_\alpha^2 v_{\alpha yx}. \tag{3.11}$$

Separating the terms with u_α from those with v_α, we have

$$M_1 = z_\alpha(h_0 u_\alpha)_{xx} + \frac{1}{2}z_\alpha^2 u_{\alpha xx}, \quad M_2 = z_\alpha(h_0 v_\alpha)_{yx} + \frac{1}{2}z_\alpha^2 v_{\alpha yx} + z_\alpha h_{tx}. \tag{3.12}$$

Using Δx to denote the grid spacing in x and i to denote the index for x in the numerical model, we employ the second-order central different formula to discretize M_1 as

$$M_{1,i} = z_{\alpha,i}\frac{(h_0u_\alpha)_{i+1} - 2(h_0u_\alpha)_i + (h_0u_\alpha)_{i-1}}{\Delta x^2} + \frac{1}{2}z_{\alpha,i}^2\frac{u_{\alpha,i+1} - 2u_{\alpha,i} + u_{\alpha,i-1}}{\Delta x^2}. \quad (3.13)$$

On the other hand, M_2 is independent of u_α. The fourth-order central difference scheme and v_α from the previous sub-time step are used to compute M_2. $\phi = u_\alpha + u_2 = u_\alpha + M_1 + M_2$ can be rearranged to be $u_\alpha + M_1 = \phi - M_2$, for which a matrix system with discretized M_1 can be set up to solve for u_α.

Similarly, writing v_2 out fully results in

$$v_2 = z_\alpha(h_0u_\alpha)_{xy} + z_\alpha(h_0v_\alpha)_{yy} + z_\alpha h_{ty} + \frac{1}{2}z_\alpha^2u_{\alpha xy} + \frac{1}{2}z_\alpha^2v_{\alpha yy}. \quad (3.14)$$

Separating the terms with u_α from those with v_α, we have

$$N_1 = z_\alpha(h_0v_\alpha)_{yy} + \frac{1}{2}z_\alpha^2v_{\alpha yy}, \quad N_2 = z_\alpha(h_0u_\alpha)_{xy} + \frac{1}{2}z_\alpha^2u_{\alpha xy} + z_\alpha h_{ty}. \quad (3.15)$$

Using Δy to denote the grid spacing in y and j to denote the index for y in the numerical model, we employ the second-order central different formula to discretize N_1 as

$$N_{1,j} = z_{\alpha,j}\frac{(h_0v_\alpha)_{j+1} - 2(h_0v_\alpha)_j + (h_0v_\alpha)_{j-1}}{\Delta y^2} + \frac{1}{2}z_{\alpha,j}^2\frac{v_{\alpha,j+1} - 2v_{\alpha,j} + v_{\alpha,j-1}}{\Delta y^2}. \quad (3.16)$$

Again, N_2 is independent of v_α. The fourth-order central difference scheme and u_α from the previous sub-time step are used to compute N_2. A matrix system based on $v_\alpha + N_1 = \psi - N_2$ with discretized N_1 can then be set up to solve for v_α.

3.1.1 Verification with analytical solutions

In Chapter 2 we presented various analytical solutions for LSWE and LWD. For both LSWE and LWD, the numerical results and the analytical solutions in con-

stant water depth are essentially identical, and thus the comparisons will not be shown here. The cases with a sloping bottom are more challenging. The 2DH LSWE case with a sloping bottom has already been discussed in Chapter 2. In this section, we shall focus on the 1DH LSWE case with a sloping bottom, for which a closed-form analytical solution, (2.73),

$$\eta(x,t) = \frac{t}{6} H \left[-(\sqrt{x} - \frac{t}{2}) \right], \tag{3.17}$$

is available for a ramp-like landslide, (2.68),

$$B(x,t) = R(\frac{1}{2}t - \sqrt{x}). \tag{3.18}$$

The analytical solution (3.18) serves as a challenging benchmark for numerical models, since it consists of a shock and a "shoreline" ($x \to 0$) in linear theory. To demonstrate this, we shall compare the numerical results with the analytical solution. The open boundary condition (derivatives equal zero) is used on the right boundary. For the left (shoreline) boundary, linear extrapolation is used to acquire the surface elevations at the ghost points located at $x \leq 0$ and the flow velocity at $x \leq 0$ is assumed to be zero, which are needed in computing the derivatives based on the central difference scheme. In addition, since the water depth at exactly $x = 0$ is 0, the first point in the numerical model is actually located at $x = \Delta x$, where Δx is the grid spacing (normalized by the landslide length).

Using two different grid spacings $\Delta x = 0.01$ and $\Delta x = 0.001$ (normalized), we computed the numerical solution due to the ramp-like landslide forcing function, and the comparison with the analytical solution is shown in figure 3.1. While the general location of the jump and the water surface elevations on the two sides of the jump are well captured, the width of the jump greatly depends on the grid spacing Δx. Overshoot of the computed surface elevation is obvious near the jump,

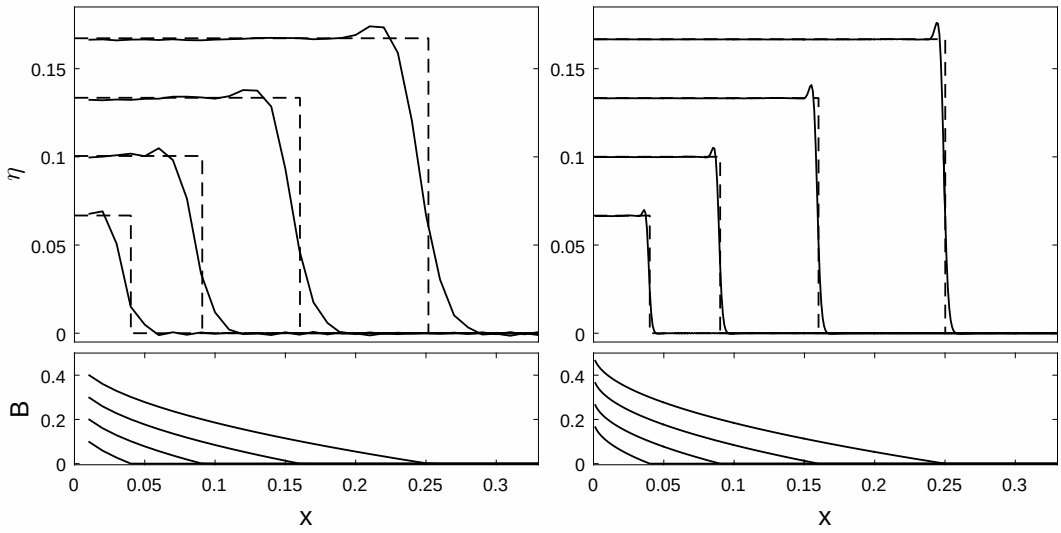

Figure 3.1: Comparison of the numerical and analytical solutions of 1DH LSWE for a ramp-like-landslide-generated waves on a constant slope at times $t = 0.4, 0.6, 0.8, 1$ (left to right). Solid line: numerical solution; dashed line: analytical solution. Left panels: numerical solution with grid spacing $\Delta x = 0.01$; right panels: numerical solution with grid spacing $\Delta x = 0.001$.

which is a common characteristic of finite difference schemes near sharp gradients. On the other hand, the numerical shoreline treatment appears to perform well in this problem, although small oscillations can still be observed in the free surface elevations away from the jump.

Even though the results presented in figure 3.1 appear satisfactory, we note that the two grid spacings used in the example ($\Delta x = 0.01$ and $\Delta x = 0.001$) are fairly fine and undesirable for larger simulation domains. Therefore, more sophisticated numerical methods are necessary to resolve the sharp gradient (jump) and the shoreline boundary with a more reasonably-sized grid spacing in a numerical model based on linear theory, and the closed-form analytical solution (3.17) serves as a convenient tool to test the effectiveness of the numerical methods. Since wave runup and shocks based on linear models are not of interest in this study, complex shoreline boundary treatment and accurate shock preservation are not necessary,

and fairly course grid spacings are used in most numerical simulations ($\Delta x = 0.02$ in 1DH and $\Delta x = \Delta y = 0.05$ in 2DH).

3.2 Nonlinear long-wave equations solver

The nonlinear governing equations (NSWE, WNWD, and FNWD) were solved by using a hybrid finite-volume/finite-difference shock-capturing numerical scheme. The spatial accuracy can be either second-order (MUSCL-Hancock with a van Leer slope limiter; see Toro 2001) for quicker computation, or fifth-order accurate (WENO; see Jiang and Shu 1996), and the temporal accuracy is third-order (SSP-RK; see Gottlieb et al. 2001). The local Riemann problem is solved by an HLLC approximate Riemann solver (Toro, 2001), which is applicable to both wet-wet cell interfaces and wet-dry cell interfaces. The advantage of employing a Riemann solver is that the shoreline (a wet-dry cell interface) is automatically captured without additional numerical treatment. Shock-capturing numerical schemes to solve long-wave equations have been implemented in many recent studies, such as Li and Raichlen (2002), Wei et al. (2006), Shiach and Mingham (2009), Shi et al. (2012), and Zhou et al. (2016). The main distinguishing features of our model are the formal allowance (the bathymetry is allowed to vary in time in the derivation of the governing equations) of a bathymetry that changes significantly in time (landslide), and the easiness in switching between different long-wave models.

After substantial rearrangement of (3.2) and (3.3) into a form suitable for the numerical solver, the dimensional mass equation in 2DH reads:

$$H_t + \Big[H(u_\alpha + u_1)\Big]_x + \Big[H(v_\alpha + v_1)\Big]_y = 0, \tag{3.19}$$

and the momentum equations read:

$$\begin{cases} \Big[H(u_\alpha+u_2)\Big]_t+\Big[H(u_\alpha+u_1)^2+\dfrac{1}{2}g(\eta^2+2\eta h)\Big]_x+\Big[H(u_\alpha+u_1)(v_\alpha+v_1)\Big]_y \\ \qquad\qquad = g\eta h_x+S_X \\ \Big[H(v_\alpha+v_2)\Big]_t+\Big[H(u_\alpha+u_1)(v_\alpha+v_1)\Big]_x+\Big[H(v_\alpha+v_1)^2+\dfrac{1}{2}g(\eta^2+2\eta h)\Big]_y \\ \qquad\qquad = g\eta h_y+S_Y \end{cases}. \tag{3.20}$$

For FNWD,

$$\begin{cases} u_1=(z_\alpha+\dfrac{1}{2}h-\dfrac{1}{2}\eta)G_{1,x}+(\dfrac{1}{2}z_\alpha^2-\dfrac{1}{6}h^2-\dfrac{1}{6}\eta^2+\dfrac{1}{6}\eta h)G_{2,x} \\ u_2=z_\alpha G_{1,x}+\dfrac{1}{2}z_\alpha^2G_{2,x}-(\eta G_1+\dfrac{1}{2}\eta^2G_2)_x \\ v_1=(z_\alpha+\dfrac{1}{2}h-\dfrac{1}{2}\eta)G_{1,y}+(\dfrac{1}{2}z_\alpha^2-\dfrac{1}{6}h^2-\dfrac{1}{6}\eta^2+\dfrac{1}{6}\eta h)G_{2,y} \\ v_2=z_\alpha G_{1,y}+\dfrac{1}{2}z_\alpha^2G_{2,y}-(\eta G_1+\dfrac{1}{2}\eta^2G_2)_y \\ S_X=H_t(u_2-u_1)+H\Big\{(u_1u_{\alpha,x}+v_1u_{\alpha,y}+u_\alpha u_{1,x}+v_\alpha u_{1,y})-\Big[\eta_t(G_1+\eta G_2)\Big]_x \\ \qquad -\Big[G_1G_{1,x}+(u_\alpha z_{\alpha,x}+v_\alpha z_{\alpha,y})(G_{1,x}+z_\alpha G_{2,x})+z_\alpha(u_\alpha G_{1,x}+v_\alpha G_{1,y})_x \\ \qquad\qquad +\dfrac{1}{2}z_\alpha^2(u_\alpha G_{2,x}+v_\alpha G_{2,y})_x\Big] \\ \qquad -\Big[\eta(G_1G_2-u_\alpha G_{1,x}-v_\alpha G_{1,y})\Big]_x-\dfrac{1}{2}\Big[\eta^2(G_2^2-u_\alpha G_{2,x}-v_\alpha G_{2,y})\Big]_x\Big\} \\ S_Y=H_t(v_2-v_1)+H\Big\{(u_1v_{\alpha,x}+v_1v_{\alpha,y}+u_\alpha v_{1,x}+v_\alpha v_{1,y})-\Big[\eta_t(G_1+\eta G_2)\Big]_y \\ \qquad -\Big[G_1G_{1,y}+(u_\alpha z_{\alpha,x}+v_\alpha z_{\alpha,y})(G_{1,y}+z_\alpha G_{2,y})+z_\alpha(u_\alpha G_{1,x}+v_\alpha G_{1,y})_y \\ \qquad\qquad +\dfrac{1}{2}z_\alpha^2(u_\alpha G_{2,x}+v_\alpha G_{2,y})_y\Big] \\ \qquad -\Big[\eta(G_1G_2-u_\alpha G_{1,x}-v_\alpha G_{1,y})\Big]_y-\dfrac{1}{2}\Big[\eta^2(G_2^2-u_\alpha G_{2,x}-v_\alpha G_{2,y})\Big]_y\Big\} \\ z_\alpha=\alpha h+(1+\alpha)\eta,\quad \alpha=-0.531 \\ G_1=(hu_\alpha)_x+(hv_\alpha)_y+h_t,\quad G_2=u_{\alpha,x}+v_{\alpha,y} \end{cases}. \tag{3.21}$$

For WNWD,

$$\begin{cases} u_1 = (z_\alpha + \frac{1}{2}h)G_{1,x} + (\frac{1}{2}z_\alpha^2 - \frac{1}{6}h^2)G_{2,x}, \quad u_2 = z_\alpha G_{1,x} + \frac{1}{2}z_\alpha^2 G_{2,x} \\ v_1 = (z_\alpha + \frac{1}{2}h)G_{1,y} + (\frac{1}{2}z_\alpha^2 - \frac{1}{6}h^2)G_{2,y}, \quad v_2 = z_\alpha G_{1,y} + \frac{1}{2}z_\alpha^2 G_{2,y} \\ S_X = H_t(u_2 - u_1), \quad S_Y = H_t(v_2 - v_1) \\ z_\alpha = \alpha h, \quad \alpha = -0.531 \\ G_1 = (hu_\alpha)_x + (hv_\alpha)_y + h_t, \quad G_2 = u_{\alpha,x} + v_{\alpha,y}. \end{cases} \quad . \tag{3.22}$$

For NSWE, $u_1 = u_2 = v_1 = v_2 = S_X = S_Y = 0$. While u_1 and v_1 are the depth-averaged higher-order velocity corrections, u_2 and v_2 do not have a physical meaning. Recall that $H(x, y, t) = \eta(x, y, t) + h(x, y, t)$ is the total water depth, and the bathymetry $h(x, y, t)$ can be written as $h(x, y, t) = h_0(x, y) - B(x, y, t)$ to separate the still water depth h_0 from the landslide B.

At each iteration in time based on the SSP-RK scheme, H in (3.19) and $\phi = H(u_\alpha + u_2)$ and $\psi = H(v_\alpha + v_2)$ in (3.20) are updated using Godunov's scheme (see Toro, 2001). The spatial derivatives in the expressions for u_1, u_2, v_1, v_2, S_X, S_Y, and the terms $g\eta h_x$ and $g\eta h_y$ on the right hand side of (3.20), are calculated by the fourth-order central difference formula; the temporal derivatives (i.e., η_t, and B_t if an analytical expression for the landslide forcing function is not available) in the expressions for G_1, S_X, and S_Y, are calculated with a two-point difference formula using the values stored at each sub-time step in the SSP-RK time-updating scheme. More detailed discussions can be found in Shi et al. (2012).

While u_α and v_α can be directly recovered in NSWE, a matrix system needs to be solved for each velocity component in FNWD and WNWD, since u_2 and v_2 are functions of u_α and v_α. As is the case for the linear solver, here we briefly explain

the process: writing u_2 out fully, we have

$$\begin{aligned} u_2 &= z_\alpha (hu_\alpha)_{xx} + z_\alpha (hv_\alpha)_{yx} + z_\alpha h_{tx} + \frac{1}{2} z_\alpha^2 u_{\alpha,xx} + \frac{1}{2} z_\alpha^2 v_{\alpha,yx} \\ &- C_{\text{FNWD}} \Big[\eta_x (hu_\alpha)_x + \eta_x (hv_\alpha)_y + \eta_x h_t + \eta (hu_\alpha)_{xx} + \eta (hv_\alpha)_{yx} \ , \\ &\qquad + \eta h_{tx} + \eta \eta_x u_{\alpha,x} + \eta \eta_x v_{\alpha,y} + \frac{1}{2} \eta^2 u_{\alpha,xx} + \frac{1}{2} \eta^2 v_{\alpha,yx} \Big] \end{aligned} \tag{3.23}$$

where $C_{\text{FNWD}} = 1$ for FNWD and $C_{\text{FNWD}} = 0$ for WNWD. Separating the terms with u_α from those with v_α, we have

$$\begin{aligned} M_1 &= z_\alpha (hu_\alpha)_{xx} + \frac{1}{2} z_\alpha^2 u_{\alpha xx} \\ &\qquad - C_{\text{FNWD}} \Big[\eta_x (hu_\alpha)_x + \eta (hu_\alpha)_{xx} + \eta \eta_x u_{\alpha,x} + \frac{1}{2} \eta^2 u_{\alpha,xx} \Big] \ . \\ M_2 &= z_\alpha (hv_\alpha)_{yx} + \frac{1}{2} z_\alpha^2 v_{\alpha yx} + z_\alpha h_{tx} \\ &- C_{\text{FNWD}} \Big[\eta_x (hv_\alpha)_y + \eta (hv_\alpha)_{yx} + \eta \eta_x v_{\alpha,y} + \frac{1}{2} \eta^2 v_{\alpha,yx} + \eta_x h_t + \eta h_{tx} \Big] \end{aligned} \tag{3.24}$$

Using Δx to denote the grid spacing in x and i to denote the index for x in the numerical model, we employ the second-order central different formula to discretize M_1 as

$$\begin{aligned} M_{1,i} &= z_{\alpha,i} \frac{(hu_\alpha)_{i+1} - 2(hu_\alpha)_i + (hu_\alpha)_{i-1}}{\Delta x^2} + \frac{1}{2} z_{\alpha,i}^2 \frac{u_{\alpha,i+1} - 2u_{\alpha,i} + u_{\alpha,i-1}}{\Delta x^2} \\ &- C_{\text{FNWD}} \Big[\eta_x \frac{(hu_\alpha)_{i+1} - (hu_\alpha)_{i-1}}{2\Delta x} + \eta \frac{(hu_\alpha)_{i+1} - 2(hu_\alpha)_i + (hu_\alpha)_{i-1}}{\Delta x^2} \ . \\ &\qquad + \eta \eta_x \frac{u_{\alpha,i+1} - u_{\alpha,i-1}}{2\Delta x} + \frac{1}{2} \eta^2 \frac{u_{\alpha,i+1} - 2u_{\alpha,i} + u_{\alpha,i-1}}{\Delta x^2} \Big] \end{aligned} \tag{3.25}$$

On the other hand, M_2 is independent of u_α. The fourth-order central difference scheme and v_α from the previous sub-time step are used to compute M_2. $\phi = H(u_\alpha + u_2) = H(u_\alpha + M_1 + M_2)$ can be rearranged to be $u_\alpha + M_1 = \phi/H - M_2$, for which a matrix system with discretized M_1 can be set up to solve for u_α.

Similarly, writing v_2 out fully results in

$$\begin{aligned} v_2 &= z_\alpha (hu_\alpha)_{xy} + z_\alpha (hv_\alpha)_{yy} + z_\alpha h_{ty} + \frac{1}{2} z_\alpha^2 u_{\alpha,xy} + \frac{1}{2} z_\alpha^2 v_{\alpha,yy} \\ &- C_{\text{FNWD}} \Big[\eta_y (hu_\alpha)_x + \eta_y (hv_\alpha)_y + \eta_y h_t + \eta (hu_\alpha)_{xy} + \eta (hv_\alpha)_{yy} \ , \\ &\qquad + \eta h_{ty} + \eta \eta_y u_{\alpha,x} + \eta \eta_y v_{\alpha,y} + \frac{1}{2} \eta^2 u_{\alpha,xy} + \frac{1}{2} \eta^2 v_{\alpha,yy} \Big] \end{aligned} \tag{3.26}$$

Separating the terms with u_α from those with v_α, we have

$$\begin{aligned} N_1 &= z_\alpha (hv_\alpha)_{yy} + \frac{1}{2} z_\alpha^2 v_{\alpha yy} \\ &\quad - C_{\mathrm{FNWD}} \Big[\eta_y (hv_\alpha)_y + \eta (hv_\alpha)_{yy} + \eta \eta_y v_{\alpha,y} + \frac{1}{2} \eta^2 v_{\alpha,yy} \Big] \\ N_2 &= z_\alpha (hu_\alpha)_{xy} + \frac{1}{2} z_\alpha^2 u_{\alpha xy} + z_\alpha h_{ty} \\ &\quad - C_{\mathrm{FNWD}} \Big[\eta_y (hu_\alpha)_x + \eta (hu_\alpha)_{xy} + \eta \eta_y u_{\alpha,x} + \frac{1}{2} \eta^2 u_{\alpha,xy} + \eta_y h_t + \eta h_{ty} \Big] \end{aligned} \quad . \tag{3.27}$$

Using Δy to denote the grid spacing in y and j to denote the index for y in the numerical model, we employ the second-order central different formula to discretize N_1 as

$$\begin{aligned} N_{1,j} &= z_{\alpha,j} \frac{(hv_\alpha)_{j+1} - 2(hv_\alpha)_j + (hv_\alpha)_{j-1}}{\Delta y^2} + \frac{1}{2} z_{\alpha,j}^2 \frac{v_{\alpha,j+1} - 2v_{\alpha,j} + v_{\alpha,j-1}}{\Delta y^2} \\ &\quad - C_{\mathrm{FNWD}} \Big[\eta_y \frac{(hv_\alpha)_{j+1} - (hv_\alpha)_{j-1}}{2\Delta y} + \eta \frac{(hv_\alpha)_{j+1} - 2(hv_\alpha)_j + (hv_\alpha)_{j-1}}{\Delta y^2} \\ &\quad + \eta \eta_y \frac{v_{\alpha,j+1} - v_{\alpha,j-1}}{2\Delta y} + \frac{1}{2} \eta^2 \frac{v_{\alpha,j+1} - 2v_{\alpha,j} + v_{\alpha,j-1}}{\Delta y^2} \Big] \end{aligned} \quad . \tag{3.28}$$

Again, N_2 is independent of v_α. The fourth-order central difference scheme and u_α from the previous sub-time step are used to compute N_2. A matrix system based on $v_\alpha + N_1 = \psi/H - N_2$ with discretized N_1 can then be set up to solve for v_α.

As an input to our nonlinear numerical solver, the global model can be specified to be FNWD, WNWD, or NSWE. In the dispersive models (FNWD and WNWD), however, local switching from the dispersive model to the nondispersive NSWE is enforced at cells that are dry at still water level (namely, all runups are calculated with NSWE). The local model switching was done by neglecting all higher-order terms (u_1, u_2, v_1, v_2, S_X, and S_Y) and modifying accordingly the matrix systems $\phi = H(u_\alpha + u_2)$ and $\psi = H(v_\alpha + v_2)$ that need to be solved to recover u_α and v_α. We remark that in many shock-capturing dispersive long-wave models – such as Tonelli and Petti 2009, Shi et al. 2012, Tissier et al. 2012, and Kazolea et al. 2014) – an additional wave breaking criterion based on local wave nonlinearity, Froude number, or wave front angle, is often used to determine the onset of model

switching to further improve the performance of the numerical model in capturing breaking waves. However, since we are not concerned with modeling intense wave breaking in this study, we find the additional wave breaking treatment unnecessary.

Various benchmark tests have been conducted to check the performance of the numerical model. A total of six select benchmark tests will be shown in this section: three wave-only tests and three landslide-generated wave tests. In all benchmark tests, FNWD was specified as the global model, and the fifth-order WENO spatial discretization scheme was employed.

3.2.1 Benchmark I: regular waves on a submerged dike

Beji and Battjes (1993) considered regular waves propagating over a submerged bar. With a $A = 0.029$ m wave height and a 2.525 s wave period, spilling breakers were observed on top of the submerged bar. The configuration is illustrated in figure 3.2. Similar experiments were later repeated in Dingemans (1994), from which the data are used here. Comparisons at these six locations are shown in figure 3.3 for five wave periods. The overall agreement is good. However, discrepancies can be seen in figure 3.3(d)(e)(f), where the waves have undergone breaking. Specifically, the computed wave peaks in figure 3.3(d) are noticeably lower than measurements, and the computed oscillatory waves in figure 3.3(e)(f) are not always in phase with measurement.

As an attempt to quantify the discrepancies, we consider the absolute difference, $|\Delta\eta(x,t)|$, between the measured surface elevation, $\eta_{exp}(x,t)$, and the computed surface elevation, $\eta_{num}(x,t)$: we consider the absolute difference between the mea-

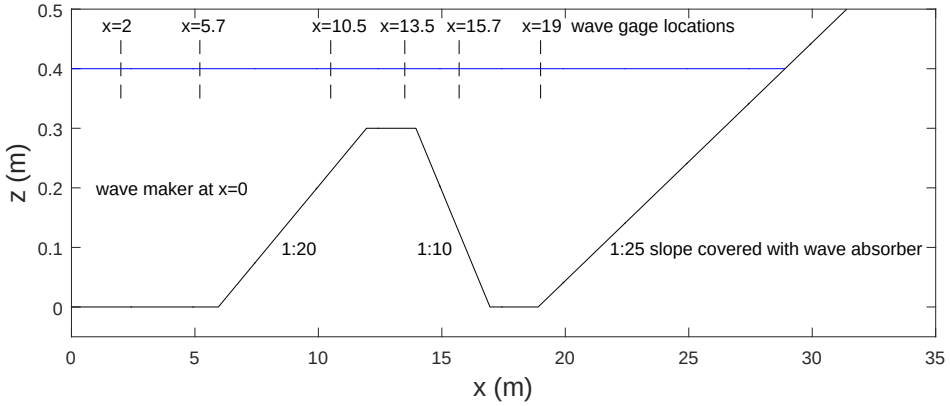

Figure 3.2: Configuration of the experiment in Beji and Battjes (1993).

sured surface elevation $\eta_{exp}(x,t)$ and the computed surface elevation $\eta_{num}(x,t)$:

$$|\Delta\eta(x,t)| = |\eta_{exp}(x,t) - \eta_{num}(x,t)|. \tag{3.29}$$

In plotting, $|\Delta\eta(x,t)|$ is normalized by the landslide incident wave height $A = 0.029$ m. Two types of absolute differences are plotting in figure 3.4 (upper panel): the absolute difference averaged over five wave periods of measurements shown in the plotting window in figure 3.3, and the maximum absolute difference in the same plotting window. While the average difference can be interpreted as the overall fit between measurements and computed results, the maximum difference highlights local discrepancies. The location of the submerged bar and a sample water surface snapshot are also shown in figure 3.4 (lower panel). It can be seen that discrepancies start to grow after $x = 10.5$ m, namely, after wave breaking has occurred on top of the submerged bar; in figure 3.4 (lower panel), it can be observed that the water surface is a lot more irregular behind the submerged bar.

3.2.2 Benchmark II: solitary wave runup on a slope

Synolakis (1987) measured water surface elevations at various locations during the

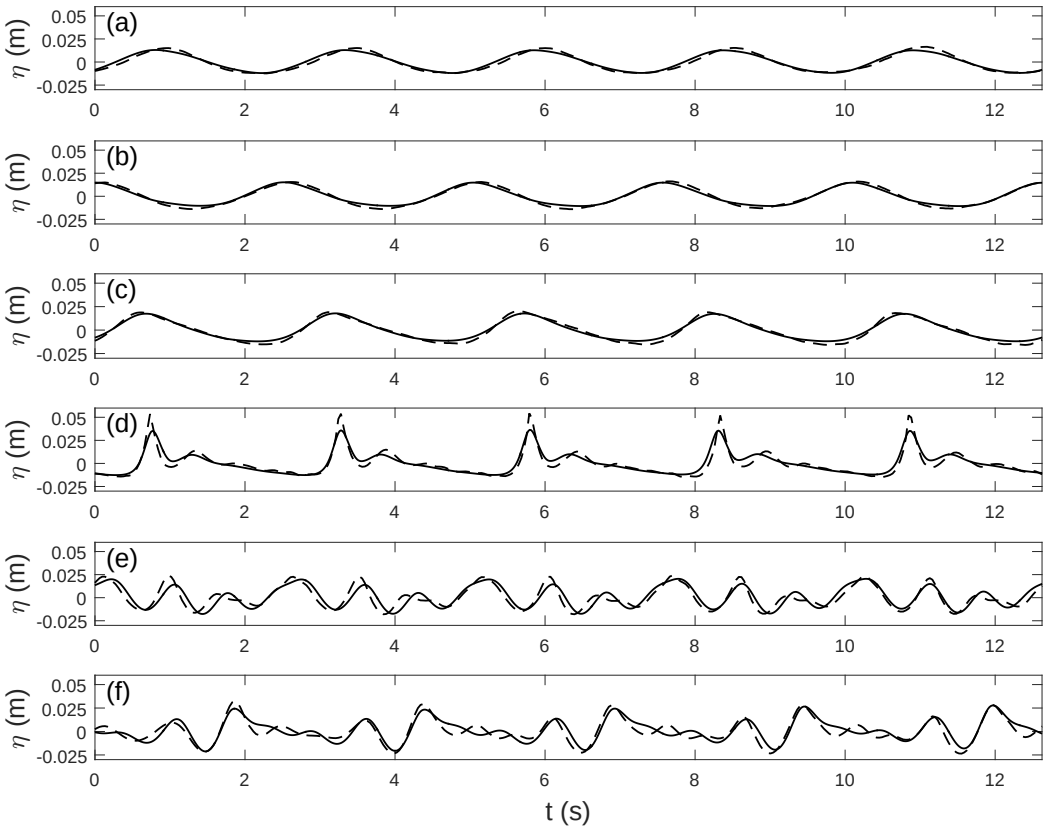

Figure 3.3: Comparison of our numerical results with the experimental data from Dingemans (1994). (a) $x = 2$ m; (b) $x = 5.7$ m; (c) $x = 10.5$ m; (d) $x = 13.5$ m; (e) $x = 15.7$ m; (f) $x = 19$ m. Dashed line: experimental data; solid line: numerical results.

runup and rundown of a solitary wave on a $1 : 19.85$ slope. Here, we used the data for a plunging solitary wave with $A/d = 0.3$ (digitized from Synolakis 1986). Snapshots of the wave field on the slope are shown in figure 3.5 at selected times. It can be seen that the overall agreement is good, although discrepancies are obvious when wave-breaking likely occurred, figure 3.5(b), and especially during back-wash and the back-wash hydraulic jump, figure 3.5(e) and (f). We further remark that due to the lack of any empirical friction terms in the numerical model, since we do not intend to tune the model to fit certain experimental data in this study, a very thin run-up tongue can be clearly seen in the numerical results.

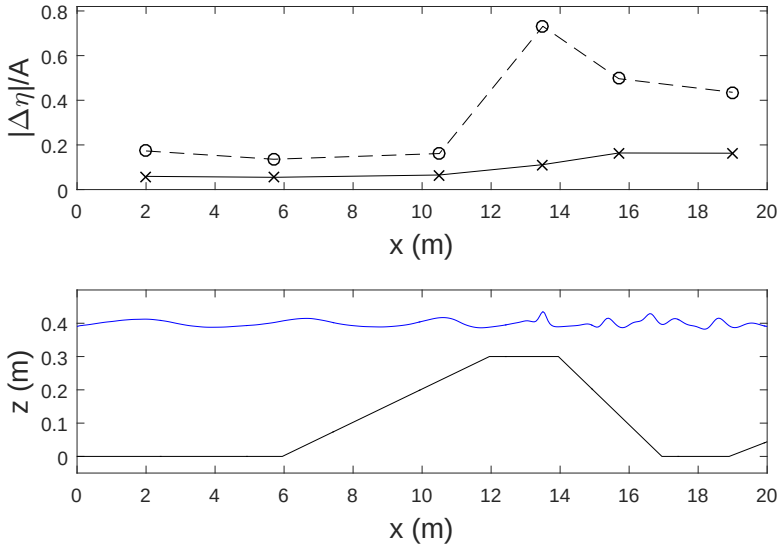

Figure 3.4: Upper panel: temporally-averaged difference (cross) and maximum-in-time difference (circle) in the free surface elevation between the experimental measurements from Dingemans (1994) and the numerical results, of regular waves propagating over a submerged bar, as functions of space. Lower panel: location of the submerged bar; a snapshot sample of the computed water surface is also shown.

As an attempt to quantify the discrepancies, we again consider the absolute difference between the measured surface elevation and the computed surface elevation. In figure 3.6, we plot the absolute differences (both averaged and maximum), normalized by the incident wave height A, as a function of time. It can be seen that figure 3.6 indeed reflects the behaviors observed in figure 3.5; namely, locally significant discrepancies at $t^* = 20$ during wave-breaking, and an overall poor match after the onset of the back-wash hydraulic jump, $t^* > 60$. We remark that such discrepancies are common in shock-capturing long-wave models without further friction and wave-breaking treatments, and that snapshots after $t^* = 60$, when the discrepancies are large, are often not shown in studies.

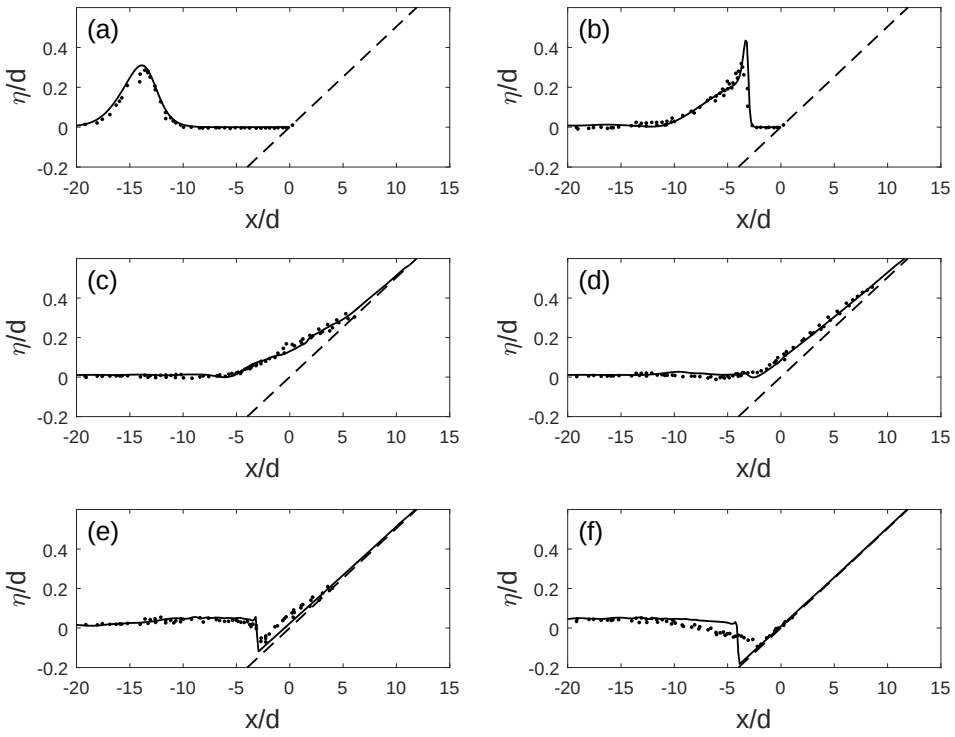

Figure 3.5: Snapshots of the run-up of a solitary wave with $A/d = 0.3$ on a $1 : 19.85$ slope. Dot: experimental data (digitized from Synolakis 1986); solid line: numerical results; dashed line: the $1 : 19.85$ slope. (a) $t^* = 10$; (b) $t^* = 20$; (c) $t^* = 30$; (d) $t^* = 40$; (e) $t^* = 60$; (f) $t^* = 70$. t^* is defined according to Synolakis (1987).

3.2.3 Benchmark III: solitary wave runup on a conical island

Liu et al. (1995) measured the runup of solitary waves on a conical island, in a wave basin 30 m wide and 25 m long. The island had a 7.2 m diameter at the base and a $1 : 4$ slope. Three different values of wave nonlinearity were tested: $\epsilon = 0.05, 0.1, 0.2$. The $\epsilon = 0.1$ case is shown here as a benchmark problem. The free surface elevation at various locations and the runup around the island were measured. The figure from Liu et al. (1995) illustrating the wave gauge locations

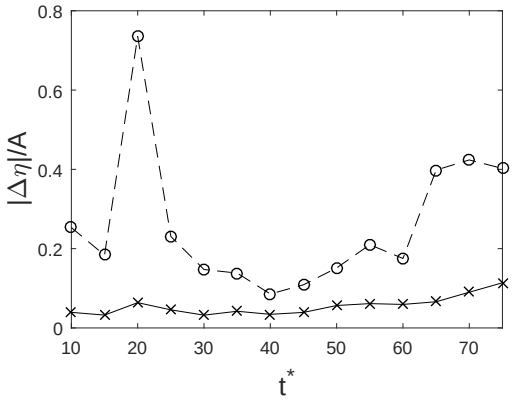

Figure 3.6: Spatially-averaged difference (cross) and maximum-in-space difference (circle) in the free surface elevation between the experimental measurements from Synolakis (1986) and the numerical results, of the runup of a $A/d = 0.3$ solitary wave on a $1 : 19.85$ slope, as a function of time.

are shown in figure 3.7.

The numerical results for the free surface elevation at six different locations are compared with experimental data (digitized from Liu et al., 1995) in figure 3.8. Overall, the main wave is captured well by the numerical model. However, the rundown is not captured accurately, which is revealed by the discrepancy between the trailing waves in figure 3.8(b)(c), i.e. wave gauge 3 and wave gauge 6, both of which are located on the slope on the front side of the island; such discrepancy is not observed at other wave gauge locations, e.g. wave gauge 10 on the side of the island and wave gauge 16 on the lee side of the island, since intense rundown occurred only on the front side. The rundown and the back-wash hydraulic jump are highly sensitive to the numerical treatment of runup, bottom friction, and wave breaking. Therefore, without additional tuning parameters in our model, we do not expect it to perform well in capturing intense rundown and wave breaking.

The maximum runup (which occurred at a different time at each location) around the island is shown in figure 3.9. Since extremely thin runup tongue exists

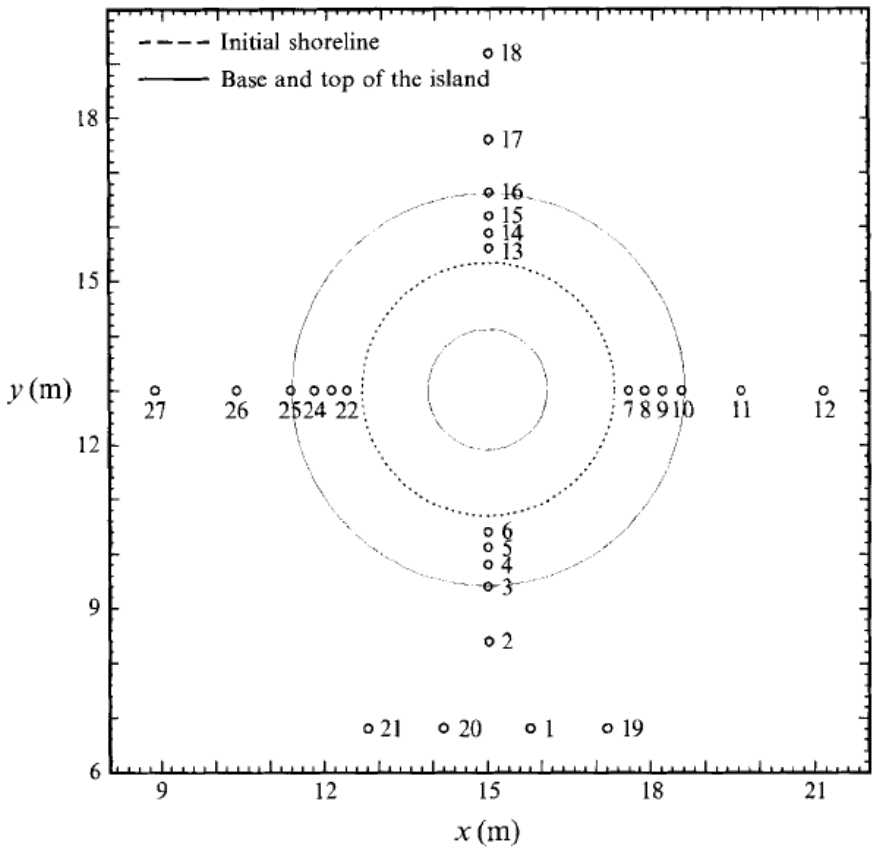

Figure 3.7: The figure from Liu et al. (1995) showing the wave gauge locations. The wave maker is located at $y = 0$.

in the numerical results due to the lack of a bottom friction term, as discussed in the previous benchmark problem, in plotting figure 3.9 the runup front is defined as the location where the total water depth becomes less than 1 mm. While discrepancy can be observed in figure 3.9, the overall agreement between the numerical results and the experimental measurement appears satisfactory.

3.2.4 Benchmark IV: landslide-generated waves in constant depth

Whittaker et al. (2015, 2017) carefully measured water waves generated by a sub-

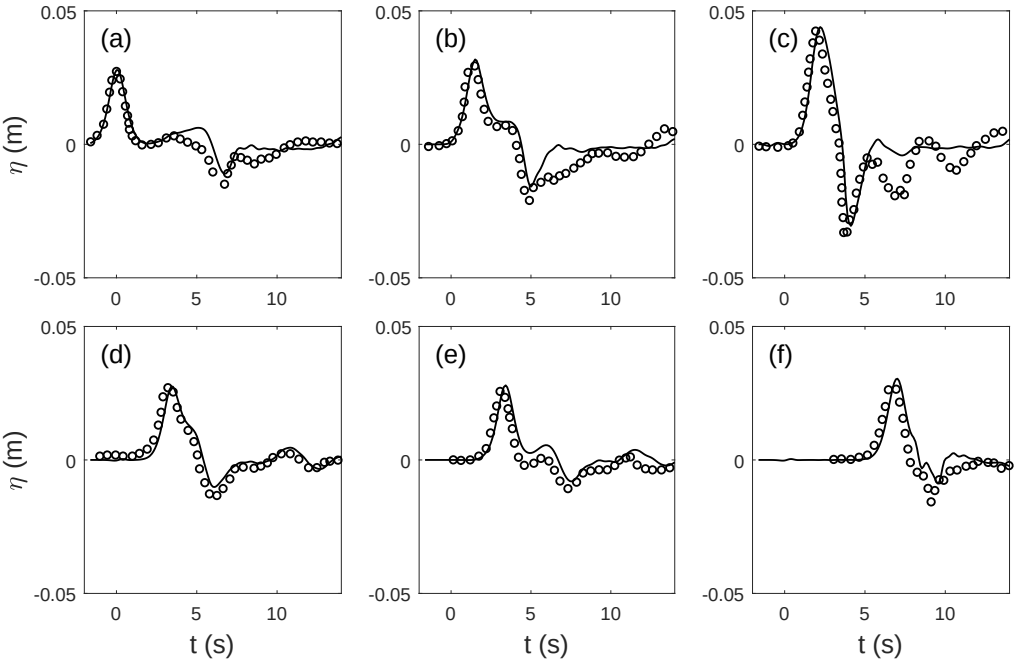

Figure 3.8: Time series of the free surface elevation due to a $\epsilon = 0.1$ solitary wave at six different locations. (a): wave gauge 1; (b): wave gauge 3; (c): wave gauge 6; (d): wave gauge 10; (e): wave gauge 12; (f): wave gauge 16. Circle: experimental data; solid line: numerical results.

marine solid landslide in constant water depth. A semi-elliptical landslide of length $L_b = 0.5$ m and height $A_b = 0.026$ m was used in the experiments. Since a semi-ellipse has discontinuities at the two edges and cannot be accurately resolved by long-wave models, in our simulations a Gaussian-shaped landslide of the same height and enclosed area is used – the two shapes are compared in figure 3.10. As has been shown in Chapter 2, matching the enclosed area is more important than matching the exact shape. Two water depths were used in the experiments, $d = 0.175$ m and $d = 0.35$ m. Here we consider only experimental cases with the shallower water depth, as frequency dispersion is significant in the deeper-depth cases and the long-wave model becomes inaccurate.

Two representative cases, Run 22 and Run 24 from Whittaker (2013), are

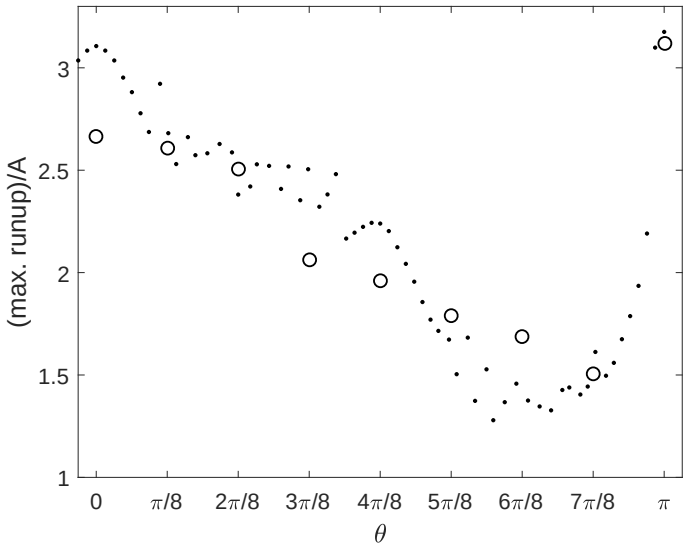

Figure 3.9: Maximum runup around a conical island (normalized by the incident wave height $A = 0.032$ m) due to a $\epsilon = 0.1$ solitary wave. $\theta = 0$ corresponds to the front side of the island, and $\theta = \pi$ corresponds to the lee side of the island. Circle: experimental data; dot: numerical results.

presented here: in Run 22, the initially stationary landslide accelerated at $0.153g$ until the speed of the landslide V_b reaches $Fr = V_b/\sqrt{gd} = 0.25$, stayed at a constant speed for 2 s, and then decelerated at $0.153g$ until the speed became zero; in Run 24, the conditions were similar, except that the landslide accelerated for a longer period of time to reach $Fr = 0.5$. High resolution data in both space and time from Whittaker (2013) are compared with the numerical results in figure 3.11 (Run 22) and figure 3.12 (Run 24) at three different times. The center of the landslide was at $x = 0$ m when $t = 0$ s. It can be seen that although the actual landslide shapes used are different, the overall wave characteristics are captured well by the numerical model. The obvious discrepancy occurs for larger Fr (Run 24), where the model underpredicts the amplitudes of the shorter oscillatory waves, e.g., figure 3.12(c). Nonetheless, we note that the long leading wave and the overall features are accurately predicted.

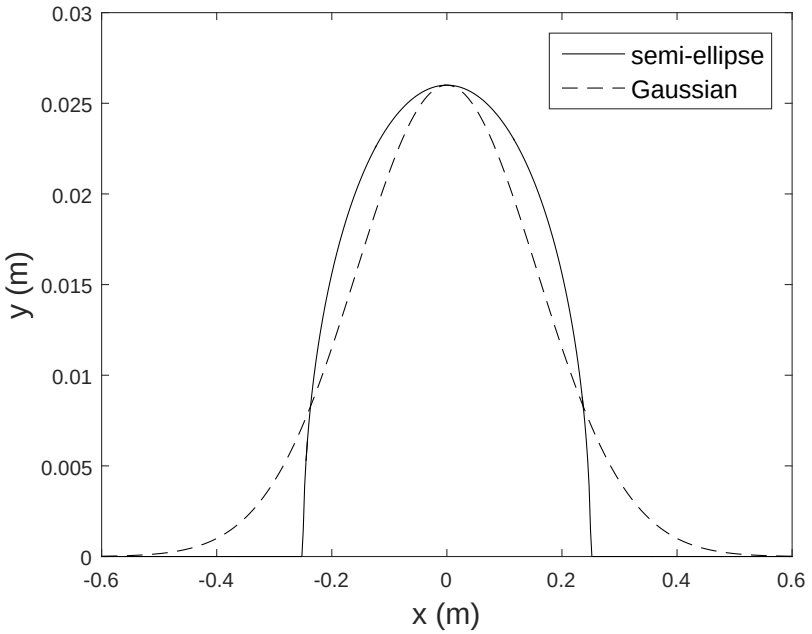

Figure 3.10: Comparison of the semi-elliptical landslide used in Whittaker (2013) with a Gaussian-shaped landslide of identical wave height and enclosed area.

As an attempt to quantify the discrepancies, we again plot both the spatially averaged absolute difference and the maximum-in-space absolute difference (over the range of the plotting window $-3\text{ m} \leq x \leq 5\text{ m}$). The differences, normalized by the landslide thickness A_b, for Run 22 are shown in figure 3.11, and those for Run 24 are shown in 3.12. Overall, the agreement is good and the absolute differences are small. However, the differences grow in time in Run 24 due to the developing short oscillatory waves observed in figure 3.12, which may be sensitive to the exact landslide shape and too dispersive to be captured accurately by FNWD.

3.2.5 Benchmark V: landslide-generated waves on a slope, I

Sue et al. (2011) performed experiments on water waves generated by a subma-

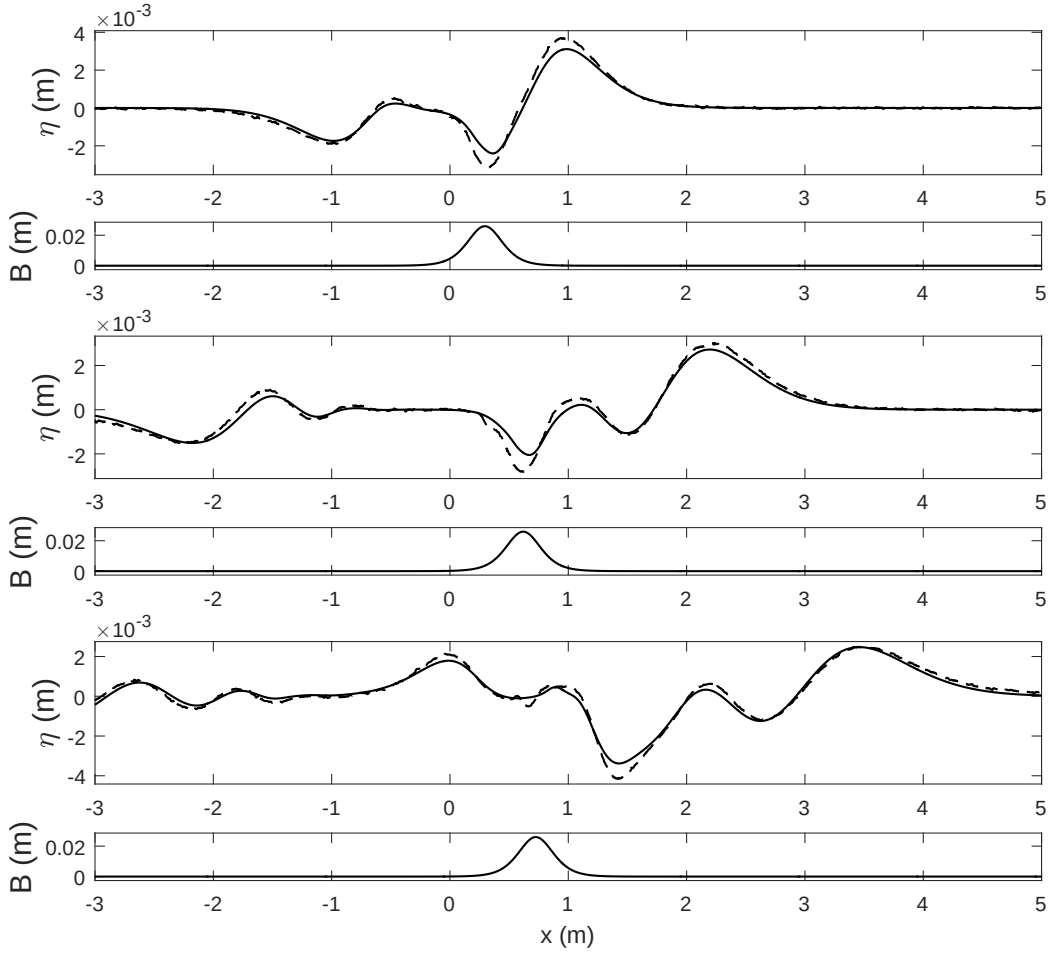

Figure 3.11: Comparison between the experimental data from Whittaker (2013) for Run 22 and our numerical results. Top two panels: $t = 1$ s; middle two panels: $t = 2$ s; bottom two panels: $t = 3$ s. Dashed line: experimental data; solid line: numerical results.

rine solid landslide, free-sliding down a 15° incline into a constant water depth of $d = 0.435$ m. In the experiments, the connection between the slope and the flat channel was smoothed by a pair of third-order polynomial guide rails (as a result, water could flow underneath the slope), which were not replicated in the numerical model. A semi-elliptical landslide (with an adjustable density) of length $L_b = 0.5$ m and height $A_b = 0.026$ m was used in the experiments. A Gaussian-shaped landslide of the same height and enclosed area was used in the numerical simulations instead. Various initial landslide submergence depths were tested in

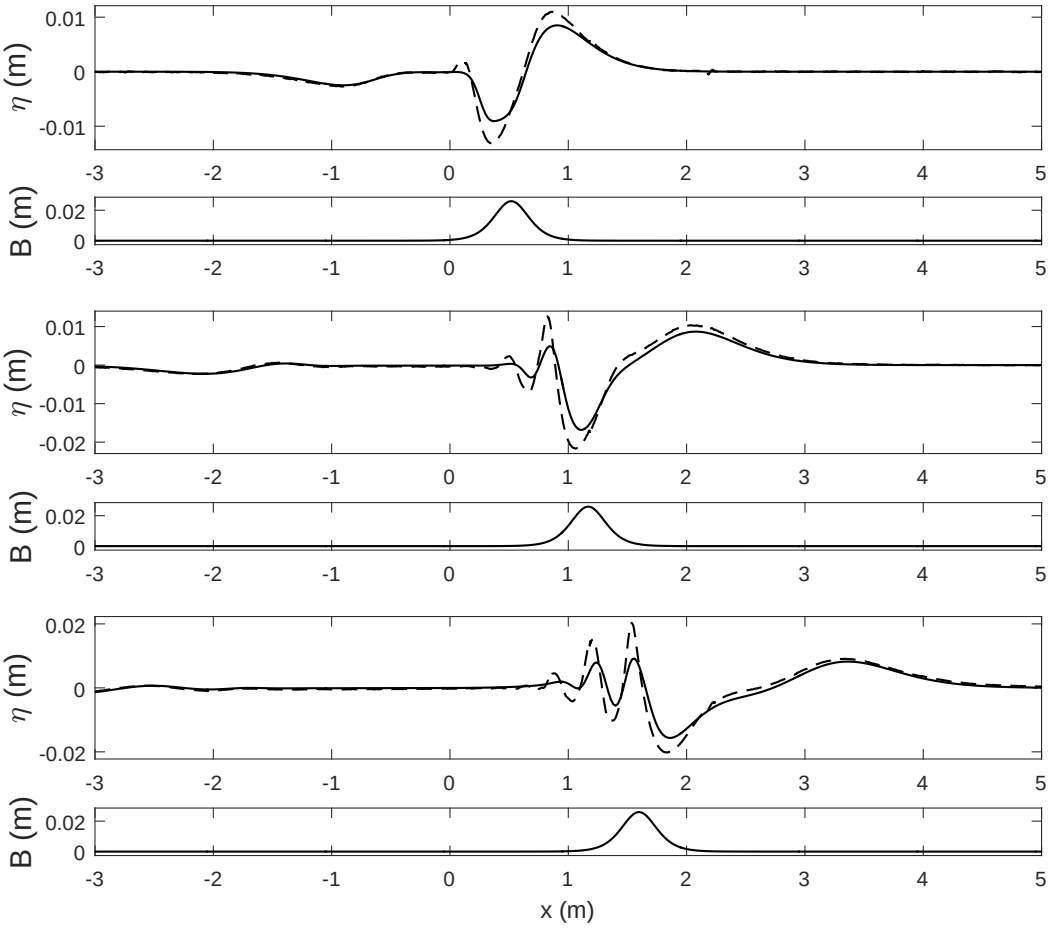

Figure 3.12: Comparison between the experimental data from Whittaker (2013) for Run 24 and our numerical results. Top two panels: $t = 1$ s; middle two panels: $t = 2$ s; bottom two panels: $t = 3$ s. Dashed line: experimental data; solid line: numerical results.

the experiments. However, since the generated waves quickly become dispersive as they travel into deeper water (the long-wave requirement $O(\mu^2) \ll 1$ is greatly violated as $\mu = d/L_b = 0.87$ in the constant depth region), to maximize long-wave model validity we consider only the case with the shallowest initial submergence depth, where the still water depth above the initial center of mass of the landslide is $0.1L_b = 0.05$ m. The landslide's specific gravity for this case is 4.02. The landslide's position in the numerical simulations was specified based on the experimental measurement, and $x = 0$ was defined at the initial shoreline and the initial

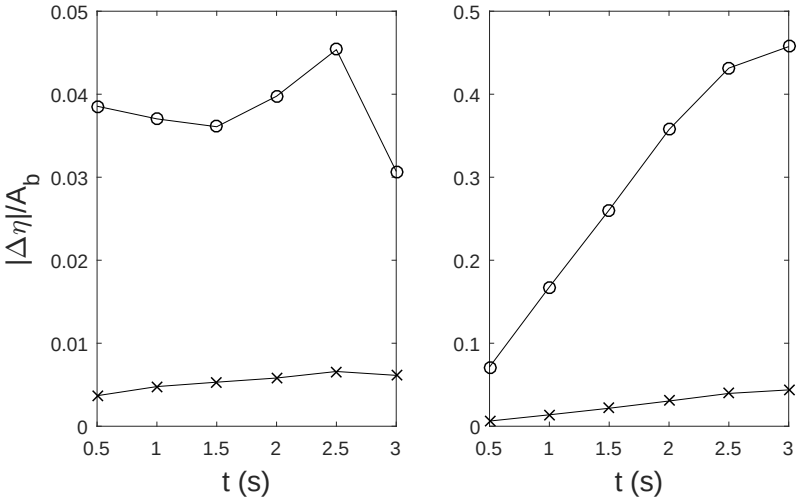

Figure 3.13: Spatially-averaged difference (cross) and maximum-in-space difference (circle) in the free surface elevation between the experimental measurements from Whittaker (2013) and the numerical results. Left panel: Run 22; right panel: Run 24.

center of mass of the landslide was at $x = 0.29$ m when $t = 0$ s.

Experimental data from Sue et al. (2011) are compared with our numerical results in figure 3.14 and figure 3.15 at six different times. While the numerical model captures the overall wave characteristics, discrepancies are noticeable. Particularly, in the numerical results, the spiky wave that starts to grow just behind the landslide in figure 3.14(b)(c) eventually overtakes the landslide and becomes short, tall, and unphysical (figure 3.14). We remark that these spiky waves are not numerical noises. They frequently occur when the long-wave assumption is greatly violated, in both numerical solutions and analytical solutions. A quick estimate of their wavelengths based on the figures yields about $\simeq 0.2$ m in a water depth of 0.435 m, which correspond to $\mu \sim 2$, far from the long-wave requirement $O(\mu^2) \ll 1$. Despite so, we note that the long-wave components (i.e. the leading waves) are still captured fairly accurately in this scenario.

Again, as an attempt to quantify the discrepancies, the spatially-averaged (over

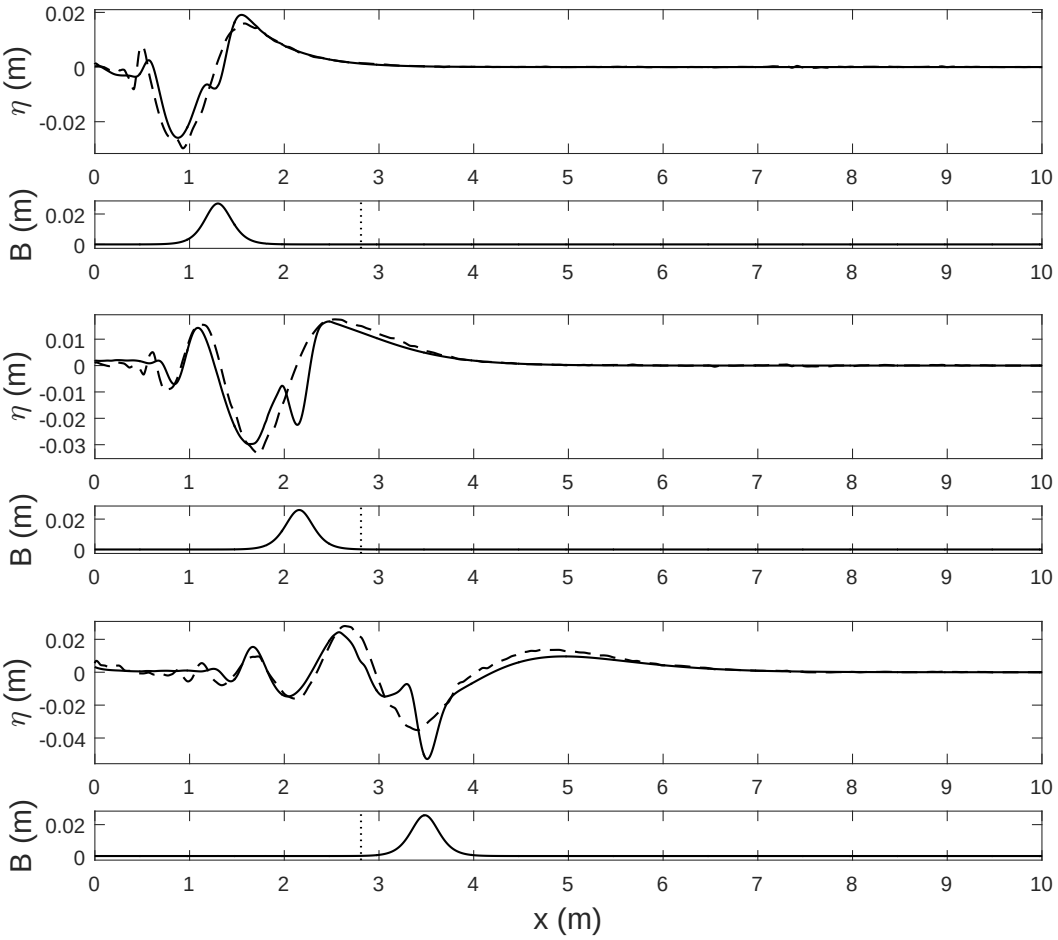

Figure 3.14: Comparison between the experimental data from Sue et al. (2011) and our numerical results. Top two panels: $t = 1.2$ s; middle two panels: $t = 1.8$ s; bottom two panels: $t = 3$ s. Dashed line: experimental data; solid line: numerical results; dotted line: the toe of the slope.

the plotting window in figures 3.14 and 3.15) difference and the maximum-in-space difference, normalized by the landslide thickness A_b, are shown in figure 3.16 as functions of time. While the average difference grows relatively steadily in time as the waves travel into deeper water (and thus the long-wave model becomes less accurate), the maximum difference clearly reflects the occurrence of the spiky waves, as the maximum difference greatly increases after $t = 3$ s, when the spiky waves become large in amplitudes.

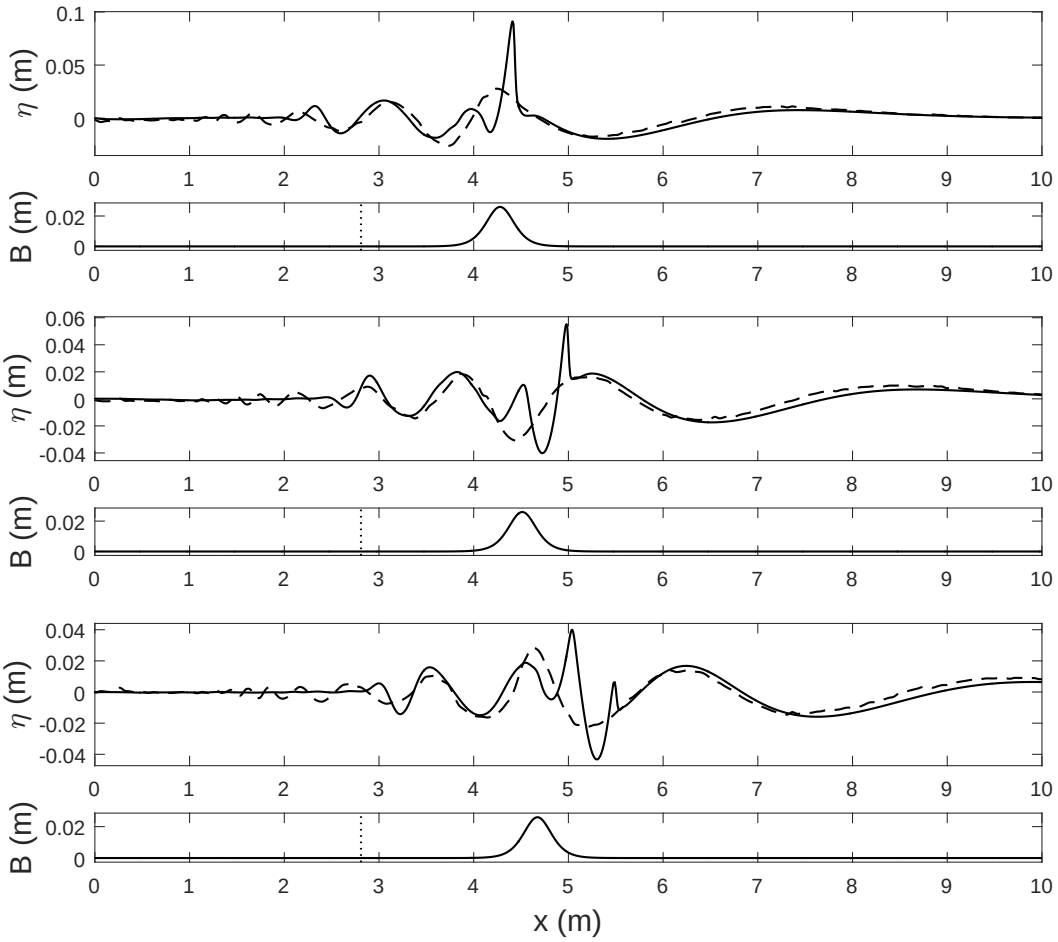

Figure 3.15: Comparison between the experimental data from Sue et al. (2011) and our numerical results. Top two panels: $t = 4.2$ s; middle two panels: $t = 4.8$ s; bottom two panels: $t = 5.4$ s. Dashed line: experimental data; solid line: numerical results; dotted line: the toe of the slope.

3.2.6 Benchmark VI: landslide-generated waves on a slope, II

Zhou (2008) and Zhou and Teng (2010) measured water waves generated by a submarine landslide on a slope, installed in a wave flume which is 9.75 m long, 0.15 m wide, and 0.41 m deep. A total of ten different cases was tested, which cover three different angles of inclination: $5°, 10°, 15°$. They designed the experiments specifically to validate their $O(\mu^4)$-accurate long-wave model. Therefore, it is pos-

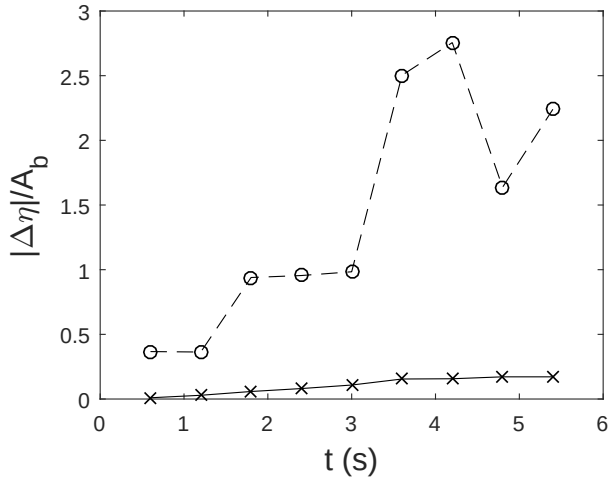

Figure 3.16: Spatially-averaged difference (cross) and maximum-in-space difference (circle) in the free surface elevation between the experimental measurements from Sue et al. (2011) and the numerical results.

sible that the generated waves are too frequency dispersive for our $O(\mu^2)$-accurate model to capture in some, if not all, cases. Since Case 1 in Zhou (2008) will be used as an application example in Chapter 6, here we test the performance of our numerical model against the experimental data for this case.

In the experiment, the landslide had a truncated cosine shape with a height of 0.033 m and an enclosed area (in 2DH) of 0.00675 m^2 and traveled down a slope of 5°. In the numerical simulation, we again used a Gaussian-shaped landslide of identical height and enclosed volume – the resulting characteristic length for the Gaussian-shaped landslide is 0.326 m. The landslide was initially located at 0.732 m (horizontal distance) away from the shoreline. It was pulled down the slope for a fixed distance by a weight connected to a pulley system before being slowed down to rest by drag and friction. Zhou (2008) curve fitted the measured landslide motion and found that the landslide location could be approximated as follows: the landslide accelerated from rest at 0.59 m^2/s for 0.89 s, and then decelerated at -1.2 m^2/s until the landslide came to rest. The curve fitted landslide location

was specified in our numerical simulation. Two wave gauges were installed in the experiment to measure the free surface elevation: wave gauge 1 was installed at 1.109 m (horizontal distance) away from the still water shoreline, and wave gauge 2 was installed at 1.657 m (horizontal distance) away from the still water shoreline.

The numerical results are compared with experimental data (digitized from Zhou, 2008) at wave gauge 1 in figure 3.17 and at wave gauge 2 in figure 3.18. Overall, the agreement is satisfactory. However, the trailing waves in figure 3.18 are not captured well by the long-wave numerical model. The water depth at this location is 0.145 m; the landslide length is 0.326 m – a quick estimate of μ gives $\mu \simeq 0.145/0.326 = 0.445$, which is likely too dispersive for the $O(\mu^2)$-accurate FNWD to capture. The absolute differences, normalized by the landslide thickness, can again be calculated to quantify the discrepancies. The averaged difference at wave gauge 1 is 0.0146, and the maximum difference is 0.0295. The average difference at wave gauge 2 is 0.0829, and the maximum difference is 0.257. The difference values at wave gauge 2 are significantly larger than those at wave gauge 1 likely because frequency dispersion has become stronger in the deeper water than can be accurately captured by FNWD. It is also possible that the actual location of wave gauge 2 was misreported, since a consistent phase difference can be observed in 3.18. In addition, many internal inconsistencies in the experimental parameters reported in Zhou (2008) were found.

3.3 Summary

In this chapter, we presented the five sets of long-wave equations that were solved numerically: LSWE, LWD, NSWE, WNWD, and FNWD. These long-wave equa-

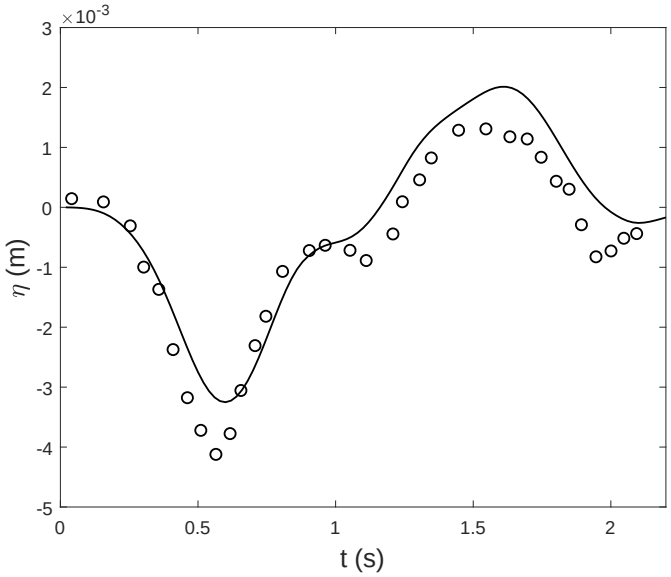

Figure 3.17: Experimental data (circle) digitized from Zhou (2008) compared with numerical results (solid line) at wave gauge 1.

tions were rederived to correctly allow for a significantly changing bathymety due to a moving landslide, and to ensure consistent scaling assumptions so that the formal accuracy of each long-wave model can be directly compared. A finite-difference-based numerical solver was constructed to solve the linear equations, and a hybrid finite-volume/finite-difference shock-capturing numerical solver was constructed to solve the nonlinear equations. Each solver was tested against either analytical solutions or experimental data. The governing equations were deliberately rearranged so that the same solvers can be easily adjusted to solve the different long-wave equations. As a result, the numerical errors were kept as universal as possible (since the same solvers were used) when comparing the numerical results predicted by different long-wave models.

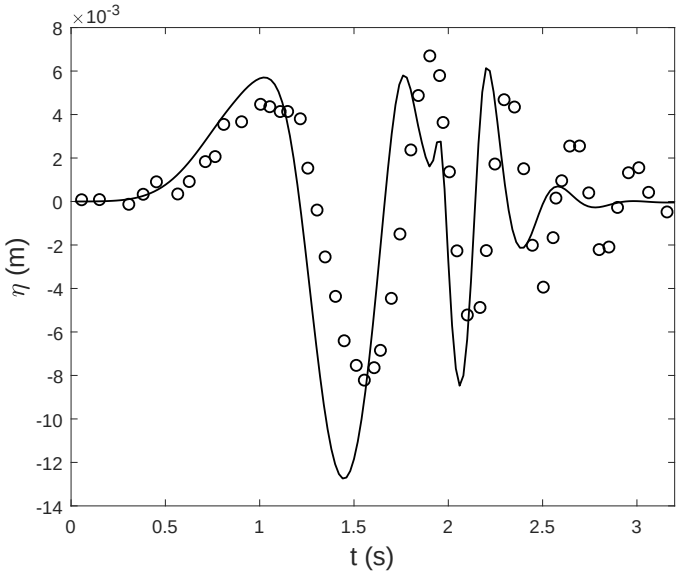

Figure 3.18: Experimental data (circle) digitized from Zhou (2008) compared with numerical results (solid line) at wave gauge 2.

CHAPTER 4

CRITERIA FOR DETERMINING MODEL VALIDITY

In this chapter, we consider four idealized submarine-landslide-generated tsunami scenarios: 1DH constant depth, 1DH on a slope, 2DH constant depth, and 2DH on a slope. In each case, a Gaussian-shaped landslide traveling at a constant speed is prescribed. As a result of specifying idealized scenarios, for each scenario three or four input parameters can be defined. The parameters cover the height of the landslide, the length of the landslide, the speed of the landslide, the water depth, and the angle of inclination. Based on the input parameters and analytical knowledge, semi-analytical expressions can then be proposed to estimate the nonlinearity and the strength of frequency dispersion in a landslide wave generation problem – the two important factors that determine the validity of a long-wave model.

By comparing the numerical results based on a linear model (LSWE or LWD) with those based on a nonlinear model (NSWE or WNWD), the threshold when nonlinearity becomes important can be determined; likewise, by comparing the numerical results based on a nondispersive model (LSWE or NSWE) with those based on a dispersive model (LWD or WNWD), the threshold when frequency dispersion becomes important can be determined. After performing numerous simulations based on FNWD and WNWD, we find that the parameter space in which FNWD is valid but WNWD is not is extremely limited in the submarine-landslide-generated tsunami problem – WNWD and FNWD are essentially interchangeable, although FNWD is computationally more expensive. Therefore, only LSWE, LWD, NSWE, and WNWD are considered as model choices. A more accurate long-wave model is also computationally more expensive. Thus, to minimize computation cost, it

may be desirable to use the simplest acceptable long-wave model to simulate the wave generation process of a landslide tsunami problem. In the following sections, we shall describe each scenario in detail, derive semi-analytical expressions, and propose criteria for determining the validity of each model.

4.1 1DH landslide-generated waves in constant depth

Consider an idealized scenario in an 1DH channel of constant depth d, as sketched in figure 4.1. The landslide is Gaussian-shaped, A_b thick, L_b long, and travels at a constant speed V_b; the dimensional landslide forcing function is

$$B'(x',t') = A_b e^{-8(\frac{x'-V_b \cdot t'}{L_b})^2}. \tag{4.1}$$

Three dimensionless input parameters describe the problem:

$$\begin{cases} Fr = V_b/\sqrt{gd}: & \text{landslide speed } (0 < Fr < 1) \\ \delta = A_b/d: & \text{landslide shape nonlinearity} \\ \gamma = d/L_b: & \text{relative water depth} \end{cases} . \tag{4.2}$$

δ is highly related to the nonlinearity of the generated waves, γ is highly related to the strength of frequency dispersion of the generated waves, and Fr controls the forcing strength of the landslide, which may have effects on both nonlinearity and frequency dispersion. Only $0 < Fr < 1$ is considered in this study. We shall consider the location x' where $B'(x',t') = A_b$ in (4.1) as the landslide location or the landslide center, and we consider the still water depth without the presence of a landslide at this location as the water depth at the landslide location.

The dimensionless LSWE analytical solution for water waves forced by a solid landslide moving at a constant speed in constant water depth has been derived by

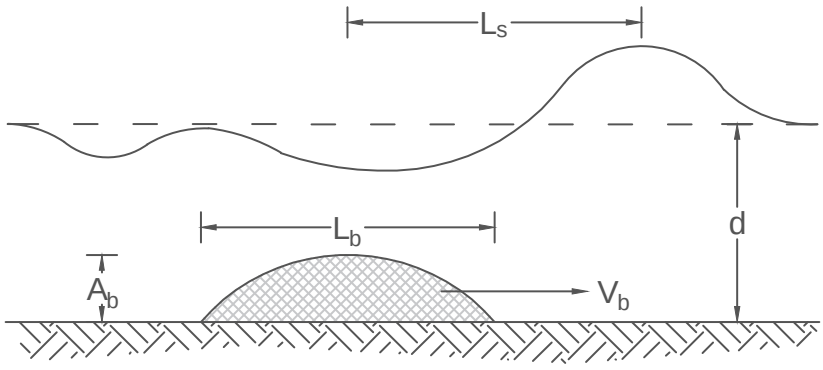

Figure 4.1: A definition sketch for the 1DH landslide-generated waves in constant depth scenario. The quantities are in dimensional form.

Tinti et al. (2001) and shown in Chapter 2:

$$\eta(x,t) = \frac{Fr}{2(1-Fr)}B(x-t) - \frac{Fr}{2(1+Fr)}B(x+t) - \frac{Fr^2}{1-Fr^2}B(x - Fr\cdot t). \quad (4.3)$$

(4.3) suggests that the solution to this problem can be seen as a superposition of three waves – a right-going wave (η_+) traveling at the wave celerity, a left-going wave (η_-) traveling at the wave celerity, and a trapped wave (η_{Fr}) that stays on top of the landslide. The right-going wave (η_+) and the trapped wave (η_{Fr}) travel in the same direction but at different speeds. Hence, after a sufficient propagation time, the two waves eventually separate and the leading wave solution is simply η_+ (for $0 < Fr < 1$). Since the horizontal length scales of η_+ and η_{Fr} are both determined by B, when the centers of η_+ and η_{Fr} are one landslide length (L_b, or one when normalized) apart, the two waves can be seen as having separated from each other.

To consistently compare the leading waves generated under different input conditions (Fr, δ, γ), we shall focus on the instant t_s when the leading wave is one wavelength ahead of the landslide (i.e., when $L_s = L_b$ in figure 4.1). This instant

marks the end of the leading wave generation process – past this instant, the landslide no long impacts the leading wave according to (4.3), and the leading wave can be treated as a freely propagating wave. Because the leading wave and the landslide each travels at a known constant speed, this instant (expressed in dimensionless form) can be straightforwardly determined based on the LSWE solution (4.3) to be $t_s = 1/(1 - Fr)$ (normalized by $L_b/\sqrt{gd}$) for the right-going leading wave.

Similarly, after a sufficient propagation time, the left-going wave η_- eventually separates from η_+ and η_{Fr} to become the left-going leading wave. The instant when the left-going wave is one landslide length (L_b, or one when normalized) away from the landslide can be found to be $t_s = 1/(1 + Fr)$. Combining the expressions for the two leading waves, we end up with

$$t_s = \frac{1}{1 - Fr\cos\theta}, \tag{4.4}$$

where $\theta = 0$ in the positive (right) x direction, and $\theta = \pi$ in the negative (left) x direction. We introduce the use of θ here, as it will later be used extensively in the 2DH case. $t = t_s$ marks the end of the landslide wave generation stage. The wave propagation stage begins past this instant. Since the leading wave is no longer affected by the landslide and propagates freely, the landslide tsunami propagation stage is essentially the same as the earthquake tsunami problem. The landslide wave generation stage is the new physics that must be accounted for in the landslide tsunami problem. The goal of this chapter is to determine which long-wave model can be used to model the landslide wave generation stage, i.e., for $0 < t < t_s$.

4.1.1 Estimators of the strength of nonlinearity and the strength of frequency dispersion

We recall that long-wave models are based on two important parameters: μ^2, which indicates how strong frequency dispersion is, and ϵ, which indicates how strong nonlinearity is. LSWE is valid only when $O(\epsilon) \ll 1$ and $O(\mu^2) \ll 1$. When ϵ becomes sufficiently large, nonlinearity becomes important and a nonlinear model (NSWE or WNWD) should be used; when μ^2 becomes sufficiently large, frequency dispersion becomes important and a dispersive model (LWD or WNWD) should be used; when both ϵ and μ^2 become sufficiently large, a nonlinear and dispersive model (WNWD) must be used. Therefore, we can quantify model validity thresholds if ϵ and μ^2 can be expressed in terms of the input parameters, and the magnitudes when they each become "sufficiently large" are found. Again, we remark that based on numerical simulations, we have found WNWD and FNWD to be essentially interchangeable for the landslide wave problems considered. Hence, FNWD will not be considered as a model choice in this chapter.

Inspecting the analytical solution (4.3), we observe that the spatial scales of generated waves are related to the landslide scales as:

$$\epsilon \simeq \delta \left| \frac{Fr \cos\theta}{2(1 - Fr\cos\theta)} \right|, \quad \mu^2 \simeq \gamma^2. \tag{4.5}$$

Nonlinear effects and frequency dispersion effects not only depend on the spatial scales of the water waves but also grow in time regardless of the initial wave conditions. Since the propagation time of interest is $t = t_s$, it is necessary that $O(t_s) \ll 1/\epsilon$ in linear models and $O(t_s) \ll 1/\mu^2$ in nondispersive models. In addition, the landslide is assumed to be thin, $O(\delta) \ll 1$, in deriving the LSWE

solution (4.3). Altogether, we write the scaling requirements as

$$\max(\epsilon, \epsilon t_s) + C_\delta \delta \leq C_\epsilon, \quad \max(\mu^2, \mu^2 t_s) \leq C_{\mu^2}, \tag{4.6}$$

where C_ϵ is a sufficiently small number that makes linear models sufficiently accurate, C_{μ^2} is a sufficiently small number that makes nondispersive models sufficiently accurate, and C_δ is an empirical coefficient added to account for the requirement on the landslide thickness. Combining (4.5) and (4.6), we have

$$\overline{\epsilon} = \delta |\frac{Fr\cos\theta}{2(1 - Fr\cos\theta)}| \max(1, t_s) + C_\delta \delta \leq C_\epsilon, \quad \overline{\mu^2} = \gamma^2 \max(1, t_s) \leq C_{\mu^2}, \tag{4.7}$$

where t_s is given by (4.4), $\theta = 0$ for the right-going wave, and $\theta = \pi$ for the left-going wave. We shall refer to $\overline{\epsilon}$ as the estimator of the strength of nonlinearity in a landslide wave generation problem, and $\overline{\mu^2}$ as the estimator of the strength of frequency dispersion in a landslide wave generation problem. Our next step is examine the performance of $\overline{\epsilon}$ and $\overline{\mu^2}$ in capturing the nonlinear and frequency dispersion effects, respectively, in the parameter space, and to empirically determine the appropriate values of C_ϵ, C_{μ^2}, and C_δ. Based on the numerical results, we later found $C_\delta = 1/5$ to be a good choice for the 1DH landslide-generated waves in constant depth scenario.

Since nonlinear effects are the only difference between LSWE and NSWE, we know nonlinearity is important in a landslide wave problem when the leading wave predicted by NSWE differs from that predicted by LSWE. Empirically, C_ϵ can be specified as a function of acceptable difference (error tolerance) between the two leading waves. Likewise, since frequency dispersion effects are the only difference between LSWE and LWD, we know frequency dispersion is important in a landslide wave problem when the leading wave predicted by LWD differs from that predicted by LSWE. Empirically, C_{μ^2} can be specified as a function of acceptable difference (error tolerance) between the two leading waves. By computing the wave fields

(via either analytical solutions or numerical simulations) for numerous cases that cover a wide range of the input parameters (Fr, δ, γ), empirical formulas for C_ϵ and C_{μ^2}, as functions of acceptable difference (error tolerance), can be found in the parameter space considered.

4.1.2 Root-mean-squared deviation

To quantify the difference between the leading waves, we calculated the root-mean-squared deviation (RMSD) based on the results predicted by two different models. Since the dimensionless linear wave celerity is one, the leading wave at $t = t_s$ is located at $x = t_s \cos\theta$, where again $\theta = 0$ for the right-going wave and $\theta = \pi$ for the left-going wave. Numerically, the front (x_f) of the leading wave is defined as the location ahead of the leading wave where the free surface first changes for more than 0.01 times the maximum leading wave amplitude. If the leading wave is oscillatory and has multiple local extreme values, the back (x_b) of the leading wave is defined to be the location of the wave trough closest to $x = t_s - 0.5$ (where the value of 0.5 corresponds to half the normalized wavelength) and between $t_s - 0.5 < x < x_f$ for the right-going wave; for the left-going wave traveling in the negative x direction, the back of the leading wave is defined to be the location of the wave peak closest to $x = -(t_s - 0.5)$ and between $x_f < x < -(t_s - 0.5)$. Otherwise, the back of the leading wave is defined as $x_b = (t_s - 0.5)\cos\theta$. The window of the complete wave field used to calculated the RMSD is maximized so that the two leading waves predicted by the two models are both included in the window. The RMSD between two leading waves, η_1 (e.g., LSWE) and η_2 (e.g., LWD or NSWE), which

are dimensionless (normalized by A_b), is defined as

$$\text{RMSD} = \frac{\sqrt{\int_{x_b}^{x_f} (\eta_2 - \eta_1)^2 dx/(x_f - x_b)}}{\max(\eta_1) - \min(\eta_1)} \times 100\%. \tag{4.8}$$

The leading wave samples and the corresponding RMSD are shown in figure 4.2. In plotting, r_2, normalized by L_b, is defined so that the waves travel towards the positive r_2 direction (i.e., r_2 is in the positive x direction for the right-going wave, and in the negative x direction for the left-going wave) and the leading wave location ($x = t_s \cos\theta$) is centered at $r_2 = 1$. It can be seen that the RMSD reflects the discrepancy between two waves reasonably well, and that a $\sim 5\%$ RMSD can be seen as a reasonable threshold for when discrepancy becomes significant.

We note that the RMSD is by no means the only means to quantify discrepancy. If a different error measure is used, we expect the numerical thresholds to change quantitatively, but not qualitatively. However, we remark that extreme care needs to be exercised in choosing an error measure. For example, if a simple error measure based only on the difference between the maximum wave heights, the wavelengths, or the peak locations, it may not accurately reflect the true difference between the two different waves. For example, two waves can have identical wave heights but very different shapes. Similarly, two waves can arrive at the same time, but have very different shapes. Instead of designing a customized error measure, in this study we chose to use a common error measure, the RMSD, and base the following analysis on this error measure.

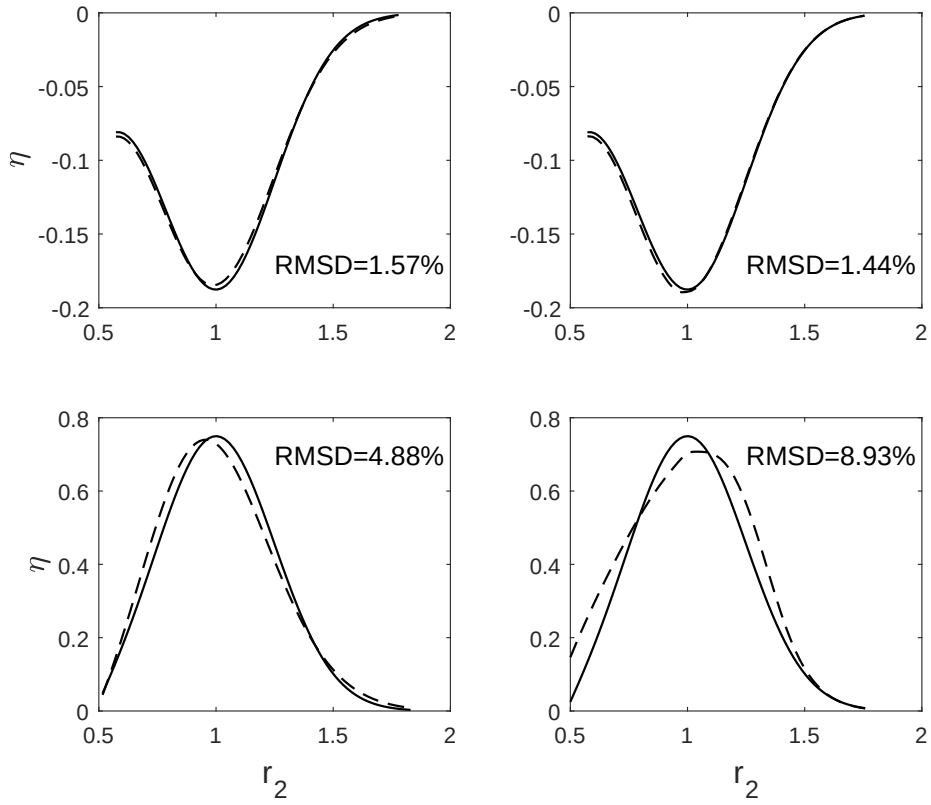

Figure 4.2: Leading wave samples in 1DH constant depth and the corresponding RMSD. Top left: the left-going leading waves predicted by LSWE (solid line) and LWD (dashed line) for $(Fr, \gamma) = (0.6, 0.05)$; bottom left: the right-going leading waves predicted by LSWE (solid line) and LWD (dashed line) for $(Fr, \gamma) = (0.6, 0.05)$; top right: the left-going leading waves predicted by LSWE (solid line) and NSWE (dashed line) for $(Fr, \delta) = (0.6, 0.05)$; bottom right: the right-going leading waves predicted by LSWE (solid line) and NSWE (dashed line) for $(Fr, \delta) = (0.6, 0.05)$.

4.1.3 Results

Analytical solutions are available for LSWE and LWD in constant water depth, so the complete wave field results for these two models are obtained directly from the analytical solutions. A total of 18 cases covering 6 different landslide speeds, $Fr = [0.3, 0.4, 0.5, 0.6, 0.7, 0.8]$, and 3 different landslide lengths, $\gamma = [0.01, 0.05, 0.1]$, is considered. We remark that the input parameter δ is irrelevant in LSWE and

LWD, since both models are linear and δ only affects the results if nonlinear effects are accounted for. For each case, the RMSDs for the two leading waves (one right-going and one left-going) predicted by LSWE and those predicted by LWD are calculated. As a result, a total of 36 points is available for determining C_{μ^2}. The results are shown in figure 4.3.

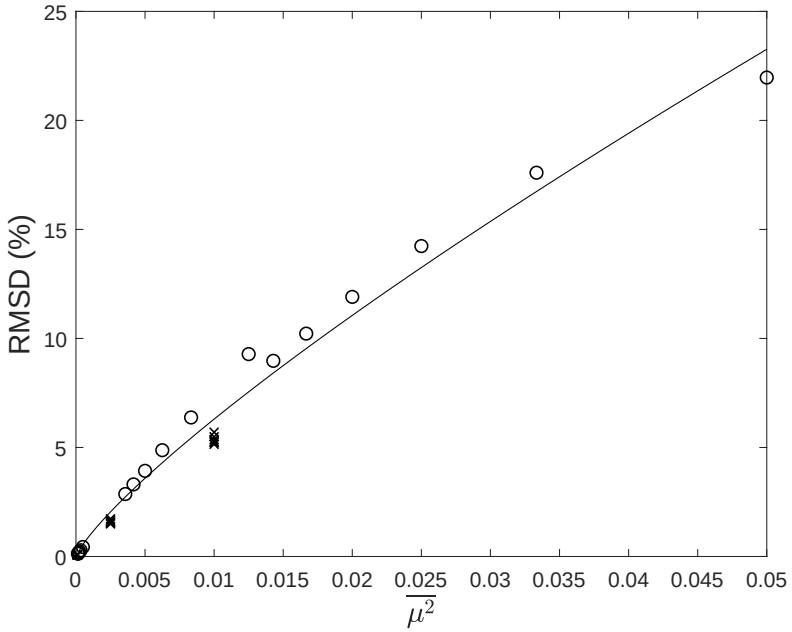

Figure 4.3: The estimator of the strength of frequency dispersion, $\overline{\mu^2}$ in (4.7), plotted as a function of RMSD of LWD from LSWE, for the 1DH landslide-generated waves in constant depth scenario. Circle: right-going leading waves; cross: left-going leading waves; solid line: fitted curve (4.9).

It can be observed that $\overline{\mu^2}$ successfully captures the strength of frequency dispersion as a function of the input parameters, as minimal scattering shows in figure 4.3. A curve based on a power function can be fitted to the data points:

$$\text{RMSD} = 264.7(\overline{\mu^2})^{0.8117}, \quad R^2 = 0.9839, \tag{4.9}$$

where R^2 is the coefficient of determination. C_{μ^2} can be determined as follows: first, one specifies the error tolerance, say, 5% RMSD, so that a nondispersive model is acceptable if it deviates from a dispersive model by no more than a 5%

RMSD. Then, one uses figure 4.3 or the fitted curve (4.9) to find the corresponding $\overline{\mu^2}$ value, which will be the C_{μ^2} for RMSD = 5% – in this case, $C_{\mu^2} \simeq 0.00752$. It is therefore more convenient to rewrite (4.9) as

$$C_{\mu^2} = (\frac{\text{RMSD}}{264.7})^{1.232}. \tag{4.10}$$

(4.10) can then be used in (4.7) to determine whether frequency dispersion is important or not in a landslide wave case in 1DH constant depth.

Similarly, C_ϵ can be determined by comparing the leading waves predicted by LSWE and NSWE. Since analytical solutions are not available for NSWE, it is solved numerically. A total of 18 cases covering 6 different landslide speeds, $Fr = [0.3, 0.4, 0.5, 0.6, 0.7, 0.8]$, and 3 different landslide thickness, $\delta = [0.01, 0.05, 0.1]$, is considered. We remark that the input parameter γ is irrelevant in LSWE and NSWE, since both models are nondispersive and γ only affects the results if dispersion effects are accounted for. For each case, the RMSDs for the two leading waves (one right-going and one left-going) predicted by LSWE and those predicted by NSWE are calculated. As a result, a total of 36 points is available for determining C_ϵ and C_δ. We found $C_\delta = 1/5$ to be a good fit that reduces scattering, and the RMSD results are shown in figure 4.4. $\bar{\epsilon}$ captures well the strength of nonlinearity as a function of the input parameters, as revealed by the minimal scattering in the figure, and a curve based on a power function can be fitted to the data points:

$$\text{RMSD} = 42.63(\bar{\epsilon})^{0.6875}, \quad R^2 = 0.9691. \tag{4.11}$$

Again, it is therefore more convenient to rewrite (4.11) as

$$C_\epsilon = (\frac{\text{RMSD}}{42.63})^{1.455}. \tag{4.12}$$

Given an acceptable RMSD, (4.12) can be used in (4.7) to determine whether nonlinearity is important or not in a landslide wave case in 1DH constant depth.

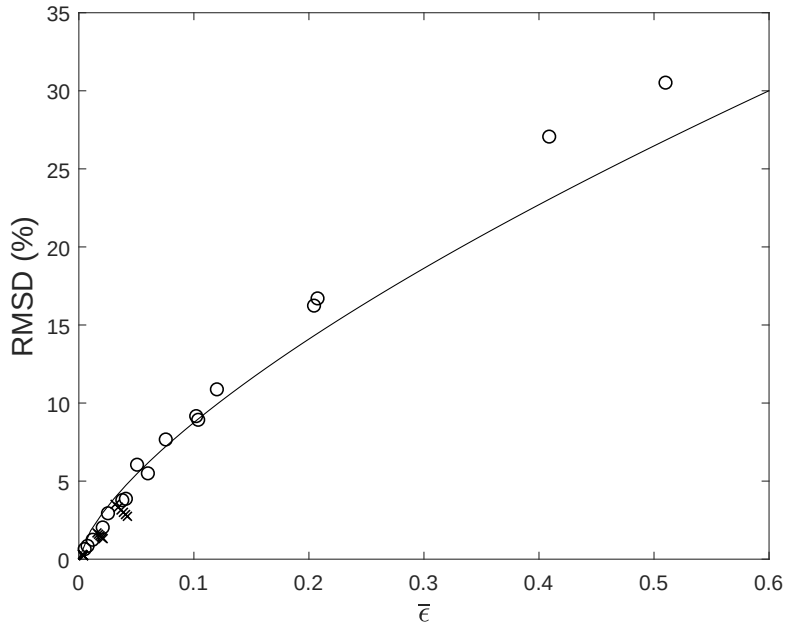

Figure 4.4: The estimator of the strength of nonlinearity, $\overline{\epsilon}$ in (4.7), plotted as a function of RMSD of NSWE from LSWE, for the 1DH landslide-generated waves in constant depth scenario. Circle: right-going leading waves; cross: left-going leading waves; solid line: fitted curve (4.11).

We remark that although a different base function can be used in (4.11) to improve the fit and better capture the observable trend in figure 4.4, we choose not to do so, and shall consistently used a power function as the base function throughout this chapter. Besides the consistency reason, we also would like to stress the "soft" nature of plots like figure 4.4 – it is important that the error measure, RMSD, reflects the general magnitude of discrepancy, but its exact numerical value is not as important, since the numerical values can change easily if a different error measure or a different numerical definition of the leading waves is used. Therefore, to keep things simple and consistent, we shall continue using a power function as the base function in curve fits like (4.11). If a more precise picture of the trend is desired, one can always infer the relation between RMSD and $\overline{\mu^2}$ or $\overline{\epsilon}$ from plots like figure 4.4 rather than empirical formulas like (4.11).

While frequency dispersion effects can be more easily isolated by comparing LSWE with LWD and a well-fitted expression can be found for C_{μ^2}, they become more complicated when comparing NSWE with WNWD, since nonlinear effects are also present in each model. As a result, unlike the LSWE-LWD comparison, δ is relevant in the NSWE-WNWD comparison and affects the wave fields. To see how the NSWE-WNWD comparison differs from the LSWE-LWD comparison, we compute the wave fields predicted by NSWE and WNWD for a total of 27 cases covering $Fr = [0.3, 0.5, 0.7]$, $\delta = [0.05, 0.1, 0.2]$, and $\gamma = [0.01, 0.05, 0.1]$. The resulting $\bar{\epsilon}$ vs. RMSD plot is shown in figure 4.5. More scattering can be seen in comparison with the LSWE-LWD case, and the δ-dependency is evident. We remark that when a very small δ is used (thus, very small nonlinearity), say $\delta = 0.01$, the NSWE-WNWD results converge to the LSWE-LWD results as expected. Despite the more significant scattering, we find that overall, $\overline{\mu^2}$ still serves as a satisfactory order-of-magnitude estimate of the strength of frequency dispersion, and (4.10) can still be used along with (4.7) to determine whether frequency dispersion is important or not, even when nonlinear effects are present – i.e., whether NSWE or WNWD should be used.

Likewise, while nonlinear effects can be more easily isolated by comparing LSWE with NSWE and a well-fitted expression can be found for C_ϵ, they become more complicated when comparing LWD with WNWD, since frequency dispersion effects are also present in each model. As a result, unlike the LSWE-NSWE comparison, γ is relevant in the LWD-WNWD comparison and affects the wave fields. To see how the LWD-WNWD comparison differs from the LSWE-NSWE comparison, we compute the wave fields predicted by LWD and WNWD for a total of 27 cases covering $Fr = [0.3, 0.5, 0.7]$, $\delta = [0.01, 0.05, 0.1]$, and $\gamma = [0.05, 0.1, 0.2]$. The resulting $\overline{\mu^2}$ vs. RMSD plot is shown in figure 4.6. More scattering can be

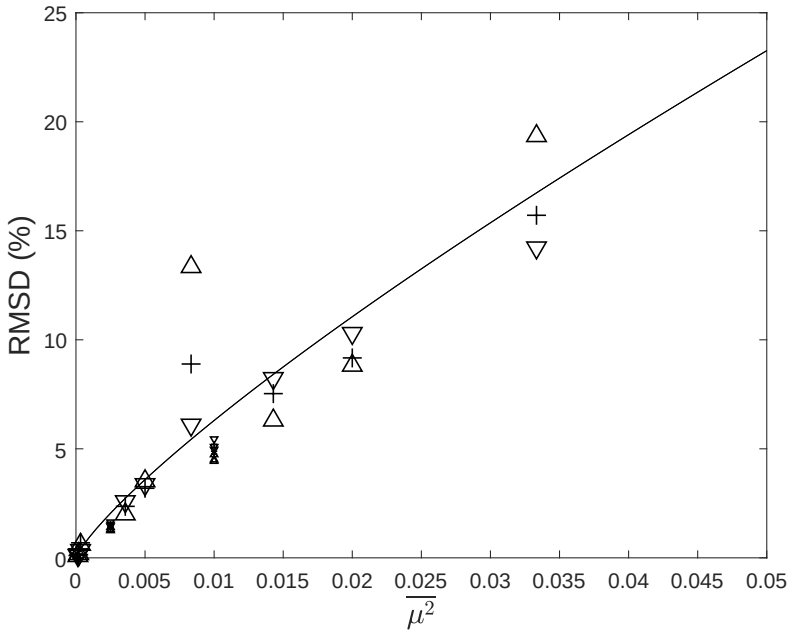

Figure 4.5: The estimator of the strength of frequency dispersion, $\overline{\mu^2}$ in (4.7), plotted as a function of RMSD of WNWD from NSWE, for the 1DH landslide-generated waves in constant depth scenario. Downward-pointing triangle: $\delta = 0.05$; plus: $\delta = 0.1$; upward-pointing triangle: $\delta = 0.2$; larger symbols: right-going leading waves; smaller symbols: left-going leading waves; solid line: fitted curve (4.9) based on the LSWE-LWD results.

seen in comparison with the LSWE-NSWE case, and the γ-dependency is evident – the larger γ is, the smaller the RMSD becomes. Again, if a very small γ is used (thus, the water depth is very shallow compared to the landslide length), say $\gamma = 0.01$, the LWD-WNWD results converge to the LSWE-NSWE results as expected. Overall, $\bar{\epsilon}$ still serves as a satisfactory conservative (since the RMSD is overestimated for larger γ) estimate of the strength of nonlinearity, and (4.12) can still be used along with (4.7) to determine whether nonlinearity is important or not, even when frequency dispersion effects are present – i.e., whether LWD or WNWD should be used.

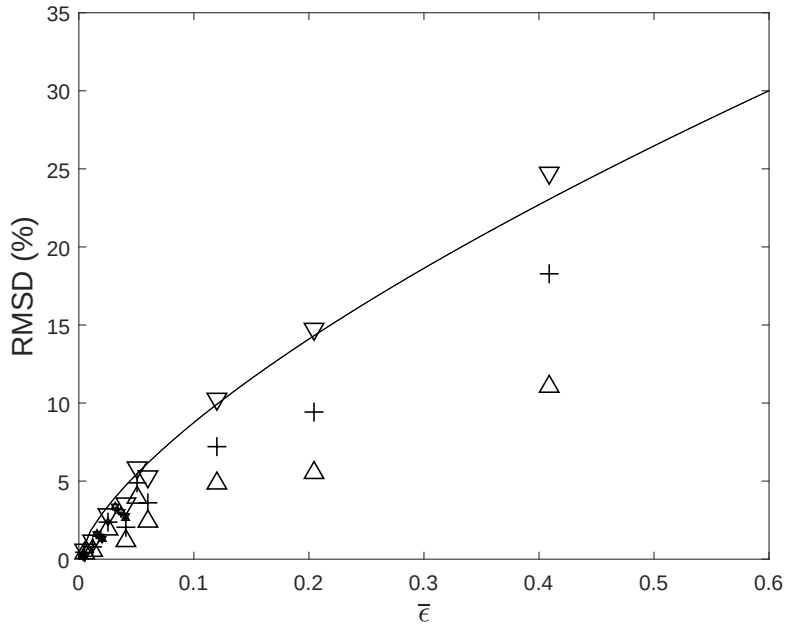

Figure 4.6: The estimator of the strength of nonlinearity, $\bar{\epsilon}$ in (4.7), plotted as a function of RMSD of WNWD from NSWE, for the 1DH landslide-generated waves in constant depth scenario. Downward-pointing triangle: $\gamma = 0.05$; plus: $\gamma = 0.1$; upward-pointing triangle: $\gamma = 0.2$; larger symbols: right-going leading waves; smaller symbols: left-going leading waves; solid line: fitted curve (4.11) based on the LSWE-NSWE results.

4.2 2DH landslide-generated waves in constant depth

We now extend the scenario from 1DH constant depth to 2DH constant depth. Since the methods have been introduced in detail in the previous section, we shall only briefly describe the methods in the following sections. The 2DH scenario is essentially the same as the sketch in figure 4.1, but with the addition of the transverse y direction (into the page in the sketch). A radially symmetric Gaussian-shaped landslide of length L_b traveling in the x direction is used – the dimensional landslide forcing function is

$$B'(x', y', t') = A_b e^{-8(\frac{x'-V_b \cdot t'}{L_b})^2} e^{-8(\frac{y'}{L_b})^2}. \tag{4.13}$$

The same three input parameters, (Fr, δ, γ) defined in (4.2), describe the problem.

As has been shown in Chapter 2, the landslide-generated waves in this scenario consist of a trapped wave that moves with the landslide, and an outward-going ring of waves (as opposed to waves in two distinct directions in 1DH) that travels at the linear long wave celerity. Since the free waves have the same characteristic length as the landslide (L_b, or one when normalized), we again focus on the instant t_s when the free waves first separate from the landslide by a distance of one wavelength (which is one when normalized) – this instant marks the end of the wave generation stage and the beginning of the wave propagation stage.

Dimensionlessly, the outward-going free waves propagate at a speed of one starting immediately after $t = 0$. Therefore, the location of the leading wave in the θ direction is $(x, y) = (t_s \cos\theta, t_s \sin\theta)$ at the instant $t = t_s$; the location of the landslide is $(Fr \cdot t_s, 0)$. Since t_s is defined to be the instant when the separation distance between the leading wave and the landslide is one, we calculate the distance between the two points to obtain the expression

$$1 = t_s\sqrt{(\cos\theta - Fr)^2 + \sin\theta^2} = t_s\sqrt{1 - 2Fr\cos\theta + Fr^2}, \tag{4.14}$$

which can be rearranged to be

$$t_s = \frac{1}{\sqrt{1 - 2Fr\cos\theta + Fr^2}}. \tag{4.15}$$

We remark that t_s in the 1DH case, (4.4), is a special case of (4.15) with $\theta = 0, \pi$.

4.2.1 Estimators of the strength of nonlinearity and the strength of frequency dispersion

A closed-form analytical solution in the far field has been derived in Chapter 2 for a radially symmetric Gaussian-shaped landslide, (2.124):

$$\eta_{\text{far}}(r,\theta,t) = \sqrt{\pi}\frac{Fr\cos\theta}{2(1-Fr\cos\theta)}r^{-\frac{1}{2}}\Omega_2(r-t). \tag{4.16}$$

Just like the 1DH case, the analytical solution (4.16) reveals how the spatial scales of the leading wave relate to the input parameters. At the instant $t = t_s$, the leading wave is located at $r = t_s$, and we have

$$\epsilon \simeq \delta|\frac{Fr\cos\theta}{2(1-Fr\cos\theta)}|t_s^{-\frac{1}{2}}, \quad \mu^2 \simeq \gamma^2. \tag{4.17}$$

Again, considering both the spatial requirements and the temporal requirements, we write the requirements altogether as

$$\overline{\epsilon} = \delta|\frac{Fr\cos\theta}{2(1-Fr\cos\theta)}|t_s^{-1/2}\max(1,t_s) + C_\delta\delta \le C_\epsilon, \quad \overline{\mu^2} = \gamma^2\max(1,t_s) \le C_{\mu^2}, \tag{4.18}$$

where C_ϵ, C_{μ^2}, and C_δ are to be determined empirically. Based on the numerical results, we later found $C_\delta = 2/5$ to be a good fit for the 2DH landslide-generated waves in constant depth scenario.

4.2.2 Results

Repeating the procedure for the 1DH case, we shall determine C_{μ^2} by comparing the results predicted by LSWE and LWD, and we shall determine C_ϵ and C_δ by comparing those predicted by LSWE and NSWE. Although analytical solutions are available for LSWE and LWD in 2DH constant water depth,

we've found the numerical solution to be much more efficient than computing the integral-form analytical solutions. Therefore, all wave fields in 2DH are computed numerically. For the LSWE-LWD comparison, a total of 18 cases covering $Fr = [0.3, 0.4, 0.5, 0.6, 0.7, 0.8]$ and $\gamma = [0.01, 0.05, 0.1]$ is considered. For each case, the RMSDs for the leading waves in 14 directions are computed ($\theta = [0, 1, 2, 3, 4, 5, 6, 10, 11, 12, 13, 14, 15, 16]\pi/16$, which are interpolated from the rectangular mesh; $\theta \sim \pi/2$ is not considered because the waves are negligibly small there). As a result, a total of 252 points is available for determining C_{μ^2}. The results are shown in figure 4.3.

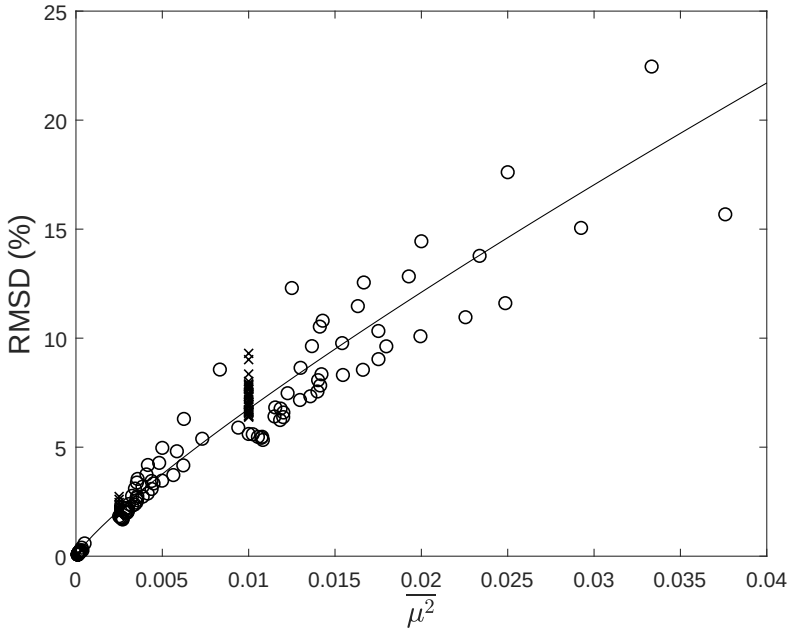

Figure 4.7: The estimator of the strength of frequency dispersion, $\overline{\mu^2}$ in (4.18), plotted as a function of RMSD of LWD from LSWE, for the 2DH landslide-generated waves in constant depth scenario. Circle: leading waves for $0 \leq \theta < \pi/2$; cross: leading waves for $\pi/2 < \theta \leq \pi$; solid line: fitted curve (4.19).

As shown in figure 4.7, $\overline{\mu^2}$ successfully captures the strength of frequency dispersion as a function of the input parameters, and a curve based on a power function (the reasons for not using a different function form has been explained in the 1DH

constant depth section) can be fitted to the data points:

$$\text{RMSD} = 326.7(\overline{\mu^2})^{0.8424}, \quad R^2 = 0.9540, \tag{4.19}$$

C_{μ^2} can be recovered from (4.19) as

$$C_{\mu^2} = (\frac{\text{RMSD}}{326.7})^{1.187}. \tag{4.20}$$

(4.20) can then be used in (4.18) to determine whether frequency dispersion is important or not in a landslide wave case in 2DH constant depth.

Similarly, C_ϵ can be determined by comparing the leading waves predicted by LSWE and NSWE. A total of 18 cases covering $Fr = [0.3, 0.4, 0.5, 0.6, 0.7, 0.8]$ and $\delta = [0.01, 0.05, 0.1]$ is considered. For each case, the RMSDs for the leading waves in 14 directions are computed ($\theta = [0, 1, 2, 3, 4, 5, 6, 10, 11, 12, 13, 14, 15, 16]\pi/16$). As a result, a total of 252 points is available for determining C_ϵ and C_δ. We found $C_\delta = 2/5$ to be a good fit that reduces scattering, and the RMSD results are shown in figure 4.8. $\bar{\epsilon}$ captures well the strength of nonlinearity as a function of the input parameters, as revealed by the minimal scattering in the figure, and a curve based on a power function (the reasons for not using a different function form has been explained in the 1DH constant depth section) can be fitted to the data points:

$$\text{RMSD} = 62.43(\bar{\epsilon})^{1.160}, \quad R^2 = 0.9111. \tag{4.21}$$

Again, it is therefore more convenient to rewrite (4.21) as

$$C_\epsilon = (\frac{\text{RMSD}}{62.43})^{0.8621}. \tag{4.22}$$

Given an acceptable RMSD, (4.22) can be used in (4.18) to determine whether nonlinearity is important or not in a landslide wave case in 2DH constant depth.

Again, to see how the NSWE-WNWD comparison differs from the LSWE-LWD comparison, we compute the wave fields predicted by NSWE and WNWD

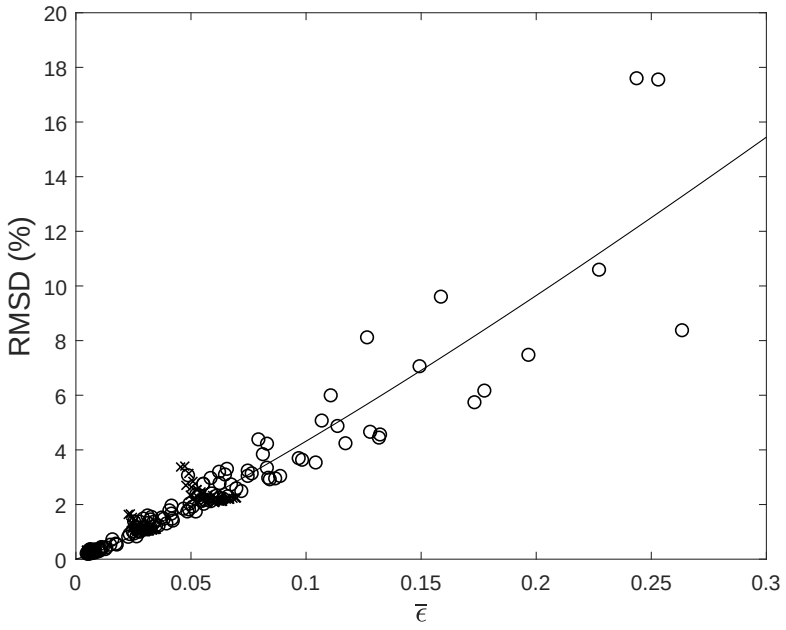

Figure 4.8: The estimator of the strength of nonlinearity, $\overline{\epsilon}$ in (4.18), plotted as a function of RMSD of NSWE from LSWE, for the 2DH landslide-generated waves in constant depth scenario. Circle: leading waves for $0 \leq \theta < \pi/2$; cross: leading waves for $\pi/2 < \theta \leq \pi$; solid line: fitted curve (4.21).

for a total of 27 cases covering $Fr = [0.3, 0.5, 0.7]$, $\delta = [0.05, 0.1, 0.2]$, and $\gamma = [0.01, 0.05, 0.1]$. The resulting $\overline{\epsilon}$ vs. RMSD plot is shown in figure 4.9. Although more scattering shows and the δ-dependency is evident, overall, $\overline{\mu^2}$ still estimates the strength of frequency dispersion satisfactorily. Therefore, (4.20) can still be used along with (4.18) to determine whether NSWE or WNWD should be used in a nonlinear landslide wave problem.

To see how the LWD-WNWD comparison differs from the LSWE-NSWE comparison, we compute the wave fields predicted by LWD and WNWD for a total of 27 cases covering $Fr = [0.3, 0.5, 0.7]$, $\delta = [0.01, 0.05, 0.1]$, and $\gamma = [0.05, 0.1, 0.2]$. The resulting $\overline{\mu^2}$ vs. RMSD plot is shown in figure 4.10. More scattering can be seen in comparison with the LSWE-NSWE case, and the γ-dependency is again evident – the larger γ is, the smaller the RMSD becomes. Nonetheless, overall $\overline{\epsilon}$

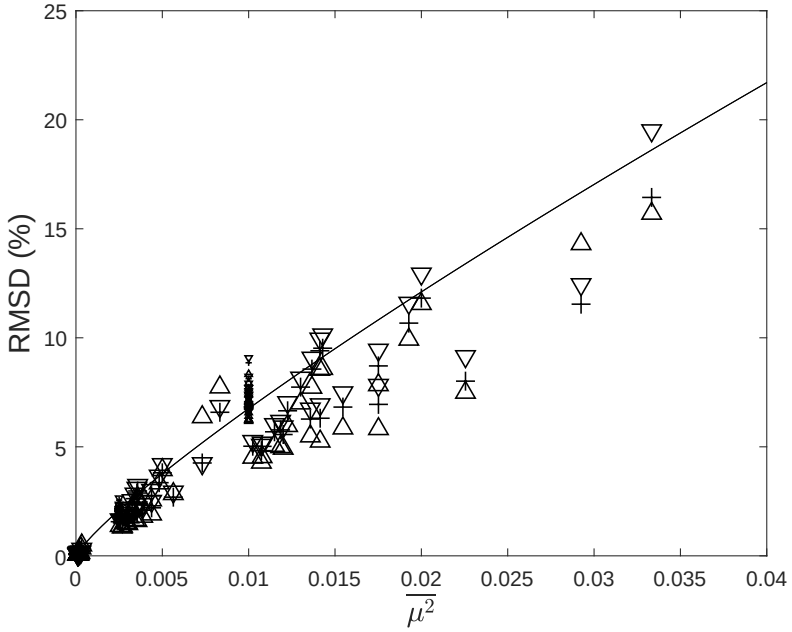

Figure 4.9: The estimator of the strength of frequency dispersion, $\overline{\mu^2}$ in (4.18), plotted as a function of RMSD of WNWD from NSWE, for the 2DH landslide-generated waves in constant depth scenario. Downward-pointing triangle: $\delta = 0.05$; plus: $\delta = 0.1$; upward-pointing triangle: $\delta = 0.2$; larger symbols: right-going leading waves; smaller symbols: left-going leading waves; solid line: fitted curve (4.19) based on the LSWE-LWD results.

still serves as a satisfactory order-of-magnitude estimate of the strength of nonlinearity, and (4.22) can still be used along with (4.18) to determine whether LWD or WNWD should be used in a frequency dispersive landslide wave problem.

4.3 1DH landslide-generated waves on a slope

Next, we consider a submarine Gaussian-shaped landslide of height A_b and length L_b traveling at a constant speed V_b down an incline of angle β, starting in a water depth of d_0. The scenario is sketched in figure 4.11. To avoid confusion with the polar angle, θ, we shall use β to denote the angle of an incline in this

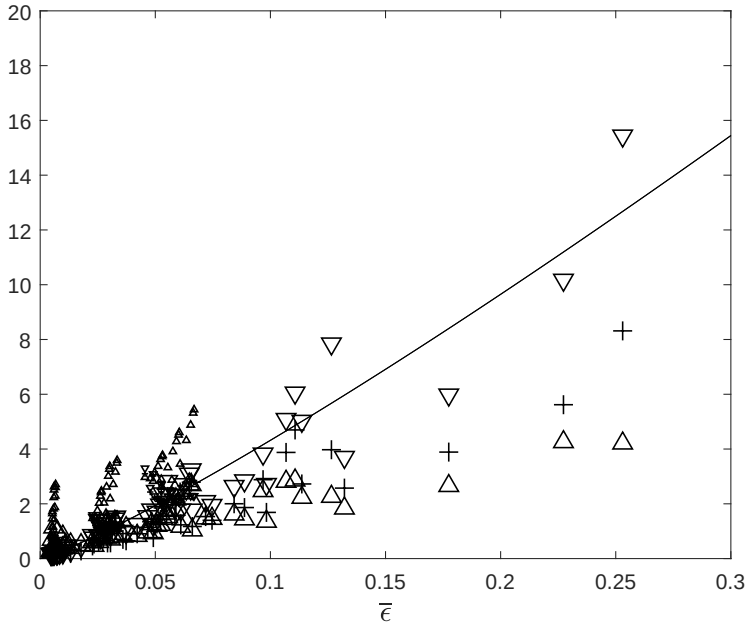

Figure 4.10: The estimator of the strength of nonlinearity, $\overline{\epsilon}$ in (4.18), plotted as a function of RMSD of WNWD from NSWE, for the 2DH landslide-generated waves in constant depth scenario. Downward-pointing triangle: $\gamma = 0.05$; plus: $\gamma = 0.1$; upward-pointing triangle: $\gamma = 0.2$; larger symbols: right-going leading waves; smaller symbols: left-going leading waves; solid line: fitted curve (4.21) based on the LSWE-NSWE results.

scenario. It should be noted that the landslide scales are specified in the slope coordinate system (x_β, z_β), where x_β is along the slope and z_β is perpendicular to the slope. Therefore, the effective landslide length in the horizontal (x) direction is $L_b \cos\beta$, the effective landslide height in the vertical direction (z) is $A_b \sec\beta$, and the effective landslide speed in the horizontal direction is $V_b \cos\beta$. These scales are used in normalization: $x = x'/(L_b \cos\beta)$, $\eta = \eta'/(A_b \sec\beta)$, and $t = t'\sqrt{gd_0}/(L_b \cos\beta)$, where the primes are used to denote the variables in dimensional form.

Dimensionally, the Gaussian-shaped landslide forcing function, B'_β, specified in

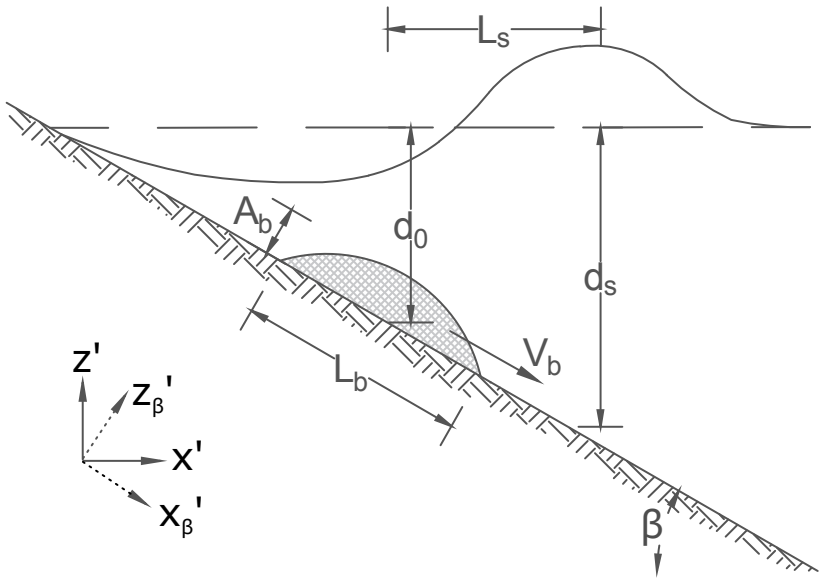

Figure 4.11: A definition sketch for the 1DH landslide-generated waves on a slope scenario. The quantities are in dimensional form.

the slope coordinate system, (x'_β, z'_β), is

$$B'_\beta(x'_\beta, t') = A_b e^{-8(\frac{x'_\beta - V_b \cdot t'}{L_b})^2}. \tag{4.23}$$

Since the governing equations are solved in the (x', z') coordinate system (horizontal-vertical), (4.23) need to be converted numerically to obtain the corresponding landslide forcing function in the (x', z') coordinate system, $B'(x', t')$. Below are the steps we took to perform the conversion to find B':

1. in the (x', z') coordinate system, given the initial center of the landslide x'_0 and the i-th grid point x'_i
2. in the (x'_β, z'_β) coordinate system, calculate the landslide height at this location, $x'_{\beta,i} = x'_i \sec\beta$:

$$B'_{\beta,i} = A_b e^{-8(\frac{x'_{\beta,i} - x'_0 \sec\beta - V_b \cdot t'}{L_b})^2} \tag{4.24}$$

3. rotate the coordinates $(x'_{\beta,i}, B'_{\beta,i})$ clockwise about the origin by an angle of β to put the landslide on a slope:

$$(a'_i, b'_i) = (x'_{\beta,i}\cos\beta + B'_{\beta,i}\sin\beta, -x'_{\beta,i}\sin\beta + B'_{\beta,i}\cos\beta) \tag{4.25}$$

4. exclude the slope from (a'_i, b'_i) to obtain the perturbation due to the landslide alone:

$$(a'_i, b'_i + a'_i\tan\beta) \tag{4.26}$$

5. repeat the above steps for all grid points to obtain the complete list of $(a'_i, b'_i + a'_i\tan\beta)$, which is the discretized landslide forcing function in the (x', z') coordinate system

6. linearly interpolate $(a'_i, b'_i + a'_i\tan\beta)$ to find (x'_i, B'_i) for all grid points, since a'_i is a new point due to rotation and may not be the same as x'_i

7. B'_i is the converted landslide forcing function, defined as the vertical perturbation to the bathymetry due to the Gaussian-shaped landslide at the grid point location x_i

In this scenario, four dimensionless input parameters describe the problem:

$$\begin{cases} Fr = V_b\cos\beta/\sqrt{gd_0}: & \text{landslide speed, } 0 < Fr < 1 \\ \delta = A_b\sec\beta/d_0: & \text{landslide shape nonlinearity} \\ \gamma = d_0/(L_b\cos\beta): & \text{relative water depth} \\ \zeta = \tan\beta/\gamma: & \text{relative steepness of the slope, } 0 < \zeta \leq 1 \end{cases}, \tag{4.27}$$

where we choose ζ instead of β as an input parameter (although they convey essentially the same information), since ζ shows up frequently in the expressions that follow. Taking a closer look at the definition of ζ, we see that it reflects how steep the slope is $(\tan\beta)$ compared to how shallow the water is (γ). The scaling

requirement on ζ can be revealed by inspecting the dimensionless mass equation, (2.62):

$$\eta_t + (uh)_x = B_t, \tag{4.28}$$

where the water depth h is normalized by the initial water depth d_0. On a slope of angle β, the dimensional water depth is $h' = d_0 + x' \tan\beta$, which becomes $h = 1 + x\zeta$ when normalized by d_0. To ensure consistent scaling arguments, each term in (4.28) has to be of $O(1)$. Therefore, $h = 1 + x\zeta = O(1)$. We thus see that $x\zeta$ cannot be too large; the scaling assumptions of LSWE quickly break down as the waves travel into deeper water. After conducting various numerical experiments, we find $\zeta > 1$ gives significantly different results than those with $0 < \zeta \leq 1$. Therefore, in this study, we consider only $0 < \zeta \leq 1$.

While general integral-form analytical solutions are available for landslide waves on a slope, they do not reveal any scaling relations between the landslide and the generated waves. In addition, the computation of the integral-form analytical solutions is generally more expensive than solving the governing equations numerically. Therefore, to devise semi-analytical expressions for $\overline{\mu^2}$ and $\overline{\epsilon}$ for landslide-generated waves on a slope, we shall make use of the closed-form analytical solutions in constant water depth and general analytical knowledge on water waves .

4.3.1 Derivation of the separation time, t_s

Although the arguments behind the derivation of the separation time, t_s, which marks the end of the wave generation stage, are straightforward, more steps are needed for the landslide wave on a slope case and the algebra can be lengthy. First, we show that waves in LSWE accelerate at $g\tan\beta/2$ (dimensional) on an incline

of angle β as they travel into deeper water (and decelerate at the same rate as they travel in the opposite direction into shallower water): dimensionally in LSWE, the local wave speed is $\sqrt{gh'}$, where h' is the local water depth. $h' = d_0 + x' \tan\beta$ on a slope if $x' = 0$ is defined at the initial landslide location. Following an outward-going wave whose location is denoted by $x'_c(t')$, we then have the relation (dimensional)

$$\frac{dx'_c}{dt'} = \sqrt{g(d_0 + x'_c \tan\beta)}, \tag{4.29}$$

which can be solved by the method of separation of variables to obtain

$$\int (gd_0 + gx'_c \tan\beta)^{-\frac{1}{2}} dx'_c = \int dt', \tag{4.30}$$

and then

$$(gx'_c \tan\beta + gd_0)^{\frac{1}{2}} = \frac{g\tan\beta}{2} t' + C, \tag{4.31}$$

where C is the integration constant. Since $x'_c = 0$ at $t' = 0$, we find $C = \sqrt{gd_0}$. The location of the wave x'_c can then be solved for as

$$x'_c = \sqrt{gd_0} t' + \frac{1}{2}\frac{g\tan\beta}{2} t'^2. \tag{4.32}$$

We therefore see that on a slope, water waves accelerate at $g\tan\theta/2$ as they travel into deeper water. Similarly, following the same argument but for waves traveling into shallower water, we find that water waves decelerate at $g\tan\theta/2$ as they travel into shallower water. For convenience and easier extension to 2DH in the next section, we shall denote the wave acceleration as $g\cos\theta\tan\beta/2$, where $\theta = 0$ for the right-going wave, and $\theta = \pi$ for the left-going wave.

Just like in the constant depth case, we expect three waves to form: one right-going wave that travels at local wave speed, one trapped wave that follows the landslide, and one left-going wave that travels at local wave speed. As soon as the free waves separate from the landslide by one characteristic wavelength, they

become independent of the landslide and the wave propagation stage begins. The instant t_s therefore marks the end of the wave generation stage. On a slope, the characteristic wavelength changes due to wave shoaling, so the shoaling effects need to be taken into consideration. The shoaling law in shallow water (LSWE) – Green's law – is well known (see Mei, 1989, for example): as a linear long wave travels from water depth d_0 to water depth d_s along a linear slope, its wavelength scales as $(d_s/d_0)^{1/2}$ and its amplitude scales as $(d_s/d_0)^{-1/4}$. As a wave travels into deeper water, its wavelength increases and its amplitude decreases.

At the instant $t' = t'_s$ (dimensional), the leading wave is located at $x'_s = \sqrt{gd_0}t'_s + g\cos\theta\tan\beta t'^2_s/4$, as given by (4.32), and the landslide is located at $x'_b = V_b\cos\beta t'_s$. The distance between the two is $x'_s - x'_b$. At $x' = x'_s$, the water depth is $d_s = d_0 + x'_s\cos\theta\tan\beta$. Since shoaling effects depend on the water depth ratio, d_s/d_0, we define

$$\begin{aligned}\chi = \frac{d_s}{d_0} = 1 + \frac{\sqrt{gd_0}}{d_0}\cos\theta\tan\beta t'_s + \frac{1}{4}\frac{g}{d_0}\cos^2\theta\tan^2\beta t'^2_s \\ = 1 + \zeta\cos\theta t_s + \frac{1}{4}(\zeta\cos\theta)^2 t_s^2\end{aligned}, \tag{4.33}$$

where t'_s is normalized as $t_s = t'_s\sqrt{gd_0}/(L_b\cos\beta)$, $\theta = 0$ for the right-going wave, and $\theta = \pi$ for the left-going wave. Due to shoaling, the characteristic wavelength of the leading waves at this instant is $L_b\cos\theta\chi^{1/2}$. Setting $x'_s - x'_b = L_b\cos\theta\chi^{1/2}$, after lengthy algebra and normalizing the results we end up with the expression

$$\begin{aligned}-\zeta\cos\theta t_s + \Big(1 - 2Fr\cos\theta + Fr^2 - \frac{1}{4}(\zeta\cos\theta)^2\Big)t_s^2 \\ +\frac{1}{2}\zeta\cos\theta(1 - Fr\cos\theta)t_s^3 + \frac{1}{16}(\zeta\cos\theta)^2 t_s^4 - 1 = 0\end{aligned}, \tag{4.34}$$

from which the dimensionless t_s can be solved for numerically. In 1DH, $\theta = 0$ for the right-going wave, and $\theta = \pi$ for the left-going wave.

4.3.2 Estimators of the strength of nonlinearity and the strength of frequency dispersion

Since no closed-form analytical solution is available for this scenario, we shall modify the analytical solution in constant water depth to assemble semi-analytical expressions, $\overline{\epsilon}$ and $\overline{\mu^2}$, which estimate the strength of nonlinearity and the strength of frequency dispersion, respectively. During the wave generation stage, $0 < t \leq t_s$, the leading wave travels from the initial water depth 1 (normalized by d_0) to the new water depth $\chi = d_s/d_0$ – we define a representative water depth $1 \leq \chi_* \leq \chi$ as

$$\chi_* = 1 + C_{\chi_*}(\chi - 1), \quad 0 \leq C_{\chi_*} \leq 1, \tag{4.35}$$

where C_{χ_*} is to be determined empirically (we later found $C_{\chi_*} = 1/4$ to be a good choice), and the expression for χ has been given in (4.33). The input parameters (Fr, δ, γ), defined in the initial water depth 1, can be redefined in the representative water depth χ_*:

$$(Fr_*, \delta_*, \gamma_*) = (Fr\chi_*^{-\frac{1}{2}}, \delta\chi_*^{-1}, \gamma\chi_*). \tag{4.36}$$

We remark that ζ_* will not be used and therefore not included in (4.36). We then use the analytical solution in constant depth, (4.3), with (4.36) as the input parameters, to write the scaling requirements as

$$\overline{\epsilon} = \delta_* |\frac{Fr_* \cos\theta}{2(1 - Fr_* \cos\theta)}| \max(1, t_s) + C_\delta \delta \leq C_\epsilon, \quad \overline{\mu^2} = \gamma_*^2 \max(1, t_s) \leq C_{\mu^2}, \tag{4.37}$$

where again $\theta = 0$ for the right-going wave, and $\theta = \pi$ for the left-going wave, and C_δ and C_{χ_*} are to be determined empirically; we later found $C_\delta = 1/3$ and $C_{\chi_*} = 1/4$ to be good choices. We note that C_δ is multiplied by the initial landslide nonlinearity δ and not δ_*, since the scaling requirement that the landslide is thin applies in the very beginning of the wave-generation process.

4.3.3 Results

C_{μ^2} is determined from the LSWE-LWD comparison, C_ϵ and C_δ are determined from the LSWE-NSWE comparison, and C_{χ_*} is determined from both the LSWE-LWD comparison and the LSWE-NSWE comparison. For the LSWE-LWD comparison, a total of 72 cases covering $Fr = [0.3, 0.4, 0.5, 0.6, 0.7, 0.8]$, $\gamma = [0.01, 0.05, 0.1]$, and $\zeta = [0.25, 0.5, 0.75, 1]$ is considered – the range of the slopes covered by these parameters is $0.143^\circ \leq \beta \leq 5.71^\circ$. Again, δ has no real effects in linear models. For each case, the RMSDs for the right-going leading wave and the left-going lead wave are computed. As a result, a total of 144 points is available for determining C_{μ^2}. The results are shown in figure 4.12. We later found that $C_{\chi_*} = 1/4$ minimizes the overall scattering in both the LSWE-LWD comparison and the LSWE-NSWE comparison (a total of 288 points).

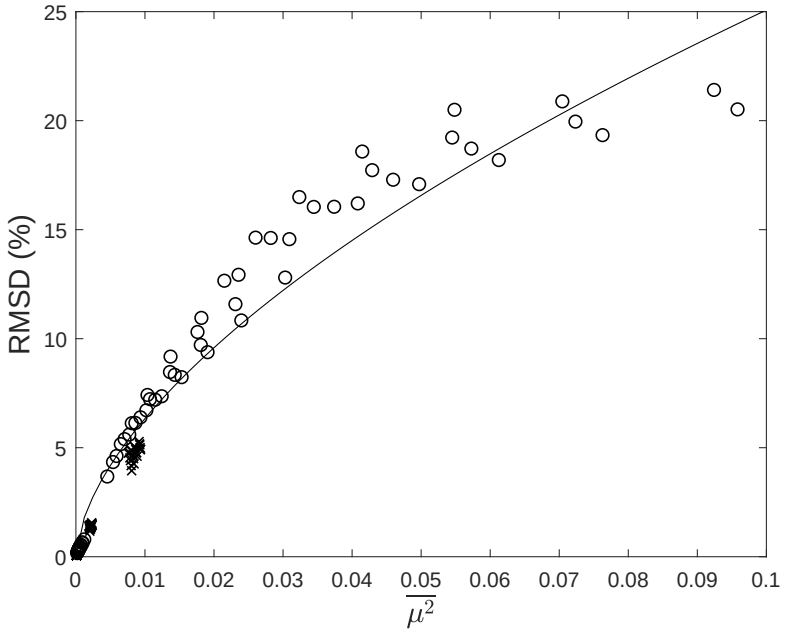

Figure 4.12: The estimator of the strength of frequency dispersion, $\overline{\mu^2}$ in (4.37), plotted as a function of RMSD of LWD from LSWE, for the 1DH landslide-generated waves on a slope scenario. Circle: leading waves for $0 \leq \theta < \pi/2$; cross: leading waves for $\pi/2 < \theta \leq \pi$; solid line: fitted curve (4.38).

As can be seen in figure 4.12, despite its empirical nature, $\overline{\mu^2}$ successfully captures the strength of frequency dispersion as a function of the input parameters, and a curve based on a power function (we again note that the reasons for not using a different function form have been discussed in the 1DH constant depth section) can be fitted to the data points:

$$\text{RMSD} = 99.21(\overline{\mu^2})^{0.5974}, \quad R^2 = 0.9549, \tag{4.38}$$

C_{μ^2} can be recovered from (4.38) as

$$C_{\mu^2} = (\frac{\text{RMSD}}{99.21})^{1.674}. \tag{4.39}$$

(4.39) can then be used in (4.37) to determine whether frequency dispersion is important or not in the 1DH landslide wave on a slope scenario.

Similarly, C_ϵ can be determined from the LSWE-NSWE comparison. A total of 72 cases covering $Fr = [0.3, 0.4, 0.5, 0.6, 0.7, 0.8]$, $\delta = [0.05, 0.1, 0.2]$, and $\zeta = [0.25, 0.5, 0.75, 1]$ is considered. Again, γ has no real effects in nondispersive models. For each case, the RMSDs for the right-going leading wave and the left-going lead wave are computed. As a result, a total of 144 points are available for determining C_ϵ and C_δ. We found $C_\delta = 1/3$ to be a good fit that reduces scattering; along with the LSWE-LWD comparison, we found $C_{\chi_*} = 1/4$ to be a good fit that reduces scattering in both cases. The resulting $\overline{\epsilon}$ v.s. RMSD plot is shown in figure 4.13. Again, despite its empirical nature, $\overline{\epsilon}$ captures well the strength of nonlinearity as a function of the input parameters, as can be seen by the minimal scattering in the figure, and a curve based on a power function can be fitted to the data points:

$$\text{RMSD} = 46.56(\overline{\epsilon})^{0.8199}, \quad R^2 = 0.9230. \tag{4.40}$$

It is more convenient to rewrite (4.40) as

$$C_\epsilon = (\frac{\text{RMSD}}{46.56})^{1.220}. \tag{4.41}$$

Given an acceptable RMSD, (4.41) can be used in (4.37) to determine whether nonlinearity is important or not in a 1DH landslide wave on a slope case.

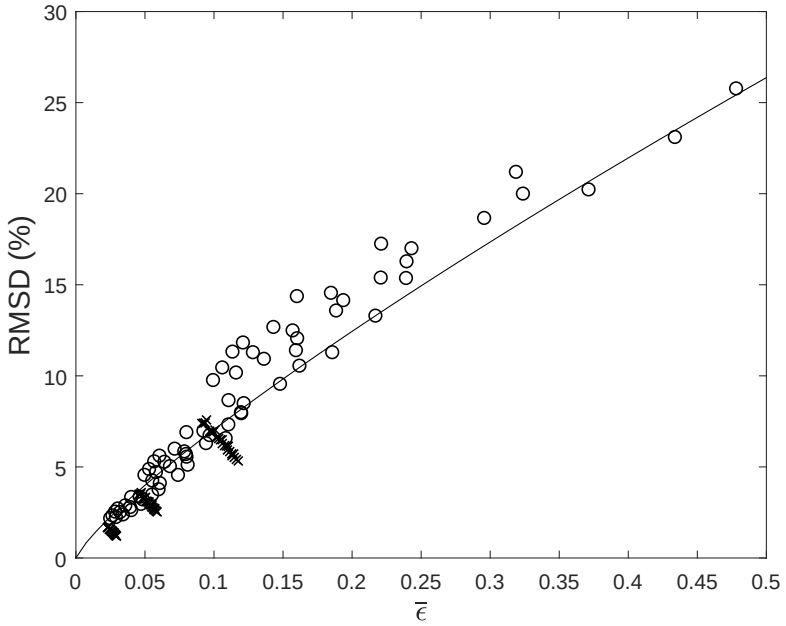

Figure 4.13: The estimator of the strength of nonlinearity, $\overline{\epsilon}$ in (4.37), plotted as a function of RMSD of NSWE from LSWE, for the 1DH landslide-generated waves on a slope scenario. Circle: leading waves for $0 \leq \theta < \pi/2$; cross: leading waves for $\pi/2 < \theta \leq \pi$; solid line: fitted curve (4.40).

Next, we examine how the NSWE-WNWD comparison differs from the LSWE-LWD comparison due to the additional nonlinear effects. A total of 108 cases covering $Fr = [0.3, 0.5, 0.7]$, $\delta = [0.1, 0.2, 0.3]$, $\gamma = [0.01, 0.05, 0.1]$, and $\zeta = [0.25, 0.5, 0.75, 1]$ is computed with NSWE and WNWD – the range of the slopes covered by these parameters is $0.143° \leq \beta \leq 5.71°$.. The resulting $\overline{\epsilon}$ vs. RMSD plot is shown in figure 4.14. Although more scattering shows and the δ-dependency is evident, overall, $\overline{\mu^2}$ still estimates the strength of frequency dispersion well. Therefore, (4.39) can still be used along with (4.37) to determine whether NSWE or WNWD should be used in a nonlinear landslide wave problem.

To see how the LWD-WNWD comparison differs from the LSWE-NSWE

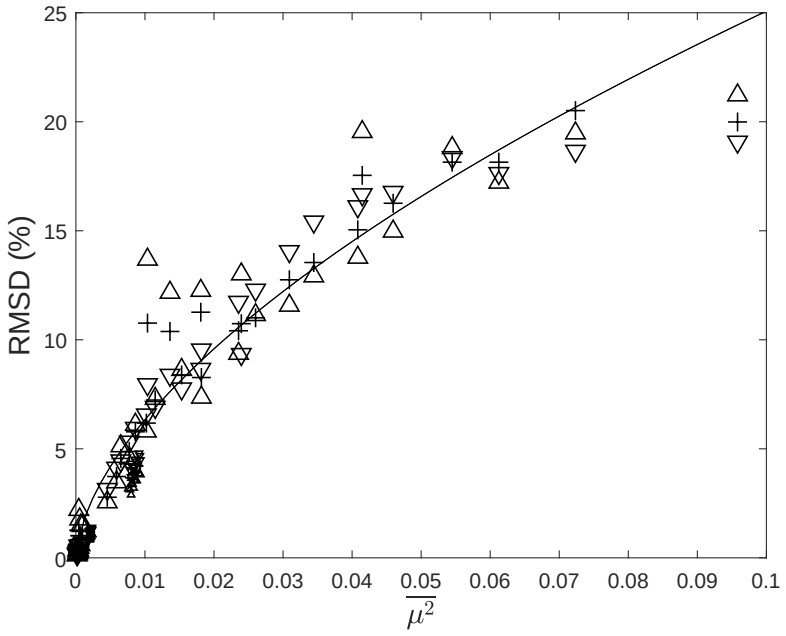

Figure 4.14: The estimator of the strength of frequency dispersion, $\overline{\mu^2}$ in (4.37), plotted as a function of RMSD of WNWD from NSWE, for the 1DH landslide-generated waves on a slope scenario. Downward-pointing triangle: $\delta = 0.1$; plus: $\delta = 0.2$; upward-pointing triangle: $\delta = 0.3$; larger symbols: right-going leading waves; smaller symbols: left-going leading waves; solid line: fitted curve (4.38) based on the LSWE-LWD results.

comparison due to the additional frequency dispersion effects, we compute the wave fields predicted by LWD and WNWD for a total of 108 cases covering $Fr = [0.3, 0.5, 0.7]$, $\delta = [0.05, 0.1, 0.2]$, $\gamma = [0.05, 0.1, 0.2]$, and $\zeta = [0.25, 0.5, 0.75, 1]$ – the range of the slopes covered by these parameters is $0.716^\circ \leq \beta \leq 11.3^\circ$. The resulting $\overline{\mu^2}$ vs. RMSD plot is shown in figure 4.15. More scattering can be seen in comparison with the LSWE-NSWE case, and the γ-dependency is evident – the larger γ is, the smaller the RMSD becomes. Nonetheless, overall $\bar{\epsilon}$ still serves as a conservative (since the RMSD is overestimated for large γ) order-of-magnitude estimate of the strength of nonlinearity, and (4.41) can still be used along with (4.37) to determine whether LWD or WNWD should be used in a frequency dispersive landslide wave problem.

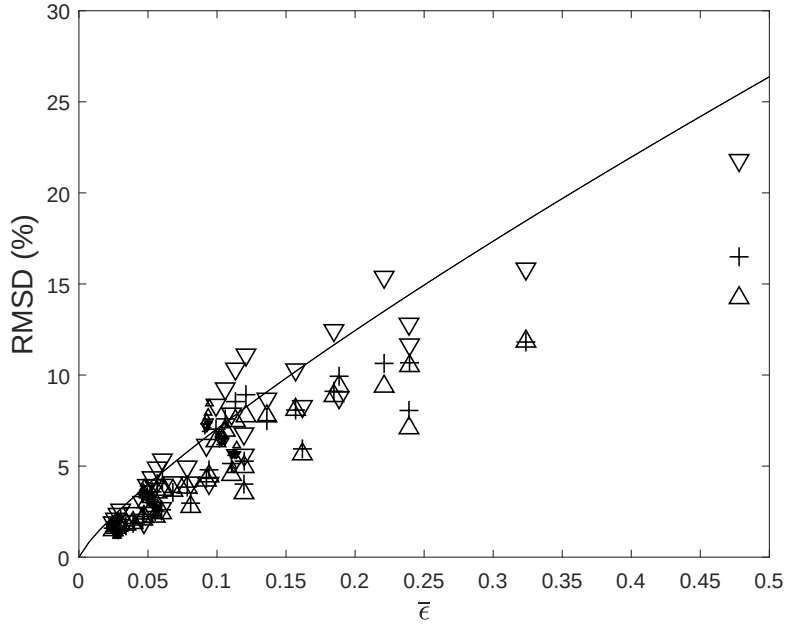

Figure 4.15: The estimator of the strength of nonlinearity, $\overline{\epsilon}$ in (4.37), plotted as a function of RMSD of WNWD from LWD, for the 1DH landslide-generated waves on a slope scenario. Downward-pointing triangle: $\gamma = 0.05$; plus: $\gamma = 0.1$; upward-pointing triangle: $\gamma = 0.2$; larger symbols: right-going leading waves; smaller symbols: left-going leading waves; solid line: fitted curve (4.40) based on the LSWE-NSWE results.

4.4 2DH landslide-generated waves on a slope

The 2DH scenario is essentially the same as the 1DH scenario (figure 4.11), but with the addition of the independent variable y in the transverse direction (into the page in the figure). A radially symmetric Gaussian-shaped landslide forcing function is specified in the slope coordinate system:

$$B'_\beta(x'_\beta, y'_\beta, t') = A_b e^{-8(\frac{x'_\beta - V_b \cdot t'}{L_b})^2} e^{-8(\frac{y'_\beta}{L_b})^2}. \tag{4.42}$$

Again, $B'_\beta(x'_\beta, y'_\beta, t')$ needs to be numerically converted to $B'(x', y', t')$ using the same steps outlined in the previous section. Since the bathymetry (without the landslide) does not vary in the y direction, $y'_\beta = y'$ and no conversion in the y direction is needed. The same four dimensionless input parameters, $(Fr, \delta, \gamma, \zeta)$ as

given in (4.27), describe the problem. Since no closed-form analytical solutions are available for landslide waves on a slope, we shall repeat the approach used in the previous section to devise semi-analytical expressions for $\bar{\epsilon}$ and $\overline{\mu^2}$, for the 2DH landslide-generated waves on a slope scenario.

4.4.1 Derivation of the separation time, t_s

The arguments to find the separation time t_s as well as the final expression are the same as those in the 1DH on a slope case. Therefore, we shall only briefly describe each step. In 2DH, θ is now an independent variable, instead of just two distinct values in the 1DH case, $\theta = 0, \pi$. Just like in the constant depth case, we expect an outward-going ring of free waves that travels at local wave speed and a trapped wave that follows the landslide. As soon as the free waves separate from the landslide by one characteristic wavelength, they become independent of the landslide and the wave propagation stage begins. The instant t_s therefore marks the end of the wave generation stage. On a slope, the characteristic wavelength changes due to wave shoaling, so the shoaling effects need to be taken into consideration.

For a wave traveling in the θ direction on a plane beach where the water depth is given by $h' = d_0 + x' \tan\beta$, the effective slope is $\cos\theta \tan\beta$ – we thus see that $\theta = 0, \pi$ in 1DH are the two special cases. Therefore, at the instant $t' = t'_s$ (dimensional), the leading wave in the θ direction is located at $(r'_s \cos\theta, r'_s \sin\theta)$, where $r'_s = \sqrt{gd_0}t'_s + g\cos\theta\tan\beta t'^2_s/4$ as given by (4.32), and the landslide is located at $(V_b \cos\beta t'_s, 0)$. Setting the distance between the two points equal to the local leading wave wavelength $L_b \cos\theta \chi^{1/2}$, where χ has been defined in (4.33), then provides an equation from which t'_s can be solved for. After lengthy algebra

and normalizing the results, we obtain the expression

$$\begin{array}{c} -\zeta\cos\theta t_s + \Big(1 - 2Fr\cos\theta + Fr^2 - \dfrac{1}{4}(\zeta\cos\theta)^2\Big)t_s^2 \\ +\dfrac{1}{2}\zeta\cos\theta(1 - Fr\cos\theta)t_s^3 + \dfrac{1}{16}(\zeta\cos\theta)^2 t_s^4 - 1 = 0 \end{array}, \tag{4.43}$$

which is the same as (4.34).

4.4.2 Estimators of the strength of nonlinearity and the strength of frequency dispersion

Just like in the 1DH landslide wave on a slope scenario, we shall modify the analytical solution in constant water depth to assemble semi-analytical expressions to estimate the strength of nonlinearity and the strength of frequency dispersion. A representative water depth $1 \le \chi_* \le \chi$ has been defined in (4.35) as

$$\chi_* = 1 + C_{\chi_*}(\chi - 1), \quad 0 \le C_{\chi_*} \le 1, \tag{4.44}$$

where C_{χ_*} is to be determined empirically. The corresponding input parameters at the representative water depth χ_* are then calculated:

$$(Fr_*, \delta_*, \gamma_*) = (Fr\chi_*^{-\frac{1}{2}}, \delta\chi_*^{-1}, \gamma\chi_*), \tag{4.45}$$

which again are the same as (4.36). We then use the scaling relations revealed by the 2DH analytical solution in constant depth, (4.16), with (4.45) as the input parameters, to write the scaling requirements as

$$\overline{\epsilon} = \delta_*\Big|\frac{Fr_*\cos\theta}{2(1 - Fr_*\cos\theta)}\Big|r_s^{-\frac{1}{2}}\max(1, t_s) + C_\delta\delta \le C_\epsilon, \quad \overline{\mu^2} = \gamma_*^2\max(1, t_s) \le C_{\mu^2}, \tag{4.46}$$

where

$$r_s = t_s + \frac{1}{4}\zeta\cos\theta t_s^2 \tag{4.47}$$

is the normalized leading wave location in the θ direction, and C_δ and C_{χ_*} are to be determined empirically; we later found $C_\delta = 2/3$ and $C_{\chi_*} = 1/4$ to be good choices.

4.4.3 Results

For the LSWE-LWD comparison, a total of 72 cases covering $Fr = [0.3, 0.4, 0.5, 0.6, 0.7, 0.8]$, $\gamma = [0.01, 0.05, 0.1]$, and $\zeta = [0.25, 0.5, 0.75, 1]$ is considered – the range of the slopes covered by these parameters is $0.143^\circ \leq \beta \leq 5.71^\circ$. Again, δ has no real effects in linear models. For each case, the RMSDs for the leading waves in 14 directions are computed ($\theta = [0, 1, 2, 3, 4, 5, 6, 10, 11, 12, 13, 14, 15, 16]\pi/16$, which are interpolated from the rectangular mesh; $\theta \sim \pi/2$ is not considered because the waves are negligibly small there). As a result, a total of 1008 points is available for determining C_{μ^2}. The results are shown in figure 4.16. We later found that $C_{\chi_*} = 1/4$ (same as in the 1DH case) minimizes the overall scattering in both the LSWE-LWD comparison and the LSWE-NSWE comparison (a total of 2016 points).

As can be seen in figure 4.16, despite its empirical nature, $\overline{\mu^2}$ successfully captures the strength of frequency dispersion as a function of the input parameters, and a curve based on a power function (the reasons for not using a different function form have been discussed in the 1DH constant depth section) can be fitted to the data points:

$$\text{RMSD} = 104.8(\overline{\mu^2})^{0.5786}, \quad R^2 = 0.9495, \tag{4.48}$$

C_{μ^2} can be recovered from (4.38) as

$$C_{\mu^2} = (\frac{\text{RMSD}}{104.8})^{1.728}. \tag{4.49}$$

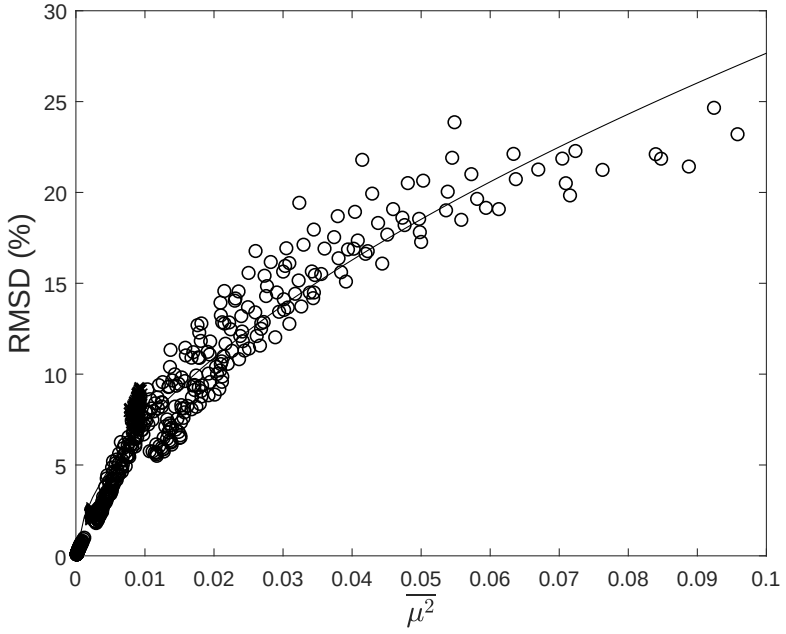

Figure 4.16: The estimator of the strength of frequency dispersion, $\overline{\mu^2}$ in (4.46), plotted as a function of RMSD of LWD from LSWE, for the 2DH landslide-generated waves on a slope scenario. Circle: leading waves for $0 \leq \theta < \pi/2$; cross: leading waves for $\pi/2 < \theta \leq \pi$; solid line: fitted curve (4.48).

(4.39) can then be used in (4.37) to determine whether frequency dispersion is important or not in a 2DH landslide wave on a slope scenario.

Similarly, C_ϵ can be determined from the LSWE-NSWE comparison. A total of 72 cases covering $Fr = [0.3, 0.4, 0.5, 0.6, 0.7, 0.8]$, $\delta = [0.05, 0.1, 0.2]$, and $\zeta = [0.25, 0.5, 0.75, 1]$ is considered. Again, γ has no real effects in nondispersive models. For each case, the RMSDs for the leading waves in 14 directions ($\theta = [0, 1, 2, 3, 4, 5, 6, 10, 11, 12, 13, 14, 15, 16]\pi/16$) are computed. As a result, a total of 1008 points are available for determining C_ϵ and C_δ. We found $C_\delta = 2/3$ to be a good fit that reduces scattering; along with the LSWE-LWD comparison, we found $C_{\chi_*} = 1/4$ to be a good fit that reduces scattering in both cases. The resulting $\bar{\epsilon}$ v.s. RMSD plot is shown in figure 4.17. A curve based on a power function (again, we note that the reasons for not using a different function form

have been discussed in the 1DH constant depth section) can be fitted to the data points:

$$\text{RMSD} = 34.74(\bar{\epsilon})^{1.040}, \quad R^2 = 0.8131. \tag{4.50}$$

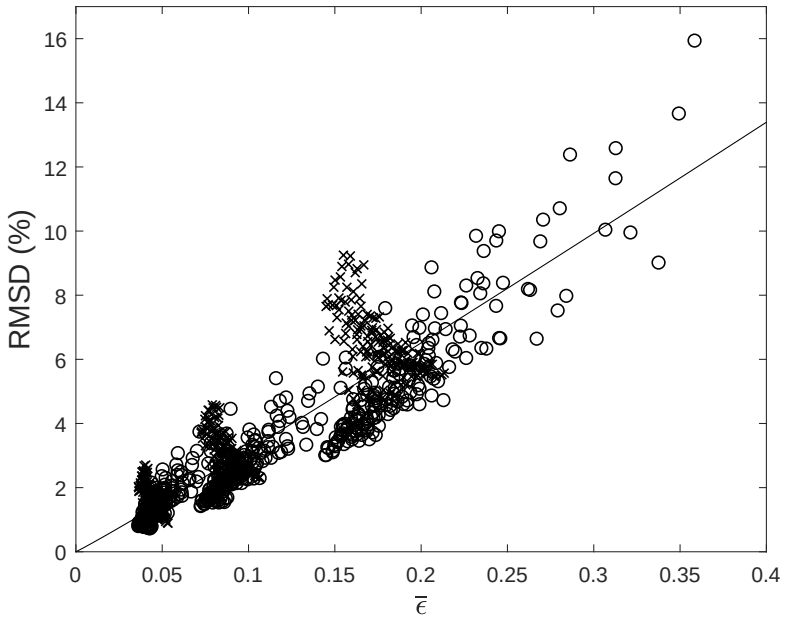

Figure 4.17: The estimator of the strength of nonlinearity, $\bar{\epsilon}$ in (4.46), plotted as a function of RMSD of NSWE from LSWE, for the 2DH landslide-generated waves on a slope scenario. Circle: leading waves for $0 \leq \theta < \pi/2$; cross: leading waves for $\pi/2 < \theta \leq \pi$; solid line: fitted curve (4.50).

Significant scattering can be observed in figure 4.17, especially for $\pi/2 < \theta \leq \pi$, and a less-than-ideal coefficient of determination $R^2 = 0.8131$ results. Upon closer examination, we found the scattering to be due primarily to the waves in the $\theta = 10\pi/16, 11\pi/16$ directions, where the waves are small and the RMSDs are therefore prone to numerical noise and contamination by the thin tails (since a Gaussian-shaped landslide is used) of the trapped waves. If data points in these two directions are discarded, a new fitted curve can improve the coefficient of determination to $R^2 = 0.9040$. However, instead of further manipulating the data to get a better fit, we shall leave (4.50) as is, since it is the best we can do with

the simple semi-analytical approach. In addition, $\overline{\epsilon}$ still captures the overall trend of the strength of nonlinearity, and where the most severe discrepancy shows is of the least importance – i.e., near $\theta = \pi/2$ where the waves are already negligibly small. We therefore proceed to rewrite (4.50) as

$$C_\epsilon = (\frac{\text{RMSD}}{34.74})^{0.9615}. \tag{4.51}$$

Given an acceptable RMSD, (4.51) can be used in (4.46) to determine whether nonlinearity is important or not in the 2DH landslide wave on a slope scenario.

To see how the NSWE-WNWD comparison differs from the LSWE-LWD comparison due to the additional nonlinear effects. A total of 108 cases covering $Fr = [0.3, 0.5, 0.7]$, $\delta = [0.1, 0.2, 0.3]$, $\gamma = [0.01, 0.05, 0.1]$, and $\zeta = [0.25, 0.5, 0.75, 1]$ is computed with NSWE and WNWD – the range of the slopes covered by these parameters is $0.143^\circ \leq \beta \leq 5.71^\circ$. The resulting $\overline{\mu^2}$ vs. RMSD plot is shown in figure 4.18. Although more scattering shows and the δ-dependency is evident, overall, $\overline{\mu^2}$ still estimates the strength of frequency dispersion well, and serves as an conservative estimate that predicts a higher RMSD. Therefore, (4.49) can still be used along with (4.46) to determine whether NSWE or WNWD should be used in a nonlinear landslide wave problem.

To see how the LWD-WNWD comparison differs from the LSWE-NSWE comparison due to the additional frequency dispersion effects, we compute the wave fields predicted by LWD and WNWD for a total of 108 cases covering $Fr = [0.3, 0.5, 0.7]$, $\delta = [0.05, 0.1, 0.2]$, $\gamma = [0.05, 0.1, 0.2]$, and $\zeta = [0.25, 0.5, 0.75, 1]$ – the range of the slopes covered by these parameters is $0.716^\circ \leq \beta \leq 11.3^\circ$. The resulting $\overline{\epsilon}$ vs. RMSD plot is shown in figure 4.19. Although more scattering shows, $\overline{\epsilon}$ still captures the order of magnitude of the strength of nonlinearity and generally serves as a conservative estimate. Therefore, (4.51) can still be used along

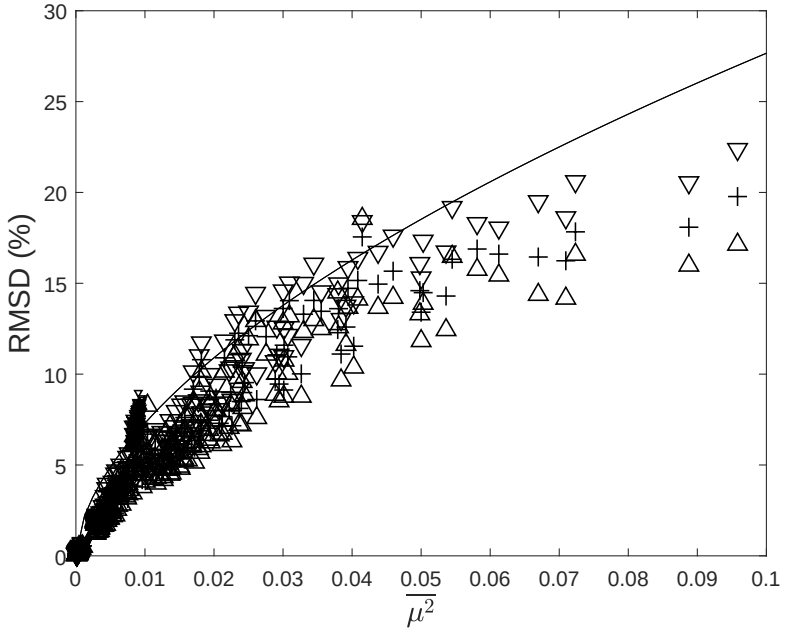

Figure 4.18: The estimator of the strength of frequency dispersion, $\overline{\mu^2}$ in (4.46), plotted as a function of RMSD of WNWD from NSWE, for the 2DH landslide-generated waves on a slope scenario. Downward-pointing triangle: $\delta = 0.1$; plus: $\delta = 0.2$; upward-pointing triangle: $\delta = 0.3$; larger symbols: right-going leading waves; smaller symbols: left-going leading waves; solid line: fitted curve (4.48) based on the LSWE-LWD results.

with (4.46) to determine whether LWD or WNWD should be used in a frequency dispersive landslide wave problem.

4.5 Summary

In this chapter, we devised criteria for determining when nonlinearity becomes important (i.e., whether a nonlinear wave model like NSWE or WNWD should be used), and when frequency dispersion becomes important (i.e., whether a dispersive wave model like LWD or WNWD should be used) in the landslide wave generation stage. A more accurate long-wave model is also computationally more expensive.

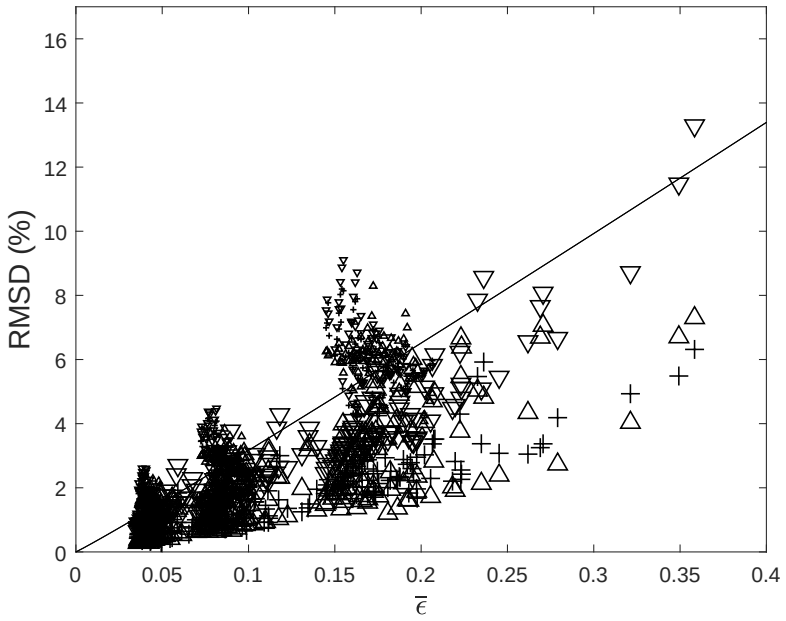

Figure 4.19: The estimator of the strength of nonlinearity, $\overline{\epsilon}$ in (4.46), plotted as a function of RMSD of WNWD from LWD, for the 2DH landslide-generated waves on a slope scenario. Downward-pointing triangle: $\gamma = 0.05$; plus: $\gamma = 0.1$; upward-pointing triangle: $\gamma = 0.2$; larger symbols: right-going leading waves; smaller symbols: left-going leading waves; solid line: fitted curve (4.50) based on the LSWE-NSWE results.

Therefore, to minimize computation cost, it may be desirable to use the simplest acceptable long-wave model to simulate the wave generation process of a landslide tsunami problem. A prescribed Gaussian-shaped landslide traveling at a constant speed was used in four idealized scenarios: 1DH constant depth, 2DH constant depth, 1DH on a slope, and 2DH on a slope. For each scenario, three or four input parameters were defined to describe the problem. Since the 2DH on a slope scenario is the most realistic, and will be examined further later in this study, we shall summarize the results for this scenario here.

The configuration of the 2DH landslide-generated waves on a slope scenario has

been sketched in figure 4.11. Four input parameters describe the problem:

$$\begin{cases} Fr = V_b \cos\beta/\sqrt{gd_0}: & \text{landslide speed, } 0 < Fr < 1 \\ \delta = A_b \sec\beta/d_0: & \text{landslide shape nonlinearity} \\ \gamma = d_0/(L_b \cos\beta): & \text{relative water depth} \\ \zeta = \tan\beta/\gamma: & \text{relative steepness of the slope, } 0 < \zeta \leq 1 \end{cases} . \tag{4.52}$$

For the leading wave in the θ direction, the instant t_s (dimensionless) when the wave generation stage ends can be iteratively solved from

$$\begin{array}{c} -\zeta\cos\theta t_s + \Big(1 - 2Fr\cos\theta + Fr^2 - \frac{1}{4}(\zeta\cos\theta)^2\Big)t_s^2 \\ +\frac{1}{2}\zeta\cos\theta(1 - Fr\cos\theta)t_s^3 + \frac{1}{16}(\zeta\cos\theta)^2 t_s^4 - 1 = 0 \end{array} . \tag{4.53}$$

After this instant, the leading wave propagates freely, no longer affected by the landslide, and the wave propagation problem becomes the same as the conventional tsunami propagation problem (i.e., water waves only; no landslide).

The criterion $\overline{\mu^2} \leq C_{\mu^2}$, taking into account the strength of frequency dispersion in both space and time, determines whether frequency dispersion is important or not for the leading wave in the θ direction (θ needs to be specified, since the outcomes in different directions differ) up until the instant $t = t_s$:

$$\overline{\mu^2} = \gamma_*^2 \max(1, t_s) \leq C_{\mu^2} = \left(\frac{\text{RMSD}}{104.8}\right)^{1.728}, \tag{4.54}$$

where RMSD is the Root-Mean-Squared Deviation error tolerance (%) to be specified by the user. Given a RMSD error tolerance and a set of input parameters, if $\overline{\mu^2} \leq C_{\mu^2}$, then frequency dispersion is considered insignificant and a nondispersive wave model can be used to model the wave generation stage (which ends at $t = t_s$) for the leading wave in the θ direction; vice versa. Similarly, the criterion $\overline{\epsilon} \leq C_\epsilon$, taking into account the strength of nonlinearity in both space and time, determines whether nonlinearity is important or not for the leading wave in the θ direction up

until the instant $t = t_s$:

$$\overline{\epsilon} = \delta_* |\frac{Fr_* \cos\theta}{2(1 - Fr_* \cos\theta)}| r_s^{-\frac{1}{2}} \max(1, t_s) + \frac{2}{3}\delta \leq C_\epsilon = (\frac{\text{RMSD}}{34.74})^{0.9615}. \tag{4.55}$$

Given a RMSD error tolerance, if $\overline{\epsilon} \leq C_\epsilon$, then nonlinearity is considered insignificant and a linear wave model can be used to model the wave generation stage (which ends at $t = t_s$) for the leading wave in the θ direction; vice versa. The additional terms in the expressions for $\overline{\mu^2}$ and $\overline{\epsilon}$ are calculated as functions of the input parameters as follows:

$$\begin{cases} r_s = t_s + \dfrac{1}{4}\zeta \cos\theta t_s^2 \\ (Fr_*, \delta_*, \gamma_*) = (Fr\chi_*^{-\frac{1}{2}}, \delta\chi_*^{-1}, \gamma\chi_*) \\ \chi_* = 1 + \dfrac{1}{4}(\chi - 1) \\ \chi = 1 + \zeta \cos\theta t_s + \dfrac{1}{4}(\zeta \cos\theta)^2 t_s^2 \end{cases}. \tag{4.56}$$

CHAPTER 5

LANDSLIDE ACCELERATION EFFECTS

Thus far, the criteria for determining model validity are based on a landslide moving at a constant speed. However, the initial acceleration of a submarine landslide is an important parameter in realistic problems. To make the criteria more applicable, in this chapter we will examine the effects of landslide acceleration so that the additional effects can be incorporated in the existing expressions, by considering a landslide that accelerates at a fixed magnitude before reaching a specified constant speed. First, we employ the Green's function approach to study the acceleration effects analytically based on 1DH LSWE. Then, we use numerical simulations based on 1DH LSWE and 2DH LSWE to obtain empirical formulas that account for the wave stretching effects due to an accelerating landslide.

5.1 Analytical investigation

As has been shown in Chapter 2, the dimensionless 1DH LSWE for the landslide-generated tsunami problem (in the domain $-\infty < x < \infty, t > 0$) is

$$\eta_{tt} - \eta_{xx} = B_{tt}, \tag{5.1}$$

with the initial conditions

$$\eta(x,0) = 0, \quad \eta_t(x,0) = B_t(x,0). \tag{5.2}$$

5.1.1 Green's function

To seek the Green's function, $G(x,t,\xi,\tau)$, for the governing equation (5.1) subject to the initial conditions (5.2), we need to solve

$$G_{tt} - G_{xx} = \delta(x-\xi)\delta(t-\tau), \tag{5.3}$$

where δ is the Dirac delta function.

After integrating the right hand side of (5.3) with respect to t to acquire the initial conditions equivalent to $\eta_t(x,0) = B_t(x,0)$ in (5.2), we have

$$G(x,0,\xi,\tau) = 0, \quad G_t(x,0,\xi,\tau) = \delta(x-\xi)H(-\tau), \tag{5.4}$$

where H is the Heaviside step function. The equation (5.3) subject to the initial conditions (5.4) can be solved in the same way as (5.1) and (5.2), by using the Laplace and Fourier transforms:

$$\widetilde{\overline{G}}(k,s,\xi,\tau) = \frac{1}{\sqrt{2\pi}}\frac{1}{s^2+k^2}e^{-ik\xi}\Big[H(-\tau) + H(\tau)e^{-\tau s}\Big]. \tag{5.5}$$

A closed-form inverse Laplace transform is available:

$$\overline{G}(k,t,\xi,\tau) = \frac{1}{\sqrt{2\pi}}\frac{e^{-ik\xi}}{k}\left[H(-\tau)\sin(kt) + H(\tau)H(t-\tau)\sin\Big(k(t-\tau)\Big)\right]. \tag{5.6}$$

A closed-form inverse Fourier transform is also available:

$$\begin{aligned} G(x,t,\xi,\tau) &= \frac{1}{4}H(-\tau)\left[\operatorname{sgn}\Big((x-\xi)+t\Big) - \operatorname{sgn}\Big((x-\xi)-t\Big)\right] \\ &+\frac{1}{4}H(\tau)H(t-\tau)\left[\operatorname{sgn}\Big((x-\xi)+(t-\tau)\Big) - \operatorname{sgn}\Big((x-\xi)-(t-\tau)\Big)\right] \end{aligned}. \tag{5.7}$$

For convenience, we consider the two terms in (5.7) separately:

$$G_1(x,t,\xi,\tau) = \frac{1}{4}H(-\tau)\left[\operatorname{sgn}\Big((x-\xi)+t\Big) - \operatorname{sgn}\Big((x-\xi)-t\Big)\right] \tag{5.8}$$

is nonzero only for $\tau < 0$ due to the step function; likewise,

$$G_2(x,t,\xi,\tau) = \frac{1}{4}H(\tau)H(t-\tau)\left[\mathrm{sgn}\Big((x-\xi)+(t-\tau)\Big)-\mathrm{sgn}\Big((x-\xi)-(t-\tau)\Big)\right] \quad (5.9)$$

is nonzero only for $0 < \tau < t$.

We can then proceed to write the solution using the Green's function:

$$\begin{aligned}\eta &= \int_{-\infty}^{\infty}\int_{-\infty}^{\infty} G(x,t,\xi,\tau)B_{\tau\tau}(\xi,\tau)d\tau d\xi \\ &= \int_{-\infty}^{\infty}\int_{-\infty}^{0} G_1(x,t,\xi,\tau)B_{\tau\tau}(\xi,\tau)d\tau d\xi + \int_{-\infty}^{\infty}\int_{0}^{t} G_2(x,t,\xi,\tau)B_{\tau\tau}(\xi,\tau)d\tau d\xi\end{aligned}. \quad (5.10)$$

Again, for convenience, we consider the two terms in (5.10) separately:

$$\eta_1(x,t) = \int_{-\infty}^{\infty}\int_{-\infty}^{0} G_1(x,t,\xi,\tau)B_{\tau\tau}(\xi,\tau)d\tau d\xi, \quad (5.11)$$

and

$$\eta_2(x,t) = \int_{-\infty}^{\infty}\int_{0}^{t} G_2(x,t,\xi,\tau)B_{\tau\tau}(\xi,\tau)d\tau d\xi. \quad (5.12)$$

Writing out the full expressions for G_1 and G_2, and observing that they each equals either zero or two depending on the integration domain, we end up with the expressions

$$\eta_1(x,t) = \frac{1}{2}\int_{-\infty}^{0}\int_{x-t}^{x+t} B_{\tau\tau}(\xi,\tau)d\xi d\tau, \quad (5.13)$$

and

$$\eta_2(x,t) = \frac{1}{2}\int_{0}^{t}\int_{x-(t-\tau)}^{x+(t-\tau)} B_{\tau\tau}(\xi,\tau)d\xi d\tau. \quad (5.14)$$

In the solution process, we further found η_2 to be the solution due to homogeneous initial conditions, $\eta(t=0) = \eta_t(t=0) = 0$, and η_1 is the additional term due to the initial condition $\eta_t(t=0) = B_t(t=0)$. If B is specified such that $B_t(t=0) = 0$, then $\eta_1 = 0$ and does not have to be considered.

5.1.2 Accelerating landslide

To admit an accelerating landslide, we consider a piecewise-defined landslide forcing function which accelerates over a timespan t_0 (normalized by the characteristic time scale, $L/\sqrt{gd}$) at a constant magnitude from zero velocity to reach a terminal velocity, Fr, after which the landslide travels indefinitely at the terminal velocity. Dimensionlessly, the acceleration is expressed as $a_0 = Fr/t_0$, and the distance traveled over the timespan t_0 is $x_0 = Fr \cdot t_0/2$. The resulting landslide forcing function is

$$B(x,t) = B(s) = \begin{cases} B(x - \frac{1}{2}a_0 t^2), & 0 \le t \le t_0 \\ B\Big(x - x_0 - Fr(t - t_0)\Big), & t > t_0 \end{cases} . \tag{5.15}$$

For this landslide forcing function, $B_t(t=0) = 0$. Therefore, $\eta_1 = 0$ and only η_2, (5.14), needs to be considered. The resulting solution during the acceleration phase, $t \le t_0$, is

$$\eta(x,t) = \frac{1}{2}\int_0^t \int_{x-(t-\tau)}^{x+(t-\tau)} B_{\tau\tau}(\xi - \frac{1}{2}a_0\tau^2)d\xi d\tau, \tag{5.16}$$

and the solution during the constant-speed phase, $t > t_0$, is

$$\begin{aligned} \eta(x,t) = &\frac{1}{2}\int_0^{t_0} \int_{x-(t-\tau)}^{x+(t-\tau)} B_{\tau\tau}(\xi - \frac{1}{2}a_0\tau^2)d\xi d\tau \\ &+\frac{1}{2}\int_{t_0}^{t} \int_{x-(t-\tau)}^{x+(t-\tau)} B_{\tau\tau}\Big(\xi - x_0 - Fr(\tau - t_0)\Big)d\xi d\tau \end{aligned} . \tag{5.17}$$

Again, for convenience, we consider the two double integrals in (5.17) separately:

$$\eta_3(x,t) = \frac{1}{2}\int_0^{t_0} \int_{x-(t-\tau)}^{x+(t-\tau)} B_{\tau\tau}(\xi - \frac{1}{2}a_0\tau^2)d\xi d\tau, \tag{5.18}$$

and

$$\eta_4(x,t) = \frac{1}{2}\int_{t_0}^{t} \int_{x-(t-\tau)}^{x+(t-\tau)} B_{\tau\tau}\Big(\xi - x_0 - Fr(\tau - t_0)\Big)d\xi d\tau. \tag{5.19}$$

We shall refer to η_3 as the solution due to the acceleration phase, and η_4 as the solution due to the constant-speed phase. During the acceleration phase, $t \leq t_0$, the solution is an integral very similar to η_3, but with t_0 in the expression for η_3 replaced by t (since $0 < t \leq t_0$).

A closed-form expression is available for η_4. Letting $u = \tau - t_0$, $s = t - t_0$, and $l = \xi - x_0$, (5.19) can be written as

$$\eta_4 = \frac{1}{2}\int_0^s \int_{(x-x_0)-(s-u)}^{(x-x_0)+(s-u)} B_{uu}(l - Fr \cdot u)dldu. \tag{5.20}$$

The double integral can be evaluated to be

$$\eta_4(x,t) = \frac{Fr^2}{2(1-Fr)}B\Big(x - x_0 - (t-t_0)\Big) - \frac{Fr^2}{1-Fr^2}B\Big(x - x_0 - Fr(t-t_0)\Big) + \frac{Fr^2}{2(1+Fr)}B\Big(x - x_0 + (t-t_0)\Big). \tag{5.21}$$

It can be further shown that (5.21) is the solution to 1DH LSWE, (5.1), subject to the homogeneous initial conditions $\eta(x, t = t_0) = 0 = \eta_t(x, t = t_0)$, where a landslide starts moving at a constant speed Fr at $(x,t) = (x_0, t_0)$.

Next, we turn our attention to the solution due to the acceleration phase, η_3. For a landslide forcing function of the form $B(x,t) = B\Big(x - f(t)\Big)$, where $f(t)$ is some continuous function, such as that considered in (5.15), its second derivative in time is

$$B\Big(x - f(t)\Big)_{tt} = B(s)_{tt} = f'^2(t)B''(s) - f''(t)B'(s). \tag{5.22}$$

In such case, η_3 can be simplified:

$$\begin{aligned}\eta_3(x,t) &= \frac{1}{2}\int_0^{t_0}\int_{x-(t-\tau)}^{x+(t-\tau)} f'^2(\tau)B''\Big(\xi - f(\tau)\Big) - f''(\tau)B'\Big(\xi - f(\tau)\Big)d\xi d\tau \\ &= \frac{1}{2}\int_0^{t_0}\Big[f'^2(\tau)B'\Big(\xi - f(\tau)\Big) - f''(\tau)B\Big(\xi - f(\tau)\Big)\Big]_{\xi=x-(t-\tau)}^{\xi=x+(t-\tau)} d\tau.\end{aligned} \tag{5.23}$$

For the specific case where $f(t) = a_0 t^2/2$, (5.23) becomes

$$\eta_3(x,t) = \frac{1}{2}\int_0^{t_0} \left[a_0^2\tau^2 B'\Big(\xi - \frac{1}{2}a_0\tau^2\Big) - a_0 B\Big(\xi - \frac{1}{2}a_0\tau^2\Big)\right]_{\xi=x-(t-\tau)}^{\xi=x+(t-\tau)} d\tau. \quad (5.24)$$

The solution due to the acceleration phase, (5.23), or (5.24), should be investigated further as it accounts for the effects of landslide acceleration.

In the limit $a_0 \to \infty$, the landslide accelerates instantaneously from zero speed to Fr and $t_0 = Fr/a_0 \to 0$. For $\tau \simeq 0$ in the $\tau-$integral, (5.24) simplifies to

$$\eta_3(x,t) = \frac{1}{2}\int_0^{\frac{Fr}{a_0}} \Big[-a_0 B(x+t)+a_0 B(x-t)\Big] d\tau = \frac{Fr}{2}B(x-t) - \frac{Fr}{2}B(x+t). \quad (5.25)$$

The full solution, $\eta = \eta_3 + \eta_4$, is then

$$\eta(x,t) = \frac{Fr}{2(1-Fr)}B(x-t) - \frac{Fr^2}{1-Fr^2}B(x-Frt) - \frac{Fr}{2(1+Fr)}B(x+t). \quad (5.26)$$

We see that in the limit $a_0 \to \infty$, the constant-speed solution, (2.43), is indeed recovered.

5.1.3 Gaussian-shaped landslide

To plot the solutions, we again use a Gaussian-shaped landslide:

$$B(s) = e^{-8s^2}. \quad (5.27)$$

The second derivative in time for the piecewise-defined landslide forcing function, (5.15), is

$$B_{tt}(x,t) = \begin{cases} 8a_0 e^{-8(x-\frac{1}{2}a_0t^2)^2}(8a_0^3t^6 - 32a_0^2t^4x + 32a_0t^2x^2 - 3a_0t^2 + 2x), \, 0 \le t \le t_0 \\ 16Fr^2\Big(16\Big(x - x_0 - Fr(t-t_0)\Big)^2 - 1\Big)e^{-8\left(x-x_0-Fr(t-t_0)\right)^2}, \, t > t_0 \end{cases}. \quad (5.28)$$

For this landslide forcing function, η_3 in (5.23) becomes

$$\eta_3(x,t) = \frac{1}{2}\int_0^{t_0} \left[a_0 e^{-8\left(x+(t-\tau)-\frac{1}{2}a_0\tau^2\right)^2} \left(8a_0^2\tau^4 - 16a_0\tau^2\big(x+(t-\tau)\big) - 1\right) \right.$$
$$\left. -a_0 e^{-8\left(x-(t-\tau)-\frac{1}{2}a_0\tau^2\right)^2} \left(8a_0^2\tau^4 - 16a_0\tau^2\big(x-(t-\tau)\big) - 1\right) \right] d\tau \quad . \tag{5.29}$$

To check the solutions, we compare the analytical solution (5.29) with the numerical solution obtained by solving 1DH LSWE directly via the finite-difference solver described in Chapter 3. For $(Fr, t_0, t) = (0.5, 2, 3)$, the results are shown in figure 5.1. As expected, the two solutions agree perfectly with each other. The accuracy of the analytical solution and that of the numerical methods are thus verified.

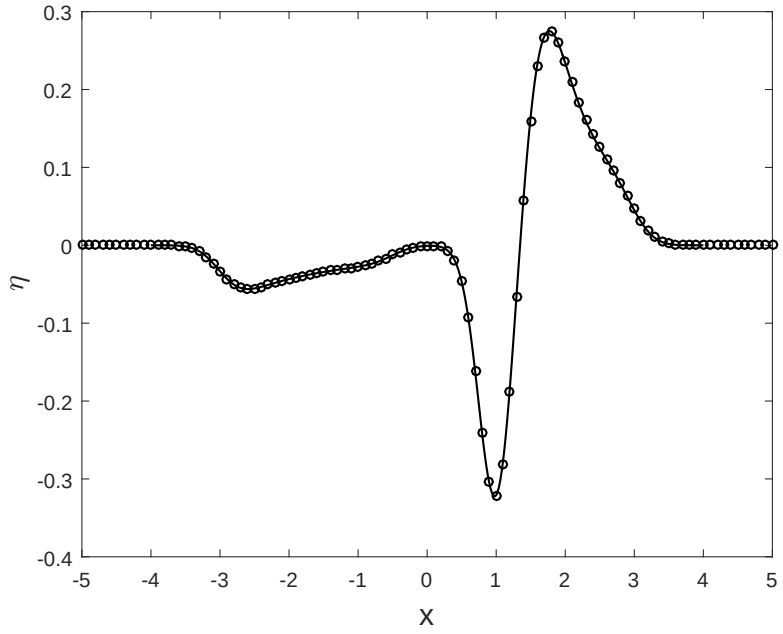

Figure 5.1: Comparison of the analytical solution (5.17), circle, with the numerical solution, solid line, for $(Fr, t_0, t) = (0.5, 2, 3)$.

Next, we look at the solution components more closely. We consider the two

terms in (5.29) separately:

$$\eta_{3-}(x+t) = \frac{1}{2}\int_0^{t_0} \left[a_0 e^{-8\left((x+t)-\tau-\frac{1}{2}a_0\tau^2\right)^2} \left(8a_0^2\tau^4 - 16a_0\tau^2\big((x+t)-\tau\big) - 1 \right) \right] d\tau \tag{5.30}$$

and

$$\eta_{3+}(x-t) = \frac{1}{2}\int_0^{t_0} \left[-a_0 e^{-8\left((x-t)+\tau-\frac{1}{2}a_0\tau^2\right)^2} \left(8a_0^2\tau^4 - 16a_0\tau^2\big((x-t)+\tau\big) - 1 \right) \right] d\tau. \tag{5.31}$$

While η_{3-} represents a free surface disturbance traveling to the left at speed one along the x-axis, η_{3+} represents that traveling to the right. For $t > t_0$, the full solution is therefore

$$\eta(x,t) = \eta_{3-}(x,t) + \eta_{3+}(x,t) + \eta_4(x,t). \tag{5.32}$$

The full solution therefore consists of η_{3-} (5.30), η_{3+} (5.31), and η_4 (5.21):

$$\eta = \eta_{3-} + \eta_{3+} + \eta_4. \tag{5.33}$$

For $(Fr, t_0, t) = (0.5, 2, 6)$, the full solution and each solution component are plotted in figure 5.2. The "three-wave structure", consisting of a right-going free wave, a right-going trapped wave which follows the landslide, and a left-going free wave, can be identified. In fact, a steady state has been reached – each of the three waves propagates away from the origin at its own velocity without changing its shape.

To see how the solution evolves in time, in figure 5.3 we plot the analytical solution for the case $(Fr, t_0) = (0.5, 2)$, for $t = 1, 2, 3, 4$. We note that for $0 < t \leq t_0$, the landslide accelerates at a constant rate from zero speed, and for $t > t_0$, the landslide travels at a constant speed. It is observed that in the acceleration phase, the generated leading waves are lengthened due to the finite acceleration.

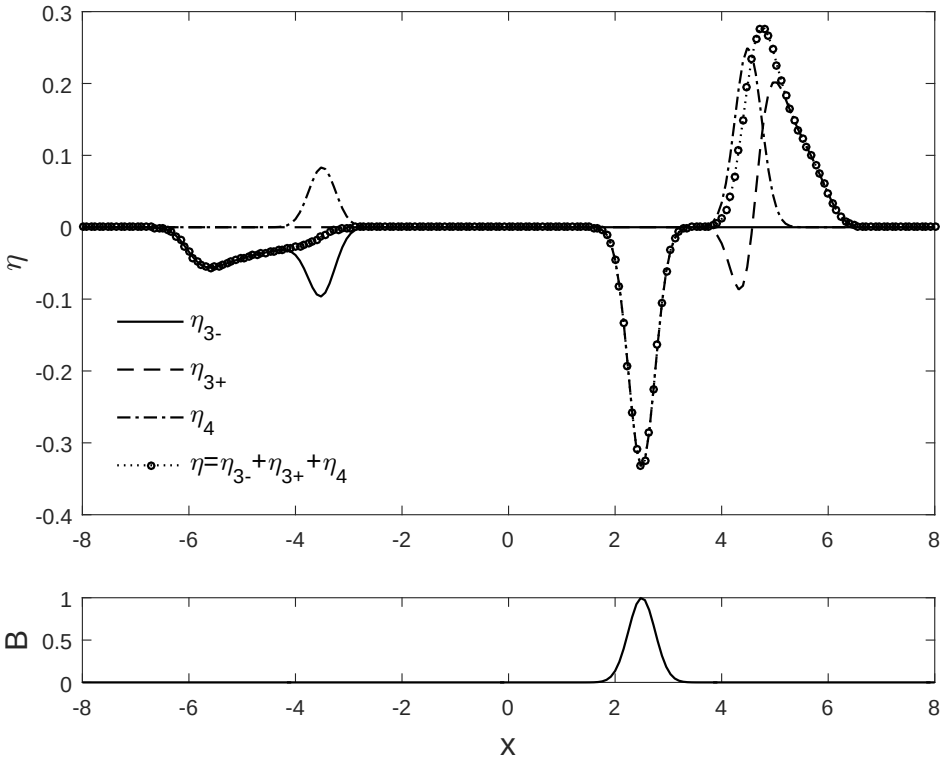

Figure 5.2: The full solution and each solution component for $(Fr, t_0, t) = (0.5, 2, 6)$.

After the acceleration phase, a steady-state solution is eventually reached, since the landslide moves at a constant speed.

To see how the solution changes with respect to t_0 (how much time the landslide takes to accelerate to Fr), we plot the snapshots for $t_0 = 3$ in figure 5.4 and those for $t_0 = 1$ in figure 5.5. The same behaviors can be observed: the generated leading waves are lengthened during the acceleration phase, and eventually reach a steady state during the constant-speed phase. Wave lengthening is less pronounced for smaller t_0 (faster acceleration), and vice versa. The constant-speed solution results in the limit $t_0 \to 0$:

$$\eta(x,t) = \frac{Fr}{2(1-Fr)} B(x-t) - \frac{Fr^2}{1-Fr^2} B(x - Fr \cdot t) - \frac{Fr}{2(1+Fr)} B(x+t). \quad (5.34)$$

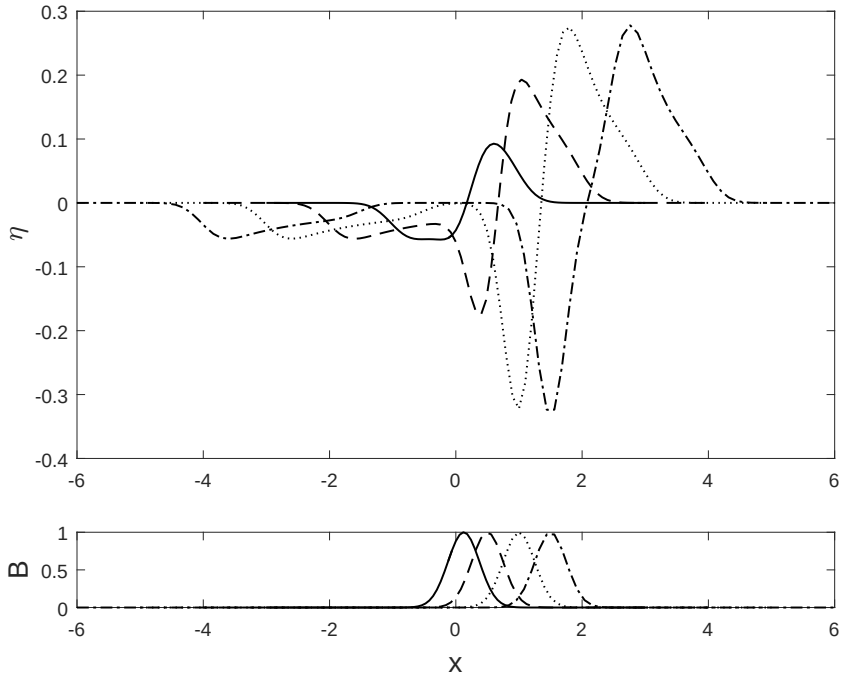

Figure 5.3: Snapshots of the wave field for the case $(Fr, t_0) = (0.5, 2)$, at $t = 1, 2, 3, 4$.

In short, we find that the slower the acceleration, the more the generated leading waves are lengthened and their amplitudes reduced, compared to the constant-speed solution (the case with infinitely large acceleration).

5.2 Numerical investigation

Although the analytical investigation yields clear, definitive results, the analytical solutions are of limited practical value. First, the analytical solution for η_3 still involves integrals that need to be evaluated numerically. While the computation cost is inexpensive, we've found that solving LSWE directly using a numerical solver is nonetheless much faster and provides similarly accurate results. Second, the extension of the analytical work to 2DH is not trivial, whereas 2DH numerical results

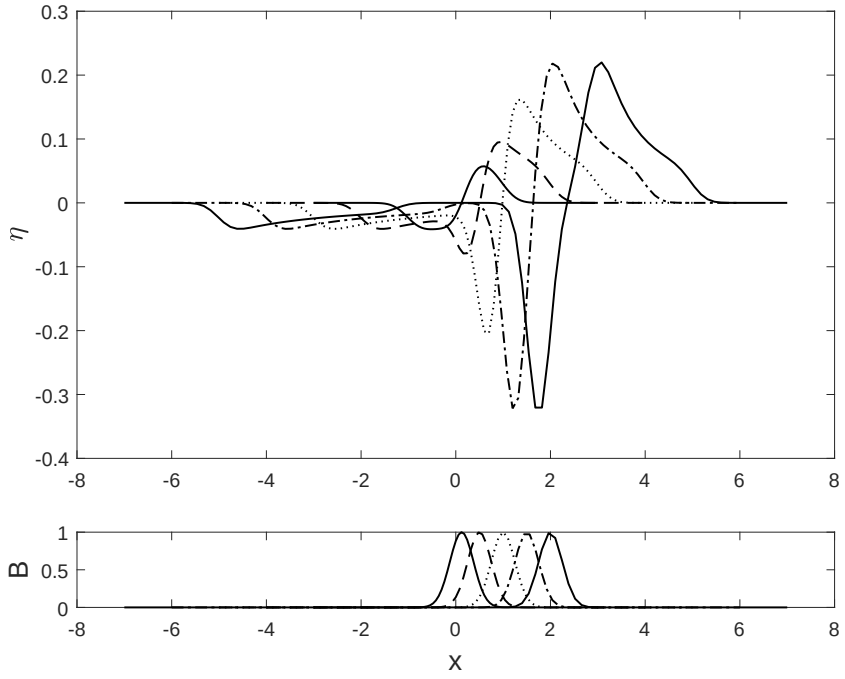

Figure 5.4: Snapshots of the wave field for the case $(Fr, t_0) = (0.5, 3)$, at $t = 1, 2, 3, 4, 5$.

can be easily obtained. Therefore, we shall utilize the insights gained from the analytical investigation, and proceed to study the effects of landslide acceleration via numerical simulations.

The key insights learned from the analytical investigation are:

1. after some time t_1, a steady state is reached, in which the waves simply propagate away from the origin but no longer change shape
2. the leading waves are stretched due to an accelerating landslide – the slower the acceleration, the longer the wavelength and the smaller the wave height, in comparison with those due to a constant-speed landslide

To see how landslide acceleration changes the results in Chapter 4 for a constant-

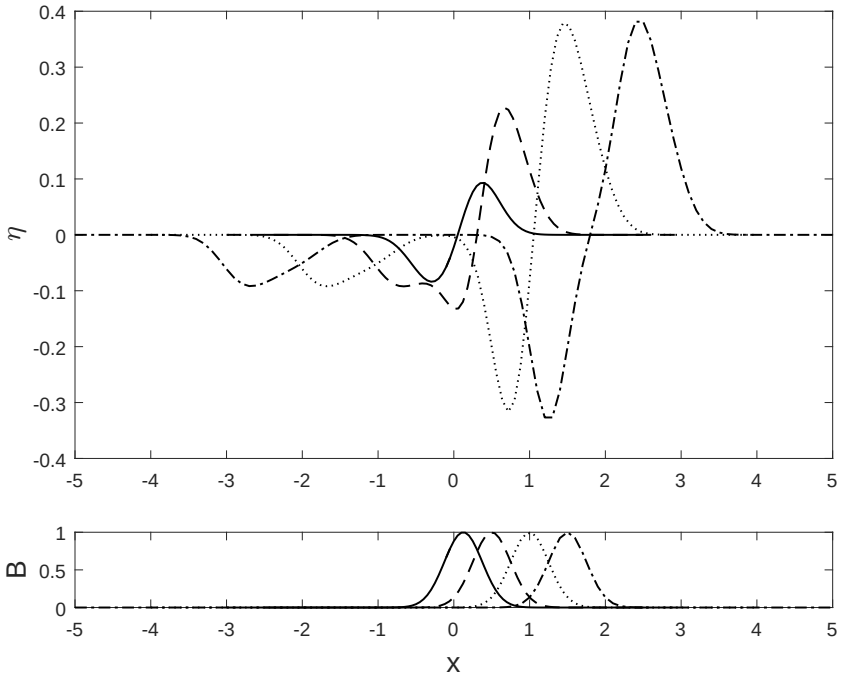

Figure 5.5: Snapshots of the wave field for the case $(Fr, t_0) = (0.5, 1)$, at $t = 0.5, 1, 2, 3$.

speed landslide, we thus need means to quantify the wave stretching effects – we shall do so by finding empirical formulas based on numerical simulations.

5.2.1 Two horizontal dimensions

Since it is simpler to derive the expressions in 2DH and then reduce them to 1DH, we shall present the 2DH case first. As a start, we inspect how the wavelength of the leading wave might be modified in LSWE due to an accelerating landslide. Consider a 2DH landslide wave problem in constant water depth. The landslide accelerates in the positive x direction from zero speed at $t = 0$ to speed Fr at $t = t_0$ (normalized by the characteristic time scale $L/\sqrt{gd}$). At the instant $t = t_0$, The landslide is located at $x = x_0 = Fr \cdot t_0/2$ (normalized by the characteristic

length L), and additional waves are generated from here (as shown by the solution for the constant-speed phase in the analytical investigation) – a trapped wave that stays with the landslide and outward going waves that propagate away from the landslide at speed one.

The first free surface disturbance is generated as soon as the landslide starts moving, and propagates outwards from the origin at a normalized speed of one – the front of this outward-propagating disturbance forms a ring of radius t centered at the origin. The last outward-propagating free surface disturbance is generated at the instant $t = t_0$ when the landslide transitions from the acceleration phase to the constant-speed phase – this disturbance travels at speed one away from the landslide at this instant, and forms a ring of radius $t - t_0$ centered at $(x, y) = (Fr \cdot t_0/2, 0)$. We expect the distance between these two rings to reflect the additional contribution to the wavelength of the leading wave due to an accelerating landslide.

To find an expression for this distance, we focus on the instant $t = t_0$. The task can then be seen as finding the distance s in the geometry problem as sketched in figure 5.6. The law of cosines then gives

$$s^2 = t_0^2 + x_0^2 - 2t_0 x_0 \cos\theta, \tag{5.35}$$

from which we obtain

$$s = t_0\sqrt{1 + \frac{1}{4}Fr^2 - Fr\cos\theta}. \tag{5.36}$$

In finding the empirical formulas, we expect the stretched wavelength to depend on s.

Based on various numerical tests, we find that $t_1 = t_0 + 4/(1 - Fr)$ is sufficient to reach the steady state (a larger time would work, too, albeit computationally more expensive), and $\Delta x = \Delta y = 0.05$ (normalized by the characteristic

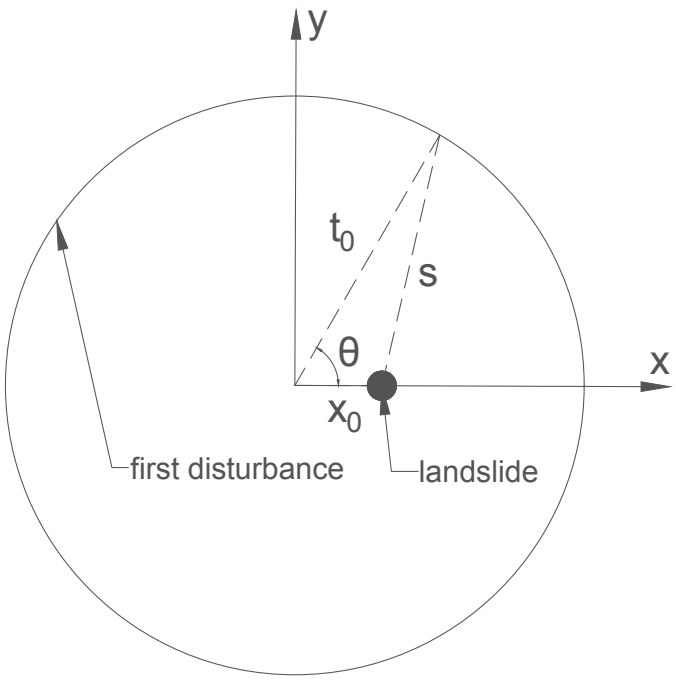

Figure 5.6: A sketch of the geometry problem for finding an expression for s.

length L) is sufficient for efficient computation. The numerical wave basin is set to be large enough so that waves do not reach the open boundaries within t_1, and a radially symmetric Gaussian-shaped landslide is used. A total of 54 numerical simulations were performed, where the parameters considered are $Fr = [0.3, 0.4, 0.5, 0.6, 0.7, 0.8]$ and $t_0 = [0, 0.25, 0.50, 0.75, 1.00, 2.00, 3.00, 4.00, 5.00]$ ($t_0 = 0$ is used to denote the constant-speed case). For each numerical simulation, the free surface elevation transects in 16 different θ directions ($\theta = [0, 1, 2, 3, 4, 5, 6, 7, 9, 10, 11, 12, 13, 14, 15, 16]/16\pi$) were linearly interpolated from the rectangular grid. Therefore, a total of 864 waves are available for use to compute the empirical formulas.

We define the wavelength modification factor due to an accelerating landslide, L_{acc}, as the wavelength of the leading wave due to an accelerating landslide, divided by that due to a constant-speed landslide – it captures how much the wave is lengthened ($L_{\text{acc}} \geq 1$) relative to the constant-speed case. The wave height

modification factor, A_{acc}, is defined as the wave height of the leading wave due to an accelerating landslide, divided by that due to a constant-speed landslide – it captures how much the wave height is reduced ($A_{\text{acc}} \leq 1$) relative to the constant-speed case.

We recall that the analytical solution is available for the constant-speed case, (2.124). The analytical solution shows that the shape of the far-field leading wave is characterized by Ω_2 (plotted in figure 2.125) for the constant-speed case, the sign of the waves reverses at $\theta = \pi/2$, and the outgoing waves decay as $r^{-1/2}$.

Numerically, it is important to define the wavelength and wave height so that they are easy to detect and are consistent across cases. We define the wave front to be where the free surface ahead of the wave first rises (for $0 < \theta < \pi/2$) or falls (for $\pi/2 < \theta < \pi$) by more than 10^{-5} (normalized by the landslide thickness A), and we define the wave tail to be where the extremum of the trailing depression (for $0 < \theta < \pi/2$) or elevation (for $\pi/2 < \theta < \pi$) is. The wave height is defined as the maximum magnitude of elevation (for $0 < \theta < \pi/2$) or depression (for $\pi/2 < \theta < \pi$), divided by $t_1^{-1/2}$ in each case. The division by $t_1^{-1/2}$ is necessary to remove the wave decay effect so that the wave heights are comparable across different cases (since the leading wave is at $r = t_1$ and the wave decays as $r^{-1/2}$). Sample plots showing the leading wave and the detected points are shown in figure 5.7.

Based on the numerical simulations, we found that L_{acc} indeed closely depends on s, defined in (5.36), and a good fit is

$$L_{\text{acc}} = 1 + 0.6237s, \quad R^2 = 0.9859, \tag{5.37}$$

where R^2 is the coefficient of determination. The actual L_{acc} and the fitted L_{acc} are compared in figure 5.8. The expressions for s, (5.36), and L_{acc}, (5.37), show that

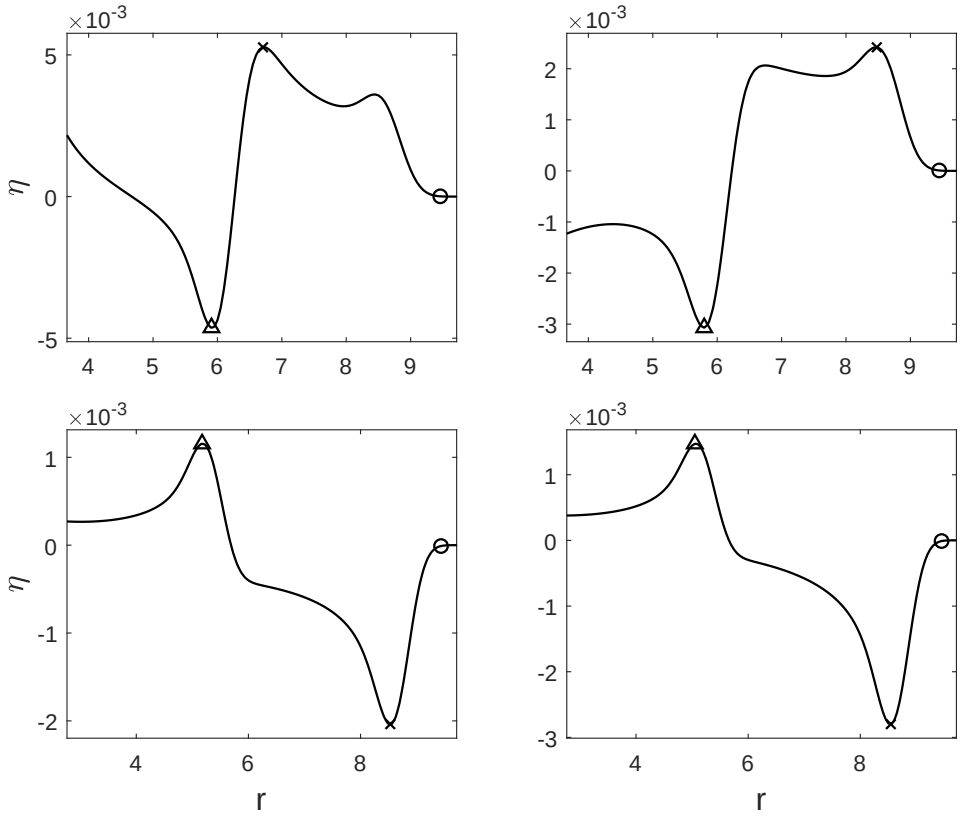

Figure 5.7: Sample plots showing the leading wave and the detected points. Circle: wave front location; cross: maximum elevation; triangle: wave tail location. Top left: $\theta = 0$; top right: $\theta = \pi/4$; bottom left: $\theta = 3\pi/4$; bottom right: $\theta = \pi$.

the slower the acceleration, the longer the wavelength, and that the wavelength is larger for larger θ. The curve fitting process is more challenging for A_{acc}. After trial-and-error and optimizing the expression, we found a good fit to be

$$A_{\text{acc}} = \min\Big[1, L_{\text{acc}}^{-2}\big(5.612 - 9.975(L_{\text{acc}} - 0.5712t_0) + 6.944(L_{\text{acc}} - 0.5712t_0)^2 \\ -1.277(L_{\text{acc}} - 0.5712t_0)^3\big)\Big], \quad R^2 = 0.9858 \tag{5.38}$$

The actual A_{acc} and the fitted A_{acc} are compared in figure 5.9. We see that how the characteristic wave scales are modified by landslide acceleration is well captured by the empirical formulas, (5.37) and (5.38), based on numerical simulations. We shall refer to them as the modification factors due to landslide acceleration. In

Chapter 6, we will demonstrate how these formulas can be used in combination with the model validity criteria presented in Chapter 4 in 2DH applications.

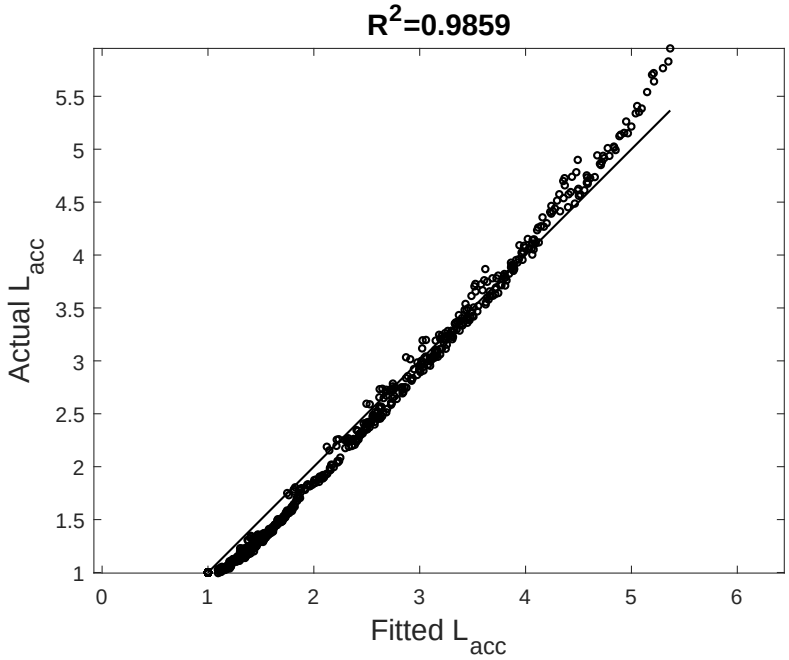

Figure 5.8: Fitted L_{acc}, (5.37) plotted against actual L_{acc} for the 2DH case.

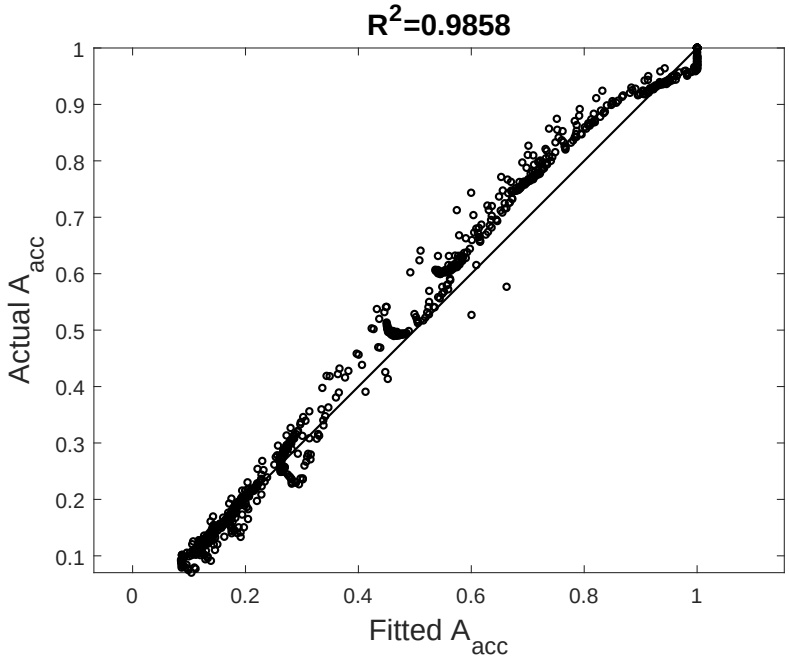

Figure 5.9: Fitted A_{acc}, (5.38) plotted against actual A_{acc} for the 2DH case.

5.2.2 One horizontal dimension

In 1DH, the argument for finding the distance s, which reflects the additional contribution to the wavelength of the leading wave due to an accelerating landslide, is essentially the same as that in 2DH. However, in 1DH, instead of having a continuous θ, only two discreet values, $\theta = 0$ (in the positive x direction) and $\theta = \pi$ (in the negative x direction), are possible. The expressions are therefore

$$s = \begin{cases} t_0\sqrt{1+\frac{1}{4}Fr^2 - Fr}, & \text{for the right-going wave} \\ t_0\sqrt{1+\frac{1}{4}Fr^2 + Fr}, & \text{for the left-going wave} \end{cases} . \tag{5.39}$$

For the 1DH numerical simulation, we find that $t_1 = t_0 + 6/(1 - Fr)$ is sufficient to reach the steady state. A finer resolution, $\Delta x = 0.02$, is used since the computation cost is significantly cheaper in 1DH. A total of 54 numerical simulations were performed, where the parameter ranges considered are the same as those in 2DH: $Fr = [0.3, 0.4, 0.5, 0.6, 0.7, 0.8]$ and $t_0 = [0, 0.25, 0.50, 0.75, 1.00, 2.00, 3.00, 4.00, 5.00]$. Two leading waves, the right-going elevation and the left-going depression, are extracted from each numerical simulation. Therefore, a total of 108 waves are available for use to compute the empirical formulas.

The wavelength and the wave height are simpler to determine in 1DH, since each wave has only one extremum – the right-going wave is an elevation, and the left-going wave is a depression. For the right-going wave, the wavelength is defined as the length of the elevation that rises by more than 10^{-5} (normalized by the landslide thickness A) from the still water level, and the wave height is the maximum elevation; for the left-going wave, the wavelength is defined as the length of the depression that falls by more than 10^{-5} from the still water level, and the

wave height is the maximum magnitude of the depression. Since the waves do not spread laterally in 1DH, the division by $t_1^{-1/2}$ is not needed for the wave height in 1DH.

Similarly to the curve fitting process in 2DH, we found a good fit for L_{acc} in 1DH to be

$$L_{\text{acc}} = 1 + 0.3912s, \quad R^2 = 0.9889. \tag{5.40}$$

The actual L_{acc} and the fitted L_{acc} are compared in figure 5.10. For A_{acc}, we found a good fit to be

$$A_{\text{acc}} = \min\Big[1, L_{\text{acc}}^{-2}\big(5.699 - 9.739(L_{\text{acc}} - 0.3723t_0) + 6.305(L_{\text{acc}} - 0.3723t_0)^2 \\ -1.060(L_{\text{acc}} - 0.3723t_0)^3\big)\Big], \quad R^2 = 0.9938 \tag{5.41}$$

The actual A_{acc} and the fitted A_{acc} are compared in figure 5.11. Again, we see that the characteristic wave scales due to an accelerating landslide are well captured by the empirical formulas, (5.40) and (5.41). We shall refer to them as the modification factors due to landslide acceleration. In Chapter 6, we will demonstrate how these formulas can be used to determine model validity in 1DH applications.

5.3 Summary

In this chapter, we examined the effects due to an accelerating landslide on the water waves it generates. Instead of moving at a constant speed indefinitely, the landslide now accelerates from rest to speed Fr over a duration of t_0 – a smaller t_0 means a faster acceleration, and the limit $t_0 \to 0$ corresponds to the constant-speed case. An analytical investigation based on 1DH LSWE in constant water depth and the Green's function approach was first attempted. It was found that

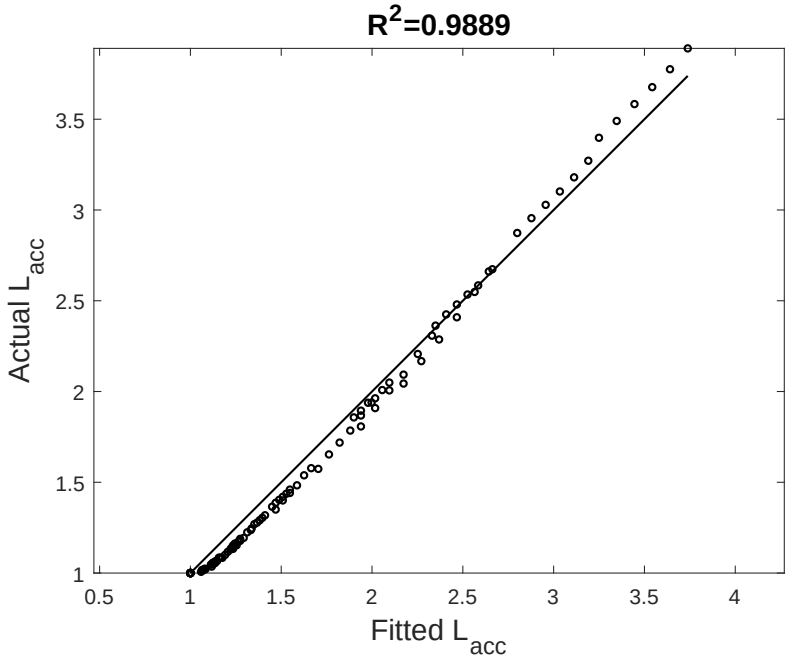

Figure 5.10: Fitted L_{acc}, (5.40) plotted against actual L_{acc} for the 1DH case.

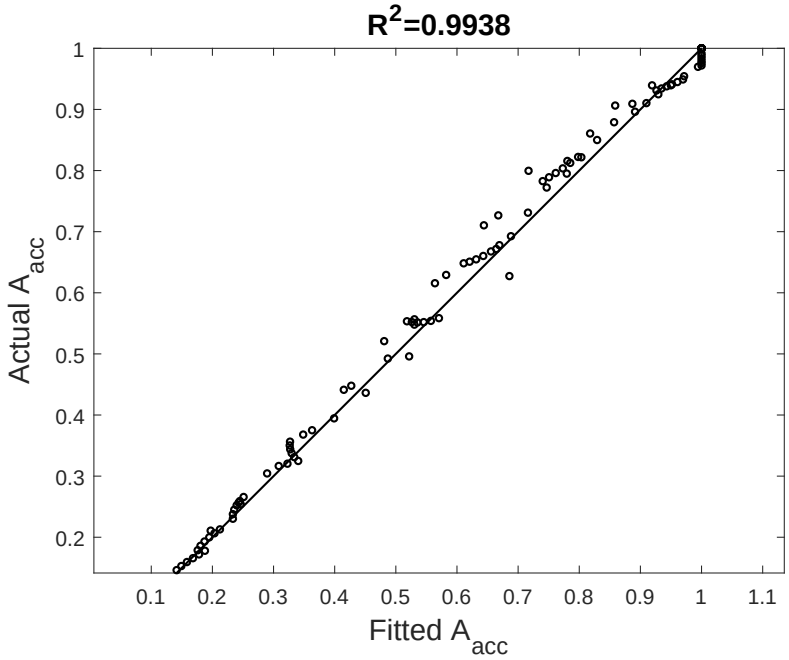

Figure 5.11: Fitted A_{acc}, (5.41) plotted against actual A_{acc} for the 1DH case.

after some time, a steady state was reached, in which the waves, generated by a accelerating landslide, no longer change shape. In addition, wave stretching due to

landslide acceleration was observed – the slower the landslide acceleration (larger t_0), the longer the wavelength and the smaller the wave height, in comparison with those in the constant-speed case.

The wave stretching effects were further examined via numerical simulations based on LSWE in both 1DH and 2DH. The wavelength modification factor, L_{acc} – how much longer the wavelength is than that in the constant-speed case – and the wave height modifcation factor, A_{acc} – how much smaller the wave height is than that in the constant-speed case – were determined empirically based on the numerical results. In 2DH, we found

$$\begin{aligned} L_{\text{acc}} &= 1 + 0.6237s, \quad s = t_0\sqrt{1 + \frac{1}{4}Fr^2 - Fr\cos\theta}, \quad R^2 = 0.9859, \\ A_{\text{acc}} &= \min\Big[1, L_{\text{acc}}^{-2}\big(5.612 - 9.975(L_{\text{acc}} - 0.5712t_0) + 6.944(L_{\text{acc}} - 0.5712t_0)^2 \\ &\qquad\qquad -1.277(L_{\text{acc}} - 0.5712t_0)^3\big)\Big], \quad R^2 = 0.9858, \end{aligned} \tag{5.42}$$

where R^2 is the coefficient of determination. Similar expressions were also determined for the 1DH case. These empirical expressions are valuable as they quantify how the characteristic wave scales are modified by an accelerating landslide, and will be incorporated in the model validity criteria proposed in Chapter 4 in the next chapter.

CHAPTER 6

APPLICATIONS

In this chapter, we shall demonstrate how the results from Chapter 4 (model validity criteria) and Chapter 5 (landslide acceleration effects) can be applied to physical landslide-generated wave problems to determine the simplest (and therefore the most computationally efficient) long-wave model that can be used in each problem. Information on the landslides in real landslide tsunami events is extremely limited, and many modeling assumptions on the landslide motion are needed. Since our goal is to test the effectiveness of the criteria for determining model validity given the input parameters, we shall consider two laboratory landslide wave experiments, in which the motion of the landslide was measured (therefore, the landslide can be prescribed without additional assumptions in the numerical simulations) and the input parameters can be precisely calculated. Although the laboratory experiments were conducted in 1DH, we extend them to 2DH via numerical simulation so that our 2DH results can also be tested. For the real world example, we consider the 1998 PNG tsunami, which is arguably the most studied real event believed to be caused by an underwater landslide, and for which extensive numerical studies are available.

6.1 1DH landslide-generated waves in constant depth

As a physical 1DH landslide wave example in constant water depth, we consider Run 24 from Whittaker (2013). We recall that Run 24 was chosen as a benchmark problem in Chapter 3 to validate the nonlinear numerical solver, and the agreement for the leading wave (which is the primary interest of this study) was good –

therefore, we are confident that this run is at most weakly dispersive and can be captured by either FNWD or WNWD. Again, these two models give essentially identical results for this problem, so we shall consider only WNWD. In Run 24, a 0.026 m thick semi-elliptical landslide of length 0.5 m in a water depth of 0.175 m accelerated at 1.5 m^2/s for 0.437 s, maintained a constant speed for 2 s (the normalized constant speed is $Fr = 0.5$), and then decelerated at 1.5 m^2/s until it stopped. In the numerical simulations, a Gaussian-shaped landslide of height 0.026 m and characteristic length 0.627 m was used to match the area enclosed by the semi-elliptical landslide. To create a shallow water environment, we make the landslide in Run 24 five times as long via numerical simulation, and shall refer to this setup as Run 24-long. To get smaller waves, we make the landslide in Run 24 one third as thick, and shall refer to this setup as Run 24-thin.

For each run, we calculate the input parameters and determine the simplest model that can be used given a 5% RMSD tolerance. Then, we compare the numerical results based on the simplest acceptable model (LSWE, LWD, or NSWE) with the WNWD results, which are regarded as the reference solution, to see how effective the 5% RMSD threshold is at capturing discrepancy in this experimental setup, which is more complex than the idealized scenarios considered in Chapter 4.

6.1.1 Run 24

In the numerical simulations for Run 24, a $A_b = 0.026$ m thick Gaussian-shaped landslide of characteristic length $L_b = 0.627$ m in a water depth of $d = 0.175$ m accelerated at 1.5 m^2/s for 0.437 s, maintained a constant speed for 2 s, and then decelerated at 1.5 m^2/s until it stopped. The input parameters for the 1DH

landslide wave in a constant depth scenario are computed:

$$(Fr, \delta, \gamma) = (0.5, 0.15, 0.28). \tag{6.1}$$

The time (normalized by $T = L_b/\sqrt{gd} = 0.478$ s) it takes for the landslide to accelerate to Fr, is

$$t_0 = 0.437/0.478 = 0.914. \tag{6.2}$$

To account for the acceleration effects, we use the empirical formula (5.40) to find the wavelength modification factors to be

$$\begin{cases} L_{\text{acc}} = 1.45, & \text{for the left-going wave} \\ L_{\text{acc}} = 1.27, & \text{for the right-going wave} \end{cases}, \tag{6.3}$$

and we use the empirical formula (5.41) to find the wave height modification factors to be

$$\begin{cases} A_{\text{acc}} = 0.774, & \text{for the left-going wave} \\ A_{\text{acc}} = 0.576, & \text{for the right-going wave} \end{cases}. \tag{6.4}$$

After the landslide has reached the constant speed phase, the time it takes for the waves to separate from the landslide by one characteristic wavelength, taking the wavelength modification factor into account, is

$$\begin{cases} t_s = L_{\text{acc}}/(1+Fr) = 0.967, & \text{for the left-going wave} \\ t_s = L_{\text{acc}}/(1-Fr) = 2.54, & \text{for the right-going wave} \end{cases}. \tag{6.5}$$

$$\tag{6.6}$$

Combining t_0 and t_s, we obtain the total time it takes for the leading waves to separate from the landslide:

$$\begin{cases} t_{\text{total}} = t_0 + t_s = 1.88, & \text{for the left-going wave} \\ t_{\text{total}} = t_0 + t_s = 3.45, & \text{for the right-going wave} \end{cases}, \tag{6.7}$$

which is dimensionless and normalized by $T = L_b/\sqrt{gd} = 0.478$ s.

Taking the acceleration effects into account, the estimators in the 1DH landslide waves in constant depth scenario, (4.7), are modified to be

$$\begin{cases} \bar{\epsilon} = \delta A_{\text{acc}} |\dfrac{Fr}{2(1+Fr)}| \max(1, t_{\text{total}}) + \dfrac{1}{5}\delta = 0.0911, & \text{for the left-going wave} \\ \bar{\epsilon} = \delta A_{\text{acc}} |\dfrac{-Fr}{2(1-Fr)}| \max(1, t_{\text{total}}) + \dfrac{1}{5}\delta = 0.228, & \text{for the right-going wave} \end{cases}, \tag{6.8}$$

and

$$\begin{cases} \overline{\mu^2} = \dfrac{\gamma^2}{L_{\text{acc}}^2} \max(1, t_{\text{total}}) = 0.160, & \text{for the left-going wave} \\ \overline{\mu^2} = \dfrac{\gamma^2}{L_{\text{acc}}^2} \max(1, t_{\text{total}}) = 0.167, & \text{for the right-going wave} \end{cases}, \tag{6.9}$$

where t_{total} is given by (6.7).

Using the empirical formulas that relate the estimators to RMSD, (4.10) and (4.12), we can determine whether nonlinear effects and frequency dispersion effects are important or not. Setting 5% RMSD as the tolerance, we find

$$C_\epsilon = 0.0442 \tag{6.10}$$

to be the threshold for determining whether a nonlinear model should be used, and

$$C_{\mu^2} = 0.00752 \tag{6.11}$$

to be the threshold for determining whether a frequency dispersive model should be used. From the values calculated in (6.8) and (6.9), we then see that both leading waves are nonlinear and frequency dispersive for this run, given a 5% RMSD tolerance. As a result, WNWD should be used. Whether this run is too frequency dispersive for WNWD needs to further examined if possible. In this case, experimental data were used to validate WNWD for the run in Chapter 3.

To verify that a linear or nondispersive model would indeed incorrectly predict the leading waves (given a 5% RMSD tolerance), we compare the results predicted by LWD, NSWE, and WNWD in figure 6.1 (in which η is normalized by A_b and x is normalized by L_b). It can be seen that the WNWD results are noticeably different from the LWD results, indicating the importance of nonlinear effects given a 5% RMSD tolerance. On the other hand, the WNWD results are significantly different from the NSWE results, indicating the important of frequency dispersion effects. For the left-going wave in figure 6.1, the difference between the LWD results and the WNWD results is not strikingly large. In fact, if a 10% RMSD tolerance is specified instead, $C_\epsilon = 0.121$ and this leading wave can be considered linear.

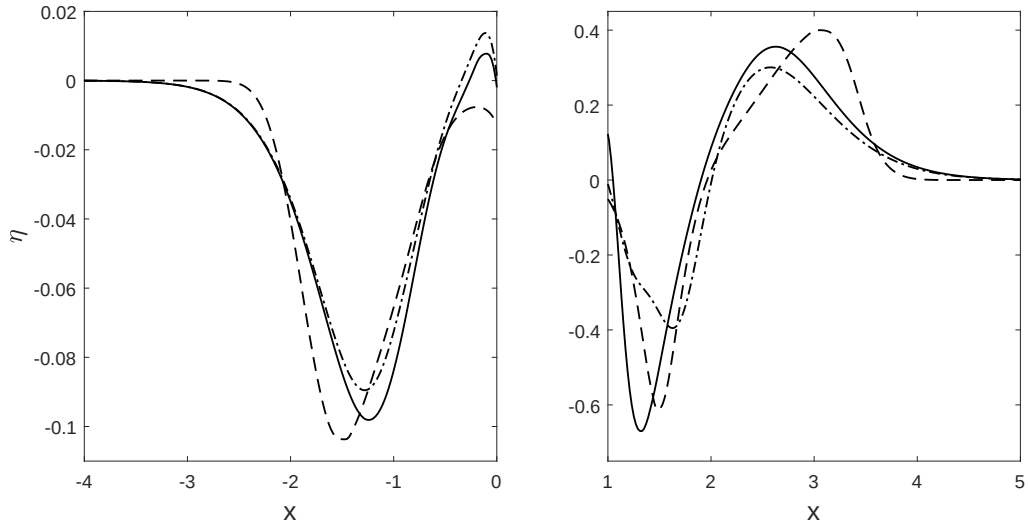

Figure 6.1: Free surface elevation predicted by different models for Run 24. Left: left-going wave at $t = t_{\text{total}} = 1.88$; right: right-going wave at $t = t_{\text{total}} = 3.45$. Solid line: WNWD; dashed line: NSWE; dash-dot line: LWD.

6.1.2 Run 24-long

In Run 24-long, we increased the landslide length by five times to $L_b = 3.135$ m, whereas everything else remains the same as in Run 24. The resulting input

parameters are

$$(Fr, \delta, \gamma) = (0.5, 0.15, 0.056). \tag{6.12}$$

The time (normalized by $T = L_b/\sqrt{gd} = 2.39$ s) it takes for the landslide to accelerate to Fr, is

$$t_0 = 0.437/2.39 = 0.183. \tag{6.13}$$

The wavelength modification factors due to acceleration are

$$\begin{cases} L_{\text{acc}} = 1.05, \quad A_{\text{acc}} = 1, & \text{for the left-going wave} \\ L_{\text{acc}} = 1.09, \quad A_{\text{acc}} = 1, & \text{for the right-going wave} \end{cases}. \tag{6.14}$$

We see that the wave stretching effects due to landslide acceleration are small, since the landslide accelerates relatively quickly (i.e., $t_0 = 0.183$ is small). After the landslide has reached the constant speed phase, the time it takes for the waves to separate from the landslide by one characteristic wavelength, taking the wavelength modification factor into account, is

$$\begin{cases} t_s = L_{\text{acc}}/(1 + Fr) = 0.73, & \text{for the left-going wave} \\ t_s = L_{\text{acc}}/(1 - Fr) = 2.11, & \text{for the right-going wave} \end{cases}. \tag{6.15}$$

Combining t_0 and t_s, we obtain the total time it takes for the leading waves to separate from the landslide:

$$\begin{cases} t_{\text{total}} = t_0 + t_s = 0.91, & \text{for the left-going wave} \\ t_{\text{total}} = t_0 + t_s = 2.29, & \text{for the right-going wave} \end{cases}, \tag{6.16}$$

which is dimensionless and normalized by $T = L_b/\sqrt{gd} = 2.39$ s.

We calculate the estimators to be

$$\begin{cases} \bar{\epsilon} = 0.0642, \quad \overline{\mu^2} = 0.0037, & \text{for the left-going wave} \\ \bar{\epsilon} = 0.200, \quad \overline{\mu^2} = 0.0064, & \text{for the right-going wave} \end{cases}. \tag{6.17}$$

The threshold values for a 5% RMSD tolerance are the same as in (6.10) and (6.11): $C_\epsilon = 0.0442$ and $C_{\mu^2} = 0.00752$. We thus conclude that both leading waves in this run are nonlinear and nondispersive, and NSWE can be used to obtain reasonably accurate results. To verify this, we compare the NSWE results with the WNWD results in figure 6.2 (in which η is normalized by A_b and x is normalized by L_b). We see that the NSWE results are highly similar to the WNWD results. Therefore, the computationally less expensive NSWE can be used to model the generation stage of the leading waves in this run.

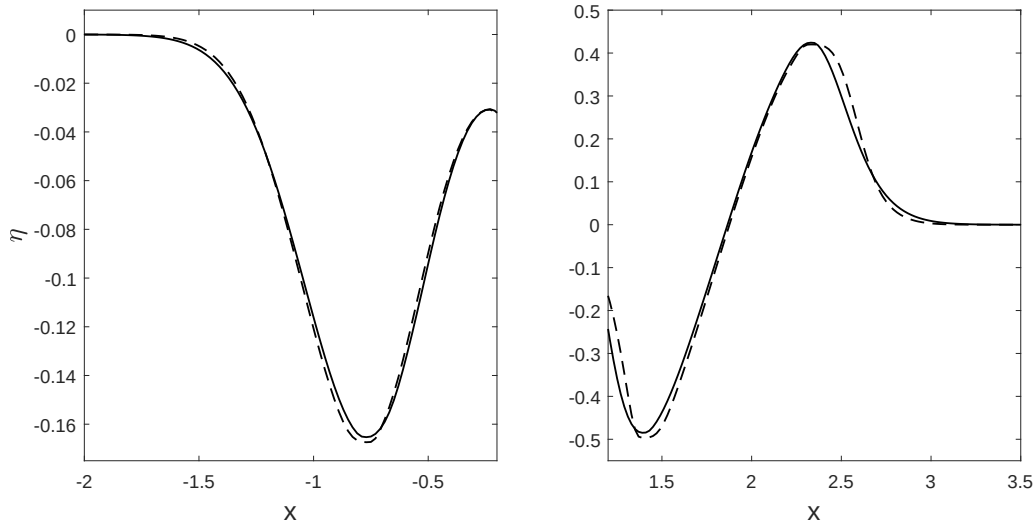

Figure 6.2: Free surface elevation predicted by different models for Run 24-long. Left: left-going wave at $t = t_{\text{total}} = 0.91$; right: right-going wave at $t = t_{\text{total}} = 2.29$. Solid line: WNWD; dashed line: NSWE.

6.1.3 Run 24-thin

In Run 24-thin, we made the landslide one third as thick so that $A_b = 0.00867$ m, whereas everything else remains the same as in Run 24. The resulting input parameters are

$$(Fr, \delta, \gamma) = (0.5, 0.05, 0.28). \tag{6.18}$$

The time (normalized by $T = L_b/\sqrt{gd} = 0.478$ s) it takes for the landslide to accelerate to Fr, is

$$t_0 = 0.437/0.478 = 0.914. \tag{6.19}$$

The wavelength modification factors due to acceleration are

$$\begin{cases} L_{\text{acc}} = 1.45, \quad A_{\text{acc}} = 0.774, & \text{for the left-going wave} \\ L_{\text{acc}} = 1.27, \quad A_{\text{acc}} = 0.576, & \text{for the right-going wave} \end{cases}. \tag{6.20}$$

After the landslide has reached the constant speed phase, the time it takes for the waves to separate from the landslide by one characteristic wavelength, taking the wavelength modification factor into account, is

$$\begin{cases} t_s = L_{\text{acc}}/(1+Fr) = 0.967, & \text{for the left-going wave} \\ t_s = L_{\text{acc}}/(1-Fr) = 2.54, & \text{for the right-going wave} \end{cases}. \tag{6.21}$$

Combining t_0 and t_s, we obtain the total time it takes for the leading waves to separate from the landslide:

$$\begin{cases} t_{\text{total}} = t_0 + t_s = 1.88, & \text{for the left-going wave} \\ t_{\text{total}} = t_0 + t_s = 3.45, & \text{for the right-going wave} \end{cases}, \tag{6.22}$$

which is dimensionless and normalized by $T = L_b/\sqrt{gd} = 0.478$ s.

We calculate the estimators to be

$$\begin{cases} \overline{\epsilon} = 0.0304, \quad \overline{\mu^2} = 0.160, & \text{for the left-going wave} \\ \overline{\epsilon} = 0.0760, \quad \overline{\mu^2} = 0.167, & \text{for the right-going wave} \end{cases}. \tag{6.23}$$

The threshold values for a 5% RMSD tolerance are the same as in (6.10) and (6.11): $C_\epsilon = 0.0442$ and $C_{\mu^2} = 0.00752$. We thus conclude that the left-going leading wave is linear and dispersive, and LWD can be used to obtain reasonably accurate results, and that the right-going leading wave is nonlinear and dispersive, and WNWD must be used – however, we note that $\overline{\epsilon} = 0.0760$ is small; if a 8%

RMSD were specified as the tolerance, both leading waves would pass as linear and dispersive. Therefore, in the LWD-WNWD comparison plot – figure 6.3 – we see minimal difference in the left-going leading waves, and small yet more noticeable difference in the right-going waves. Again, the estimators perform very well for this experimental setup.

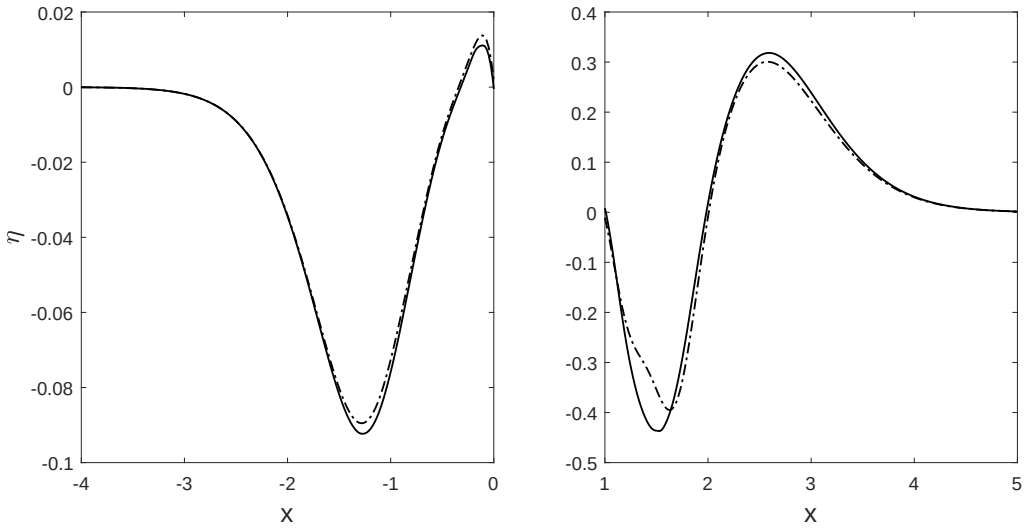

Figure 6.3: Free surface elevation predicted by different models for Run 24-thin. Left: left-going wave at $t = t_{\text{total}} = 1.88$; right: right-going wave at $t = t_{\text{total}} = 3.45$. Solid line: WNWD; dash-dot line: LWD.

6.2 2DH landslide-generated waves in constant depth

To test how the criteria for determining model validity perform in 2DH, we numerically extend the Whittaker (2013) experiments to 2DH, while holding the landslide motion fixed. Run 24 will again be considered, and we shall refer to its extension to 2DH as Run 24-2DH. In the numerical simulations for Run 24-2DH, a 0.026 m thick radially symmetric Gaussian-shaped landslide of characteristic length 0.627 m traveled in the x direction in an open basin of constant water depth of 0.175 m.

The landslide accelerated from rest at 1.5 m^2/s for 0.437 s, maintained a constant speed for 2 s (the normalized constant speed is $Fr = 0.5$), and then decelerated at 1.5 m^2/s until it stopped. To create a shallow water environment, Run 24-2DH-long is considered, in which the landslide length is increased to be five times as long. In Run 24-2DH and Run 24-2DH-long, linear models are valid in capturing the leading waves in certain directions. Thus, an additional run with decreased landslide thickness is not needed.

6.2.1 Run 24-2DH

In Run 24-2DH, the input parameters are

$$(Fr, \delta, \gamma) = (0.5, 0.15, 0.28). \tag{6.24}$$

The time (normalized by $T = L_b/\sqrt{gd} = 0.478$ s) it takes for the landslide to accelerate to Fr, is

$$t_0 = 0.437/0.478 = 0.914. \tag{6.25}$$

After the landslide has reached the constant speed phase, the time it takes for the waves to separate from the landslide by one characteristic wavelength, taking the wavelength modification factor into account, is

$$t_s = L_{\text{acc}}/(\sqrt{1 - 2Fr\cos\theta + Fr^2}). \tag{6.26}$$

Combining t_0 and t_s, we obtain the total time it takes for the leading waves to separate from the landslide:

$$t_{\text{total}} = t_0 + t_s, \tag{6.27}$$

which is dimensionless and normalized by $T = L_b/\sqrt{gd} = 0.478$ s. Taking the acceleration effects into account, the estimators in the 2DH landslide waves in

constant depth, (4.18), are modified to be

$$\begin{aligned} \overline{\epsilon} &= \delta A_{\text{acc}} | \frac{Fr\cos\theta}{2(1-Fr\cos\theta)} | t_{\text{total}}^{-1/2} \max(1, t_{\text{total}}) + \frac{2}{5}\delta \leq C_{\epsilon} \\ \overline{\mu^2} &= \frac{\gamma^2}{L_{\text{acc}}^2} \max(1, t_{\text{total}}) \leq C_{\mu^2} \end{aligned} , \tag{6.28}$$

where t_{total} is given by (6.27).

We shall consider the leading waves in two different directions: $\theta = 5\pi/6$ and $\theta = \pi/6$. We then calculate the following:

$$\begin{cases} L_{\text{acc}} = 1.70, A_{\text{acc}} = 0.49, t_{\text{total}} = 2.08, & \text{for the wave in the } \theta = 5\pi/6 \text{ direction} \\ L_{\text{acc}} = 1.45, A_{\text{acc}} = 0.62, t_{\text{total}} = 3.26, & \text{for the wave in the } \theta = \pi/6 \text{ direction} \end{cases} , \tag{6.29}$$

and the estimators are

$$\begin{cases} \overline{\epsilon} = 0.0752, \quad \overline{\mu^2} = 0.0563, & \text{for the wave in the } \theta = 5\pi/6 \text{ direction} \\ \overline{\epsilon} = 0.123, \quad \overline{\mu^2} = 0.120, & \text{for the wave in the } \theta = \pi/6 \text{ direction} \end{cases} . \tag{6.30}$$

The threshold values for a 5% RMSD tolerance are: $C_{\epsilon} = 0.113$ and $C_{\mu^2} = 0.00700$. We thus conclude that the leading wave in the $\theta = 5\pi/6$ direction is linear and dispersive and can be modeled with LWD, and the leading wave in the $\theta = \pi/6$ direction is nonlinear and dispersive and needs to be modeled with WNWD. However, if a 5.5% RMSD tolerance is specified, the leading wave in the $\theta = \pi/6$ direction would pass as linear and LWD can be used. As expected, in the comparison plot, figure 6.4 (in which η is normalized by A_b and r is normalized by L_b), the difference between the LWD results and the WNWD results is minimal for the wave in the $\theta = 5\pi/6$ direction, whereas the difference between the LWD results and the WNWD results is small yet more noticeable for the wave in the $\theta = \pi/6$ direction. We see that the criteria for determining model validity performs well for this run.

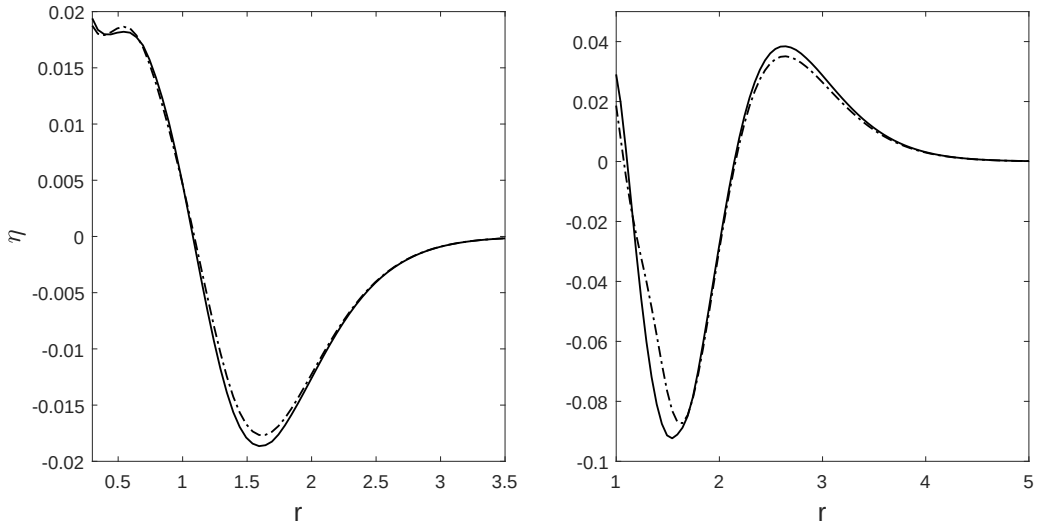

Figure 6.4: Free surface elevation predicted by different models for Run 24-2DH. Left: wave in the $\theta = 5\pi/6$ direction at $t = t_{\text{total}} = 2.08$; right: wave in the $\theta = \pi/6$ direction at $t = t_{\text{total}} = 3.26$. Solid line: WNWD; dash-dot line: LWD.

6.2.2 Run 24-2DH-long

In Run 24-2DH-long, the landslide is five times as long, and the input parameters are

$$(Fr, \delta, \gamma) = (0.5, 0.15, 0.056). \tag{6.31}$$

The time (normalized by $T = L_b/\sqrt{gd} = 2.39$ s) it takes for the landslide to accelerate to Fr, is

$$t_0 = 0.437/2.39 = 0.183. \tag{6.32}$$

We shall consider the leading waves in two different directions: $\theta = 5\pi/6$ and $\theta = \pi/6$. We then calculate the following:

$$\begin{cases} L_{\text{acc}} = 1.14, A_{\text{acc}} = 1, t_{\text{total}} = 0.97, & \text{for the wave in the } \theta = 5\pi/6 \text{ direction} \\ L_{\text{acc}} = 1.09, A_{\text{acc}} = 1, t_{\text{total}} = 1.94, & \text{for the wave in the } \theta = \pi/6 \text{ direction} \end{cases}, \tag{6.33}$$

and the estimators are

$$\begin{cases} \overline{\epsilon} = 0.0823, \quad \overline{\mu^2} = 0.00232, & \text{for the wave in the } \theta = 5\pi/6 \text{ direction} \\ \overline{\epsilon} = 0.139, \quad \overline{\mu^2} = 0.00510, & \text{for the wave in the } \theta = \pi/6 \text{ direction} \end{cases} . \quad (6.34)$$

The threshold values for a 5% RMSD tolerance are the same as in Run 24-2DH: $C_\epsilon = 0.113$ and $C_{\mu^2} = 0.00700$. We thus conclude that the leading wave in the $\theta = 5\pi/6$ direction is linear and nondispersive and can be modeled with LSWE, and the leading wave in the $\theta = \pi/6$ direction is nonlinear and nondispersive and needs to be modeled with NSWE. However, if a 6.3% RMSD tolerance is specified, the leading wave in the $\theta = \pi/6$ direction would pass as linear and LSWE can be used. As expected, in the comparison plot, figure 6.5 (in which η is normalized by A_b and r is normalized by L_b), the difference between the LSWE results and the WNWD results is small for the wave in the $\theta = 5\pi/6$ direction, and the difference between the NSWE results and the WNWD results is small for the wave in the $\theta = \pi/6$ direction – however, the LSWE results are also shown, and the difference between the LSWE results and the WNWD results is also small yet more noticeable. We see that the criteria for determining model validity performs well for this run.

6.3 1DH landslide-generated waves on a slope

As a physical 1DH landslide wave example on a slope, we consider Case 1 from Zhou (2008). We recall that Case 1 was chosen as a benchmark problem in Chapter 3 to validate the nonlinear numerical solver, and the agreement for the leading wave (which is the primary interest of this study) was satisfactory. Thus, we are confident that the leading waves in this case can be modeled with our $O(\mu^2)$-accurate model reasonably well. In the experiment for Case 1, a 0.033 m thick truncated-cosine-shaped landslide of length 0.281 m accelerated at 0.59 m^2/s for

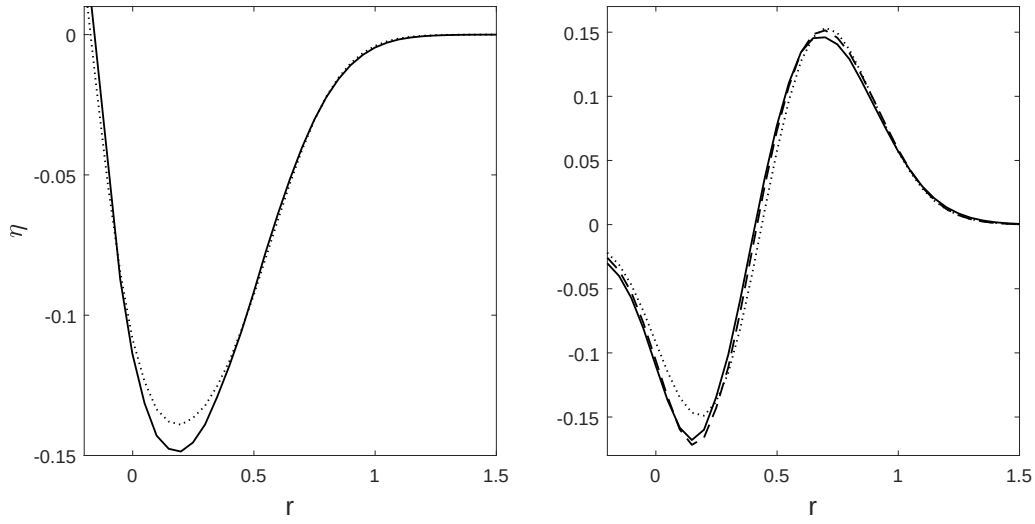

Figure 6.5: Free surface elevation predicted by different models for Run 24-2DH-long. Left: wave in the $\theta = 5\pi/6$ direction at $t = t_{\text{total}} = 0.97$; right: wave in the $\theta = \pi/6$ direction at $t = t_{\text{total}} = 1.94$. Solid line: WNWD; dash-dot line: LWD; dotted line: LSWE.

0.89 s and then decelerated at -1.2 m^2/s until at rest, along a slope of $\beta = 5^\circ$ (we shall use β to denote the slope angle in this chapter to avoid confusion with the polar angle θ) in an initial depth of $d_0 = 0.097$ m. In the numerical simulations, a Gaussian-shaped landslide of height $A_b = 0.033$ m and characteristic length $L_b = 0.326$ m was used to match the area enclosed by the truncated-cosine-shaped landslide. The effective landslide thickness in the vertical direction is $A = A_b \sec\beta = 0.033$, and the effective landslide length in the horizontal direction is $L = L_b \cos\beta = 0.325$ m. To show how the landslide scales affect model validity, in Case 1-long-thin we make the landslide three times as long, and half as thick. Again, we find no noticeable difference between the WNWD results and the FNWD results in either case. Therefore, it suffices to consider the four model options as: LSWE, LWD, NSWE, and WNWD.

6.3.1 Case 1

We shall use the initial water depth in normalization – the time scale used in normalization is $T = L/\sqrt{gd_0} = 0.333$ s. Thus, the normalized acceleration time is

$$t_0 = 0.89/T = 2.67. \tag{6.35}$$

We shall decompose the wave-generation process into two parts: the acceleration phase ($t \leq t_0$) and the post-acceleration phase ($t > t_0$). We expect the acceleration phase and the beginning of the post-acceleration phase to have the strongest effects on the leading wave, and the exact landslide motion during the post-acceleration phase is expected to have minimal effects on the leading wave. Therefore, we approximate the post-acceleration phase as a landslide traveling at a constant speed on a slope, i.e., one of the idealized scenarios considered in Chapter 4. The acceleration phase provides the adjusted input parameters for the post-acceleration phase and need to be examined first.

Dimensionally, after accelerating at 0.59 m^2/s for 0.89 s along a slope of $\beta = 5^\circ$ and in an initial water depth of $d_0 = 0.097$ m, the landslide reached a maximum horizontal speed of $V = 0.59 \cdot 0.89 \cdot \cos\beta = 0.523$ m/s in a water depth of $d_1 = 0.117$ m. We calculate the initial input parameters at the initial landslide location as

$$(Fr_0, \delta_0, \gamma_0, \zeta_0) = (\frac{V}{\sqrt{gd_0}}, \frac{A}{d_0}, \frac{d_0}{L}, \frac{\tan\beta}{\gamma_0}) = (0.536, 0.342, 0.299, 0.293). \tag{6.36}$$

Dimensionlessly, the landslide traveled a distance of $Fr_0 \cdot t_0/2$ (normalized by L) during the acceleration phase to reach a new dimensionless water depth of $1 + \frac{1}{2}Fr_0\zeta_0 t_0$ (normalized by d_0). We therefore define the water depth ratio as

$$\frac{d_1}{d_0} = \chi_0 = 1 + \frac{1}{2}Fr_0\zeta_0 t_0 = 1.21. \tag{6.37}$$

The four adjusted input parameters at this water depth will be used as the inputs for the post-acceleration phase, and are related to the initial input parameters by

$$(Fr, \delta, \gamma, \zeta) = (Fr_0\chi_0^{-1/2}, \delta_0\chi_0^{-1}, \gamma_0\chi_0, \zeta_0\chi_0^{-1}) = (0.488, 0.282, 0.361, 0.242). \quad (6.38)$$

Next, we calculate the modification factors due to the acceleration. We find from (5.40) and (5.41) using the above adjusted input parameters:

$$\begin{array}{ll} L_{\rm acc} = 2.30, & A_{\rm acc} = 0.439, \quad \text{for the left-going wave} \\ L_{\rm acc} = 1.79, & A_{\rm acc} = 0.259, \quad \text{for the right-going wave} \end{array} . \quad (6.39)$$

Since $L_{\rm acc} > 1$, the time (t_s) it takes for the leading wave to separate from the landslide during the post-acceleration phase is slightly different from (4.34): instead of setting the separation distance to be one effective landslide length plus shoaling effects, $1 \cdot \chi^{1/2}$ (normalized by L), we need to include the wave lengthening effect due to landslide acceleration and set the separation distance to be $L_{\rm acc} \cdot \chi^{1/2}$. The resulting dimensionless equation for solving for t_s is

$$\begin{array}{l} -L_{\rm acc}^2\zeta\cos\theta t_s + \Big(1 - 2Fr\cos\theta + Fr^2 - \dfrac{1}{4}(\zeta\cos\theta)^2\Big)t_s^2 \\ \quad + \dfrac{1}{2}\zeta\cos\theta(1 - Fr\cos\theta)t_s^3 + \dfrac{1}{16}(\zeta\cos\theta)^2 t_s^4 - L_{\rm acc}^2 = 0 \end{array} , \quad (6.40)$$

where $\theta = \pi$ for the left-going wave, and $\theta = 0$ for the right-going wave. We see that (4.34) is recovered by setting $L_{\rm acc} = 1$, i.e., without acceleration effects. From (6.40), we found

$$\begin{cases} t_s = 1.35, & \text{for the left-going wave} \\ t_s = 3.41, & \text{for the right-going wave} \end{cases} \quad (6.41)$$

for Case 1. Here we note that t_s found from (6.40) is normalized by the time scale at the new water depth d_1. To normalize the separation by the time scale at the initial water depth d_0, a conversion factor $\chi_0^{-1/2}$ is needed, where χ_0 is given in (6.37). Therefore, the total time (normalized by $T = L/\sqrt{gd_0} = 0.333$ s) it takes

for the leading wave to separate is

$$\begin{cases} t_{\text{total}} = t_0 + t_s \chi_0^{-1/2} = 3.90, & \text{for the left-going wave} \\ t_{\text{total}} = t_0 + t_s \chi_0^{-1/2} = 5.78, & \text{for the right-going wave} \end{cases} . \tag{6.42}$$

We shall regard the post-acceleration phase as the idealized 1DH landslide-generated waves on a slope scenario with the above adjusted input parameters, (6.38) and separation time, (6.41), to determine the strength of nonlinearity and the strength of frequency dispersion. We recall from Chapter 4 that the input parameters at a representative depth, given in (4.36) need to be calculated:

$$\begin{cases} (Fr_*, \delta_*, \gamma_*) = (0.507, 0.305, 0.334), & \text{for the left-going wave} \\ (Fr_*, \delta_*, \gamma_*) = (0.436, 0.226, 0.452), & \text{for the right-going wave} \end{cases} . \tag{6.43}$$

With all the required parameters determined, we can now calculate the estimators $\overline{\epsilon}$ and $\overline{\mu^2}$, accounting for the acceleration effects, as:

$$\overline{\epsilon} = \delta_* A_{\text{acc}} | \frac{Fr_* \cos\theta}{2(1 - Fr_* \cos\theta)} | \max(1, t_{\text{total}}) + \frac{1}{3}\delta, \quad \overline{\mu^2} = \frac{\gamma_*^2}{L_{\text{acc}}^2} \max(1, t_{\text{total}}). \tag{6.44}$$

We obtain

$$\begin{cases} \overline{\epsilon} = 0.182, \quad \overline{\mu^2} = 0.0823, & \text{for the left-going wave} \\ \overline{\epsilon} = 0.146, \quad \overline{\mu^2} = 0.367, & \text{for the right-going wave} \end{cases} . \tag{6.45}$$

Using a 10% RMSD tolerance, from (4.41) and (4.39) we find the thresholds to be $C_\epsilon = 0.153$ and $C_{\mu^2} = 0.0215$. Therefore, we conclude that the left-going leading wave is nonlinear and dispersive and needs to be modeled with WNWD, and the right-going leading wave is linear and dispersive and can be modeled with LWD. To see how accurate the predictions are, in figure 6.6 (in which x is normalized by L, η is normalized by A, and the initial shoreline is located at $x = 0$) we compare the results predicted by different models. For the left-going wave, we see that both the LWD results and the NSWE results deviate from the WNWD

results significantly, indicating that the wave is both nonlinear and dispersive. For the right-going wave, we see that the difference between the LWD results and the WNWD results is reasonably small given a 10% RMSD tolerance, indicating that the wave is only borderline nonlinear. Therefore, we conclude that the criteria for determining model validity perform well for this case.

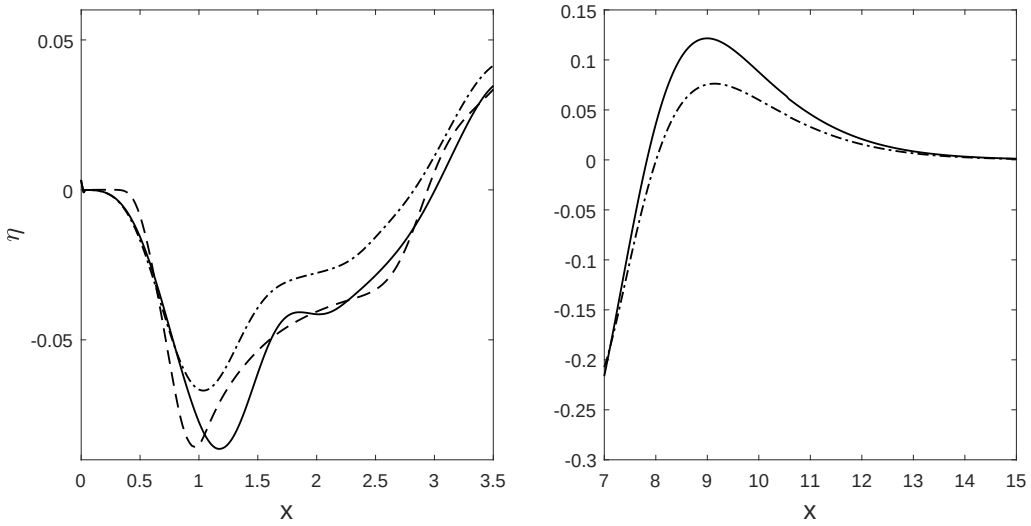

Figure 6.6: Free surface elevation predicted by different models for Case 1. The initial shoreline is located at $x = 0$. Left: left-going wave at $t = t_{\text{total}} = 3.90$; right: right-going wave at $t = t_{\text{total}} = 5.78$. Solid line: WNWD; dashed line: NSWE; dash-dot line: LWD.

6.3.2 Case 1-long-thin

In Case 1-long-thin, the landslide is three times as long and half as thick than in Case 1, while everything else remains unchanged. Therefore, $L = 0.974$ m and $A = 0.0166$ m. The time scale used in normalization is $T = L/\sqrt{gd_0} = 0.999$ s. The normalized acceleration time is

$$t_0 = 0.89/T = 0.891. \tag{6.46}$$

Following the same procedure as in Case 1, we calculate the four initial parameters first:

$$(Fr_0, \delta_0, \gamma_0, \zeta_0) = (0.536, 0.171, 0.0996, 0.879). \tag{6.47}$$

From (6.37) we find $\chi_0 = 1.21$. The four adjusted input parameters for the post-acceleration phase are then found to be

$$(Fr, \delta, \gamma, \zeta) = (0.488, 0.141, 0.121, 0.726). \tag{6.48}$$

The modification factors due to the acceleration are

$$\begin{array}{ll} L_{\text{acc}} = 1.43, & A_{\text{acc}} = 0.777, \quad \text{for the left-going wave} \\ L_{\text{acc}} = 1.26, & A_{\text{acc}} = 0.586, \quad \text{for the right-going wave} \end{array} . \tag{6.49}$$

The time it takes for the leading wave to separate from the landslide during the post-acceleration phase is

$$\begin{cases} t_s = 0.745, & \text{for the left-going wave} \\ t_s = 2.39, & \text{for the right-going wave} \end{cases} . \tag{6.50}$$

The total time, accounting for the different time scale used to normalize t_s, it takes for the leading wave to separate is

$$\begin{cases} t_{\text{total}} = t_0 + t_s \chi_0^{-1/2} = 1.57, & \text{for the left-going wave} \\ t_{\text{total}} = t_0 + t_s \chi_0^{-1/2} = 3.06, & \text{for the right-going wave} \end{cases} , \tag{6.51}$$

which again is dimensionless and normalized by $T = 0.999$ s. The input parameters at a representative depth, given in (4.36) need to be calculated:

$$\begin{cases} (Fr_*, \delta_*, \gamma_*) = (0.519, 0.160, 0.106), & \text{for the left-going wave} \\ (Fr_*, \delta_*, \gamma_*) = (0.383, 0.0870, 0.196), & \text{for the right-going wave} \end{cases} . \tag{6.52}$$

The estimators, accounting for the acceleration effects, are

$$\begin{cases} \overline{\epsilon} = 0.0803, & \overline{\mu^2} = 0.00864, \quad \text{for the left-going wave} \\ \overline{\epsilon} = 0.0687, & \overline{\mu^2} = 0.0733, \quad \text{for the right-going wave} \end{cases} . \tag{6.53}$$

The thresholds for a 10% RMSD tolerance are the same: $C_\epsilon = 0.153$ and $C_{\mu^2} = 0.0215$. Therefore, we conclude that the left-going leading wave is linear and nondispersive and can be modeled with LSWE, and the right-going leading wave is linear and dispersive and can be modeled with LWD. To see how accurate the predictions are, in figure 6.7 (in which x is normalized by L, η is normalized by A, and the initial shoreline is located at $x = 0$) we compare the results predicted by different models. For the left-going wave, we see that the LSWE results agree well with the WNWD results given a 10% RMSD tolerance, indicating that the wave is linear and nondispersive. However, it should be noted that linear models may not be the most reliable very close to the shoreline, $x = 0$, as has been pointed out in Chapter 3. For the right-going wave, we see that the LWD results agree well with the WNWD results, indicating that the wave is linear. We conclude that the criteria for determining model validity perform well for this case.

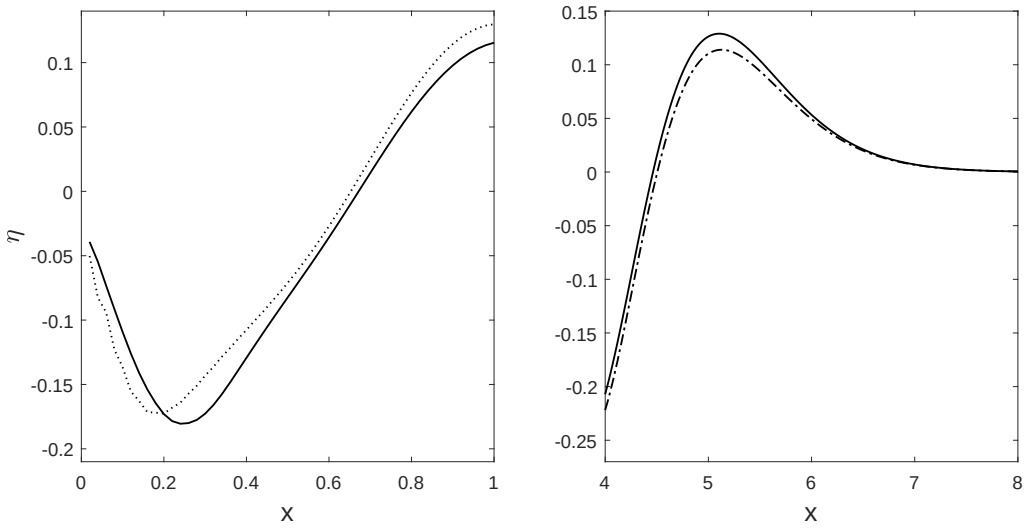

Figure 6.7: Free surface elevation predicted by different models for Case 1-long-thin. The initial shoreline is located at $x = 0$. Left: left-going wave at $t = t_{\text{total}} = 1.57$; right: right-going wave at $t = t_{\text{total}} = 3.06$. Solid line: WNWD; dash-dot line: LWD; dotted line: LSWE.

6.4 2DH landslide-generated waves on a slope

In this section, we extend the 1DH cases on a slope to 2DH via numerical simulations. A radially symmetric Gaussian-shaped landslide following the same motion as that in the 1DH cases is specified in 2DH on a plane beach. In Case 1-2DH, a $A_b = 0.033$ m thick Gaussian-shaped landslide of length $L_b = 0.326$ m accelerated in the x direction at 0.59 m^2/s for 0.89 s and then decelerated at -1.2 m^2/s until at rest, along a slope of $\beta = 5^\circ$ (again, we use β to denote the slope angle in this chapter to avoid confusion with the polar angle θ) in an initial depth of $d_0 = 0.097$ m. The effective landslide thickness in the vertical direction is $A = A_b \sec\beta = 0.033$, and the effective landslide length in the horizontal direction is $L = L_b \cos\beta = 0.325$ m. To create a shallow water environment so that a nondispersive model applies, we make the landslide twice as long, and shall refer to this case as Case 1-2DH-long. Again, we find no noticeable difference between the WNWD results and the FNWD results in either case. Therefore, it suffices to consider only four available model choices: LSWE, LWD, NSWE, and WNWD. We will focus on the leading waves in two θ directions: $\theta = 5\pi/6$ and $\theta = \pi/6$.

6.4.1 Case 1-2DH

The procedure for calculating the necessary parameters is the same as in the 1DH cases. The time scale used in normalization is $T = L/\sqrt{gd_0} = 0.333$ s. Thus, the normalized acceleration time is

$$t_0 = 0.89/T = 2.67. \tag{6.54}$$

The four initial input parameters are

$$(Fr_0, \delta_0, \gamma_0, \zeta_0) = (0.536, 0.342, 0.299, 0.293), \tag{6.55}$$

and $\chi_0 = 1.21$. Therefore, the four adjusted input parameters for the post-acceleration phase are

$$(Fr, \delta, \gamma, \zeta) = (0.488, 0.282, 0.361, 0.242). \tag{6.56}$$

In 2DH, the modification factors due to the acceleration are

$$\begin{array}{l} L_{\text{acc}} = 3.03, \quad A_{\text{acc}} = 0.215, \quad \text{for the wave in the } \theta = 5\pi/6 \text{ direction} \\ L_{\text{acc}} = 2.33, \quad A_{\text{acc}} = 0.261, \quad \text{for the wave in the } \theta = \pi/6 \text{ direction} \end{array}. \tag{6.57}$$

The time it takes for the leading wave to separate from the landslide during the post-acceleration phase is calculated from (6.40) as

$$\begin{cases} t_s = 1.78, \quad \text{for the wave in the } \theta = 5\pi/6 \text{ direction} \\ t_s = 3.87, \quad \text{for the wave in the } \theta = \pi/6 \text{ direction} \end{cases}. \tag{6.58}$$

The total time, accounting for the different time scale used to normalize t_s, it takes for the leading wave to separate is

$$\begin{cases} t_{\text{total}} = t_0 + t_s \chi_0^{-1/2} = 4.29, \quad \text{for the wave in the } \theta = 5\pi/6 \text{ direction} \\ t_{\text{total}} = t_0 + t_s \chi_0^{-1/2} = 6.19, \quad \text{for the wave in the } \theta = \pi/6 \text{ direction} \end{cases}, \tag{6.59}$$

which again is dimensionless and normalized by $T = 0.333$ s. At $t = t_{\text{total}}$, the representative location r_{total} of the leading wave in the θ direction, which starts traveling outwards immediately after $t = 0$ from the origin at local wave speed, can be expressed as (normalized by L)

$$r_{\text{total}} = t_{\text{total}} + \frac{1}{4}\zeta_0 \cos\theta t_{\text{total}}. \tag{6.60}$$

We find

$$\begin{cases} r_{\text{total}} = 3.12, \quad \text{for the wave in the } \theta = 5\pi/6 \text{ direction} \\ r_{\text{total}} = 8.62, \quad \text{for the wave in the } \theta = \pi/6 \text{ direction} \end{cases}. \tag{6.61}$$

The input parameters at a representative depth, given in (4.45) need to be calculated:

$$\begin{cases} (Fr_*, \delta_*, \gamma_*) = (0.510, 0.308, 0.331), & \text{for the wave in the } \theta = 5\pi/6 \text{ direction} \\ (Fr_*, \delta_*, \gamma_*) = (0.437, 0.227, 0.450), & \text{for the wave in the } \theta = \pi/6 \text{ direction} \end{cases}. \tag{6.62}$$

In 2DH, the estimators $\bar{\epsilon}$ and $\overline{\mu^2}$, modified from (4.46) to account for the acceleration effects, are:

$$\bar{\epsilon} = \delta_* A_{\text{acc}} |\frac{Fr_* \cos\theta}{2(1 - Fr_* \cos\theta)}| r_{\text{total}}^{-\frac{1}{2}} \max(1, t_{\text{total}}) + \frac{2}{3}\delta, \quad \overline{\mu^2} = \frac{\gamma_*^2}{L_{\text{acc}}^2} \max(1, t_{\text{total}}). \tag{6.63}$$

For the two waves of interest, we have:

$$\begin{cases} \bar{\epsilon} = 0.213, \quad \overline{\mu^2} = 0.0512, & \text{for the wave in the } \theta = 5\pi/6 \text{ direction} \\ \bar{\epsilon} = 0.226, \quad \overline{\mu^2} = 0.230, & \text{for the wave in the } \theta = \pi/6 \text{ direction} \end{cases}. \tag{6.64}$$

The thresholds for a 10% RMSD tolerance are calculated from (4.51) and (4.49): $C_\epsilon = 0.302$ and $C_{\mu^2} = 0.0173$. Therefore, we conclude that both leading waves are linear and dispersive and can be modeled with LWD, given a 10% RMSD tolerance. To see how accurate the predictions are, in figure 6.8 (in which r is normalized by L and η is normalized by A) we compare the results predicted by LWD and WNWD. We see that the differences are indeed small as predicted, and we therefore conclude that the criteria for determining model validity perform well for this case.

6.4.2 Case 1-2DH-long

In this case, the landslide is increased to be twice as long. Therefore, $L = 0.650$ m. The time scale used in normalization is $T = L/\sqrt{gd_0} = 0.666$ s. Thus, the

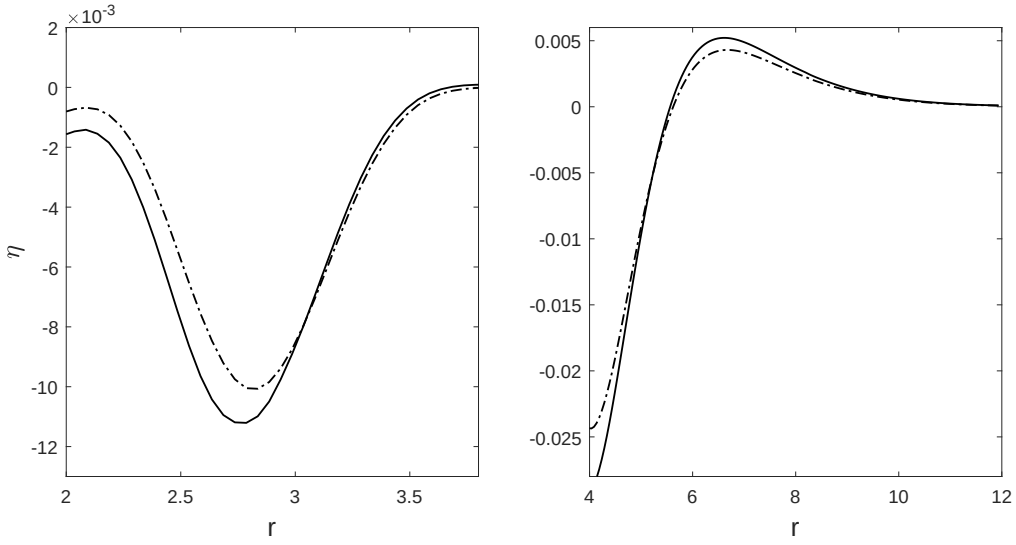

Figure 6.8: Free surface elevation predicted by different models for Case 1-2DH. Left: wave in the $\theta = 5\pi/6$ direction at $t = t_{\text{total}} = 4.29$; right: wave in the $\theta = \pi/6$ direction at $t = t_{\text{total}} = 6.19$. Solid line: WNWD; dash-dot line: LWD.

normalized acceleration time is

$$t_0 = 0.89/T = 1.34. \tag{6.65}$$

The four initial parameters are

$$(Fr_0, \delta_0, \gamma_0, \zeta_0) = (0.536, 0.342, 0.149, 0.586), \tag{6.66}$$

and $\chi_0 = 1.21$. Therefore, the four adjusted input parameters for the post-acceleration phase are

$$(Fr, \delta, \gamma, \zeta) = (0.488, 0.282, 0.181, 0.484). \tag{6.67}$$

The modification factors due to the acceleration are

$$\begin{array}{llll} L_{\text{acc}} = 2.01, & A_{\text{acc}} = 0.370, & \text{for the wave in the } \theta = 5\pi/6 \text{ direction} \\ L_{\text{acc}} = 1.67, & A_{\text{acc}} = 0.478, & \text{for the wave in the } \theta = \pi/6 \text{ direction} \end{array} . \tag{6.68}$$

The time it takes for the leading wave to separate from the landslide during the post-acceleration phase is calculated from (6.40) as

$$\begin{cases} t_s = 1.12, & \text{for the wave in the } \theta = 5\pi/6 \text{ direction} \\ t_s = 2.79, & \text{for the wave in the } \theta = \pi/6 \text{ direction} \end{cases}. \tag{6.69}$$

The total time, accounting for the different time scale used to normalized t_s, it takes for the leading wave to separate is

$$\begin{cases} t_{\text{total}} = t_0 + t_s \chi_0^{-1/2} = 2.35, & \text{for the wave in the } \theta = 5\pi/6 \text{ direction} \\ t_{\text{total}} = t_0 + t_s \chi_0^{-1/2} = 3.87, & \text{for the wave in the } \theta = \pi/6 \text{ direction} \end{cases}, \tag{6.70}$$

which again is dimensionless and normalized by $T = 0.666$ s. At $t = t_{\text{total}}$, the representative location r_{total} of the leading wave in the θ direction, is

$$\begin{cases} r_{\text{total}} = 1.65, & \text{for the wave in the } \theta = 5\pi/6 \text{ direction} \\ r_{\text{total}} = 5.78, & \text{for the wave in the } \theta = \pi/6 \text{ direction} \end{cases}. \tag{6.71}$$

The input parameters at a representative depth, given in (4.45) need to be calculated:

$$\begin{cases} (Fr_*, \delta_*, \gamma_*) = (0.515, 0.315, 0.162), & \text{for the wave in the } \theta = 5\pi/6 \text{ direction} \\ (Fr_*, \delta_*, \gamma_*) = (0.415, 0.205, 0.249), & \text{for the wave in the } \theta = \pi/6 \text{ direction} \end{cases}. \tag{6.72}$$

The estimators $\overline{\epsilon}$ and $\overline{\mu^2}$ are calculated to be:

$$\begin{cases} \overline{\epsilon} = 0.221, \quad \overline{\mu^2} = 0.0152, & \text{for the wave in the } \theta = 5\pi/6 \text{ direction} \\ \overline{\epsilon} = 0.233, \quad \overline{\mu^2} = 0.0866, & \text{for the wave in the } \theta = \pi/6 \text{ direction} \end{cases}. \tag{6.73}$$

The thresholds for a 10% RMSD tolerance are the same as in Case 1-2DH: $C_\epsilon = 0.302$ and $C_{\mu^2} = 0.0173$. Therefore, we conclude that the leading wave in the $\theta = 5\pi/6$ direction is linear and nondispersive, given a 10% RMSD. Therefore, it can be modeled with LSWE. On the other hand, the leading wave in the $\theta = \pi/6$ direction is linear and dispersive, so it can be modeled with LWD. In figure 6.9

(in which r is normalized by L and η is normalized by A) we compare the results predicted by LSWE, LWD, and WNWD – the differences between the results are indeed not too significant, given a 10% RMSD tolerance. We see that the predictions are fairly accurate and the criteria for determining model validity again perform well for this case.

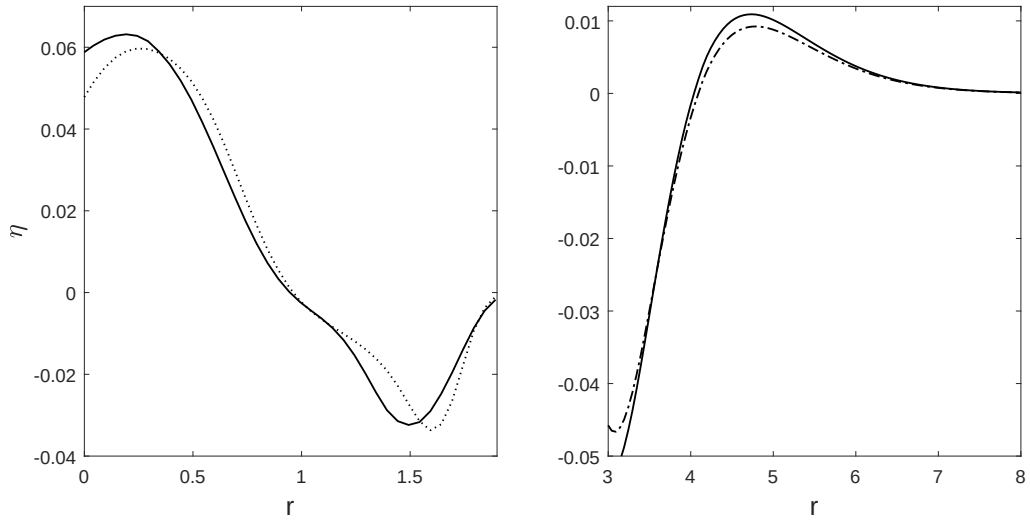

Figure 6.9: Free surface elevation predicted by different models for Case 1-2DH-long. Left: wave in the $\theta = 5\pi/6$ direction at $t = t_{\text{total}} = 2.35$; right: wave in the $\theta = \pi/6$ direction at $t = t_{\text{total}} = 3.87$. Solid line: WNWD; dash-dot line: LWD; dotted line: LSWE.

6.5 The 1998 Papua New Guinea tsunami

As the next and last example, we consider the 1998 PNG tsunami, which is commonly believed to have been caused by an underwater landslide (e.g., Synolakis et al., 2002; Lynett et al., 2003; Sweet and Silver, 2003; Watts et al., 2003). Specifying zero velocity and a free surface profile as the initial conditions for a landslide-generated tsunami, most numerical studies of the PNG event (e.g., Tappin et al., 2001; Synolakis et al., 2002; Lynett et al., 2003; Watts et al., 2003) modeled the

wave propagation stage, but not the wave generation stage. Generally, the initial free surface profile was tuned so that the predicted maximum water elevation over dry land agrees with the field observations. Lynett et al. (2003) performed numerical simulations using both NSWE and WNWD using the same initial conditions, and found that while the results for the maximum water elevation over dry land agree well with each other, the offshore wave height and the wave shape predicted by NSWE differed significantly from those predicted by WNWD, indicating the importance of frequency dispersion Therefore, we regard WNWD as the appropriate wave propagation model to use in this example.

Since our study focuses on the wave generation stage, we shall examine the initial conditions (which are the outcomes of the wave generation stage) used in existing studies more carefully. While specifying zero initial flow velocity is reasonable for earthquake-generated water waves, it is unphysical for landslide-generated waves. As shown by both the analytical solutions and the numerical results, landslide-generated waves, at the end of the wave-generation process, are directional – therefore, words such as "the left-going wave", "the right-going wave", and "the wave in the θ direction" are frequently used throughout this study. Without nonzero initial flow velocity, the specified initial free surface profile is allowed to spread freely in all possible directions, i.e., left and right in 1DH, and radially in 2DH; thus, the wave amplitude is at most half of the initial wave height. To investigate this problem, we shall simulate the wave generation stage based on the simplest acceptable model to obtain a wave profile. Then, in a separate wave propagation model based on WNWD, we examine the effects the initial conditions for the landslide-generated tsunami have in the wave propagation stage. Two cases will be considered: one case in which the full wave profile, including both the free surface elevation and the flow velocity, is specified as the initial conditions. In the

other case, zero initial flow velocity is specified.

6.5.1 Model validity for the wave generation stage

As the first step, we specify the landslide parameters and check the model validity for the wave generation stage. The primary location of interest in most studies (e.g. Synolakis et al., 2002; Lynett et al., 2003; Sweet and Silver, 2003) is the Sissano Lagoon, which is approximately in the $\theta = 3\pi/4$ direction based on the landslide's direction of travel. Therefore, we shall calculate the landslide parameters in the $3\pi/4$ direction. The 1998 PNG tsunami can be classified as the idealized 2DH landslide on a slope scenario with landslide acceleration. Aside from crude estimates of the landslide scales (length, height, volume, displacement distance, etc.), very limited information on the landslide and its motion is available. Rather than making up our own estimates, we seek to utilize the estimates and approximations provided by existing studies as much as possible. Watts et al. (2003) estimated the landslide specific gravity to be 2.15, length to be $L_b = 4500$ m, the width to be 5000 m, the height to be $A_b = 760$ m, the initial water depth to be $d_0 = 1500$ m, the slope near the landslide to be 12°, the initial landslide acceleration to be 0.36 m^2/s, and the maximum landslide speed to be 11.6 m/s. The duration of the acceleration phase is therefore $11.6/0.36 = 32.22$ s.

Since we are more concerned with the average slope between the landslide location and the shoreline, as opposed to the 12° slope immediately next to the landslide, we estimate the average slope to be $\beta = 3.43°$, which is calculated based on the fact that the landslide is approximately 25000 m offshore in a water depth of 1500 m (we remark that while the estimates may vary, our results in this section are insensitive to this variation in the estimated β). In the numerical simulations,

a radially symmetric Gaussian shaped landslide of characteristic length L_b and height A_b traveling down a plane beach of slope $\beta = 3.43^\circ$ was considered.

With the values given above, we then proceed to calculate all necessary parameters in the $\theta = 3\pi/4$ direction. The time scale used in normalization is $T = L_b \cos\beta/\sqrt{gd_0} = 37.0$ s. Thus, the normalized acceleration time is

$$t_0 = 32.22/T = 0.870. \tag{6.74}$$

The four initial input parameters are

$$(Fr_0, \delta_0, \gamma_0, \zeta_0) = (0.0951, 0.508, 0.334, 0.180). \tag{6.75}$$

and $\chi_0 = 1.01$. Therefore, the four input parameters for the post-acceleration phase are

$$(Fr, \delta, \gamma, \zeta) = (0.0951, 0.504, 0.336, 0.178). \tag{6.76}$$

The modification factors due to landslide acceleration are

$$L_{\text{acc}} = 1.56, \quad A_{\text{acc}} = 0.542. \tag{6.77}$$

The time it takes for the leading wave to separate from the landslide during the post-acceleration phase is calculated from (6.40) as

$$t_s = 1.39. \tag{6.78}$$

The total time, accounting for the different time scale used to normalized t_s, it takes for the leading wave to separate is

$$t_{\text{total}} = t_0 + t_s \chi_0^{-1/2} = 2.25, \tag{6.79}$$

which again is dimensionless and normalized by $T = 37.0$ s. At $t = t_{\text{total}}$, the representative location r_{total} of the leading wave in the $\theta = 3\pi/4$ direction, is

$$r_{\text{total}} = 2.09. \tag{6.80}$$

The input parameters at a representative depth, given in (4.45) need to be calculated:

$$(Fr_*, \delta_*, \gamma_*) = (0.0971, 0.526, 0.322). \tag{6.81}$$

The estimators $\bar{\epsilon}$ and $\overline{\mu^2}$ are calculated to be:

$$\bar{\epsilon} = 0.350, \quad \overline{\mu^2} = 0.0960. \tag{6.82}$$

The thresholds for a 10% RMSD tolerance in the 2DH landslide wave on a slope scenario are: $C_\epsilon = 0.302$ and $C_{\mu^2} = 0.0173$. Therefore, we conclude that the leading wave in the $\theta = 3\pi/4$ direction is nonlinear and dispersive and must be modeled with WNWD, given a 10% RMSD. However, if a 12% RMSD tolerance is specified, the leading wave would pass as linear and dispersive. Therefore, we expect nonlinearity to be important, but not overwhelmingly so. In fact, based on (4.50), a 11.7% RMSD is expected between the leadings wave predicted by a linear model and that predicted by a nonlinear model. In figure 6.10, the wave profile in the $\theta = 3\pi/4$ direction based on WNWD is compared with that based on LWD, and a contour plot is shown in figure 6.11. To give a sense of the physical scales, the plots are not normalized. As expected, the difference between the LWD results and the WNWD results is noticeable but reasonable, as characterized by an expected RMSD of 11.7%. Nonetheless, given a 10% RMSD tolerance, we shall use WNWD to model the wave generation stage.

6.5.2 Initial conditions for the wave propagation stage

Next, we examine the importance of specifying the initial flow velocity for landslide tsunamis. Based on the NSWE-WNWD comparison in Lynett et al. (2003) for the PNG event, we regard WNWD as the appropriate model to use for the wave

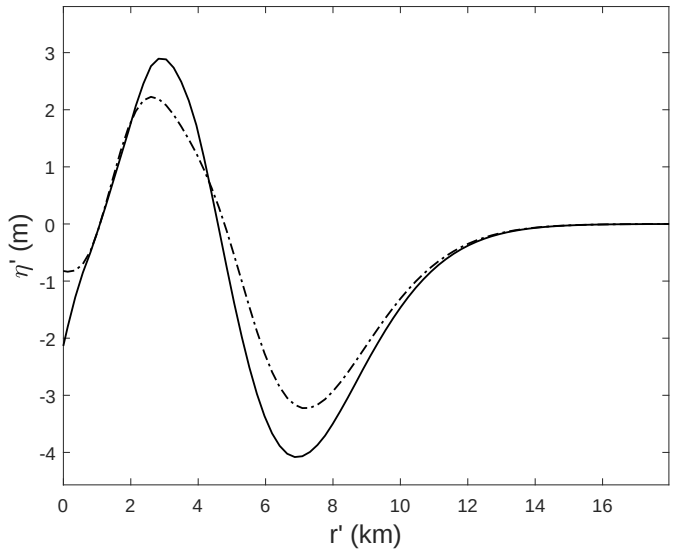

Figure 6.10: Free surface elevation in the $\theta = 3\pi/4$ direction at $t' = t'_{\text{total}} = 83.3$ s predicted by different models for the PNG event. Solid line: WNWD; dash-dot line: LWD.

propagation model. Therefore, we shall use WNWD, which was found to be the appropriate model to use in the previous section, to simulate the wave generation stage on a plane beach of slope $\beta = 3.43°$ up to $t = t_{\text{total}}$. Then, using the wave profile at the end of the wave generation stage as the initial conditions, we run a separate simulation (now without the landslide) on a plane beach of slope $\beta = 3.43°$ to see how the waves spread during the wave propagation stage. Two cases shall be considered – one with both the free surface elevation and the flow velocity specified as the initial conditions, and one with the free surface elevation and zero flow velocity specified as the initial conditions. The free surface profile based on WNWD has already been shown in figure 6.11(right). The flow velocity based on WNWD, given as (u'_α, v'_α), which are interpreted as the representative velocities at a depth of z_α (see Chapter 3 for details), is shown in figure 6.12. It can be seen that the flow velocity is not negligibly small and must be considered.

Comparisons of the results due to the two different initial conditions are shown

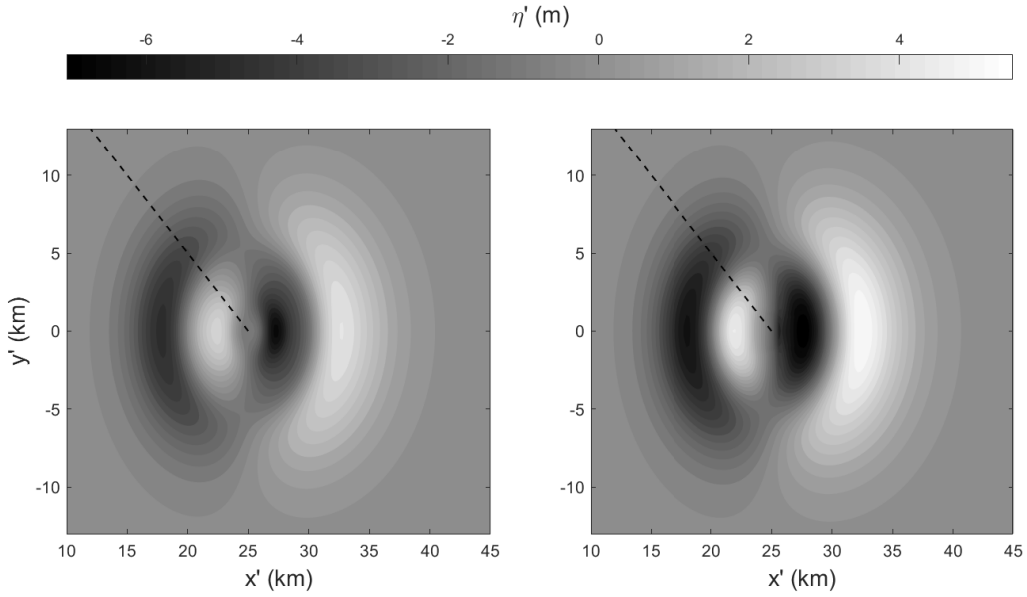

Figure 6.11: Contour plot of the free surface elevation at $t' = t'_{\text{total}} = 83.3$ s predicted by different models for the PNG event. The shoreline is located at $x' = 0$ m. Left: LWD; right: WNWD. Dashed line: the $\theta = 3\pi/4$ direction.

in figure 6.13 for $t' = t'_{\text{total}} + 100 = 183.3$ s, and in figure 6.13 for $t' = t'_{\text{total}} + 200 = 283.3$ s. The ring feature due to the waves spreading radially outwards can be observed in both cases. However, the wave amplitudes and the trailing waves are completely different. A closer look in the $\theta = 3\pi/4$ direction, figure 6.15, reveals that the amplitude of the leading wave differs by at least a factor of 2, and even more for that of the trailing waves. Because using the zero velocity initial condition results in wave amplitudes at most half as large, a larger initial wave height was specified in many numerical studies. For example, the initial wave profile in Synolakis et al. (2002); Lynett et al. (2003) has a peak in the offshore direction of about 16 m, and a depression in the onshore direction of about -18 m. In comparison, our initial wave profile in figure 6.11 has two peaks and two depressions – the peak in the offshore direction has an elevation of about 5.5 m, the depression in the offshore direction has an elevation of about -7.1 m, the peak in the onshore direction has an elevation of about 4.7 m, and the depression in the

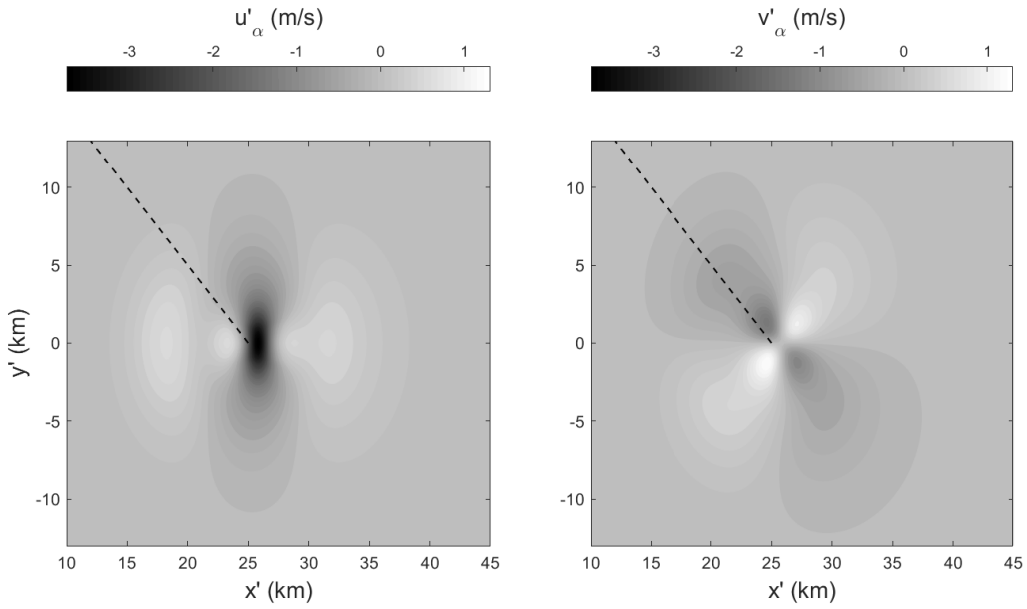

Figure 6.12: Contour plot of the flow velocity at $t' = t'_{\text{total}} = 83.3$ s predicted by WNWD for the PNG event. The shoreline is located at $x' = 0$ m. Left: representative velocity in the x' direction, u'_α; right: representative velocity in the y' direction, v'_α. Dashed line: the $\theta = 3\pi/4$ direction.

onshore direction has an elevation of about -5.8 m,

Although great uncertainty exists in the landslide motion in real events and therefore the profile of the resulting tsunami, we remark that it is unphysical to specify a landslide tsunami as an initial water surface profile with zero initial flow velocity. If the wave generation stage is modeled separately from the wave propagation stage, both the water surface profile and the flow velocity from the wave generation model need to be transferred to the wave propagation model.

6.6 Summary

In this section, we demonstrated step by step, through several examples, how the model validity criteria from Chapter 4 and the wave modification factors due to

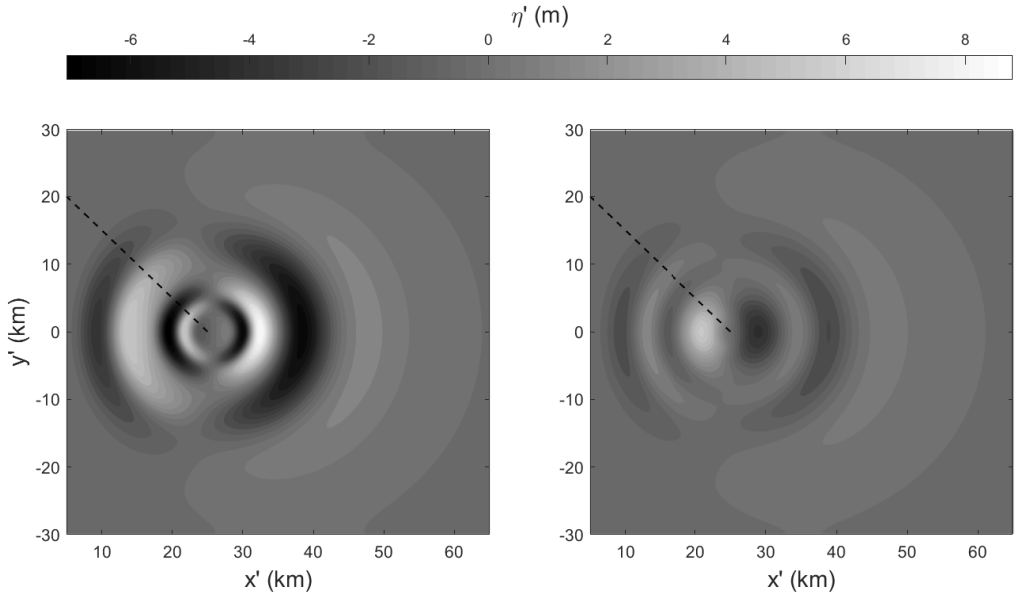

Figure 6.13: Comparison of the free surface elevations at $t' = t'_{\text{total}} + 100 = 183.3$ s predicted by WNWD under different initial conditions. The shoreline is located at $x' = 0$ m. Left: nonzero initial flow velocity; right: zero initial flow velocity. Dashed line: the $\theta = 3\pi/4$ direction.

landslide acceleration from Chapter 5 can be applied to determine the simplest wave model that can be used to model the wave generation stage. The examples covered all four idealized scenarios discussed in Chapter 4: 1DH in constant depth, 2DH in constant depth, 1DH on a slope, and 2DH on a slope. The 1998 Papua New Guinea (PNG) tsunami, classified as the 2DH on a slope scenario, was included as an example. It was found that for the leading wave in the $\theta = 3\pi/4$ direction (where the primary location of interest in most existing studies was – the Sissano Lagoon), both nonlinear effects and frequency dispersive effects were important during the wave generation stage given a 10% RMSD tolerance. Therefore, WNWD or a more accurate wave model must be used to simulate the wave generation stage. However, while nonlinearity was important, it was not overwhelmingly so. If a slightly more generous error tolerance were used (say, RMSD=12%), then the wave generation stage would pass as linear and dispersive, and LWD could be used.

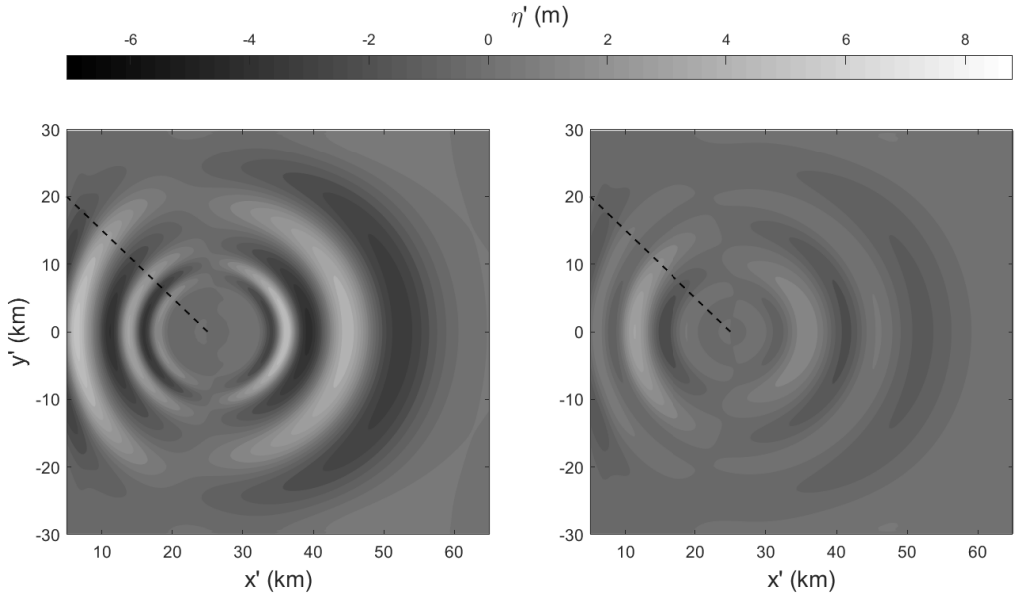

Figure 6.14: Comparison of the free surface elevations at $t' = t'_{\text{total}} + 200 = 283.3$ s predicted by WNWD under different initial conditions. The shoreline is located at $x' = 0$ m. Left: nonzero initial flow velocity; right: zero initial flow velocity. Dashed line: the $\theta = 3\pi/4$ direction.

Using the PNG example, we further pointed out the importance of specifying the flow velocity when a landslide-generated tsunami is inputed as the initial conditions in a conventional tsunami propagation model, in which the landslide is not resolved. In many existing numerical studies of the PNG event, the landslide-generated tsunami was modeled as an initial free surface elevation with zero initial velocity, just like an earthquake-generated tsunami. Doing so is unphysical, since landslide-generated tsunamis have directionality, as revealed by both the analytical solutions and the numerical results in this study. We demonstrated via numerical simulations that with zero initial flow velocity, in order to produce comparable leading wave amplitude, the initial wave height needed to be more than twice as large as that in the case with nonzero initial flow velocity. On the other hand, the trailing waves were characteristically incomparable regardless of the initial wave height.

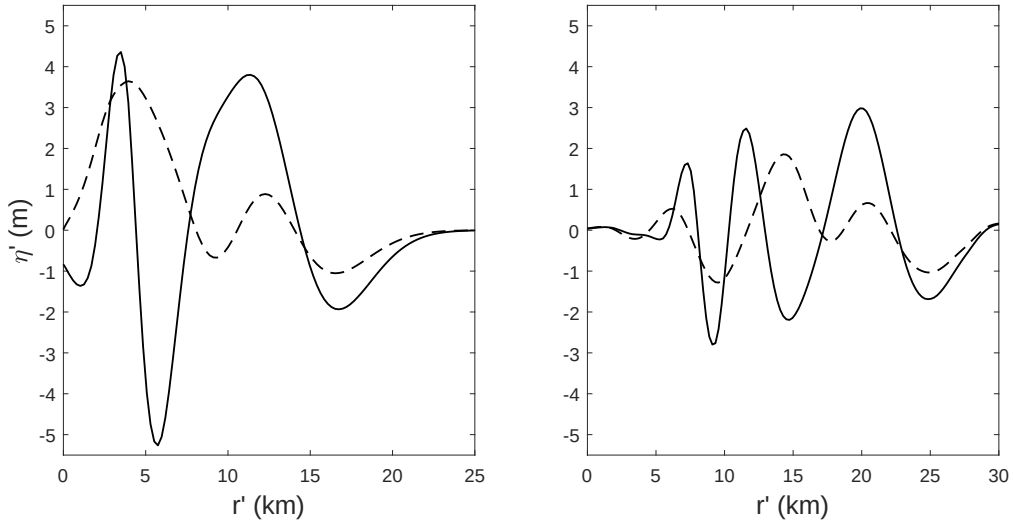

Figure 6.15: Comparison of the free surface elevations in the $\theta = 5\pi/6$ direction predicted by WNWD under different initial conditions. Left: $t' = t'_{\text{total}} + 100 = 183.3$ s; right: $t' = t'_{\text{total}} + 200 = 283.3$ s. Solid line: nonzero initial flow velocity; dashed line: zero initial flow velocity.

CHAPTER 7

CLOSED-FORM LANDSLIDE TSUNAMI GENERATION MODELS

Inspired by the 1998 Papua New Guinea example in Chapter 6, in this chapter we seek to examine closed-form landslide tsunami generation models more closely. So far, this study provides only guidelines for choosing the simplest acceptable long-wave equations to model the landslide wave generation stage. Once the simplest wave model is determined, a numerical simulation is still needed to obtain the resulting wave profile at the end of the wave generation stage. The wave profile, including both the free surface elevation and the flow velocity, is then specified as the initial conditions in a wave propagation model to calculate the wave evolution process in a larger domain and the eventual runup onshore.

In practice, since landslide tsunami generation models are not widely available while tsunami propagation models are, it is more useful to be able to acquire the landslide tsunami wave profile quickly without having to run a separate wave generation simulation. Hence, closed-form landslide tsunami generation models, able to provide this information as a function of the important input parameters, come into play. In this chapter, we shall first review some of the existing models, none of which provides information on the flow velocity. Then, we shall utilize both the analytical solutions and the numerical results from this study to propose a new semi-analytical landslide tsunami generation model, which includes information on both the wave shape and the flow velocity, for landslide-generated waves due to an accelerating landslide on a plane beach in 2DH.

7.1 A brief review of existing models

Here we summarize select existing studies that provided predictive formulas for tsunamis generated by a submarine landslide on a slope. Using energy conservation, scaling arguments, and assuming the wave form to be solitary waves, Striem and Miloh (1976) proposed semi-analytical equations to predict the wave height and wave period of landslide-generated tsunamis. Based on 1DH LFD, Pelinovsky and Poplavsky (1996) found an expression for the maximum water surface elevation on top of a moving landslide. Watts (1998) performed landslide-wave experiments with a solid triangular block on a 45° incline connected to a channel of constant depth, and provided an empirical formula for the characteristic wave height. Murty (2003) attempted to relate the landslide tsunami wave height to the landslide volume based purely on field observations. However, the resulting empirical formula did not agree with numerical simulations. Utilizing many of their previous works, Grilli and Watts (2005); Watts et al. (2005) provided empirical equations for the characteristic wave height and the characteristic wavelength, based on the 1DH numerical results predicted by the fully nonlinear potential flow theory at the initial landslide location. To the best of our knowledge, this is the first and only comprehensive empirical submarine landslide wave generation model currently available, and was used in many numerical studies of the PNG event.

The (dimensional) empirical wave generation model from Grilli and Watts (2005) and Watts et al. (2005) is as follows:

$$\eta(x,y) = -H\mathrm{sech}^2(\kappa_1 \frac{y-y_0}{w+\lambda})\left(e^{-(\frac{x-x_0-\Delta x}{\lambda})^2} - \kappa_2 e^{-(\frac{x-x_0-2\Delta x}{\lambda})^2}\right), \qquad (7.1)$$

in which the hyperbolic secant term was artificially introduced to account for the 2DH effects, and the wave form consisting of two exponential functions was assumed. In (7.1), two types of submarine mass failures were distinguished: slides

– translational failures, and slumps – rotational failures. The empirical formulas for the wave heights are, based on their 1DH numerical simulations:

$$\begin{cases} H = 0.0286A(1-0.750\sin\beta)(\dfrac{L\sin\beta}{d_0})^{1.25}(\dfrac{w}{w+\lambda}), & \text{for a slide} \\ H = 0.0654A(\sin\beta)^{0.25}(\dfrac{L}{d_0})^{1.25}(\dfrac{R}{L})^{0.37}(\Delta\phi)^{1.39}(\dfrac{w}{w+\lambda}), & \text{for a slump} \end{cases} . \quad (7.2)$$

The other terms in (7.1) and (7.2) are:

$$\begin{cases} A : \text{landslide thickness} & L : \text{landslide length} \\ w : \text{landslide width} & d_0 : \text{initial water depth} \\ \beta : \text{slope angle} & \lambda : \text{characteristic wavelength} \\ R : \text{radius of curvature} & \Delta\phi : \text{displacement angle} \\ \kappa_1 : \text{fitting parameter} & \kappa_2 : \text{fitting parameter} \\ \Delta x : \text{fitting parameter} & x_0 : \text{initial landslide location} \end{cases} . \quad (7.3)$$

We see that three fitting parameters are needed, and the model does not specify the instant after the landslide motion first starts when (7.1) should be applied.

The common shortcomings of many of the existing landslide wave generation models, including (7.1) reviewed above, are:

1. the lack of information other than the characteristic wave height – the flow velocity is neglected or assumed to be zero, and the wave shape is also neglected or assumed.
2. the empirical formulas are all based on 1DH experiments. The extension to 2DH is often based on simple semi-analytical assumptions or tuning.
3. the definition of the characteristic wave height is somewhat arbitrary across studies – it is often defined at where a wave gauge happened to be installed in an experiment, where field observations are available, or on top of the initial landslide location.

Combining both the analytical and numerical findings of this study, we shall construct a new closed-form wave generation model that addresses all three shortcomings listed above.

On the other hand, although beyond the scope of this study, we acknowledge the various studies that provided empirical equations to describe water waves generated by subaerial landslides, e.g., Fritz et al. (2003); Heller and Hager (2010); Heller and Spinneken (2015). These studies tend to be experimental, in which granular materials slid down a steep slope of $\sim 45^\circ$ to create violent impact water waves. The wave generation process by a subaerial landslide is very different from that by a submarine landslide, and most likely cannot be modeled with depth-averaged long-wave equations, the focus of this study.

7.2 A semi-analytical landslide tsunami generation model

As realistic tsunamigenic submarine landslides (e.g., that in the 1998 PNG event) are most likely to occur on a continental slope in the open sea, we shall construct a semi-analytical landslide tsunami generation model for tsunamis generated by a submarine landslide on a plane beach in 2DH. Similar models for the other three scenarios (1DH in constant depth, 2DH in constant depth, and 1DH on a slope) can be constructed using the same ideas, but will not be considered in the present work.

7.2.1 Derivation of the semi-analytical model

We recall that the far-field (large r and away from the landslide) free surface solution (normalized by the landslide thickness A_b) based on LSWE for a double-Gaussian-shaped landslide of aspect ratio σ moving at a constant speed is, (2.136),

$$\eta_{\text{far}}(r,\theta,t) = \sqrt{\pi}\frac{Fr\cos\theta}{2(1-Fr\cos\theta)} r^{-\frac{1}{2}}\nu^{-\frac{3}{4}}\Omega_2\Big(\frac{r-t}{\nu^{\frac{1}{2}}}\Big), \tag{7.4}$$

where $\Omega_2(s)$ is a closed-form function given by

$$\Omega_2(s) = |s|^{\frac{3}{2}}e^{-4s^2}\left[I_{\frac{5}{4}}\big(4s^2\big) - I_{\frac{1}{4}}\big(4s^2\big) + \frac{1}{8s^2}I_{\frac{1}{4}}\big(4s^2\big) + \text{sgn}(s)\Big(I_{-\frac{1}{4}}\big(4s^2\big) - I_{\frac{3}{4}}\big(4s^2\big)\Big)\right]. \tag{7.5}$$

ν, given in (2.137) as

$$\nu = \sigma\cos^2\theta + \frac{1}{\sigma}\sin^2\theta, \tag{7.6}$$

is the wave stretching factor due to the landslide x-to-y aspect ratio, σ, of a double-Gaussian-shaped landslide. The double-Gaussian landslide shape has been defined in (2.134) as

$$B_0(x,y) = e^{-8(\frac{x}{\sqrt{\sigma}})^2}e^{-8(y\sqrt{\sigma})^2}. \tag{7.7}$$

With the free surface solution known, the far-field velocity solutions (normalized by $\epsilon\sqrt{gd}$) in the radial (r) and tangent directions (θ) are simply

$$R(r,\theta,t) = \eta_{\text{far}}(r,\theta,t), \quad \Theta(r,\theta,t) = 0, \tag{7.8}$$

and the velocity components in the x and y directions are

$$u(r,\theta,t) = \eta_{\text{far}}(r,\theta,t)\cos\theta, \quad v(r,\theta,t) = \eta_{\text{far}}(r,\theta,t)\sin\theta. \tag{7.9}$$

Closed-form analytical solutions, e.g., (7.4) are available only for landslides moving at a constant speed in constant water depth. The effects due to landslide acceleration and a sloping bottom need to be accounted for empirically. In Chapter

5, we've shown that the effects due to landslide acceleration can be accounted for by the modification factors $L_{\rm acc}$ and $A_{\rm acc}$. Due to acceleration, the leading wave is $L_{\rm acc}$ times as long as that in the constant-speed case, and the leading wave is $A_{\rm acc}$ times as high as that in the constant-speed case. Empirical formulas for $L_{\rm acc}$ and $A_{\rm acc}$ in 2DH have been given in (5.37) and (5.38), respectively, as

$$\begin{aligned} s &= t_0\sqrt{1+\frac{1}{4}Fr^2 - Fr\cos\theta} \\ L_{\rm acc} &= 1 + 0.6237s \\ A_{\rm acc} &= \min\Big[1, L_{\rm acc}^{-2}\big(5.612 - 9.975(L_{\rm acc}-0.5712t_0) + 6.944(L_{\rm acc}-0.5712t_0)^2 \\ &\qquad -1.277(L_{\rm acc}-0.5712t_0)^3\big)\Big] \end{aligned} \quad . \tag{7.10}$$

To account for a sloping bottom, we utilize the results from Chapter 4, in which we estimate the spatial scales of the leading wave at the end of the wave generation stage, $t = t_s$, as

$$\epsilon = \delta_*|\frac{Fr_*\cos\theta}{2(1-Fr_*\cos\theta)}|r_s^{-\frac{1}{2}}, \quad \mu^2 = \gamma_*^2, \tag{7.11}$$

where

$$\begin{aligned} (Fr_*, \delta_*, \gamma_*) &= (Fr\chi_*^{-\frac{1}{2}}, \delta\chi_*^{-1}, \gamma\chi_*) \\ \chi_* &= 1 + \frac{1}{4}(\chi - 1) \\ \chi &= 1 + \zeta\cos\theta t_s + \frac{1}{4}(\zeta\cos\theta)^2 t_s^2 \end{aligned} \quad . \tag{7.12}$$

We recall that χ_* is the representative water depth ratio defined to capture the shoaling effects on a slope, and t_s for the wave in the θ direction is solved from (6.40):

$$\begin{aligned} &-L_{\rm acc}^2\zeta\cos\theta t_s + \Big(1 - 2Fr\cos\theta + Fr^2 - \frac{1}{4}(\zeta\cos\theta)^2\Big)t_s^2 \\ &+\frac{1}{2}\zeta\cos\theta(1-Fr\cos\theta)t_s^3 + \frac{1}{16}(\zeta\cos\theta)^2 t_s^4 - L_{\rm acc}^2 = 0 \end{aligned} \quad . \tag{7.13}$$

For the accelerating landslide on a slope scenarios, we showed in Chapter 6 how to relate the initial input parameters $(Fr_0, \delta_0, \gamma_0, \zeta_0)$, which can be immediately

calculated in each problem, to the adjusted input parameters, $(Fr, \delta, \gamma, \zeta)$, which are used as the inputs in the above equations:

$$\begin{aligned} &\chi_0 = 1 + \frac{1}{2} Fr_0 \zeta_0 t_0 \\ &(Fr, \delta, \gamma, \zeta) = (Fr_0 \chi_0^{-1/2}, \delta_0 \chi_0^{-1}, \gamma_0 \chi_0, \zeta_0 \chi_0^{-1}) \end{aligned} . \tag{7.14}$$

In addition, the total time, accounting for the different time scale used to normalized t_s determined from (7.13), it takes for the leading wave to separate is

$$t_{\text{total}} = t_0 + t_s \chi_0^{-1/2}. \tag{7.15}$$

Putting all the results listed above, we then assemble the semi-analytical landslide tsunami generation model for the wave in the $\theta = \psi$ direction (the model outputs a complete wave profile in space, but the profile is most accurate in the $\theta = \psi$ direction) as

$$\begin{aligned} \eta_{\text{model}}(r, \theta) = \sqrt{\pi} A_{\text{acc}}(\theta) \nu(\theta)^{-\frac{3}{4}} &\frac{Fr_*(\theta)\cos\theta}{2\Big(1 - Fr_*(\theta)\cos\theta\Big)} r_*(\theta)^{-\frac{1}{2}} \\ &\Omega_2\Big(\frac{r - r_*(\theta)}{L_{\text{acc}}(\theta)\chi_*(\theta)^{\frac{1}{2}}\nu(\theta)^{\frac{1}{2}}}\Big) \tanh(6r) \\ R_{\text{model}}(r, \theta) = \eta_{\text{model}}(r, \theta), \quad \Theta_{\text{model}}(r, \theta) = 0 \quad &, \\ \text{(velocity componenets in the } r \text{ and } \theta \text{ directions)} \\ u_{\text{model}}(r, \theta) = \eta_{\text{model}}(r, \theta)\cos\theta, \quad v_{\text{model}}(r, \theta) = \eta_{\text{model}}(r, \theta)\sin\theta \\ \text{(velocity componenets in the } x \text{ and } y \text{ directions)} \end{aligned} \tag{7.16}$$

where

$$r_*(\theta) = t_* + \frac{1}{4}\zeta_0 \cos\theta t_*^2 \tag{7.17}$$

is the representative distance traveled by the leading wave from $t = 0$ to $t = t_*$. t_* is empirically determined as

$$t_* = C_{t_*} t_0 + t_s \chi_0^{-1/2}, \quad 0 \le C_{t_*} \le 1, \tag{7.18}$$

in which t_s is calculated from (7.13) for the direction $\theta = \psi$. The function $\tanh(6r)$ is introduced to remove possible discontinuity at the origin, and the factor of six in the argument is introduced so that $\tanh(6r)$ increases from 0 to more than 0.995 within half the normalized distance (in other words, half the characteristic length scale), i.e., $\tanh(6 \cdot 0.5) = 0.9951$.

An empirical t_* is needed to account for the fact that the location of the leading wave peak is not captured in the empirical formulas for the landslide acceleration effects – only the characteristic wavelength, L_{acc}, and the characteristic wave height, A_{acc}, are captured. $C_{t_*} = 1$ corresponds to the largest possible leading wave location (thus, the earliest arrival time), and $C_{t_*} = 0$ corresponds to the smallest possible leading wave location (thus, the latest arrival time). For now, we choose $C_{t_*} = 1/2$ since it works well in the examples that will be shown in the next section. In the future, more empirical work similar to that done to determine L_{acc} and A_{acc} can be performed to improve the form of C_{t_*}.

We recall that the analytical expressions, such as (7.16), are normalized as follows: the spatial variables (x, y, r, etc.) are normalized by $L_b \cos\beta$, where L_b is the characteristic landslide length along an incline of angle β, η is normalized by $A_b \sec\beta$, where A_b is the maximum landslide thickness along the incline, t_{total} is normalized by $L_b \cos\beta/\sqrt{gd_0}$, where d_0 is the still water depth (excluding landslide thickness) at the initial location of the landslide, and the velocities (u, v, R, Θ) are normalized by $\epsilon\sqrt{gd_0}$, where $\epsilon = A_b \sec\beta/d_0$.

The semi-analytical model (7.16) provides a complete landslide-generated tsunami profile in space, including both the free surface profile and the flow velocity, at the instant $t = t_{\text{total}}$ when the wave generation stage is over in the $\theta = \psi$ direction. Therefore, the model is the most accurate for the waves traveling in

the $\theta = \psi$ direction. In practice, ψ can be chosen based on the most important location of interest, e.g., $\psi = 3\pi/4$ in the PNG example. We further stress that many of the parameters in (7.16) are expressed as functions of θ, an independent spatial variable in the polar coordinate system.

The semi-analytical model (7.16) is unprecedented, as it is based on the newly derived 2DH LSWE analytical solution for landslide-generated waves. Unlike existing models, the new model provides information on not only the wave height, but also the complete wave profile of the landslide-generated tsunami, including both the shape of the wave and the flow velocity. Both the free surface profile and the flow velocity are specified according to analytical findings, rather than purely empirical assumptions. Similarly, the 2DH effects are also based on analytical findings, rather than empirical assumptions. Furthermore, the model considers the duration of the wave generation process, which is critical for landslide-generated tsunamis, as the waves cannot be seen as being generated instantly, which is the case for earthquake-generated tsunamis.

Lastly, we remark that although the expressions in (7.16) are determined for a double-Gaussian-shaped landslide based on LSWE, we've shown in Chapter 2 that the exact landslide shape has minimal effects on the far-field leading wave generated by the landslide. In reality, the exact shape of the landslide is impossible to determine. Therefore, we find (7.16) to be an adequate closed-form wave generation model, whose main value is to quickly provide an approximate landslide-generated tsunami wave profile.

7.2.2 Accuracy of the semi-analytical model

Two questions on the accuracy of the semi-analytical model need to be answered: first, how well does the semi-analytical model, based on LSWE, actually approximate the exact LSWE results? Second, given a landslide tsunami problem, how accurate is LSWE at describing the wave generation process? While the second question has been answered in the previous chapters, in which criteria were proposed to determine model validity, the first question requires further attention. In this section, we shall focus on comparing the semi-analytical model results with the actual LSWE results, for five cases based on the 1998 PNG event.

We recall that in the 1998 PNG example in Chapter 6, the essential parameters (based on the estimates from Watts et al., 2003) were

$$(Fr_0, \delta_0, \gamma_0, \zeta_0, t_0, \sigma) = (0.0951, 0.508, 0.334, 0.180, 0.870, 0.9). \tag{7.19}$$

We remark that we now take the landslide width, 5000 m, into consideration as well. Therefore, $\sigma = 4500/5000 = 0.9$. To see how well the semi-analytical model compares with the actual LSWE results, we consider a total of five cases on based the parameters for the PNG event. The parameters for each case are listed in Table 7.1. We shall focus on the leading waves in four select directions: $\theta = \pi, 3\pi/4, \pi/4, 0$.

First, we look at Case PNG. The contour plots of the results are shown in figure 7.1, figure 7.2, and figure 7.3, for the free surface elevation, the velocity in the x direction (u), and the velocity in the y direction (v), respectively. The trapped wave that follows the landslide can be clearly seen in the numerical results near the origin. It is completely absent in the semi-analytical model results since the trapped wave solution is not included in the model. The separation of the

Table 7.1: A list of the parameters for each of the five cases chosen to test the semi-analytical model results against the actual LSWE results.

Case	Fr_0	δ_0	γ_0	ζ_0	t_0	σ
PNG	0.0951	0.508	0.334	0.180	0.870	0.9
PNG-2Fr_0	$0.0951 \cdot 2$	0.508	0.334	0.180	0.870	0.9
PNG-2ζ_0	0.0951	0.508	0.334	$0.180 \cdot 2$	0.870	0.9
PNG-2t_0	0.0951	0.508	0.334	0.180	$0.870 \cdot 2$	0.9
PNG-2σ	0.0951	0.508	0.334	0.180	0.870	$0.9 \cdot 2$

outward-going leading waves from the trapped wave can be clearly seen in the figures. To the naked eyes, the agreement between the LSWE numerical results and the semi-analytical results for the leading waves away from the landslide is exceptional.

To get a closer look at the comparison, we plot the results along the $\theta = \psi$ line in figure 7.4 for the free surface elevation and in figure 7.5 for the flow velocities (in the radial direction and in the tangential direction). Discrepancies can now be seen more clearly. Whereas the free surface results still show good overall agreement, major differences appear in the velocity results. Specifically, the velocities due to the trapped wave near the origin (near $r = 0$) are apparent. Nonetheless, near the leading waves, where our primary focus is and where the wave generation model is the most accurate, the agreement is good. Therefore, we conclude that for Case PNG, the semi-analytical wave generation model represents well the actual LSWE results, and serves as a quick and effective way to acquire the wave profile for the leading waves generated by a submarine landslide.

Next, we vary the parameters to see how the performance of the semi-analytical model changes, by comparing the results for the other four cases listed in Table 7.1. The four cases are: Case PNG-2Fr_0, in which Fr_0 is twice as large (in other words,

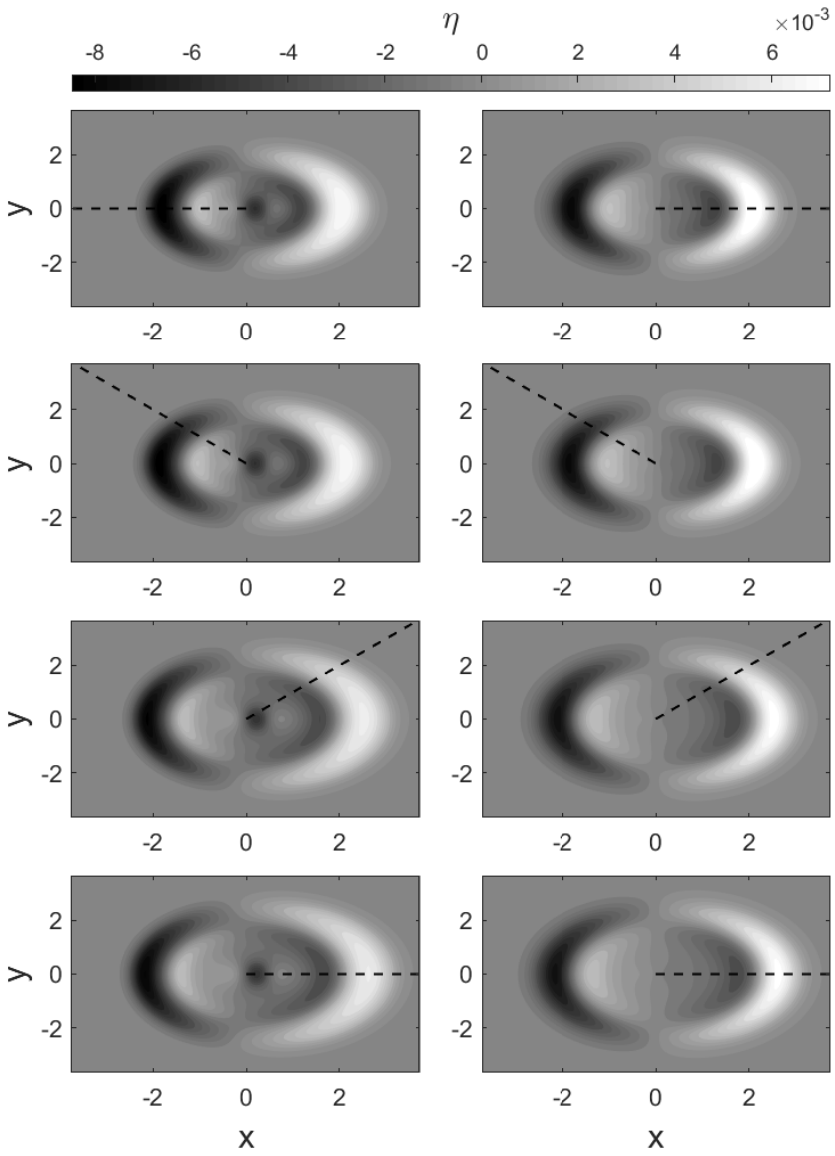

Figure 7.1: Comparison of the LSWE numerical free surface results (left column) with the semi-analytical model free surface results (right column) for Case PNG at $t = t_{\text{total}}$. From top row to bottom row: $\psi = \pi, 3\pi/4, \pi/4, 0$ and $t_{\text{total}} = 2.19, 2.25, 2.57, 2.64$. Dashed line: the $\theta = \psi$ direction.

the terminal velocity of the landslide is twice as large), Case PNG-$2\zeta_0$, in which ζ_0 is twice as large (in other words, the slope is twice as steep), Case PNG-$2t_0$, in which t_0 is twice as large (in other words, the landslide accelerates half as fast), and Case PNG-2σ, in which σ is twice as large (in other words, the landslide is $\sqrt{2}$ times as long and $1/\sqrt{2}$ times as wide). To reduce the number of plots, we shall

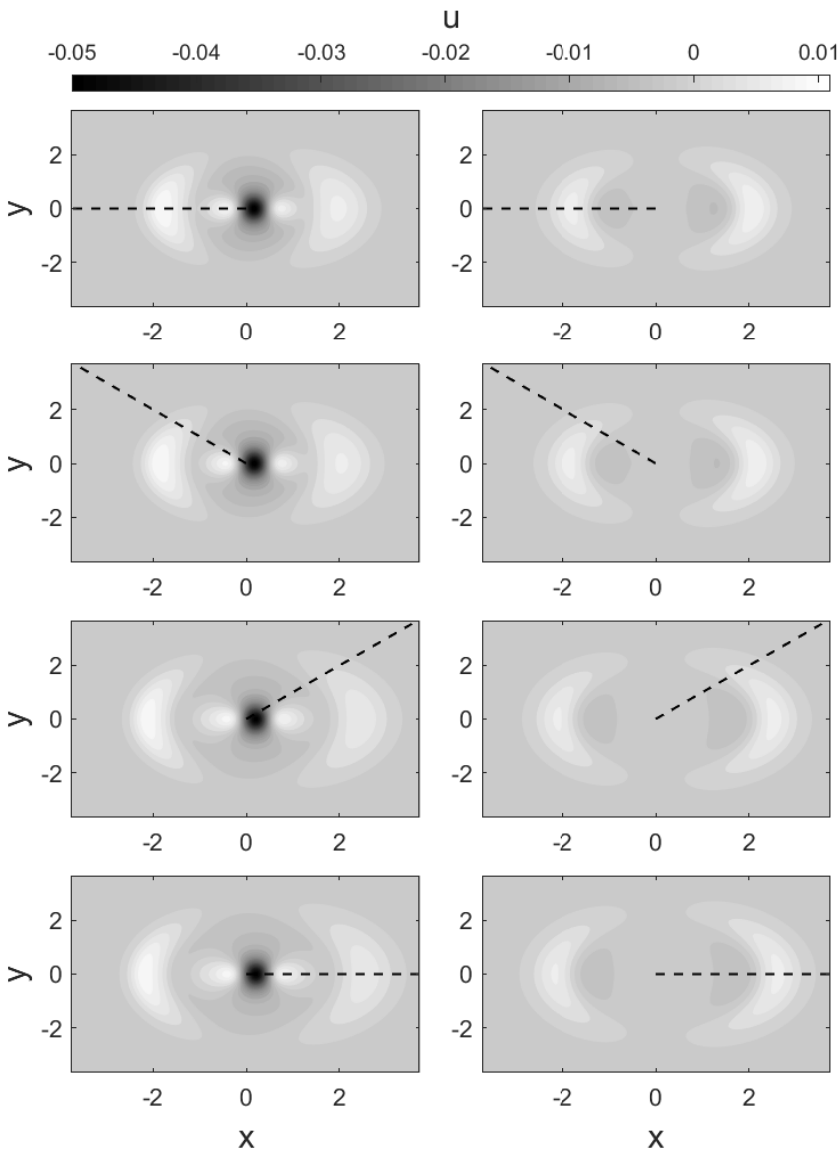

Figure 7.2: Comparison of the LSWE numerical u-velocity results (left column) with the semi-analytical model u-velocity results (right column) for Case PNG at $t = t_{\text{total}}$. From top row to bottom row: $\psi = \pi, 3\pi/4, \pi/4, 0$ and $t_{\text{total}} = 2.19, 2.25, 2.57, 2.64$. Dashed line: the $\theta = \psi$ direction.

show the results only for $\psi = 3\pi/4$.

The contour plots are shown in figure 7.6, figure 7.7, and figure 7.8. Overall, the semi-analytical model remains satisfactory at capturing the leading waves. However, larger discrepancies can be seen in Case PNG-$2t_0$, in which case the

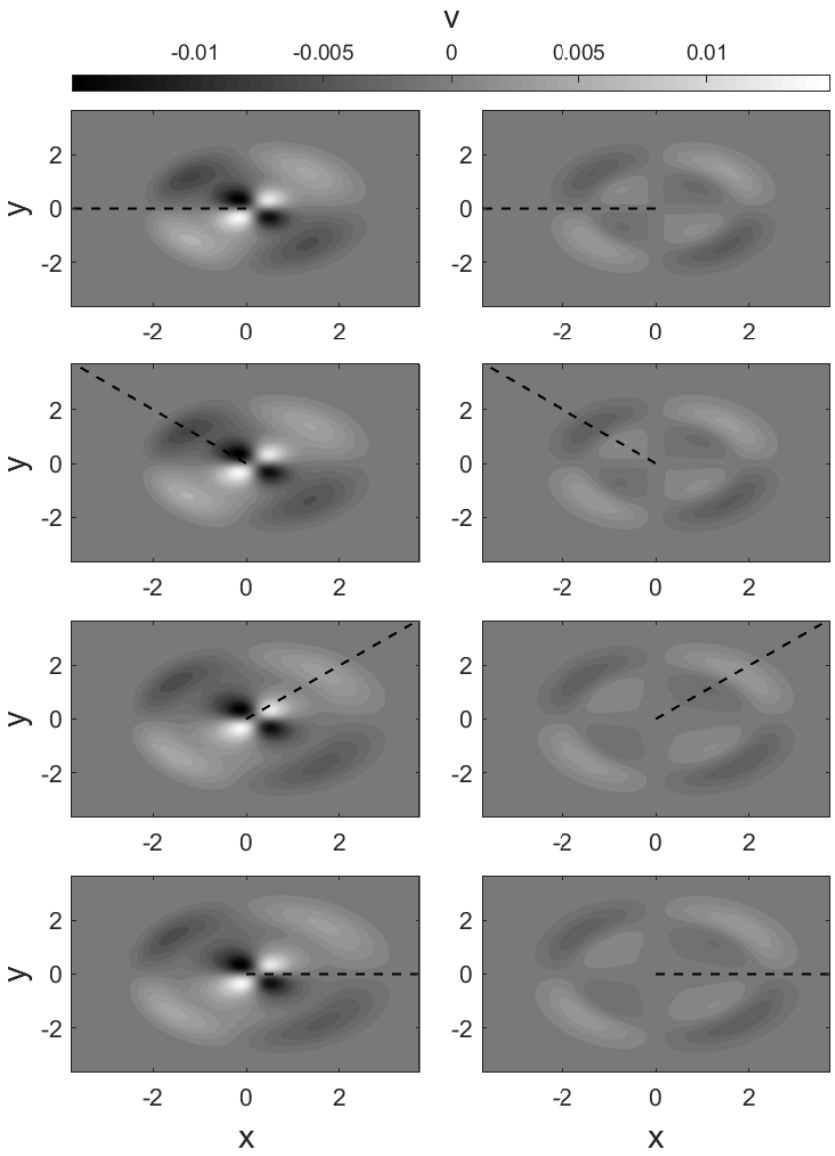

Figure 7.3: Comparison of the LSWE numerical v-velocity results (left column) with the semi-analytical model v-velocity results (right column) for Case PNG at $t = t_{\text{total}}$. From top row to bottom row: $\psi = \pi, 3\pi/4, \pi/4, 0$ and $t_{\text{total}} = 2.19, 2.25, 2.57, 2.64$. Dashed line: the $\theta = \psi$ direction.

landslide accelerates half as fast. As mentioned previously, the present empirical formulas do not capture the change in the location of the wave peak due to landslide acceleration, and the curve fitting parameter C_{t_*} can be further tuned in the future to better capture the location of the peak.

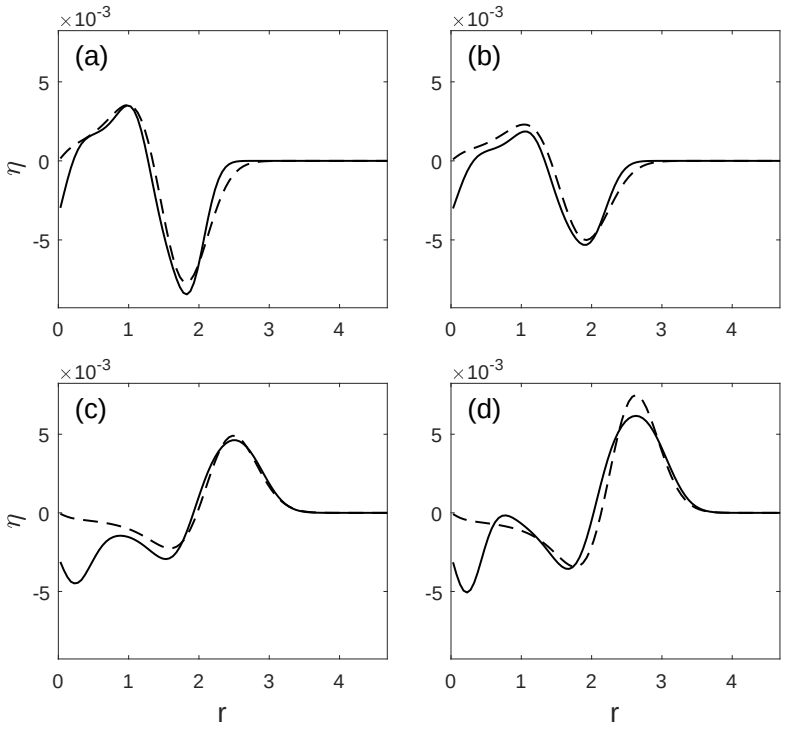

Figure 7.4: Comparison of the LSWE numerical free surface results (solid line) with the semi-analytical model free surface results (dashed line) for Case PNG in the direction $\theta = \psi$ at $t = t_{\text{total}}$. (a) $\psi = \pi$ and $t_{\text{total}} = 2.19$; (b) $\psi = 3\pi/4$ and $t_{\text{total}} = 2.25$; (c) $\psi = \pi/4$ and $t_{\text{total}} = 2.57$; (d) $\psi = 0$ and $t_{\text{total}} = 2.64$.

To get a closer look at the results, we plot the results along the $\theta = \psi = 3\pi/4$ direction in figure 7.9 for the free surface and in figure 7.10 for the flow velocities (in the radial direction and in the tangential direction). Again, the overall level of performance of the semi-analytical model remains similar – it captures the free surface well, and the flow velocity under the leading wave satisfactorily, but the trapped wave near the origin, which can create large flow velocities, is not captured at all. The discrepancy in Case PNG-$2t_0$ can now be seen clearly – although the characteristic wave height and the characteristic wavelength of the leading wave are captured, the exact shape and the location of the wave peak are not. The more the leading wave is stretched due to a slower acceleration, the less accurate the location of the wave peak is in the semi-analytical model (without changing the value of the

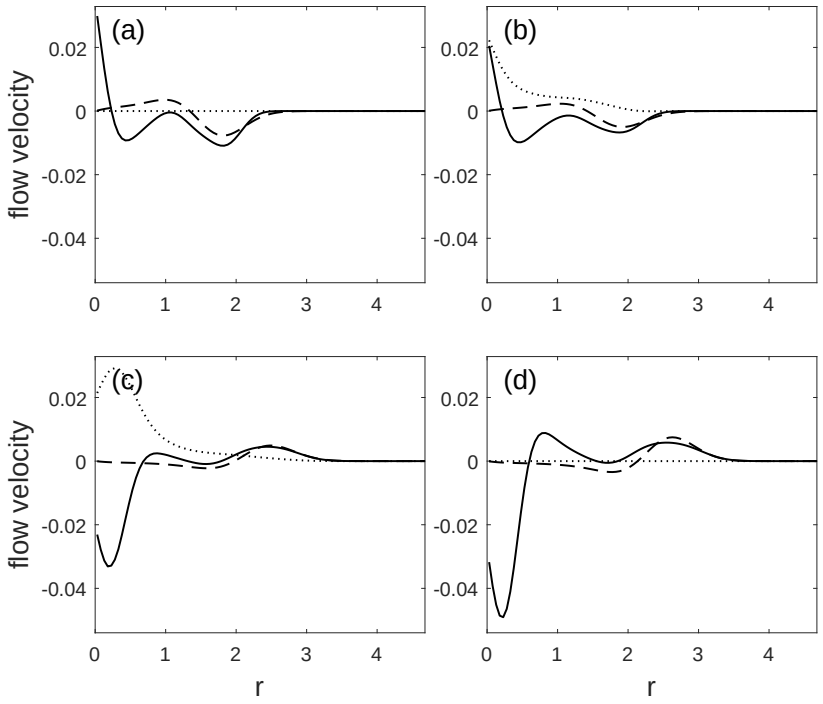

Figure 7.5: Comparison of the LSWE numerical velocity results with the semi-analytical model free surface velocity results for Case PNG in the direction $\theta = \psi$ at $t = t_{\text{total}}$. Solid line: numerical results for the velocity (R) in the radial (r) direction; dashed line: semi-analytical model results for the velocity (R) in the radial (r) direction; dotted line: numerical results for the velocity (Θ) in the tangential (θ) direction; the semi-analytical model results for the velocity (Θ) in the tangential (θ) direction are zero. (a) $\psi = \pi$ and $t_{\text{total}} = 2.19$; (b) $\psi = 3\pi/4$ and $t_{\text{total}} = 2.25$; (c) $\psi = \pi/4$ and $t_{\text{total}} = 2.57$; (d) $\psi = 0$ and $t_{\text{total}} = 2.64$.

tuning parameter C_{t_*}, at least). Fortunately, a slower landslide acceleration results in significantly smaller waves, and is less likely to cause damaging tsunamis.

7.3 Simulating the 1998 Papua New Guinea tsunami using different initial conditions

To see how the different wave generation models perform, we again use the PNG event as an example, and computed the wave propagation stage based on WNWD

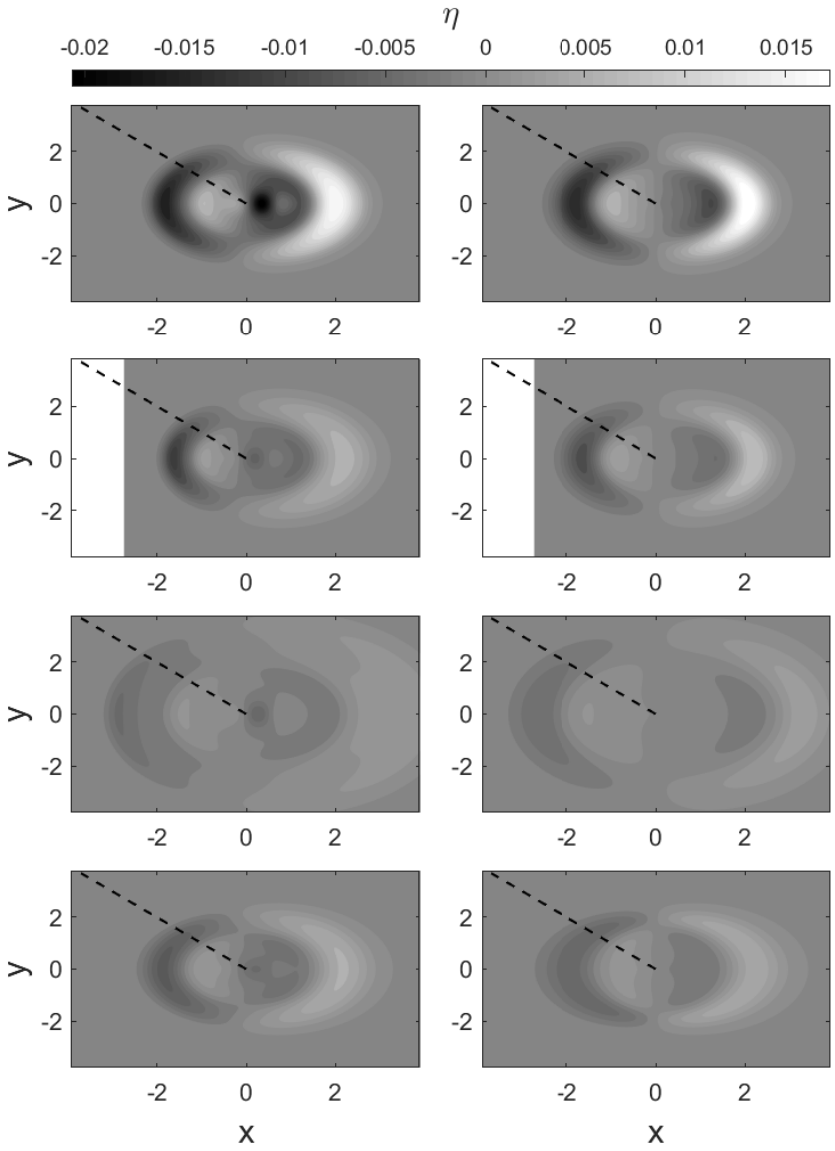

Figure 7.6: Comparison of the LSWE numerical free surface results (left column) with the semi-analytical model free surface results (right column) for four different cases at $t = t_{\text{total}}$ with $\psi = 3\pi/4$. From top row to bottom row: Case PNG-2Fr_0, Case PNG-2ζ_0, Case PNG-2t_0, Case PNG-2σ, and $t_{\text{total}} = 2.17, 2.17, 3.57, 2.25$. Dashed line: the $\theta = \psi$ direction.

using three different initial conditions: the landslide tsunami wave profile (including both the free surface elevation and nonzero flow velocity) computed numerically using WNWD, the landslide tsunami wave profile (including both the free surface elevation and nonzero flow velocity) given by the new wave generation model

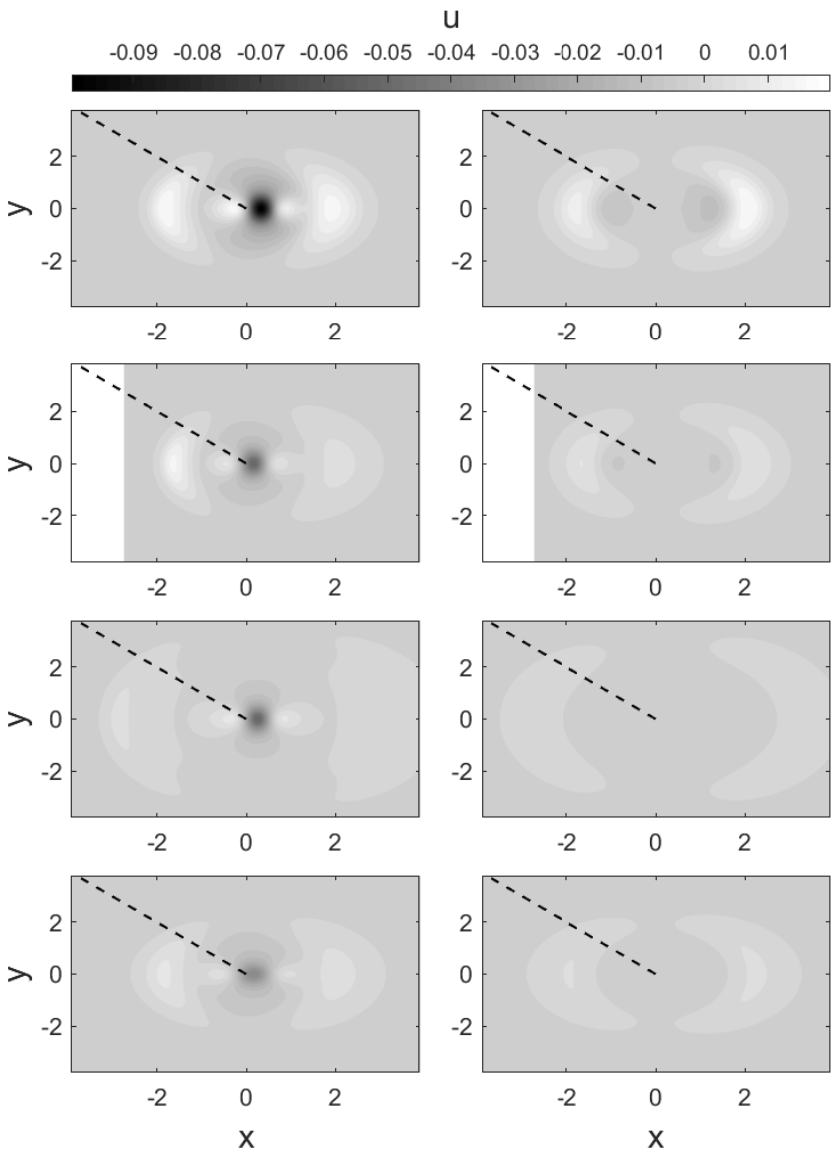

Figure 7.7: Comparison of the LSWE numerical u-velocity results (left column) with the semi-analytical model u-velocity results (right column) for four different cases at $t = t_{\text{total}}$ with $\psi = 3\pi/4$. From top row to bottom row: Case PNG-$2Fr_0$, Case PNG-$2\zeta_0$, Case PNG-$2t_0$, Case PNG-2σ, and $t_{\text{total}} = 2.17, 2.17, 3.57, 2.25$. Dashed line: the $\theta = \psi$ direction.

(7.16), and the landslide tsunami wave profile (with zero flow velocity) given by the empirical model from Watts et al. (2005).

Since the new wave generation model, (7.16), is based on LSWE, the approximation error due to using LSWE to model the wave generation stage can be

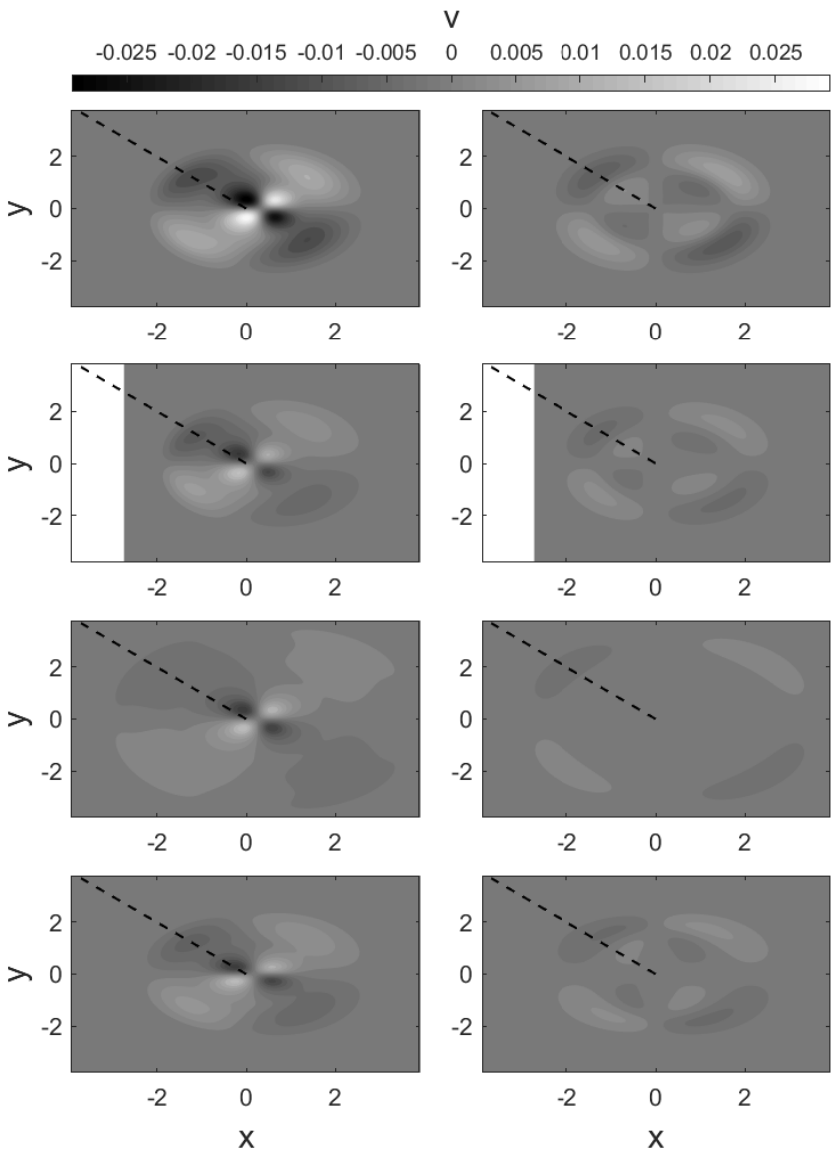

Figure 7.8: Comparison of the LSWE numerical v-velocity results (left column) with the semi-analytical model v-velocity results (right column) for four different cases at $t = t_{\text{total}}$ with $\psi = 3\pi/4$. From top row to bottom row: Case PNG-$2Fr_0$, Case PNG-$2\zeta_0$, Case PNG-$2t_0$, Case PNG-2σ, and $t_{\text{total}} = 2.17, 2.17, 3.57, 2.25$. Dashed line: the $\theta = \psi$ direction.

estimated in advance using the model validity criteria. In Chapter 6, we found the two estimators to be $\overline{\mu^2} = 0.0960$ and $\bar{\epsilon} = 0.350$ for the leading wave in the $\theta = 3\pi/4$ direction. Using the fitted formulas relating the estimators to the RMSDs, (4.48) and (4.50), we expect a $\sim 12\%$ RMSD if a linear model is used,

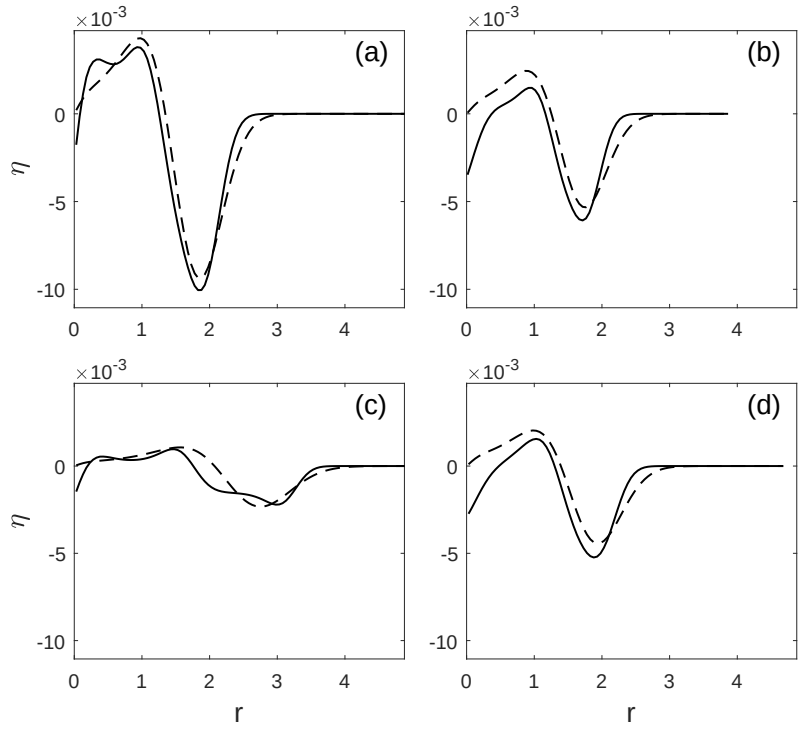

Figure 7.9: Comparison of the LSWE numerical free surface results (solid line) with the semi-analytical model free surface results (dashed line) for four different cases in the direction $\theta = \psi = 3\pi/4$ at $t = t_{\text{total}}$. (a) Case PNG-2Fr_0 and $t_{\text{total}} = 2.17$; (b) Case PNG-2ζ_0 and $t_{\text{total}} = 2.17$; (c) Case PNG-2t_0 and $t_{\text{total}} = 3.57$ (d) Case PNG-2σ and $t_{\text{total}} = 2.25$.

and a $\sim$ 27% RMSD if a nondispersive model is used. Therefore, by using the wave generation model based on LSWE (linear and nondispersive), we are expecting an approximation error on the order of $\sim$ 27% RMSD. While this may seem large, one should keep in mind the large uncertainties inherent in the estimates of the input parameters in a real event, and that the only way to get a more accurate wave profile (given the same input parameters with large uncertainties) is to simulate the wave generation stage numerically. Furthermore, we stress that this approximation error can be estimated in advance and can guide the decision making process in the study of a landslide tsunami problem.

The three initial conditions are shown in figure 7.11. It can be seen that since

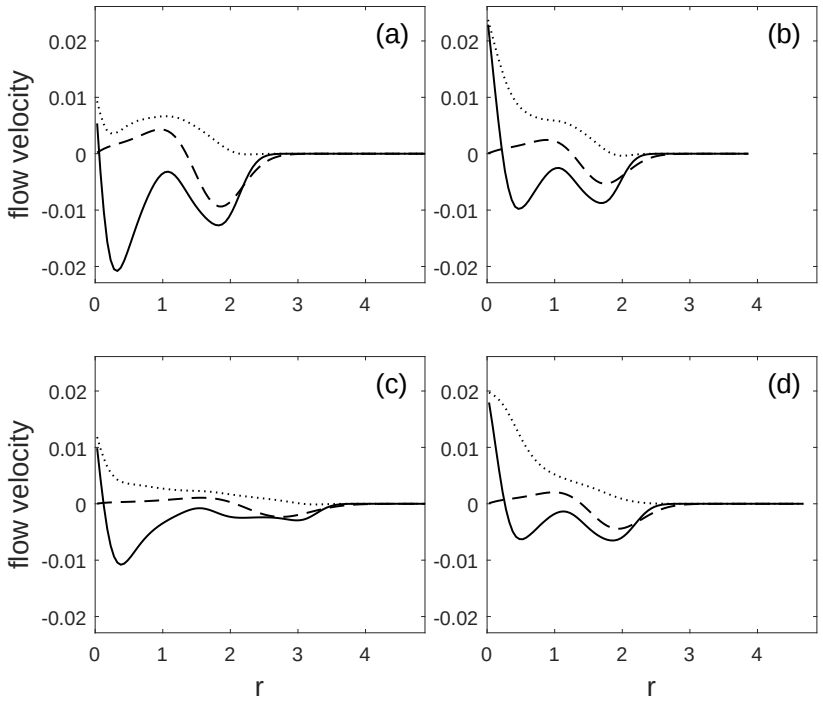

Figure 7.10: Comparison of the LSWE numerical velocity results with the semi-analytical model free surface velocity results for four different cases in the direction $\theta = \psi = 3\pi/4$ at $t = t_{\text{total}}$. Solid line: numerical results for the velocity (R) in the radial (r) direction; dashed line: semi-analytical model results for the velocity (R) in the radial (r) direction; dotted line: numerical results for the velocity (Θ) in the tangential (θ) direction; the semi-analytical model results for the velocity (Θ) in the tangential (θ) direction are zero. (a) Case PNG-2Fr_0 and $t_{\text{total}} = 2.17$; (b) Case PNG-2ζ_0 and $t_{\text{total}} = 2.17$; (c) Case PNG-2t_0 and $t_{\text{total}} = 3.57$ (d) Case PNG-2σ and $t_{\text{total}} = 2.25$.

the empirical model does not account for the wave generation time, it is out of phase with the other two. As a result, when comparing the wave fields, the results based on the initial conditions given by the empirical model need to be time-shifted. In addition, the three fitting parameters in the empirical model (7.1), have been tuned to improve the match of the wave shape. The values used are: $\kappa_1 = 3$, $\kappa_2 = 0.83$, and $\Delta x = \lambda = 3.7$ km.

The wave fields at 100 s and 200 s after the end of the wave generation stage are compared in figure 7.12 and figure 7.13, respectively. In these plots, the results

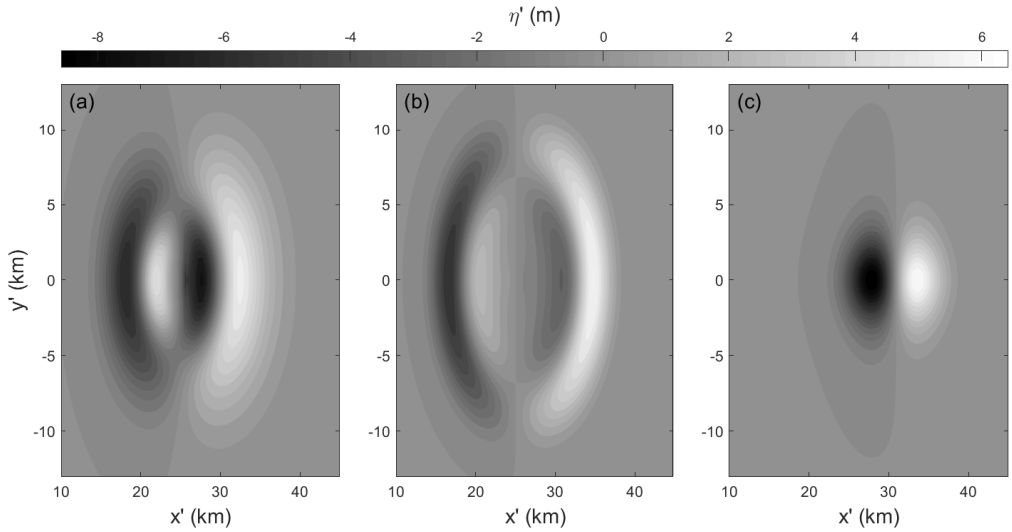

Figure 7.11: The three different initial conditions used to simulate the PNG event. (a): numerical results based on WNWD; flow velocity is nonzero; (b): new closed-form wave generation model (7.16); flow velocity is nonzero; (c): empirical model from Watts et al. (2005) (the fitting parameters have been tuned to match the wave shapes at a later time); flow velocity is assumed to be zero. (c) is out of phase with (a) and (b) and will need to be time-shifted later when comparing the wave fields.

based on the empirical wave generation model have been time-shifted so that the leading waves in the $3\pi/4$ direction are in phase. It can be observed that, characteristically, the waves due to the empirical wave generation model, (c) in the figures, are quite different from those due to the other two models, (a) and (b) in the figures. While visible differences between the results due to the other two models, (a) and (b) in the figures, show, the overall characteristics are comparable.

To examine the results closer, we plot the free surface elevations in the $\theta = 3\pi/4$ direction in figure 7.14. It can be seen that due to the lack of nonzero initial flow velocity, the leading wave amplitude based on the empirical wave generation model (dash-dot line in the figure) is less than half of that based on the full numerical simulation (solid line in the figure). Although the locations of the first depression and the first elevation agree well, we remark that it is a result of parameter tuning

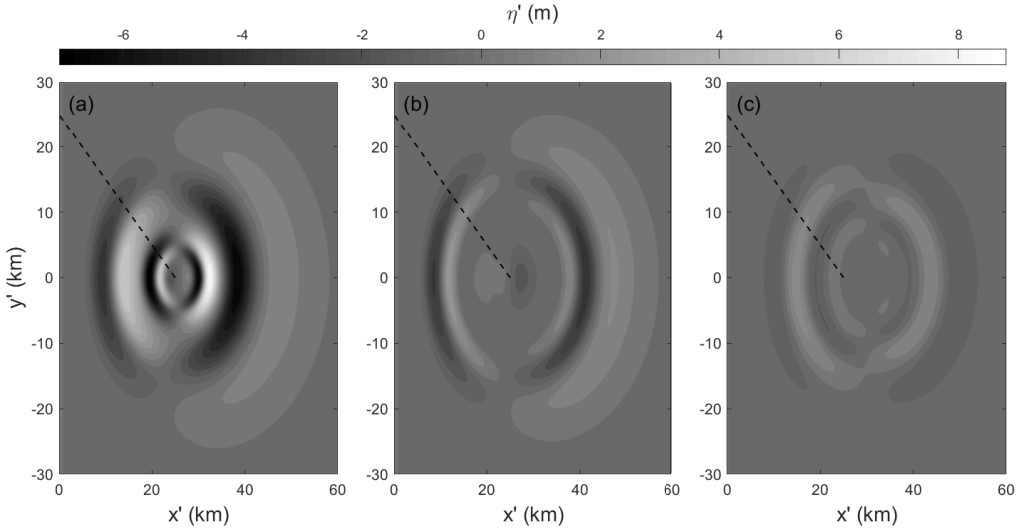

Figure 7.12: The wave fields due to the three different initial conditions at 100 s after the end of the wave generation stage. (a): wave field computed using the initial conditions based on the WNWD numerical simulation; (b): wave field computed using the initial conditions based on the new closed-form wave generation model (7.16); (c): wave field computed using the initial conditions based on the empirical model from Watts et al. (2005), which has been time-shifted so that the leading waves are in phase.

and time-shifting. On the other hand, the new wave generation model (dashed line in the figure) captures the leading wave well, which is a depression in this case, given an expected RMSD of $\sim 27\%$. Although the first elevation is also captured by the new wave generation model, the location and the amplitude are noticeably different. This is not surprising, since a $\sim 27\%$ RMSD is expected for this example, and the new wave generation model is best at capturing the leading wave, not the trailing waves.

The performance of the empirical model from Watts et al. (2005) relies heavily on tuning. If field data are available to tune the model against and if the wave height is allowed to be tuned (which shouldn't be, strictly speaking, given how the model was constructed), the empirical model can be tuned to yield good agreement with observations. On the other hand, the performance of the new wave generation

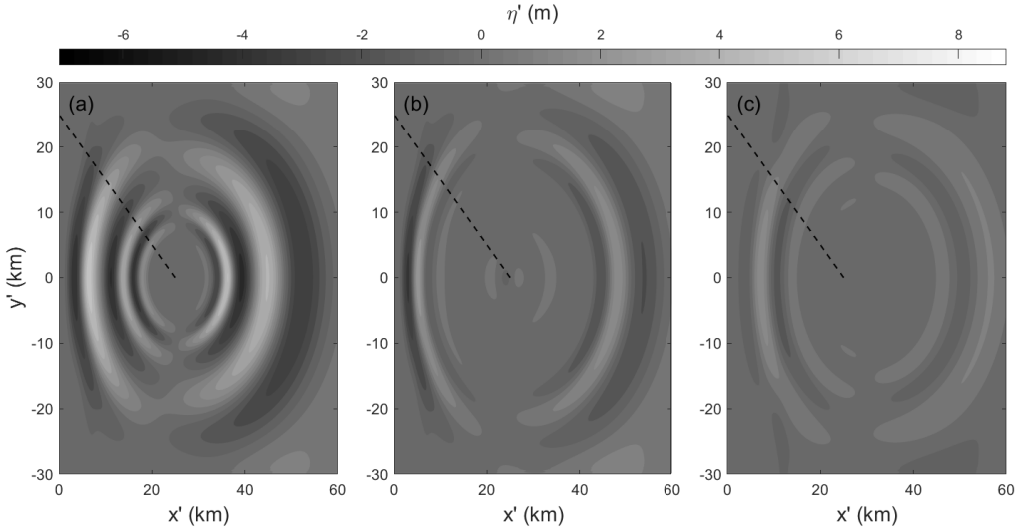

Figure 7.13: The wave fields due to the three different initial conditions at 200 s after the end of the wave generation stage. (a): wave field computed using the initial conditions based on the WNWD numerical simulation; (b): wave field computed using the initial conditions based on the new closed-form wave generation model (7.16); (c): wave field computed using the initial conditions based on the empirical model from Watts et al. (2005), which has been time-shifted so that the leading waves are in phase.

model relies on how well LSWE approximates the wave generation stage in a landslide tsunami problem. While the performance of the new wave generation model can be predicted in terms of the expected RMSD due to using LSWE, the model has little room for tuning to improve the match with field data, if available.

7.4 Summary

In this chapter, using both the analytical solutions and the numerical findings, we constructed a new closed-form semi-analytical landslide wave generation model, (7.16). The wave generation model outputs a complete landslide tsunami wave profile, including both the free surface elevation and flow velocity, at the end of the wave generation stage, as a closed-form function (which requires essentially no

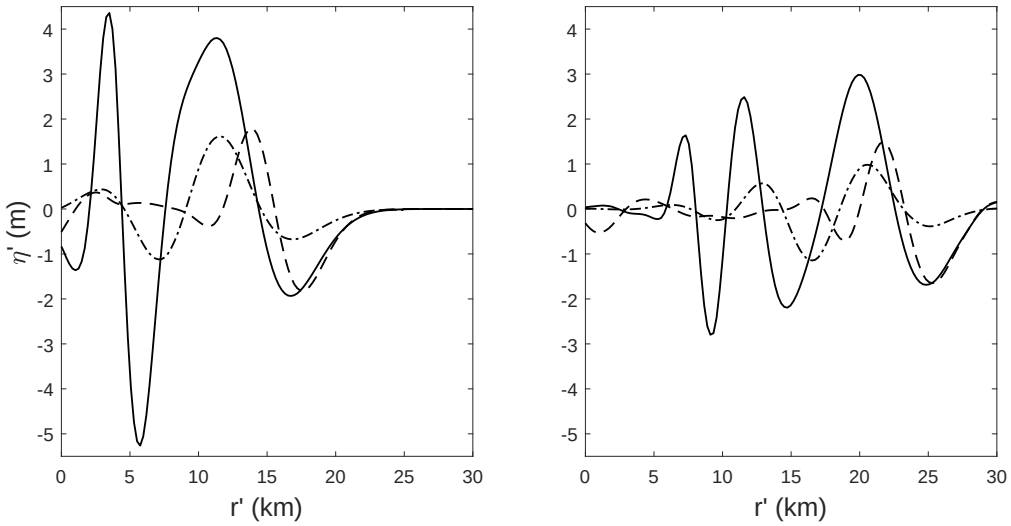

Figure 7.14: Comparison of the free surface elevations in the $\theta = 3\pi/4$ direction due to the three different initial conditions. Left: 100 s after the end of the wave generation stage; right: 200 s after the end of the wave generation stage. Solid line: computed results using the initial conditions based on WNWD numerical simulation; dashed line: computed results using the initial conditions based on the new closed-form wave generation model (7.16); dash-dot line: computed results using the initial conditions based on the empirical model from Watts et al. (2005), which has been tuned and time-shifted to improve the match.

computation time) of the input parameters. The wave profile can then be specified as the initial conditions in a standard tsunami wave propagation model to study the evolution and the eventual runup of the landslide tsunami. The new wave generation model is summarized as follows:

$$\begin{aligned}
&\eta_{\text{model}}(r,\theta) = \sqrt{\pi} A_{\text{acc}}(\theta)\nu(\theta)^{-\frac{3}{4}} \frac{Fr_*(\theta)\cos\theta}{2\Big(1 - Fr_*(\theta)\cos\theta\Big)} r_*(\theta)^{-\frac{1}{2}}, \\
&\qquad\qquad \Omega_2\Big(\frac{r - r_*(\theta)}{L_{\text{acc}}(\theta)\chi_*(\theta)^{\frac{1}{2}}\nu(\theta)^{\frac{1}{2}}}\Big)\tanh(6r), \\
&R_{\text{model}}(r,\theta) = \eta_{\text{model}}(r,\theta), \quad \Theta_{\text{model}}(r,\theta) = 0, \\
&\qquad\qquad \text{(velocity componenets in the } r \text{ and } \theta \text{ directions)} \\
&u_{\text{model}}(r,\theta) = \eta_{\text{model}}(r,\theta)\cos\theta, \quad v_{\text{model}}(r,\theta) = \eta_{\text{model}}(r,\theta)\sin\theta, \\
&\qquad\qquad \text{(velocity componenets in the } x \text{ and } y \text{ directions)} \\
&\nu = \sigma\cos^2\theta + \frac{1}{\sigma}\sin^2\theta, \quad r_*(\theta) = t_* + \frac{1}{4}\zeta_0\cos\theta t_*^2, \quad t_* = \frac{1}{2}t_0 + t_s\chi_0^{-1/2}
\end{aligned} \tag{7.20}$$

where t_s is determined from

$$\begin{aligned} -L_{\text{acc}}^2\zeta\cos\theta t_s + \Big(1 - 2Fr\cos\theta + Fr^2 - \frac{1}{4}(\zeta\cos\theta)^2\Big)t_s^2 \\ +\frac{1}{2}\zeta\cos\theta(1 - Fr\cos\theta)t_s^3 + \frac{1}{16}(\zeta\cos\theta)^2 t_s^4 - L_{\text{acc}}^2 = 0 \end{aligned} \tag{7.21}$$

for the leading wave in the $\theta = \psi$ direction (ψ needs to be specified).

The wave generation model was constructed based on LSWE – it is a closed-form approximation of the exact LSWE results. Therefore, its accuracy is also limited to the accuracy of LSWE. The approximation error due to using LSWE to model the wave generation stage in a landslide tsunami problem can be estimated in advance by calculating the estimators $\overline{\mu^2}$ and $\overline{\epsilon}$ and using the formulas that relate the estimators to the RMSDs:

$$\text{RMSD} = \max\Big(104.8(\overline{\mu^2})^{0.5786}, 34.74(\overline{\epsilon})^{1.040}\Big). \tag{7.22}$$

The new wave generation model is an improvement over existing models in many ways: first, the new model specifies nonzero initial flow velocity, which is an important component missing in most existing models; second, the 2DH effects and the wave shape are accounted for based on the newly derived analytical solutions in this study, as opposed to a semi-empirical approach; third, the wave generation time is considered so that the information on time is not lost. The 1998 PNG event was used as an example to demonstrate the differences between three different wave generation models: a full numerical simulation (which is regarded as the reference solution in this example), the new wave generation model, and the empirical wave generation model from Watts et al. (2005). It was found that the new wave generation model captures the overall characteristics of the landslide tsunami significantly better. However, since the empirical model allows for and relies heavily on tuning, it can be tuned to obtain a good fit with field data or the reference solution, if available.

CHAPTER 8

CONCLUSION

In this study, we investigated submarine-landslide-generated water waves using primarily long-wave models, which are approximate wave models particularly suitable for tsunami simulations in a large domain, due to the relatively cheap computation cost. The main objectives were to devise a set of criteria to determine the simplest, and therefore the least computationally expensive, long-wave model that can be used to simulate the wave generation stage of a landslide tsunami problem, and to construct a closed-form landslide wave generation model that requires minimal computational effort. Since the properties and motion of realistic tsunamigenic landslides are mostly unknown, we did not find constructing a complex multiphysics landslide wave model particularly useful, as the relevance of the modeling assumptions to realistic tsunamigenic landslides cannot be verified. To circumvent the difficulties posed by limited knowledge on realistic tsunamigenic landslides, we considered idealized scenarios for which the problem could be parameterized, with important landslide parameters specified as the input parameters. As a result, generalizable results were obtained given the input parameters. The exact properties and motion of realistic tsunamigenic landslides – in other words, the likely ranges of the input parameters in realistic events – were left to be studied by future studies, if at all possible. Lastly, utilizing both the analytical and the numerical findings of this study, we proposed a closed-form semi-analytical landslide tsunami generation model, which can be used to quickly obtain a leading-order-accurate tsunami wave profile due to a submarine landslide. In contrast to existing closed-form wave generation models, the new semi-analytical model was based on the newly derived 2DH analytical solutions, considered the duration of the wave generation stage, and provided information on both the free surface elevation and

the flow velocity.

As a first step of this study, we sought to learn as many insights as possible from analytical knowledge to help parameterize the landslide wave problem. In Chapter 2, both existing and new analytical solutions based on linear wave theory (including LFD, LWD, and LSWE) were presented. Solutions for both 1DH and 2DH, in constant water depth and on a slope, were discussed. Key new findings by our study include: first, the volume, not the exact shape, of a landslide has the strongest effect on the leading tsunami the landslide generates. Second, closed-form analytical solutions (for LSWE, LWD, and LFD) for landslide-generated waves in 2DH constant depth were derived for the first time. The solutions revealed how the waves spread in 2DH – the leading wave decays in time as $t^{-1/2}$ due to frequency dispersion and in space as $r^{-1/2}$ due to radial spreading, and how the landslide speed impacts the wave height – wave amplitude is scaled by $Fr\cos\theta/2(1-Fr\cos\theta)$. Third, ambiguities in the initial conditions used in existing analytical solutions were clarified.

Numerical solvers were needed to obtain the results for cases where analytical solutions were not available. Two numerical solvers, one for the linear wave equations (LSWE and LWD) and the other for the nonlinear wave equations (NSWE, WNWD, and FNWD), were introduced in Chapter 3. The linear numerical solver employed the fourth-order finite difference scheme in space and the third-order SSP-RK scheme in time, and was verified with the analytical solutions discussed in Chapter 2. The nonlinear numerical solver employed a hybrid finite-volume/finite-difference shock-capturing scheme combined with the third-order SSP-RK time-marching scheme. Six select benchmark problems, including three landslide-generated wave experiments, were presented to check the perfor-

mance of the nonlinear numerical solver. For each solver, the governing equations were formulated consistently so that the same solver could be easily instructed to solve the different governing equations. In addition, the governing equations were derived meticulously to ensure an accurate admission of a temporally varying bathymetry, which was interpreted as a moving landslide in a long-wave model.

In Chapter 4, four idealized landslide tsunami scenarios, in which a Gaussian-shaped solid landslide traveled at a constant speed, were considered – 1DH landslide-generated waves in constant depth, 1DH landslide-generated waves on a slope, 2DH landslide-generated waves in constant depth, and 2DH landslide-generated waves on a slope. For each scenario, three or four input parameters were defined, accounting for the height of the landslide, the length of the landslide, the speed of the landslide, and the angle of inclination. Analytical knowledge was applied to propose semi-analytical expressions based on the input parameters to estimate the strength of nonlinearity and the strength of frequency dispersion in a landslide wave problem. To establish an empirical validity threshold of each model, a large number of numerical simulations based on different wave models and covering a wide range of the parameter space was performed. Linear models were inaccurate in cases where nonlinearity was significant, and nondispersive models were inaccurate in cases where frequency dispersion was significant. For each of the four scenarios, two empirical formulas relating the input parameters to expected model error were proposed – one formula to determine the validity of linear models, and the other formula to determine the validity of nondispersive models. In addition, FNWD was found to offer little advantage over WNWD in the landslide tsunami problem – the parameter space in which FNWD was valid yet WNWD was invalid was highly limited. While FNWD had a higher formal accuracy than WNWD, FNWD also required more complex and expensive nu-

merical treatments. As a result, only LSWE, LWD, NSWE, and WNWD were considered as the model choices in this study. A more accurate model is also computationally more expensive. Therefore, to minimize computation cost, it may be desirable to use the simplest acceptable (given an error tolerance) model in a landslide-generated tsunami problem.

Since realistic landslides accelerate from rest instead of suddenly moving at a constant speed, in Chapter 5 we studied the effects of landslide acceleration so that the results in Chapter 4 for a constant-speed landslide could be extended to an accelerating landslide. An analytical investigation was attempted, which revealed a steady state reached by the generated waves after some time and the wave stretching effects due to an accelerating landslide – the faster the acceleration, the shorter the wavelength and the bigger the wave height. Numerical simulations based on LSWE were then performed to obtain empirical formulas that quantify the change in the characteristic wavelength and the change in the characteristic wave amplitude of the leading wave generated by an accelerating landslide.

In Chapter 6, we demonstrated through five examples how to apply the model validity criteria from Chapter 4 along with the empirical formulas from Chapter 5. The five examples include two laboratory experiments in 1DH, two numerical extensions of the laboratory experiments from 1DH to 2DH, and the 1998 PNG tsunami. It was shown that the criteria successfully predicted the model validity in each case for the wave generation stage. For the PNG event, we further pointed out the importance of specifying the initial flow velocity for a landslide-generated tsunami, when it is modeled by specifying the initial conditions in a wave-only tsunami propagation model.

Lastly, motivated by the PNG example, we combined both the analytical and

the numerical findings of this study to construct a closed-form semi-analytical landslide tsunami generation model in Chapter 7. A closed-form model is valuable as it provides a quick, leading-order-accurate landslide tsunami wave profile with minimal, if any, computational effort. The core of the new closed-form semi-analytical model was based on the newly derived 2DH LSWE analytical solutions in Chapter 2. The sloping bottom, the duration of the wave generation stage, the landslide acceleration, and the shoaling effects were accounted for by the empirical means discussed in Chapter 4 and Chapter 5. In contrast to all existing closed-form landslide tsunami generation model, the new model provided information on both the free surface elevation and the flow velocity. Therefore, it could be regarded as the most complete closed-form model currently available. The approximation error of the new wave generation model in a given landslide wave problem could also be estimated using the criteria proposed in Chapter 4.

Overall, this study served as a milestone in modeling landslide-generated tsunamis with long-wave equations. Both new and existing knowledge were reviewed and utilized to better understand the landslide tsunami generation process and the validity of different long-wave models in the landslide tsunami problem. However, great challenges remain in knowing the material properties and the motion of real tsunamigenic landslides. Without concrete geological evidence, any modeling assumption on the landslide dynamics remains effectively discretionary to each modeler. As a result, this study left key landslide parameters open as input parameters and proceeded to examine long-wave model validity in the parameter space. Future studies on means to measure or estimate the key landslide parameters of real tsunamigenic landslides would be highly desired.

APPENDIX A

ANALYTICAL SOLUTIONS FOR STORM-GENERATED WAVES

The analytical solutions discussed in this study for landslide-generated waves can be easily extended to storm-generated waves (storm surge), since the governing equations and the solution methods are essentially identical. For 1DH LSWE, Proudman (1929) first presented the analytical solutions for waves generated by a storm, which is modeled as an atmospheric pressure field moving at a constant speed. Mei (1989) presented the general solution form based on LFD which admits an atmospheric pressure forcing term. Greenspan (1956) presented the integral-form LSWE solution for storm-generated waves on a plane beach in 2DH. More recently, Vennell (2007) and Vennell (2010) utilized some of the analytical knowledge to study the scattering, resonance, and trapping of storm-generated waves. We also note that the storm surge problem is sometimes seen as analogous to the ship wave problem in shallow water, since a moving ship can be approximated as a moving pressure field on the free surface. In this section, we shall extend our new solutions in 2DH constant depth to admit an atmospheric pressure forcing term.

A.1 2DH linear and fully dispersive model in constant depth

The linear and fully dispersive wave model (LFD), first presented in (2.75), can be modified to include a moving atmospheric pressure field, which is well known and

has been shown in Mei (1989):

$$\begin{aligned} \mu^2\phi_{xx} + \mu^2\phi_{yy} + \phi_{zz} = 0, \quad & -1 < z < 0 \\ \phi_z = \mu^2 B_t, \quad & z = -1 \\ \phi_z = \mu^2 \eta_t, \quad & z = 0 \\ \phi_t + \eta = -P, \quad & z = 0 \end{aligned} \quad , \tag{A.1}$$

where $P(x, y, t)$ is a moving atmospheric pressure field acting on the still water surface $z = 0$. The dimensionless P is normalized by $\rho g A$, where ρ is the density of water. After Laplace and Fourier transformations, (A.1) becomes

$$\begin{aligned} -\mu^2(k^2 + l^2)\overset{\sim\sim}{\overset{\cdots}{\phi}} + \overset{\sim\sim}{\overset{\cdots}{\phi}}_{zz} = 0, \quad & -1 < z < 0 \\ \overset{\sim\sim}{\overset{\cdots}{\phi}}_z = \mu^2 s\overset{\sim\sim}{\overset{\cdots}{B}} - \mu^2\widetilde{\overline{B(x, y, t = 0)}}, \quad & z = -1 \\ \overset{\sim\sim}{\overset{\cdots}{\phi}}_z = \mu^2 s\overset{\sim\sim}{\overset{\cdots}{\eta}} - \mu^2\widetilde{\overline{\eta(x, y, t = 0)}}, \quad & z = 0 \\ s\overset{\sim\sim}{\overset{\cdots}{\phi}} - \widetilde{\overline{\phi(x, y, z = 0, t = 0)}} + \overset{\sim\sim}{\overset{\cdots}{\eta}} = -\overset{\sim\sim}{\overset{\cdots}{P}}, \quad & z = 0 \end{aligned} \quad . \tag{A.2}$$

Combine the boundary conditions at $z = 0$ and we obtain

$$\overset{\sim\sim}{\overset{\cdots}{\phi}}_z + \mu^2 s^2\overset{\sim\sim}{\overset{\cdots}{\phi}} = \mu^2 s\widetilde{\overline{\phi(x, y, 0, 0)}} - \mu^2 s\overset{\sim\sim}{\overset{\cdots}{P}} - \mu^2\widetilde{\overline{\eta(x, y, 0)}}, \quad z = 0. \tag{A.3}$$

The same solution approach discussed in Chapter 2 can be used to obtain the transformed solutions:

$$\begin{aligned} \overset{\sim\sim}{\overset{\cdots}{\phi}} = \frac{1}{\cosh \mu q}\frac{1}{s^2 + q^2 D^2}\Bigg(& \Big(s\widetilde{\overline{\phi(x, y, 0, 0)}} - \widetilde{\overline{\eta(x, y, 0)}} - s\overset{\sim\sim}{\overset{\cdots}{P}}\Big)\cosh\Big(\mu q(z + 1)\Big) \\ & -\Big(s\overset{\sim\sim}{\overset{\cdots}{B}} - \widetilde{\overline{B(x, y, 0)}}\Big)\cosh(\mu q z) + \frac{\mu s^2}{q}\Big(s\overset{\sim\sim}{\overset{\cdots}{B}} - \widetilde{\overline{B(x, y, 0)}}\Big)\sinh(\mu q z)\Bigg) \end{aligned} , \tag{A.4}$$

and

$$\overset{\sim\sim}{\overset{\cdots}{\eta}} = -\overset{\sim\sim}{\overset{\cdots}{P}} - s\widetilde{\overline{\phi(x, y, 0, t)}} + \widetilde{\overline{\phi(x, y, 0, 0)}}. \tag{A.5}$$

In the storm surge problem, $B(x, y, t) = 0$ and $P(x, y, t) \neq 0$, and the characteristic length (L) and the characteristic pressure head magnitude (A) of the

pressure field are used for normalization. For a translating pressure field

$$P(x,y,t) = P(x - Fr \cdot t, y), \quad \dddot{\widetilde{P}} = \frac{\widetilde{\overline{P_0}}(k,l)}{s + ik \cdot Fr}, \tag{A.6}$$

we can inverse Laplace transform (A.5) to obtain the analytical solution

$$\begin{aligned}
&\eta(x,y,t) = \eta_{Fr}(x,y,t) + \eta_+(x,y,t) \\
&\eta_{Fr}(x,y,t) = -\frac{1}{2\pi}\int_{-\infty}^{\infty}\int_{-\infty}^{\infty}\widetilde{\overline{P_0}}(k,l)\frac{D^2}{D^2 - Fr^2\frac{k^2}{q^2}}e^{-ik\cdot Fr\cdot t}e^{ikx}e^{ily}dkdl \\
&\eta_+(x,y,t) = \frac{1}{2\pi}\int_{-\infty}^{\infty}\int_{-\infty}^{\infty}\widetilde{\overline{P_0}}(k,l)\Big(\frac{D}{2(D - Fr\frac{k}{q})}e^{-iqDt} + \frac{D}{2(D + Fr\frac{k}{q})}e^{iqDt}\Big) \\
&\qquad\qquad e^{ikx}e^{ily}dkdl
\end{aligned} \tag{A.7}$$

We remark that this solution is very similar yet different from the landslide-generated wave solution (2.89):

$$\begin{aligned}
&\eta(x,y,t) = \eta_{Fr}(x,y,t) + \eta_+(x,y,t) \\
&\eta_{Fr}(x,y,t) = -\frac{1}{2\pi}\int_{-\infty}^{\infty}\int_{-\infty}^{\infty}\frac{\widetilde{\overline{B_0}}(k,l)}{\cosh(\mu q)}\frac{Fr^2\frac{k^2}{q^2}}{D^2 - Fr^2\frac{k^2}{q^2}}e^{-ik\cdot Fr\cdot t}e^{ikx}e^{ily}dkdl \\
&\eta_+(x,y,t) = \frac{1}{2\pi}\int_{-\infty}^{\infty}\int_{-\infty}^{\infty}\frac{\widetilde{\overline{B_0}}(k,l)}{\cosh(\mu q)}\Big(\frac{Fr\frac{k}{q}}{2(D - Fr\frac{k}{q})}e^{-iqDt} - \frac{Fr\frac{k}{q}}{2(D + Fr\frac{k}{q})}e^{iqDt}\Big) \\
&\qquad\qquad e^{ikx}e^{ily}dkdl
\end{aligned} \tag{A.8}$$

Some similarities include: the existence of a fixed-shaped trapped wave η_{Fr} that moves with the pressure field and a free wave η_+, and the dependence of wave amplitudes on D and Fr. Some differences include: the numerators consist of D instead of Fr, the absence of $\cosh(\mu q)$ to reduce the amplitudes of the short-wave components, and the two terms in η_+ share the same sign.

Again, since η_{Fr} is of a permanent shape and no additional analytical investigation is necessary, we will focus on the free wave η_+. Written in polar coordinates,

$$\begin{aligned}
\eta_+(r,\theta,t) = \frac{1}{2\pi}\int_0^{2\pi}\int_0^{\infty}\widetilde{\overline{P_0}}(q,\psi)\Big(&\frac{D}{2(D - Fr\cos\psi)}e^{-iqDt} \\
&+\frac{D}{2(D + Fr\cos\psi)}e^{iqDt}\Big)qe^{iqr\cos(\psi-\theta)}dqd\psi
\end{aligned} \tag{A.9}$$

Following the same solution approach, we then find the far-field solution (valid for large r) to be

$$\begin{aligned}\eta_{\text{far}} &= \frac{1}{\sqrt{2\pi}} r^{-\frac{1}{2}} \int_0^\infty \widetilde{\overline{P_0}}(q,\theta) \frac{D}{2(D - Fr\cos\theta)} q^{\frac{1}{2}} e^{i\left(q(r-Dt)-\frac{\pi}{4}\right)} dq \\ &\quad + \frac{1}{\sqrt{2\pi}} r^{-\frac{1}{2}} \int_0^\infty \widetilde{\overline{P_0}}(q,\pi+\theta) \frac{D}{2(D - Fr\cos\theta)} q^{\frac{1}{2}} e^{-i\left(q(r-Dt)-\frac{\pi}{4}\right)} dq \end{aligned}, \tag{A.10}$$

and the far-field leading wave solution (valid for large r, t and near $r = t$) is

$$\eta_{\text{lead}}(r,\theta,t) = \frac{2V_P}{3\sqrt{\pi}} \frac{1}{2(1 - Fr\cos\theta)} r^{-\frac{1}{2}} (\frac{2}{\mu^2 t})^{\frac{1}{2}} \Omega_1\Big((\frac{2}{\mu^2 t})^{\frac{1}{3}}(r-t)\Big), \tag{A.11}$$

where V_P is the volume enclosed by the shape of the pressure field $P_0(x, y)$.

Comparing (A.11) with the landslide wave solution (2.109),

$$\eta_{\text{lead}}(r,\theta,t) = \frac{2V_B}{3\sqrt{\pi}} \frac{Fr\cos\theta}{2(1 - Fr\cos\theta)} r^{-\frac{1}{2}} (\frac{2}{\mu^2 t})^{\frac{1}{2}} \Omega_1\Big((\frac{2}{\mu^2 t})^{\frac{1}{3}}(r-t)\Big), \tag{A.12}$$

we see that for the same shape functions $P_0 = B_0$, the only difference is the scaling of the wave amplitude: (A.11) is scaled by $1/2(1 - Fr\cos\theta)$ whereas (A.12) is scaled by $Fr\cos\theta/2(1 - Fr\cos\theta)$. An interesting outcome is that for $0 < Fr < 1$, the storm surge leading wave has the same sign everywhere, whereas the landslide-generated leading wave changes sign depending on the direction θ. As is the case for landslide-generated waves, in this study we focus only on the case when $0 < Fr < 1$.

Velocity solutions similar to those for landslide-generated waves can be obtained. Just like in the landslide wave problem, in the far field, the horizontal velocity in the tangential (θ) direction is zero, and the far-field leading wave velocity solutions are still given by (2.112) and (2.114).

A.2 2DH linear shallow water wave equations in constant depth

In the shallow water limit $\mu \to 0$, the far-field solution (valid for large r) (A.10) becomes

$$\begin{aligned}\eta_{\text{far}} &= \frac{1}{\sqrt{2\pi}} r^{-\frac{1}{2}} \frac{1}{2(1-Fr\cos\theta)} \int_0^\infty \widetilde{\overline{P_0}}(q,\theta) q^{\frac{1}{2}} e^{i\left(q(r-t)-\frac{\pi}{4}\right)} dq \\ &+ \frac{1}{\sqrt{2\pi}} r^{-\frac{1}{2}} \frac{1}{2(1-Fr\cos\theta)} \int_0^\infty \widetilde{\overline{P_0}}(q,\pi+\theta) q^{\frac{1}{2}} e^{-i\left(q(r-t)-\frac{\pi}{4}\right)} dq \end{aligned}, \quad \text{(A.13)}$$

where again the integrals can be evaluated in closed-form for certain pressure field shape functions $\widetilde{\overline{P_0}}$, such as the ones discussed in Chapter 2. The storm surge solution is different from the landslide wave solution in only two ways: first, B_0 in the landslide wave solution is replaced with P_0; second, the forcing magnitude $Fr\cos\theta/2(1-Fr\cos\theta)$ in the landslide wave solution is replaced with $1/2(1-Fr\cos\theta)$. On the other hand, the expressions for the far-field velocities are the same as (2.126) and (2.127).

The shallow water solution can also be obtained by solving LSWE directly. Dimensionlessly, 2DH LSWE admitting both an atmospheric pressure field and a landslide (for the storm surge problem, $B = 0$) reads

$$\begin{aligned}&\frac{\partial \eta}{\partial t} + \frac{\partial u}{\partial x} + \frac{\partial v}{\partial y} = \frac{\partial B}{\partial t} \\ &\frac{\partial u}{\partial t} = -\frac{\partial \eta}{\partial x} - \frac{\partial P}{\partial x}, \quad \frac{\partial v}{\partial t} = -\frac{\partial \eta}{\partial y} - \frac{\partial P}{\partial y}\end{aligned}. \quad \text{(A.14)}$$

The three equations can be combined into one:

$$\eta_{tt} - \eta_{xx} - \eta_{yy} = B_{tt} + P_{xx} + P_{yy}, \quad \text{(A.15)}$$

which can be solved using the same approach discussed in Chapter 2 to obtain the same solutions presented above.

BIBLIOGRAPHY

S. Beji and J.A. Battjes. Experimental investigations of wave propagation over a bar. *Coastal Eng.*, 19:151–162, 1993. doi: 10.1016/0378-3839(93)90022-Z.

M. W. Dingemans. Comparison of computations with boussinesq-like models and laboratory measurements. *Technical Report H1684.12 at Delft Hydraulics*, 1994.

C. E. Synolakis. *The runup of long waves.* PhD thesis, California Institude of Technology, 1986.

C. E. Synolakis. The runup of solitary waves. *J. Fluid Mech.*, 185:523–545, 1987. doi: 10.1017/S002211208700329X.

P. L.-F. Liu, Y.-S. Cho, M. J. Briggs, U. Kanoglu, and C. E. Synolakis. Runup of solitary waves on a circular island. *J. Fluid Mech.*, 302:259–289, 1995. doi: 10.1017/S0022112095004095.

C. N. Whittaker. *Modelling of tsunami generated by the motion of a rigid block along a horizontal boundary.* PhD thesis, University of Canterbury, 2013.

L. P. Sue, R. I. Nokes, and M. J. Davidson. Tsunami generation by submarine landslides: comparison of physical and numerical models. *Environ. Fluid Mech.*, 11:133–165, 2011. doi: 10.1007/s10652-010-9205-9.

H. Zhou. *A higher-order depth-integrated model for water waves and currents generated by underwater landslides.* PhD thesis, University of Hawaii at Manoa, 2008.

P. Watts, S. T. Grilli, D. R. Tappin, and G. J. Fryer. Tsunami generation by submarine mass failure. ii: Predictive equations and case studies. *J. Waterway, Port, Coastal, Ocean Eng.*, 131(6):298–310, 2005. doi: 10.1061/ASCE0733-950X2005131:6298.

N. Mori, T. Takahashi, T. Yasuda, and H. Yanagisawa. Survey of 2011 tohoku earthquake tsunami inundation and run-up. *Geophys. Res. Lett.*, 38:L00G14, 2011. doi: 10.1029/2011GL049210.

E. A. Okal, H. M. Fritz, C. E. Synolakis, J. C. Borrero, R. Weiss, P. Lynett, V. Titov, S. Foteinis, B. E. Jaffe, P. L.-F. Liu, and I.-C. Chan. Field survey of the samoa tsunami of 29 september 2009. *Seismo. Res. Lett.*, 81(4):577–591, 2010. doi: 10.1785/gssrl.81.4.577.

P. L.-F. Liu, P. Lynett, H. Fernando, B. E. Jaffe, H. Fritz, B. Higman, R. Morton, J. Goff, and C. E. Synolakis. Observations by the international tsunami survey team in sri lanka. *Science*, 308:1595, 2005a. doi: 10.1126/science.1110730.

D. R. (and 18 others) Tappin. Sediment slump likely caused 1998 papua new guinea tsunami. *Eos*, 80:329, 1999. doi: 10.1029/99EO00241.

C. E. Synolakis, J. P. Bardet, J. C. Borrero, H. Davies, E. A. Okal, E. A. Silver, S. Sweet, and D. R. Tappin. Slump origin of the 1998 papua new guinea tsunami. *Proc. R. Soc. Lond. A*, 458:763–789, 2002. doi: 10.1098/rspa.2001.0915.

P. J. Lynett, J. C. Borrero, P. L.-F. Liu, and C. E. Synolakis. Field survey and numerical simulations: A review of the 1998 papua new guinea tsunami. *Pure Appl. Geophys.*, 160:2119–2146, 2003. doi: 10.1007/s00024-003-2422-0.

H. M. Fritz, F. Mohammed, and J. Yoo. Lituya bay landslide impact generated mega-tsunami 50th anniversary. *Pure Appl. Geophys.*, 166:153–175, 2009. doi: 10.1007/s00024-008-0435-4.

C. Harbitz, G. Pedersen, and B. Gjevik. Numerical simulations of large water waves due to landslides. *J. Hydraul. Eng*, 119(12):1325–1342, 1993. doi: 10.1061/(ASCE)0733-9429(1993)119:12(1325).

E. A. Kulikov, A. B. Rabinovich, R. E. Thomson, and B. D. Bornhold. The landslide tsunami of november 3, 1994, skagway harbor, alaska. *J. Geophys. Res.*, 101(C3):6609–6615, 1996. doi: 10.1029/95JC03562.

S. N. Ward and S. Day. Cumbre vieja volcano – potential collapse and tsunami at la palma, canary islands. *Geophys. Res. Lett.*, 28(17):3397–3400, 2001. doi: 10.1029/2001GL013110.

F. Løvholt, G. Pedersen, and G. Gisler. Oceanic propagation of a potential tsunami from the la palma island. *J. Geophys. Res.*, 113(C9), 2008. doi: 10.1029/2007JC004603.

S. Tinti, E. Bortolucci, and C. Chiavettieri. Tsunami excitation by submarine slides in shallow-water approximation. *Pure Appl. Geophys.*, 158:759–797, 2001. doi: 10.1007/PL00001203.

E. O. Tuck and L.-S. Hwang. Long wave generation on a sloping beach. *J. Fluid Mech.*, 51:449–461, 1972. doi: 10.1017/S0022112072002289.

P. L.-F. Liu, P. Lynett, and C. E. Synolakis. Analytical solutions for forced long waves on a sloping beach. *J. Fluid Mech.*, 478:101–109, 2003. doi: 10.1017/S0022112002003385.

I. I. Didenkulova, I. F. Nikolkina, E. N. Pelinovsky, and N. Zahibo. Tsunami waves generated by submarine landslides of variable volume: analytical solutions for a basin of variable depth. *Nat. Hazards Earth Syst. Sci.*, 10:2407–2419, 2010. doi: 10.5194/nhess-10-2407-2010.

I. I. Didenkulova, I. F. Nikolkina, and E. N. Pelinovsky. Resonant amplification of tsunami waves from an underwater landslide. *Dokl. Earth Sci.*, 436:66–69, 2011. doi: 10.1134/S1028334X11010028.

P. Sammarco and E. Renzi. Landslide tsunami propagating along a plane beach. *J. Fluid Mech.*, 598:107–119, 2008. doi: 10.1017/S0022112007009731.

E. Renzi. *Landslide tsunami*. PhD thesis, Università degli Studi di Roma Tor Vergata, 2010.

E. Renzi and P. Sammarco. Landslide tsunamis propagating around a conical island. *J. Fluid Mech.*, 650:251–285, 2010. doi: 10.1017/S0022112009993582.

E. Renzi and P. Sammarco. The influence of landslide shape and continental shelf on landslide generated tsunamis along a plane beach. *Nat. Hazards Earth Syst. Sci.*, 12:1503–1520, 2012. doi: 10.5194/nhess-12-1503-2012.

S. N. Seo and P. L.-F. Liu. Edge waves generated by the landslide on a sloping beach. *Coastal Eng.*, 73:133–150, 2013. doi: 10.1016/j.coastaleng.2012.10.008.

C. C. Mei. *The Applied Dynamics of Ocean Surface Waves*. World Scientific, 1989.

P. Heinrich. Nonlinear water waves generated by submarine and aerial landslides. *J. Waterway, Port, Coastal, Ocean Eng.*, 118(3):249–266, 1992. doi: 10.1061/(ASCE)0733-950X(1992)118:3(249).

S. Assier Rzadkiewicz, C. Mariotti, and P. Heinrich. Numerical simulation of submarine landslides and their hydraulic effects. *J. Waterway, Port, Coastal, Ocean Eng.*, 123(4):149–157, 1997. doi: 10.1061/(ASCE)0733-950X(1997)123:4(149).

P. Watts. *Water waves generated by underwater landslides*. PhD thesis, California Institude of Technology, 1997.

P. Watts. Tsunami features of solid block underwater landslides. *J. Waterway, Port, Coastal, Ocean Eng.*, 126:144–152, 2000. doi: 10.1061/(ASCE)0733-950X(2000)126:3(144).

P. L.-F. Liu, T.-R. Wu, F. Raichlen, C. E. Synolakis, and J. Borrero. Runup and rundown generated by three-dimensional sliding masses. *J. Fluid Mech.*, 536: 107–144, 2005b. doi: 10.1017/S0022112005004799.

A. Panizzo, P. De Girolamo, and A. Petaccia. Forecasting impulse waves generated by subaerial landslides. *J. Geophys. Res.*, 110:C12025, 2005. doi: 10.1029/2004JC002778.

F. Enet and S. T. Grilli. Experimental study of tsunami generation by three-dimensional rigid underwater landslides. *J. Waterway, Port, Coastal, Ocean Eng.*, 133:442–454, 2007. doi: 10.1061/(ASCE)0733-950X(2007)133:6(442).

M. Di Risio, G. Bellotti, A. Panizzo, and P. De Girolamo. Three-dimensional experiments on landslide generated waves at a sloping coast. *Coastal Eng.*, 56: 659–671, 2009. doi: 10.1016/j.coastaleng.2009.01.009.

G. Sælevik, A. Jensen, and G. Pedersen. Experimental investigation of impact generated tsunami; related to a potential rock slide, western norway. *Coastal Eng.*, 56:897–906, 2009. doi: 10.1016/j.coastaleng.2009.04.007.

E. Lindstrøm, G. Pedersen, A. Jensen, and S. Glimsdal. Experiments on slide generated waves in a 1:500 scale fjord model. *Coastal Eng.*, 92:12–23, 2014. doi: 10.1016/j.coastaleng.2014.06.010.

H. M. Fritz, W. H. Hager, and H.-E. Minor. Near field characteristic of landslide generated impulse waves. *J. Waterway, Port, Coastal, Ocean Eng.*, 130:187–302, 2004. doi: 10.1061/(ASCE)0733-950X(2004)130:6(287).

V. Heller and W. H. Hager. Impulse product parameter in landslide generated impulse waves. *J. Waterway, Port, Coastal, Ocean Eng.*, 136(3):145–155, 2010. doi: 10.1061/(ASCE)WW.1943-5460.0000037.

F. Mohammed and H. M. Fritz. Physical modeling of tsunamis generated by three-dimensional deformable granular landslides. *J. geophys. Res.*, 117:C11015, 2012. doi: 10.1029/2011JC007850.

L. Jiang and P. H. LeBlond. The coupling of a submarine slide and the surface waves which it generates. *J. Geophys. Res.*, 97(C8):12731–12744, 1992. doi: 10.1029/92JC00912.

L. Jiang and P. H. LeBlond. Three-dimensional modeling of tsunami generation due to a submarine mudslide. *J. Phys. Oceanogr.*, 24:559–572, 1994. doi: 10.1175/1520-0485(1994)024<0559:TDMOTG>2.0.CO;2.

L. Jiang and P. H. LeBlond. Numerical modeling of an underwater bingham plastic mudslide and the waves which it generates. *J. Geophys. Res.*, 98(C6):10303–10317, 1993. doi: 10.1029/93JC00393.

P. Lynett and P. L.-F. Liu. A numerical study of submarine-landslide-generated waves and run-up. *Proc. R. Soc. Lond.*, A 458:2885–2910, 2002. doi: 10.1098/rspa.2002.0973.

D. Dutykh and H. Kalisch. Boussinesq modeling of surface waves due to underwater landslides. *Nonlin. Processes Geophys.*, 20:267–285, 2013. doi: 10.5194/npg-20-267-2013.

S. T. Grilli and P. Watts. Tsunami generation by submarine mass failure i: Modeling, experimental validation, and sensitivity analyses. *J. Waterway, Port, Coastal, Ocean Eng.*, 131(6):283–297, 2005. doi: 10.1061/(ASCE)0733-950X(2005)131:6(283).

H. Zhou and M. H. Teng. Extended fourth-order depth-integrated model for water

waves and currents generated by submarine landslides. *J. Eng. Mech.*, 136(4): 506–516, 2010. doi: 10.1061/(ASCE)EM.1943-7889.0000087.

C. N. Whittaker, R. I. Nokes, and M. J. Davidson. Tsunami forcing by a low froude number landslide. *Environ. Fluid Mech.*, 15(6):1215–1239, 2015. doi: 10.1007/s10652-015-9411-6.

C. N. Whittaker, R. I. Nokes, H.-Y. Lo, and P. L.-F. Liu. Physical and numerical modelling of tsunami generation by a moving obstacle at the bottom boundary. *Environ. Fluid Mech.*, In press, 2017. doi: 10.1007/s10652-017-9526-z.

P. Watts, J. C. Borrero, D. R. Tappin, J.P. Bardet, S. T. Grilli, and C. E. Synolakis. Novel simulation technique employed on png event. *Proc. 22nd Gen. Assemb. International Union of Geodesy and Geophysics*, 1999.

P. Watts, S. T. Grilli, J. T. Kirby, G. J. Fryer, and D. R. Tappin. Landslide tsunami case studies using a boussinesq model and a fully nonlinear tsunami generation model. *Nat. Hazards Earth Syst. Sci.*, 3:391–402, 2003. doi: 10.5194/nhess-3-391-2003.

S. M. Abadie, J. C. Harris, S. T. Grilli, and R. Fabre. Numerical modeling of tsunami waves generated by the flank collapse of the cumbre vieja volcano (la palma, canary islands): Tsunami source and near field effects. *J. Geophys. Res.*, 117(C5), 2012. doi: 10.1029/2011JC007646.

C. M. Bender and S. A. Orszag. *Advanced mathematical methods for scientists and engineers*. Springer, 1999.

S. Tinti and E. Bortolucci. Energy of water waves induced by submarine landslides. *Pure Appl. Geophys.*, 157:281–318, 2000. doi: 10.1007/s000240050.

O. Nwogu. Alternative form of boussinesq equations for nearshore wave propagation. *J. Waterway, Port, Coastal, Ocean Eng.*, 119(6):618–638, 1993. doi: 10.1061/(ASCE)0733-950X(1993)119:6(618).

G. Wei, J. T. Kirby, S. T. Grilli, and R. Subramanya. A fully nonlinear boussinesq model for surface waves. part 1. highly nonlinear unsteady waves. *J. Fluid Mech.*, 294:71–92, 1995. doi: 10.1017/S0022112095002813.

A. D. Poularikas. *The Transforms and Applications Handbook*. CRC Press, 2 edition, 2000.

Werner Rosenheinrich. Table of some indefinite integrals of bessel functions. http://www.eah-jena.de/∼rsh/Forschung/Stoer/besint.pdf, 2015.

I. S. Gradshteyn and I. M. Ryzhik. *Table of integrals, series, and products*. Academic Press, 7 edition, 2007.

K. Kajiura. The leading wave of a tsunami. *Bull. Earthq. Res. Inst.*, 41:535–571, 1963.

E. A. Okal and C. E. Synolakis. Sequencing of tsunami waves: why the first wave is not always the largest. *Geophys. J. Int.*, 204(2):719–735, 2016. doi: 10.1093/gji/ggv457.

A. B. Kennedy, J. T. Kirby, Q. Chen, and R. A. Dalrymple. Boussinesq-type equations with improved nonlinear performance. *Wave Motion*, 33:225–243, 2001. doi: 10.1016/S0165-2125(00)00071-8.

F. Shi, J. T. Kirby, J. C. Harris, J. D. Geiman, and S. T. Grilli. A high-order adaptive time-stepping tvd solver for boussinesq modeling of breaking waves and coastal inundation. *Ocean Model.*, 43–44:36–51, 2012. doi: 10.1016/j.ocemod.2011.12.004.

S. Gottlieb, C.-W. Shu, and E. Tadmor. Strong stability-preserving high-order time discretization methods. *SIAM Rev.*, 43(1):89–112, 2001. doi: 10.1137/S003614450036757X.

E. F. Toro. *Shock-capturing methods for free-surface shallow flows*. Wiley, 2001.

G.-S. Jiang and C.-W. Shu. Efficient implementation of weighted eno schemes. *J. Comput. Phys.*, 126:202–228, 1996. doi: 10.1006/jcph.1996.0130.

Y. Li and F. Raichlen. Non-breaking and breaking solitary runup. *J. Fluid Mech.*, 456:295–318, 2002. doi: 10.1017/S0022112001007625.

Y. Wei, X. Z. Mao, and K. F. Cheung. Well-balanced finite-volume model for long-wave runup. *J. Waterway, Port, Coastal, Ocean Eng.*, 132:114–124, 2006. doi: 10.1061/(ASCE)0733-950X(2006)132:2(114).

J. B. Shiach and C. G. Mingham. A temporally second-order accurate godunov-type scheme for solving the extended boussinesq equations. *Coastal Eng.*, 56: 32–45, 2009. doi: 10.1016/j.coastaleng.2008.06.006.

Q. Zhou, J. Zhan, and Y. Li. High-order finite volume weno schemes for boussinesq modelling of nearshore wave processes. *J. Hydraul. Res.*, 54:646–662, 2016. doi: 10.1080/00221686.2016.1175520.

M. Tonelli and M. Petti. Hybrid finite volume-finite difference scheme for 2dh improved boussinesq equations. *Coastal Eng.*, 56:609–620, 2009. doi: 10.1016/j.coastaleng.2009.01.001.

M. Tissier, P. Bonneton, F. Marche, F. Chazel, and D. Lannes. A new approach to handle wave breaking in fully non-linear boussinesq models. *Coastal Eng.*, 67: 54–66, 2012. doi: 10.1016/j.coastaleng.2012.04.004.

M. Kazolea, A. I. Delis, and C. E. Synolakis. Numerical treatment of wave breaking on unstructured finite volume approximations for extended boussinesq-type equations. *J. Comput. Phys.*, 271:281–305, 2014. doi: 10.1016/j.jcp.2014.01.030.

S. Sweet and E. A. Silver. Tectonics and slumping in the source region of the 1998 papua new guinea tsunami from seismic reflection images. *Pure Appl. Geophys.*, 160:1945–1968, 2003. doi: 10.1007/s00024-003-2415-z.

D. R. Tappin, P. Watts, G. M. McMurtry, Y. Lafoy, and T. Matsumoto. The sissano, papua new guinea tsunami of july 1998 – offshore evidence on the source mechanism. *Marine Geology*, 175:1–23, 2001. doi: 10.1016/S0025-3227(01)00131-1.

H. L. Striem and T. Miloh. Tsunamis induced by submarine slumpings off the coast of israel. *Int. Hydrogr. Rev.*, 2:41–55, 1976.

E. Pelinovsky and A. Poplavsky. Simplified model of tsunami generation by submarine landslide. *Phys. Chem. Earth, Part A Solid Earth Geod.*, 21(12):13–17, 1996. doi: 10.1016/S0079-1946(97)00003-7.

P. Watts. Wavemaker curves for tsunamis generated by underwater landslides. *J. Waterway, Port, Coastal, Ocean Eng.*, 124(3):127–137, 1998. doi: 10.1061/(ASCE)0733-950X(1998)124:3(127).

T. S. Murty. Tsunami wave height dependence on landslide volume. *Pure Appl. Geophys.*, 160:2147–2153, 2003. doi: 10.1007/s00024-003-2423-z.

H. M. Fritz, W. H. Hager, and H.-E. Minor. Landslide generated impulse waves, part 2: Hydrodynamic impact craters. *Exp. Fluids.*, 35:520–532, 2003. doi: 10.1007/s00348-003-0660-7.

V. Heller and J. Spinneken. On the effect of the water body geometry on landslide-tsunamis: physical insight from laboratory tests and 2d to 3d wave parameter transformation. *Coast. Eng.*, 104(10):113–134, 2015. doi: 10.1016/j.coastaleng.2015.06.006.

J. Proudman. The effects on the sea of changes in atmospheric pressure. *Geophys. J. Int.*, 2:197–209, 1929. doi: 10.1111/j.1365-246X.1929.tb05408.x.

H. P. Greenspan. The generation of edge waves by moving pressure distributions. *J. Fluid Mech.*, 1:574–592, 1956. doi: 10.1017/S002211205600038X.

R. Vennell. Long barotropic waves generated by a storm crossing topography. *J. Phys. Oceanogr.*, 37:2809–2823, 2007. doi: 10.1175/2007JPO3687.1.

R. Vennell. Resonance and trapping of topographic transient ocean waves generated by a moving atmospheric disturbance. *J. Fluid Mech.*, 650:427–442, 2010. doi: 10.1017/S0022112009993739.